Doctoral Thesis in Life Sciences and Computer Science

Neuromechanical basis of airflow-dependent antennal positioning in hawkmoths

DINESH NATESAN

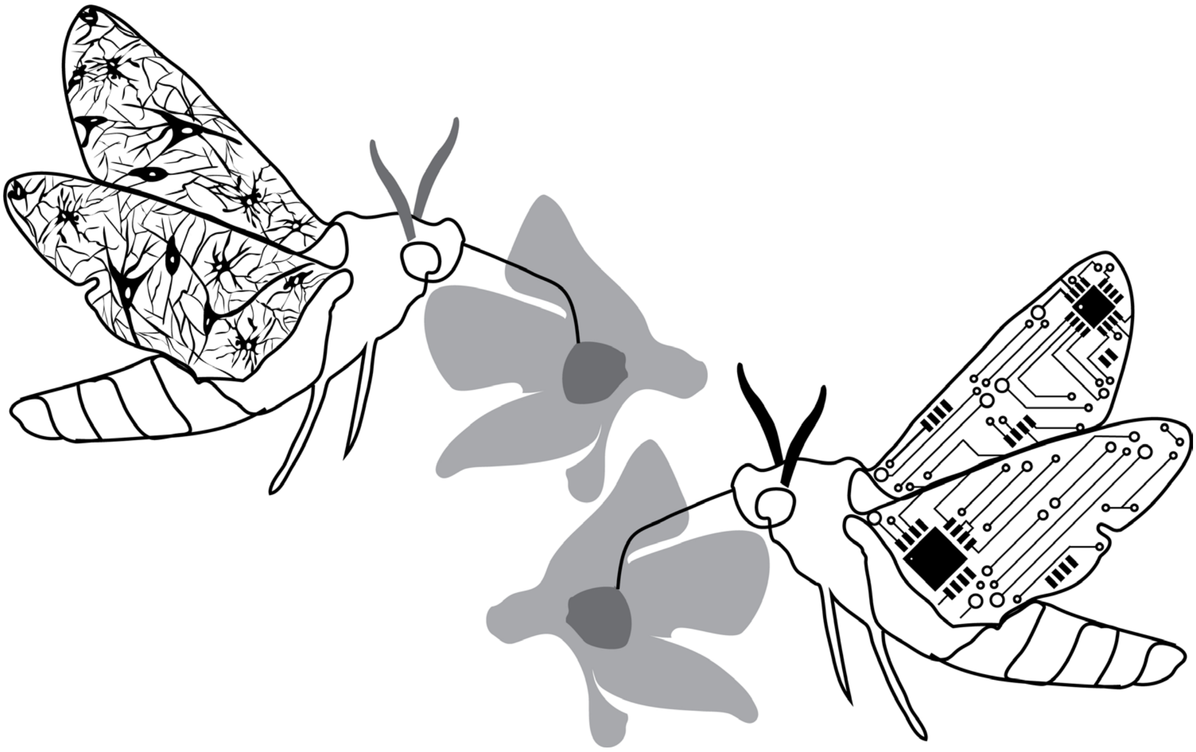

Bangalore, India & Stockholm, Sweden 2020

Neuromechanical basis of airflow-dependent antennal positioning in hawkmoths

A Thesis

Submitted to the
Manipal Academy of Higher Education
and
KTH Royal Institute of Technology

towards a joint
Doctor of Philosophy (PhD)
in
Life Sciences
and
Computer Science

by
Dinesh Natesan

Under the guidance of

Prof. Sanjay P. Sane and Prof. Örjan Ekeberg
NCBS, Bangalore KTH, Stockholm

National Centre for Biological Sciences (NCBS), Bangalore
KTH Royal Institute of Technology, Stockholm
Manipal Academy of Higher Education, Manipal

September, 2020

TRITA-EECS-AVL-2020:62
ISBN: 978-91-7873-697-3

Tryck: Universitetsservice US-AB

Declaration

I declare that this thesis, submitted for a joint Doctor of Philosophy in Life Sciences and Computer Science to *Manipal Academy of Higher Education* and *KTH Royal Institute of Technology*, as part of the **Erasmus Mundus Joint Doctorates** programme **EuroSPIN**, is my original work, conducted under the supervision of my advisors **Sanjay P. Sane** and **Örjan Ekeberg**. I also wish to inform that no part of the research has been submitted for a degree or examination at any other university. References, help and material obtained from other sources have been duly acknowledged.

N. Dinesh

Dinesh Natesan

September, 2020

MANIPAL ACADEMY *of* HIGHER EDUCATION
(Deemed to be University under Section 3 of the UGC Act, 1956)
INSPIRED BY LIFE

ncbs

KTH VETENSKAP OCH KONST

Declaration of originality of research work

I have not committed plagiarism in any of the forms described in the plagiarism policy of Manipal Academy of High Education and KTH Royal Institute of Technology. I have documented all methods, data and processes truthfully and I have not manipulated any data. I have mentioned all persons who were significant facilitators of the work. The work has been screened electronically for plagiarism.

N. Dinesh

Dinesh Natesan **Place:** Bangalore
Registration Number: 139000001 **Date:** September, 2020

We, Prof. Sanjay P. Sane and Prof. Örjan Ekeberg, certify and attest that the work done by Dinesh Natesan is original and vouch that there is no plagiarism. The work is being submitted for a joint Doctor of Philosophy in Life Sciences and Computer Science to Manipal Academy of Higher Education and KTH Royal Institute of Technology under the Erasmus Mundus Joint Doctorates programme EuroSPIN, and has not been submitted to any other University for any other degree.

Sanjay P. Sane **Place:** Bangalore
National Centre for Biological Sciences **Date:** September, 2020
Bangalore 560065, India

Örjan Ekeberg **Place:** Stockholm
KTH Electrical Engineering and Computer Science, **Date:** September, 2020
S-100 44 Stockholm, Sweden

MANIPAL
ACADEMY of HIGHER EDUCATION
(Deemed to be University under Section 3 of the UGC Act, 1956)

ncbs

KTH
VETENSKAP OCH KONST

Certificate

This is to certify that the work incorporated in this thesis **Neuromechanical basis of airflow-dependent antennal positioning in hawkmoths** submitted by **Dinesh Natesan** was carried out under my supervision. The thesis is being submitted to *Manipal Academy of Higher Education* and *KTH Royal Institute of Technology* for a joint Doctor of Philosophy in Life Sciences and Computer Science, as a part of the **Erasmus Mundus Joint Doctorates** programme **EuroSPIN.** No part of this thesis has been submitted for a degree or examination at any other university. References, help and material obtained from other sources have been duly acknowledged.

Sane

Sanjay P. Sane
National Centre for Biological Sciences
Tata Institute of Fundamental Research,
Bellary Road,
Bangalore 560065,
Karnataka,
India

September, 2020

MANIPAL
ACADEMY of HIGHER EDUCATION
(Deemed to be University under Section 3 of the UGC Act, 1956)
INSPIRED BY LIFE

ncbs

KTH
VETENSKAP
OCH KONST

Certificate

This is to certify that the work incorporated in this thesis **Neuromechanical basis of airflow-dependent antennal positioning in hawkmoths** submitted by **Dinesh Natesan** was carried out under my supervision. The thesis is being submitted to *Manipal Academy of Higher Education* and *KTH Royal Institute of Technology* for a joint Doctor of Philosophy in Life Sciences and Computer Science, as a part of the **Erasmus Mundus Joint Doctorates** programme **EuroSPIN**. No part of this thesis has been submitted for a degree or examination at any other university. References, help and material obtained from other sources have been duly acknowledged.

Örjan Ekeberg
KTH Electrical Engineering and Computer Science,
S-100 44 Stockholm

September, 2020

Certificate

I certify that this thesis entitled **"Neuromechanical basis of airflow-dependent antennal positioning in hawkmoths"** comprises research work carried out by **Dinesh Natesan** at *National Centre for Biological Sciences* and *KTH Royal Institute of Technology* under the supervision of **Prof. Sanjay P. Sane** and **Prof. Örjan Ekeberg** during the period 2013 - 2019. The research work in this thesis was done towards a joint Doctor of Philosophy (PhD) in Life Sciences and Computer Science from *Manipal Academy of Higher Education, Manipal, India* and *KTH Royal Institute of Technology, Stockholm, Sweden*, respectively, under the **Erasmus Mundus Joint Doctorates** programme **EuroSPIN**. The results presented in this thesis have not been submitted previously to this or any other University for a PhD or any other degree.

Head of Academics
National Centre for Biological Sciences
Tata Institute of Fundamental Research
Bangalore

Dedicated to:

Thāthā

for saying yes to all
my ridiculus demands,
and whose immense curiosity
about all aspects of life
inspires me everyday.

Amma & Appa

for all the support
from the materialistic
to the pyschological.

Kavya

Acknowledgments

I came into science fresh after BITS, not knowing the vastness of its seas or the thrill of scientific exploration. It was a very fortuitous sequence of events that led me here - from picking a dual degree in biological sciences along with my bachelors in electronics, to experimenting with where to do my internship. However, once here, I was quickly hooked, and I felt at home in its turbulent waters. Academia, despite having a slower timescale than the world outside, began to consistently change me. Apart from becoming older (an unpleasant side-effect), I grew intellectually, and by the end of my PhD, I was no longer the naïve, impatient college kid who entered the campus. There are a ton of people who catalyzed this change, without whom my intellectual growth would not have been possible.

A huge portion of this is due to my advisor, Sanjay. He mentored me as an intern, took me in as a JRF and inspired me to get into science. It is because of him that I first saw the beauty in well designed experiments, learned the skepticism required to analyze data and felt the thrill of scientific exploration. When I wanted to do a PhD at the interface between Neuroscience and Computer Science, he somehow became part of the EuroSPIN program, formed a project with Örjan, and strongly urged me to apply there. Both my journey in academia and my PhD started with him.

Everybody needs a voice that says, "Wait, why are you doing that again?". My advisor, Örjan, was that voice for me, and slowly trained me to ask such critical questions by myself. Throughout my PhD, he instilled in me the value of recognizing and explicitly stating assumptions that are inherent to every experiment and simulation. My current inclination towards first testing out a hypothesis using a simulation before following it up with experiments is a mindset that I learned from him.

It is good to have out-of-the-box thinkers who continually surprise you by providing alternate lines of thought. My thesis committee members Upi, Madhu, and Vatsala fulfilled this role. Throughout my TCM, they challenged my experiments, data and models, and provided the kindling for new ideas. Additionally, Upi, Vatsala and Sanjay also took part in journal clubs where they mentored us on how to read papers and digest papers far from our expertise. Their lectures in the basic neurobiology course formed my conceptual foundation, for which I am incredibly thankful.

Nearly every member in my lab helped me improve and become better throughout the course of my PhD. My sincere thanks to all of them. The older lab folk especially influenced my first few years by teaching me the ropes and mentoring me in the ways of the field. My thanks to Nitesh, the first person I worked with as an intern, for becoming both a close friend and a collaborator, and helping me immensely throughout my PhD. Aravin, for taking me to my first ever field trip, and teaching me the pleasure of sitting outside and observing nature. Anand, for imparting all his knowledge about antennal positioning as well as for seeding the idea of me working on the airflow response. Tanvi, for her radiantly positive and confident attitude. Taruni and Harshada for all the lively moments in the lab, and the funny stories, as well as the long conversations about antennal positioning in insects. Umesh, for inspiring in me the DIY culture, and for the tremendous help in designing setups, and sometimes really random things.

Then there were my peers, people who joined the lab at roughly the same time as me. Each of them brought in a new perspective from which it was fascinating to discover and learn. My thanks to Ajinkya, who continued where Aravin left off, and taught me much about observing moths in the wild, as well as helped me design my first set of greenhouse experiments (and lectured me on some worldly skills as well). Amritansh for opening my eyes to the world of art, as well as teaching me about the fascinating lives of termites. Akash for discussions ranging from the wing-hinge in insects to using dynamical systems to solve scientific problems. Abin for prolonged and uninhibited discussions about crazy ideas, as well as for teaching me about photography. Sree Krishna for all the discussions on politics, philosophy, and the torrent of not-so-great jokes. Payel and Maitri for the so many favors they have done for me; they were ones I could count on for getting things done. As it happens often, my peers were the ones I hung out with most often. Quite a bit of my free time during my PhD was spent sharing laughs with Nitesh, Ajinkya, Amritansh, Akash and Abin, as well as mulling over big questions of life during stimulated thought sessions. I am particularly thankful for all those moments.

Finally, I am thankful to the newer members, Agnish, Chinmayee, Shipra, Subha, Simran, Vidur, Sujay, and Shivansh. They brought in a fresh perspective - asking what/how/why to assumptions which the older folks had made their peace with. Shivansh, especially, brought in a clear logical way of thinking which I quite liked, and I am extremely grateful that he decided to collaborate with me. He questioned everything I had already done, and began to improve upon my hacks, which helped both of us grow as we worked on the project. Apart from them, there was also a constant supply of kids fresh out of high school who made things interesting in the lab.

Outside of NCBS, I was fortunate enough to spend roughly half my time in KTH, Stockholm. The group in KTH was a fun and nerdy group, with people's interests ranging from neuronal properties to machine learning and artificial intelligence. This made for really interesting and fun conversations, and it was an absolute delight to be part of them. I am really thankful to these folks for making Stockholm feel like home during my visits there. Anu Nair, my fellow batchmate, looked out for me during my visits, almost like an older brother. From picking me up at the airport, to finding an apartment for me, to making sure I settled in nicely, he helped me immensely. Jyotika, for all the fun trips around Stockholm and for introducing me to so many awesome books, and inculcating the value of reading widely. I am especially thankful to her for introducing me to Valentino Braitenberg's book - Vehicles. Both Anu and Jyotika became my Indian gang, and we discussed all sorts of topics ranging from the state of politics in India to computations in the brain. Peter was one of the first Swedes I met. Apart from sharing the same birthday, we took courses together and loved improving our productivity using apps, which we discussed often (thereby ironically reducing our productivity). He became my guide to Swedish culture. Ramon and Ylva - for so many interesting discussions, ranging from culture and science to philosophy. I am extremely thankful to Ramon for inculcating in me the ways of conscious rational thought (LessWrong and HPMOR), as well as for introducing me to many interesting books and conversations. Matthias (and Peter) for working on the NEAT algorithm as a side project and for teaching me how to make Python code beautiful (in the sense of mathematical beauty). The rest of the computational biology department for the lunch time, basking in the sun, discussions - Emil, Luiz, Jan, Georgios, Daniel, Martino, Arvind and several others. A huge thanks to Arvind and his wife Anu, who hosted many dinners at his place and treated us with Indian food. He especially timed it during Indian festivals and helped us get over our homesickness. Apart from dinners. the discussions with him were extremely engrossing and so full of passion that we never felt the time pass.

Apart from the labs I was part of, I am fortunate to have met several interesting people who helped me along the way. The neuroscience gang - Venkat, Sahil, Sriram, Anchal and Ananth - for all those discussions about how brains perform computation, and on deciphering the code, as well as the stimulated thought sessions about everything under the sun. Every discussion with them helped me learn something new, from the latest trends in optogenetics from Sriram to the hot papers in neuroscience from Venkat. I am thankful to Rohit, Sahil, Sriram and Krishnan for helping me take many informal courses in NCBS ranging from the basics of coding, to machine learning and statistics (as well as RUSMALAI). I am especially thankful to Rohit for projects and discussions about computers and coding, and teaching me how to make beautiful figures in Illustrator.

Then, there's the "just fun, so let's do it" stuff. The improv group - an eccentric group of people who taught me how to "yes, and", not just literally for the show, but also in life. The music maestro - Ananth, who taught me the basics of musical notions (even the underlying philosophy) and inspired me to start learning the piano. The Counterstrike group - for all those days when you wanted to release stress by shooting people (in videogames). And of course, Aparna, Chaitra, Sree Krishna, Ebi, Sruthi and Rohit for all the game nights and cookouts. Not to mention, the parties and visits to Druid Garden with friends.

I would not have achieved even a modicum of work-life balance, if I had not met Sruthi. Sincere thanks to her for being there throughout, teaching me to appreciate food and helping me come fashionable, and of course, keeping me reading by subtly gifting books I ought to be reading. I definitely would not have grown if not for this constant positive influence.

Finally, my family. My grandparents and my uncle for making me visit Coimbatore for well-deserved breaks. It was always fun, watching movies with my Grandpa, teach-

ing him how to use a computer, getting force-fed by my grandma, and my uncle who just happened to be around right when we need a ride. My sister, for giving financial advice in times of need, ranging from mutual funds to t-shirts. And finally my mom and dad. Both of them gave me quite a bit of freedom, allowing me to do whatever I felt like, from my decision to do a dual degree, to leaving industry and pursuing my PhD. Both my sister and parents were always worried about me, silently wondering why I was working on flies and moths, but allowed me to do what I liked and supported me in times of need - I couldn't have done it without them.

Summary

Fast behaviors, seen in varied life forms, are often considered to be stereotypic and reflexive and the control neural circuits to be hard-wired. However, many such reflexes have been shown to respond in a context-dependent manner. The work presented in this dissertation focuses on uncovering the principles of one such context-dependent behavior - antennal positioning in insects.

Insect antennae acquire multimodal sensory cues that are required for a wide range of behaviors. These include odor, temperature, humidity, as well as mechanical vibrations from the surroundings. Each modality encodes a different aspect of the environment and is used appropriately to control behavior. Antennal vibrations, for instance, provide feedback relevant for flight stabilization, and is used to modulate wing movements on short, stroke-to-stroke, timescales. Olfactory cues, on the other hand, indicate presence of food and mates, and are used to alter flight trajectories over longer timescales of multiple wing-strokes. Therefore, for a proper behavioral response, the antennae must optimally acquire sensory cues over multiple timescales. Context-dependent modulation of the antennae perhaps enhances their functionality by tuning their dynamic range.

This dissertation focuses on one context, namely airflow, and its effect on antennal positioning. Hawkmoths, and diverse insects, actively position their antennae at the onset of flight by bringing them forward. During flight, they dynamically alter this position based on airflow. Two antennal mechanosensors are involved in this behavior, one being the Böhm's bristles, which monitors and feeds back the position of the antennae, and the second being the Johnston's organs, which are stimulated by frontal airflow generated during flight.

The first part of the thesis concerns the control algorithms that underlie the sensory integration of antennal mechanosensory input to produce airflow-dependent antennal positioning. Using the Oleander hawkmoth, *Daphnis nerii*, as a system of study, the behavior is investigated with a combination of experiments and computational techniques. We find that the dynamics of this behavior can be captured by a tunable feedback loop consisting of two components. One, a negative feedback loop that stably maintains antennae at a preferred position, or set-point, using positional feedback from the Böhm's bristles. Two, a dynamic set-point that is modulated by airflow (and other context specific cues). Furthermore, a minimalistic model neural circuit based on these components simulate airflow-dependent modulation of antennae. Such circuits could enable moths to maintain stable antennal position on short timescales while retaining context-based flexibility over longer durations.

The latter half of the thesis focuses on each of the individual components. The neural mechanisms underlying modulation of set-point by the Johnston's organs are investigated using behavioral and electrophysiological experiments. The positional feedback, sensed and encoded by the Böhm's bristles, is investigated using biomechanical models. These provide an understanding of how airflow-dependent, or more generally, context-dependent antennal positioning arises as a result of these individual components. As a whole, this dissertation provides a conceptual framework that utilizes experimental and computational techniques to formally describe and understand context-dependent behaviors.

Sammanfattning

Snabba rörelser hos olika djur ses ofta som stereotypa reflexer, genererade av fixa neurala sensomotoriska återkopplingar. Många reflexer har dock visat sig variera beroende på situationen. Denna avhandling fokuserar på att försöka förstå en sådan situationsberoende reflex: insekters positionering av antennerna.

Antennerna hos insekter är fyllda med sensorer av olika typ som behövs för alla möjliga beteenden. Där finns t.ex. sensorer för lukt, temperatur, fuktighet och vibrationer. Var och en fångar upp viktig information från omgivningen som används för att påverka olika beteenden. Vibrationer, till exempel, ger återkoppling som behövs för att styra vingarnas rörelser så att insekten kan flyga stabilt. Detta kräver att återkopplingen är mycket snabb, från ett vingslag till nästa. Lukt, som används för att lokalisera föda och partners, påverkar flygningen över betydligt längre tidsskalor. Antennernas position påverkar alla dessa sensorer samtidigt och det är därför inte förvånande att reflexerna som styr positionen behöver anpassas till situationen.

Denna avhandling fokuseras på hur antennernas positionering påverkas av en specifik faktor, nämligen vindhastigheten. Fjärilar, och många andra insekter, vinklar aktivt sina antenner framåt i samband med att de börjar flyga. Under flygningen anpassas sedan vinkeln aktivt beroende på vindhastigheten. Detta beteende är kopplat till två olika mekanosensorer; dels Böhm's hårsensorer som registrerar antennens position, dels Johnston's organ, vibrationssensorer som bl.a. reagerar på vindhastigheten.

Första delen av avhandlingen presenterar en kartläggning av hur de olika sensoriska signalerna integreras för att åstadkomma den vindberoende positioneringen av antennerna. Specifikt studeras här fjärilsarten Oleandersvärmare som analyseras med en kombination av beteendeexperiment och datormodeller. Vi visar att beteendet kan beskrivas som en justerbar reflex bestående av två delar: dels en snabb negativ återkopplingsloop som håller positionen vid ett börvärde baserat på signaler från Böhm's hårsensorer; dels en långsammare justering av detta börvärde baserat på vindhastigheten. En minimalistiskt neural modell baserad på dessa delar kan i simuleringar reproducera beteendet kvantitativt. Modellen förklarar hur fjärilar kan hålla antennernas positionen stabil med snabba reaktioner på störningar samtidigt som de kan anpassa positionen baserat på långsammare signaler.

I avhandlingens andra halva analyseras systemets komponenter i detalj. De neurala mekanismerna bakom hur Johnston's organ ändrar börvärdet undersöks med såväl beteende- som elektrofysiologiska experiment. Den snabba återkopplingen via Böhm's hårsensorer analyseras med hjälp av biomekaniska modeller. Detta ger en förklaringsmodell för hur antennernas positionsreflex påverkas av vindhastigheten, och mer generellt av situationen, baserat på samspelet mellan systemets delar. Som helhet utgör denna avhandling ett exempel på hur experimentella och beräkningstekniska metoder kan kombineras för att entydigt beskriva och förstå situationsberoende beteenden.

Publications

1. **D. Natesan**, N. Saxena, Ö. Ekeberg and S. P. Sane. Tuneable reflexes control antennal positioning in flying hawkmoths. *Nature Communications*, 10(1), 5593 (December 06, 2019). `https://doi.org/10.1038/s41467-019-13595-3`
   Content from the above publication has been reproduced/adapted in this thesis.
2. N. Saxena*, **D. Natesan*** and S. P. Sane. Odor source localization in complex visual environments by fruit flies. *Journal of Experimental Biology*, 221, no. 2 (January 19, 2018): jeb172023. `https://doi.org/10.1242/jeb.172023`
3. **D. Natesan** and S. P. Sane. Peering into the neuromechanical black box. *Review in preparation.*
4. **D. Natesan***, S. D. Dave*, N. Saxena, and S. P. Sane. Neural mechanisms of airflow-dependent antennal positioning in hawkmoths. *Manuscript in preparation.*
5. **D. Natesan***, N. Wadhwa* and S. P. Sane. Kinematics of free flight pitch-up maneuvers in the housefly, *Musca domestica. Manuscript in preparation.*

Parts of this work has been presented in

1. N. Saxena*, **D. Natesan*** and S. P. Sane. How flies determine the location of an odor source. *Integrative and Comparative Biology*, 57, E398-E398 (January 03, 2017).
2. **D. Natesan**, N. Saxena, Ö. Ekeberg and S. P. Sane. Airflow mediated antennal positioning in flying hawkmoths. *Integrative and Comparative Biology*, 56, E159-E159 (January 06, 2016).
3. N. Saxena*, **D. Natesan*** and S. P. Sane. Odor tracking behavior of fruit flies in the presence of landmark cues. *Integrative and Comparative Biology*, 54, E184-E184 (January 01, 2014).

* Equal contribution

Organization of the thesis

Chapter 1: This chapter provides a conceptual framework to investigate multi-sensory behaviors in insects. Behaviors are the cumulative output of neural circuits and the associated biomechanics of body parts in response to input sensory stimuli. The neuromechanical black box underlying these behaviors can be mathematically described using control theory. This representation also allows for an iterative investigation of the properties of individual components, thereby unravelling the neural computation performed by circuits that control behavior. This conceptual framework is used in the subsequent chapters to investigate airflow-dependent antennal positioning in hawkmoths.

Chapter 2: Airflow-dependent antennal positioning is investigated using a combination of experiments and computational tools (framework provided in Chapter 1). The structure of the underlying neural circuits is first determined based on experiments. Next, their properties are extracted and modelled using control theoretic tools. Finally, a possible model neural network is proposed that could maintain antennae stably on short timescales, and flexibly on longer ones.

Chapter 3: Johnston's organ (JO) mediated set-point modulation is investigated using behavior and electromyograms. Using unilateral JO restriction experiments the structure of the modulation circuit is determined. Next, using fine flagellar vibrations to stimulate the JOs while simultaneous recording from the antennal muscles, the responses of modulation circuit is characterized.

Chapter 4: The antennal hair plate (Böhm's bristles) mechanosensory system, that is the transformation of antennal positioning to sensory hair stimulation, is investigated in this chapter. Because the shape, size and position of the hair plates on the antennal joint dictate its encoding properties, describing this transformation requires the use of biomechanical models. Here, we develop the necessary tools and use it to estimate the sensitivity of the antennal hair plates to antennal movements.

List of Figures

Contents

Chapter 1

Peering into the neuromechanical black box

1.1 Introduction

Neuroethology is the study of the neural basis of animal behavior. The foundation of both neurobiology and ethology lies in the description of animal behavior (Tinbergen, 1963), albeit at different levels. Whereas systems-level algorithms try to explain behaviors as responses to sensory stimuli experienced by an animal (Tinbergen, 1963), neuroethologists go a step further and investigate the neural implementation of such algorithms (Ewert, 1980).

Identifying the neural basis of animal behavior poses several challenges. First, the behavioral response to a sensory context must be consistent and robust. Behaviors with high variability are harder to investigate due to the possibility of unaccounted sensory inputs as well as changes in internal states of the animal (Lorenz and Leyhausen, 1973; Tinbergen, 1951). Second, the nervous system should be sufficiently tractable to identify brain regions (or neural circuits) involved in behavior (Bargmann, 2012; Bargmann and Marder, 2013). This would enable experimental manipulations that highlight the neural mechanisms behind control of behavior. However, this approach could also run into problems if redundant circuits control the same behavior (Ramaswamy, 2019). Third, the behavior should arise as a result of processing cues from multiple sensory modalities, i.e. the behavior should be sufficiently multimodal. Studying such behaviors would provide insights into the general principles of neural computation (Wessnitzer and Webb, 2006).

Insects, in this context, are excellent study systems for neuroethologists. Behaviors in insects, especially those involved in escape, are typically fast and robust (Card, 2012). These allow for clear mathematical descriptions of motor outputs as a function of sensory inputs (Cowan et al., 2006; Land and Collett, 1974; Roth et al., 2016; Sponberg et al., 2015). Additionally, the small brain size implies comparatively fewer neurons may be involved, which would imply less redundancy in their implementation (Ramaswamy, 2019). Finally, insects typically combine information from multiple modalities to generate context-dependent behaviors (Card, 2012; Hengstenberg, 1993; Ritzmann et al., 2012; Ritzmann and Büschges, 2007; Staudacher et al., 2005). Here, we present a conceptual framework to investigate behaviors in insects, which can be extended to more complex behaviors.

1.2 Mathematical description of a behavior

All behaviors can be described as neuromechanical "black boxes", or input-output systems, which convert sensory cues (inputs) into body/limb movements (outputs) [Figure 1.1; Rosenblueth et al. (1943)]. Such descriptions can be algorithmic or mathematical or a combination of both (Marr and Poggio, 1976; Rosenblueth and Wiener, 1945). The neural networks that carry out this transformation are called sensorimotor circuits.

Investigating sensorimotor circuits that underlie behaviors first requires an explicit description of behavior (Krakauer et al., 2017; Marr and Poggio, 1976). Qualitative descriptions, that capture the broad features of a behavior, can be a set of algorithms that are activated by various sensory cues (e.g. stickleback courtship - Tinbergen, 1951; Drosophila courtship - Greenspan and Ferveur, 2000; odor tracking - Kennedy, 1983; Saxena et al., 2018; van Breugel and Dickinson, 2014). Mathematical descriptions, on the other hand, quantitatively describe the temporal dynamics of a behavior in detail (e.g. chasing behavior of houseflies: Land and Collett, 1974; nematode movement: Stephens et al., 2008; odor tracking: Vergassola et al., 2007). Typically, behavioral descriptions begin as algorithmic descriptions, and slowly evolve into mathematical descriptions as fine temporal data is gathered.

Mathematical descriptions have been shown to be incredibly useful. Because such an approach accurately describes the computations performed by sensorimotor circuits, it gives critical insights into what is being computed (Krakauer et al., 2017; Marr and Poggio, 1976; Reichardt et al., 1979). For instance, the Hassenstein-Reichardt detector, which describes motion detection computation in insects, was conceptualized by investigating visual cue induced turning in beetles (Borst et al., 2010; Reichardt, 1961; Reichardt et al., 1979). Additionally, identifying the mathematical computation performed by sensorimotor circuits provides crucial insights on their neural implementation. For example, the famous Jeffress model, a neural implementation of binaural sound localization, was built on studies identifying interaural time difference as the computation underlying sound localization in humans (Carr, 1993; Jeffress, 1948; Stevens and Newman, 1936).

Because of these reasons, our conceptual framework begins with a mathematical description of behavior. We chose to use the formal language of control theory to describe behaviors because of its well-defined notion of feedback, a property that is critical to nervous systems (Wiener, 1961). Additionally, it allows a convenient traversal from describing the overall computation to identifying its likely neural basis (Cowan et al., 2014; Roth et al., 2014) In this section, we describe how these tools may be applied to formally describe behavior. Although this approach is universal for animals or robots,

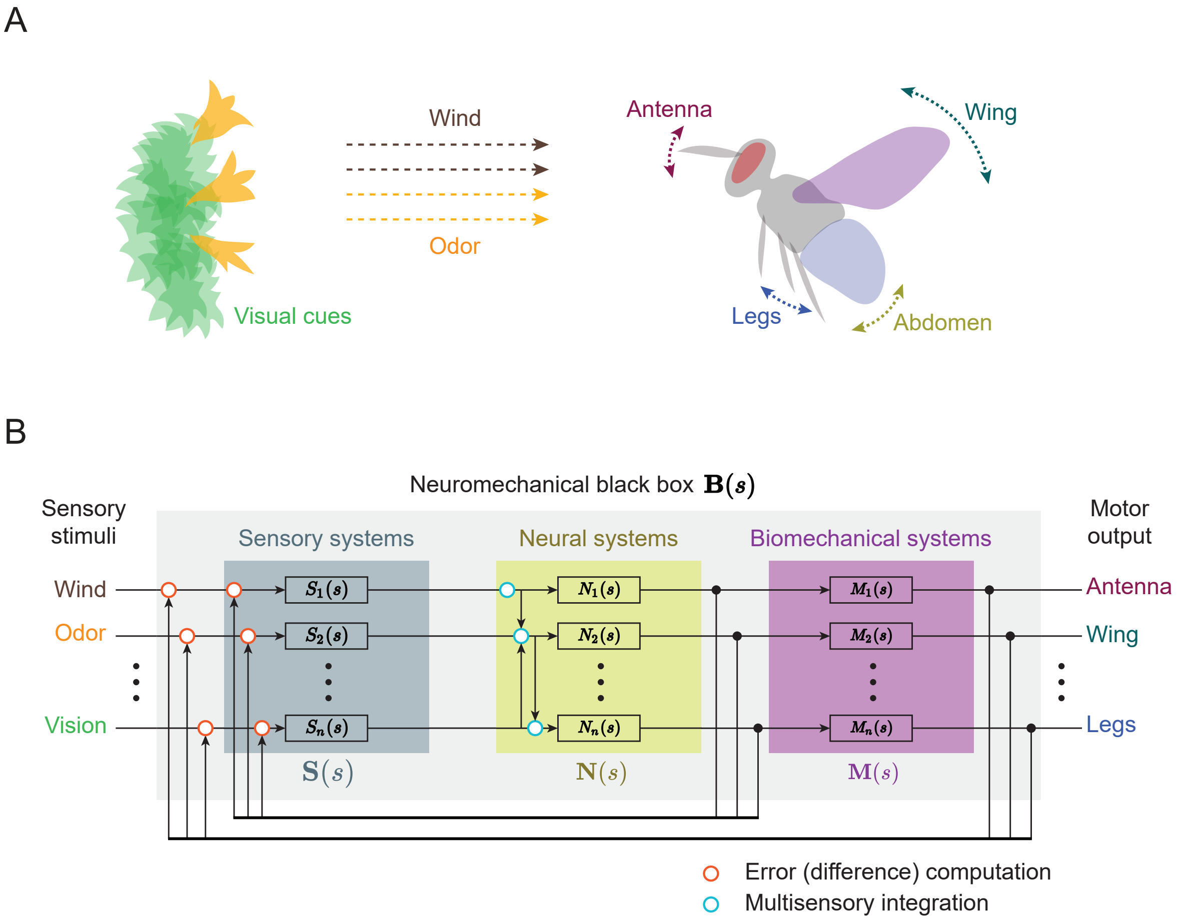

Fig. 1.1 : Neuromechanical black box describing insect behavior
(A) Multimodal behaviors in insects. Illustrative examples of multiple sensory modalities guiding the movements of an insect's body parts. Such behaviors can provide a convenient means of investigating multi-sensory integration in nervous systems. **(B) Neuromechanical black box.** The multimodal behavior can be mathematically described as a neuromechanical black box ($\mathbf{B}(s)$) that takes in sensory stimuli as input and produces the relevant motor output. The neuromechanical black box ($\mathbf{B}(s)$) can be broken down into three components - sensory systems ($\mathbf{S}(s)$), neural systems ($\mathbf{N}(s)$) and biomechanical systems ($\mathbf{M}(s)$). Sensory-feedback and reafferent-feedback connections modify the inputs to the sensory system (red circles), thereby changing the dynamics of the system. Additionally, neural systems integrate information from multiple modalities (cyan circles) to control signals to biomechanical systems that move insect body parts.

we focus in particular on insect behavior, which is the main topic of this thesis.

In the language of control theory, the transformation of sensory cues to body movements can be represented as a transfer function (Figure 1.1). It captures the input-output characteristics of the neuromechanical black box as a mathematical function in the Laplace (complex frequency) domain (Åström and Murray, 2008; Oppenheim et al., 1996). The input to such a transfer function is a time-series, which also can be represented as a weighted integral (superposition) of several different sinusoids of multiple frequencies (Fourier Transforms - Oppenheim et al. (1996)). For each sinusoidal frequency, the transfer function specifies the change in amplitude and phase caused by the black box. The output is also a timeseries, which is effectively a superposition of the input sinusoid frequencies, but whose individual amplitude and phase has been uniquely modified by the transfer function (Åström and Murray, 2008; Dorf and Bishop, 2017).

Because the transfer function specifies how the black box alters sinusoids over the entire frequency range, construction of such a description requires the inputs to be 'frequency rich' (Åström and Murray, 2008; Dorf and Bishop, 2017). Typically, sensory inputs are provided in the form of impulses, steps (Beatus et al., 2015; Natesan et al., 2019; Ristroph et al., 2010; Whitehead et al., 2015), sinusoids (Fender and Nye, 1961; Stark, 1968), sum-of-sinusoids (Dyhr et al., 2013; Roth et al., 2011, 2016), band-limited Gaussian noise and m-sequences (Marmarelis, 1978; Ringach and Shapley, 2004; Theobald et al., 2010a,b) in order to estimate transfer functions.

This approach assumes that the sensory-motor transformation is linear (Linear Time Invariant systems - Åström and Murray, 2008; Dorf and Bishop, 2017; Oppenheim et al., 1996). In a linear system, the output timeseries has exactly the same sinusoidal frequencies present in the input sinusoid, albeit altered in amplitude and phase. That is, the transfer function can only modify the input sinusoids and cannot generate sinusoids of new frequencies. Linearity of behavior, and the validity of this assumption, can be explicitly confirmed using experiments that test for superposition and time-invariance of input-output transformations (e.g. pupil response: Clynes, 1961; jamming avoidance response in electric fish: Madhav et al., 2013; refuge tracking in electric fish: Roth et al., 2011; flower tracking in hawkmoths: Roth et al., 2016). However, linear transfer functions are sufficient to capture the dynamics for a wide variety of behaviors such as thigmotaxis in cockroaches, head stabilization in flies, eye movements in humans, chasing behavior in houseflies, etc. (Cowan et al., 2006; Hengstenberg, 1993; Land and Collett, 1974; Robinson, 1981). Additionally, several non-linear behaviors turn out to be linear over a small range of stimuli, allowing the use of these methods to describe the behavior over the linear range (pupil response: Stark and Sherman (1957); head stabilization in locusts: Thorson (1964)).

Description of behavior using linear (control theoretic) models is prevalent in the study of behaviors and was especially prolific in the latter half of the 20th century (Buchner, 1984; McIntyre and Bizzi, 1993; Reichardt and Poggio, 1976; Stark, 1968; Varjú, 1977). During this time, these methods were applied to describe a diverse set of insect behaviors including prey capture in mantids (Mittelstaedt, 1957, 1962), visual orientation in walking beetles (Reichardt, 1961; Varju, 1975; Varjú, 1976), optomotor reactions in flies (Götz, 1975; Götz et al., 1979), small object tracking in houseflies (Land and Collett, 1974), head stabilization of blowflies (Hengstenberg et al., 1986; Hengstenberg, 1991, 1993) and flower feeding in hawkmoths (Farina et al., 1994, 1995; Kern and Varjú, 1998). A substantial portion of this has been to understand how insects process optical information and use it to maintain a constant visual orientation (Reichardt et al., 1979). In additional to setting the foundation of describing the "phenomenological level", i.e. the input-output transformation of behaviors, these studies also developed several innovative experimental paradigms to investigate the subsystems of the black box (Götz, 1968; Reichardt, 1961; Reichardt and Poggio, 1976). By using newer technologies recent studies build on this foundation, to describe thigmotaxis, abdominal response and luminance-dependent visual processing in insects (Cowan et al., 2006; Dyhr et al., 2013; Sponberg et al., 2015), as well as better describe already studied behaviors such as head stabilization and flower feeding in better detail (Goulard et al., 2015; Roth et al., 2016; Viollet and Zeil, 2013). These descriptions highlight the sensory modalities involved, the information derived from each modality, and their influence on behavior.

1.3 Structure of the neuromechanical black box

To identify the neural circuits and the algorithms underlying these reflexes (Marr and Poggio, 1976; Reichardt et al., 1979), we need to identify the components of the black box. The neuromechanical black box can be coarsely broken down into three subsystems - sensory system, neural system, and biomechanical system (Figure 1.1). The sensory system transforms an external sensory context by amplifying the relevant cues and filtering out the rest. The neural system uses this filtered input to appropriately control the behavior by generating relevant motor commands, which are then carried out by the biomechanical plant.

This coarse categorization explicitly decomposes the overall input-output transformation (behavior) into sensing, control/computation and movement, each with its own dynamics. The act of identifying them as these three subsystems also brings in modularity. For instance, optic flow is sensed by the "visual system", which can be the same for different optic-flow dependent behaviors (e.g. optic flow based positioning of the antenna, head and abdomen - Hengstenberg, 1993; Khurana and Sane, 2016; Taylor et al., 2013). Similarly, different sensory modalities which activate the same body part can use the same biomechanical system to produce different types of movement (e.g. visual and mechanosensory control of flight - Bartussek and Lehmann, 2016; Mamiya and Dickinson, 2015; Sherman and Dickinson, 2004). Additionally, this approach allows the flow of information between the components, especially due to feedback, to be easily represented and analyzed.

There are two ways in which information could flow between subsystems. In the first type, information flows serially from one subsystem to the other. These are called feedforward or open loop systems [Figure 1.2; Åström and Murray (2008)]. Prey capture in cuttlefish is a good example of feedforward (open loop) behavior. Cuttlefish visually

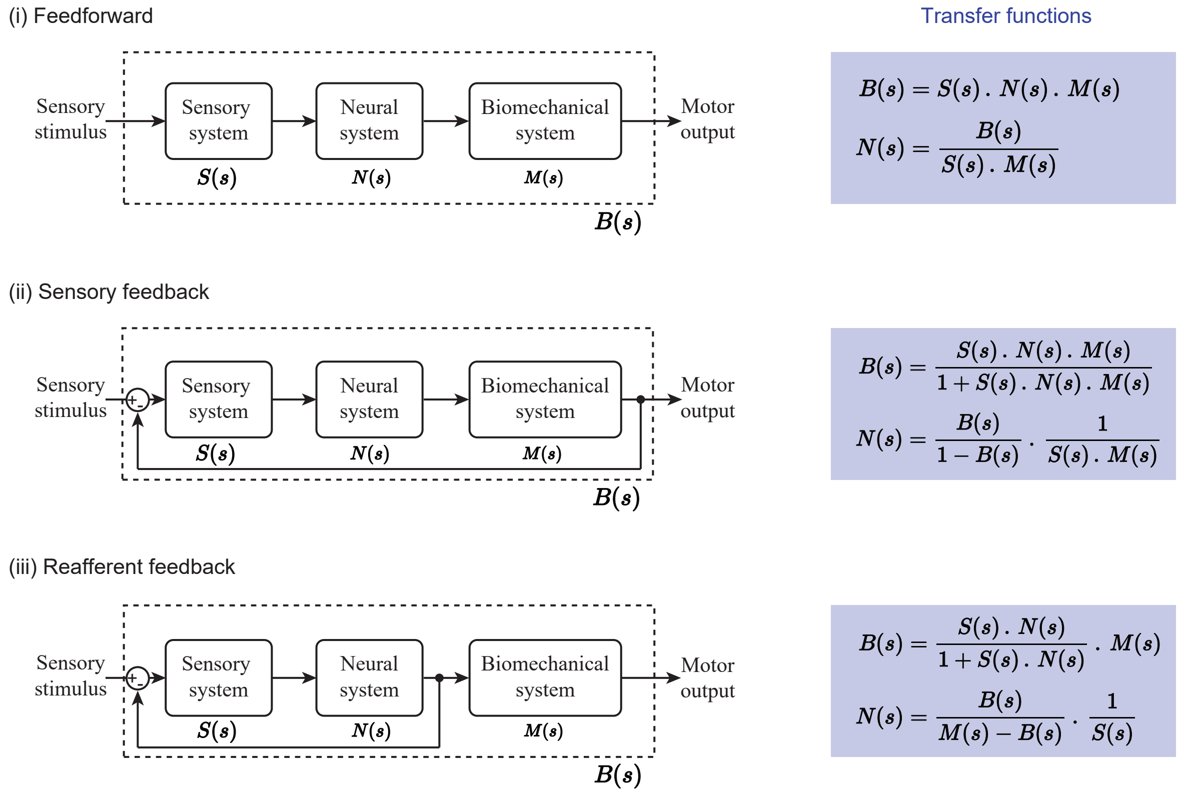

$$B(s) = S(s)\,.\,N(s)\,.\,M(s)$$

$$N(s) = \frac{B(s)}{S(s)\,.\,M(s)}$$

$$B(s) = \frac{S(s)\,.\,N(s)\,.\,M(s)}{1 + S(s)\,.\,N(s)\,.\,M(s)}$$

$$N(s) = \frac{B(s)}{1 - B(s)} \cdot \frac{1}{S(s)\,.\,M(s)}$$

$$B(s) = \frac{S(s)\,.\,N(s)}{1 + S(s)\,.\,N(s)}\,.\,M(s)$$

$$N(s) = \frac{B(s)}{M(s) - B(s)} \cdot \frac{1}{S(s)}$$

Fig. 1.2 : Flow of information inside a neuromechanical black box
Flow of information between the components of a neuromechanical black box can be classified into three categories - **(i)** feedforward systems where information flows sequentially from one component to the other, **(ii)** sensory feedback systems where self-motion changes the stimuli sensed by the insect, and **(iii)** reafferent feedback systems where the neural control signal directly affects the inputs to the sensory system. The flow of information affects both the overall transfer function ($B(s)$) and also the type of control exerted by the neural system ($N(s)$). Estimating the neural computation underlying a particular behavior requires both the knowledge of the contribution of other components and the flow of information between them.

track their prey, such as shrimp, and capture them using a rapid tentacle strike that lasts ~30 ms (Messenger, 1968). Once prey capture is initiated, the visual input at the time of initiation is sequentially transformed to generate the tentacle strike. If the prey moves after initiation, the capture is unsuccessful (Messenger, 1968). Additionally, absence of visual input after initiation does not affect capture (if the prey does not move). This is the key feature of feedforward behaviors – once initiated the behavior does not consider movements of the prey, or disturbances to its own movements, and moves in a stereotypical manner. Such systems typically underly rapid movements such as escape responses and prey capture behaviors (Card, 2012; Messenger, 1968; Mittelstaedt, 1957).

In the other type, information does not flow sequentially, and outputs are fed back as inputs to the earlier subsystems. These are called feedback or closed loop systems (Figure 1.2). Feedback connections are especially important as they completely change the dynamics of a system. Unstable systems can be made stable using closed loop feedback and vice versa (Åström and Murray, 2008; Dorf and Bishop, 2017). Many reflexes are closed loop behaviors because motor actions in response to an external sensory context also automatically alter the detected sensory inputs (Cowan et al., 2014; Roth et al., 2014). The new set of sensory inputs depends both on the external change and the change due to self-generated motion (Figure 1.1). This influence of self-generated movement on sensory inputs, i.e. the feedback from the output to input, dictates both the overall transfer function and the stability of the system.

Perhaps the most studied form of feedback is sensory feedback, where the final behavioral output affects the input sensory context (Figure 1.2). For instance, flower feeding in hawkmoths is a closed loop sensory feedback system (Farina et al., 1994, 1995). Movements of the flower are continuously tracked using both visual and mechanosensory input, and flight is controlled to compensate for the flower movements (Roth et al., 2016). Additionally, errors made when hovering in front of the flower are sensed and compensated for by such a system. The defining characteristic of such sensory feedback behaviors is error-correction (Åström and Murray, 2008). Tracking of object movements by eyes, stabilization of heads by insects, tracking of prey by cuttlefish and mantids, etc., all have a component of sensory feedback (Hengstenberg, 1993; Messenger, 1968; Mittelstaedt, 1962; Robinson, 1981; Viollet and Zeil, 2013).

In some systems, a copy of the neural command to the biomechanical system is fed back to the sensory system (Figure 1.2). This feedback is called reafferent feedback, sometimes also called corollary discharge or efference copy, and is a special case of closed-loop feedback systems (Sperry, 1950; von Holst and Mittelstaedt, 1950). An interesting aspect of reafferent feedback is its ability to subtract changes in inputs due to self-generated movements (Varjú, 1990; von Holst and Mittelstaedt, 1950). For instance, when visually tracking an object, eye movements will themselves cause the visual world to move in the opposite direction. In the presence of reafferent feedback, the optic flow due to self-motion can be subtracted out, giving rise to a stable representation of the visual world (MacKay, 1973). Reafferent feedback can be found in a variety of systems, ranging from vision to electroception (Bell, 1981; Heisenberg and Wolf, 1988; Kim et al., 2015; MacKay, 1973; Sperry, 1950; von Holst and Mittelstaedt, 1950).

Complex behaviors, like chasing behavior in houseflies, flower feeding in hawkmoths etc. (Land and Collett, 1974; Roth et al., 2016), use multiple modalities and produce coordinated movements of multiple body (Figure 1.1). For example, prey capture in praying mantids involves a tracking phase where the head tracks the position of the prey, using both vision and head position in a sensorimotor closed loop (Mittelstaedt, 1957). Once the prey position is determined, the strike is initiated using the front legs, which is an open loop behavior (Mittelstaedt, 1957, 1962). Complex behaviors, therefore, activate multiple sensory and motor systems. They do so by using different behavioral modules in open or closed loop configurations, harnessing both sensory and reafferent feedback (Figure 1.1, Figure 1.2). This increases the speed, stability and the robustness of such behaviors.

1.4 Unpacking the neuromechanical black box

Teasing out the computation performed by the neural system requires knowledge of the individual contributions of the other two systems as well as the structure of feedback between them. This is because the neural system sits between the sensory system and the biomechanical system; control by neural circuits strongly depends on the fidelity of the sensory system, the controllability of biomechanical system and flow of information between the three systems (Figure 1.1, Figure 1.2).

The contribution of sensory and biomechanical systems can be identified using open-loop measurements (reviewed extensively in Roth et al. (2014)). In these experiments, the feedback is artificially cut and the response of the sensory and biomechanical systems are separately measured. The amplification and filtering properties of sensory systems can be measured using open-loop electrophysiological experiments by recording from the sensory neurons directly, while presenting the insect with sensory stimuli. This approach has had a lot of success, especially with mechanosensation (Sane and McHenry, 2009) and olfaction (Kaissling, 1971).

Similarly, the biomechanical system, which describes both the musculoskeletal system and its effect of the environment, can be studied in an open loop manner. Because biomechanical systems are sometimes independently stable for small perturbations, their properties affect the type of control and computation the neural system needs to perform (reviewed in Chiel and Beer, 1997; Dickinson et al., 2000; Tytell et al., 2011). Experimentally altering neural control signals and measuring their effects on the biomechanical system would characterize the contribution of the biomechanical system (Sponberg et al., 2011a,b). The effective biomechanics depends not just on the musculoskeletal system, but also the timing of muscle activation during a behavior. Based on the activation timing, muscles can act as motors, breaks, struts or springs (reviewed extensively in Dickinson et al. (2000)). Analyzing the work done by the muscles during a behavior, using methods like the work loop technique, can lead to descriptions of the biomechanical filters that act on neural control signals to produce movements (Dickinson et al., 2000; Josephson, 1999).

Determining the flow of information between components requires a combination of behavior and neuroanatomy experiments. Stability of behaviors and its ability to correct errors is typically illustrative of the presence of sensory feedback (Cowan et al., 2014). Severing this feedback by restricting or ablating the sensor would typically give rise to catastrophic failures. For instance, fishes normally maintain a dorsal-side-up equilibrium position, even in dark, a behavior that is lost when the labyrinth system is destroyed (von Holst and Martin, 1973). This suggests that normal postural orientation requires sensory feedback from the labyrinth system. Similar experiments have been done with flies and moths to show that the halteres and antennae, respectively, are necessary for controlled flight (Fraenkel and Pringle, 1938; Sane et al., 2007).

The results of the ablation experiments only inform the presence of sensory feedback. Identifying the nature of feedback and its role in behavior requires clever behavior experiments as well as neuroanatomical and electrophysiological studies. For instance, haltere ablation causes unstable flights in flies (Fraenkel and Pringle, 1938; Pringle, 1948). Inferring that they provide proprioceptive feedback on angular velocities during flight required behavior experiments which characterized the effect of this feedback on flight (Dickinson, 1999; Mureli and Fox, 2015; Nalbach, 1993; Pringle, 1948). These were supplemented by neuroanatomical and electrophysiological studies which investigated the arrangement of the campaniform sensillae on the haltere and their activity during flight (Agrawal et al., 2017; Chan and Dickinson, 1996; Fayyazuddin and Dickinson, 1996; Pringle, 1948; Smith, 1969). Theoretical studies built on this to help understand the torques experienced by the halteres during flight (Chang and Wang, 2014; Nalbach, 1993, 1994; Pringle, 1948).

Note that ablation experiments work only for cases with one (critical) sensory feedback. Multiple sets of feedback might exist that keep the behavior robustly stable. Expanding on the previous example, postural orientation in fishes with their labyrinth destroyed is relatively normal in fishes with an overhead light source, suggesting that this behavior utilizes both visual and labyrinth systems (von Holst and Martin, 1973). In cases like these, multiple experiments under different conditions need to be performed to tease out the sensory feedbacks involved.

Reafferent feedback connections, unlike sensory feedback, are ingrained within the nervous system (Figure 1.2). Because such connections send a copy of the motor command to the sensory system, detecting their presence requires analyzing how the same input is sensed by the sensory system in the presence or absence of voluntary movement. The classic example of reafference is the subtraction of self-motion by the human eye – when the extra-ocular muscles are paralyzed and the eye voluntarily tries to move in one direction, it gives rise to a movement of the visual field in the same direction of motion (von Helmholtz, 1867; von Helmholtz and Southall, 2000). Because the muscles were paralyzed and there was not actual movement of the eye, this effect was due to feedback of the motor command to the sensory system, i.e. reafferent feedback (von Holst and Mittelstaedt, 1950). Similar experiments have been performed with fruit flies, by recording from optic-flow processing cells while presenting tethered flies (open loop) with identical visual input during straight flight and active turns. The output of the same cells was different in response to the same stimuli based on the state of flight, thereby showing the presence of reafferent feedback (Kim et al., 2015).

Establishing reafferent feedback connections requires an explicit marriage between behavior and electrophysiology. This is because voluntary behavior affects the sensory system by modulating activity of the sensory neurons. Such reafferent connections to visual, auditory and electroceptive systems have been studied in several animals (Bell (1981); Poulet and Hedwig (2002); Roy and Cullen (2004); reviewed in Crapse and Sommer (2008)). Determining the information sent to effectively cancel out self-motion has been harder to establish and has been shown only in a few cases (Kim et al., 2015; Poulet and Hedwig, 2006).

Once the components and the feedbacks in the neuromechanical black box are known, the computation of the neural system can be determined from the overall neuromechanical transfer function and the transfer functions associated with the sensory and the motor systems (Figure 1.2). The obtained transfer function of the neural system describes the computation performed by the neural circuits. With this computation in mind (Krakauer et al., 2017; Marr and Poggio, 1976), the neural implementation can be then investigated using both experimental methods such as electrophysiology and optogenetics, as well as computational methods such as spiking neural network simulations (Clark et al., 2013; Pearson et al., 2006).

1.5 Advantages and challenges

The proposed framework uses a top-down approach to investigate behaviors, with the overall behavior described as a transfer function. This implies that any description of the subsystems, and the feedback connections between them, must add up to the overall transfer function (Figure 1.2). This also means that knowing the behavior and the sensory and motor subsystems would allow one to determine the computation performed by the neural subsystem (Figure 1.2). Such a guess would aid in the conception of precise electrophysiological and neuroanatomical experiments to understand the neural control exerted on a particular behavior, as well as in the specific implementation of these control algorithms (Krakauer et al., 2017; Marr and Poggio, 1976; Reichardt et al., 1979).

A corollary of using this framework is modularity of individual subsystems. Both sensory systems and motor systems are shared over a variety of behaviors. For instance, insects use optic flow to position various parts of their body including the head, abdomen and antennae (Hengstenberg, 1993; Khurana and Sane, 2016; Taylor et al., 2013). The same optic flow is also used to stabilize flight, avoid obstacles and determine flight paths over longer timescales, as well as to initiate and control landing in insects (Balebail et al., 2019; van Breugel and Dickinson, 2012; Collett and Land, 1975; Reichardt and Wenking, 1969; Srinivasan and Zhang, 2004; Wagner, 1982). All these behaviors, which are typically studied in isolation, have the same sensory subsystem. Ideally, knowing the ‘complete’ visual subsystem would allow it to be utilized to unpack the black box of each of these behaviors. If a repository of sensory and motor system descriptions exists, one can determine the computation performed by the neural system by knowing the overall behavior of interest as a transfer function and filling in the descriptions of the relevant sensory and motor systems (Figure 1.2).

Non-linearity in the subsystems will pose an interesting challenge to the proposed framework. The non-linearity of subsystems giving rise to linear behaviors highlights a fascinating problem - how are multiple non-linear processes in a system giving rise to overall linear behavioral responses to stimuli? For example, the visual system in fruit flies is known to employ non-linear processes to extract directional information from optic flow, which is also influenced by the behavioral state of the animal (Chiappe et al., 2010; Gruntman et al., 2018; Strother et al., 2018). However, linear neuromechanical models can explain the effect of changes in luminance on visual processing (Sponberg et al., 2015). This suggests that the neural system actively controls for the non-linearities and keeps the overall system working in the linear regime. The proposed framework would enable identification and investigation of such behaviors.

Finally, identification of the transfer functions of individual subsystems would allow for more focused experiments that aid in understanding its workings (Reichardt et al., 1979). It also enables integration of multiple experimental and computational tools to generate possible hypotheses of mechanisms behind these transfer functions (Cowan et al., 2006; Mongeau et al., 2013, 2015). Combinations of such tools to generate and falsify hypotheses allows for iterative investigations of the neuromechanical black box. For instance, knowledge of the neural computation underlying a behavior allows the use of biological neural network models to propose testable hypotheses of neural mechanisms (Marr and Poggio, 1976; Reichardt et al., 1979). Predictions of these models could be tested using electrophysiology and optogenetics. If these hypotheses are falsified, the generated data could be used to narrow down the space of all hypotheses, generating a new set of plausible ones. Such a process eventually leads to a hypothesis that stands the test of experiments. The recent emergence of such computational tools would greatly aid this endeavor (Bower and Beeman, 1998; Carnevale and Hines, 2006; Goodman and Brette, 2009; Linssen et al., 2018; Ray and Bhalla, 2008; Stimberg et al., 2014).

1.6 Antennal positioning in insects

We use antennal positioning in hawkmoths to investigate the proposed framework for several reasons. First, the behavior is critical for flight. Positioning of antennae enables insects to sense mechanosensory cues required for flight control; when deprived of antennal mechanosensory input, most insects are unable to control their flight (Sane et al., 2007). Second, antennal positioning behavior is guided by sensory inputs from multiple modalities, including odor, optic flow and airflow (Gewecke, 1974; Heran, 1959; Honegger, 1981; Khurana and Sane, 2016; Krishnan and Sane, 2014; Lambin et al., 2005; Mamiya and Dickinson, 2015; Okada and Toh, 2006; Yamawaki and Ishibashi, 2014). Third, the individual components required for proper antennal positioning are well known (Böhm, 1911; Krause et al., 2013; Krishnan et al., 2012; Okada and Toh, 2000; Sant and Sane, 2016, 2018). Finally, the neural basis of this multi-sensory behavior is not well studied.

The above combination of known components with unknown neural computation makes antennal positioning behavior a natural candidate for this framework. The computation of the underlying neural circuits can be identified by describing the overall neuromechanical black box, its components and the connectivity between them. Electrophysiological and computational tools can then be used to further characterize the subsystems in the antennal positioning behavior. In the upcoming chapters, I describe my investigations of antennal positioning behavior using the Oleander hawkmoth, Daphnis nerii as my model organism.

During flight, antennal position is controlled by rapid mechanosensory feedback from Böhm's bristles and modulated by slower feedback based on frontal airflow via the Johnston's organ (JO). What control algorithm underlies the integration of these disparate mechanosensory inputs? In chapter 2, we use a combination of experiments and control theoretic tools to investigate airflow-dependent antennal positioning. Based on behavioral experiments, we first describe the behavior as well as the structure of the underlying neuromechanical black box (section 1.2; section 1.3). The black box consists of two sub-circuits, one that maintains the antenna at a preferred position or set-point whereas the other modulates this set-point based on sensory context. Next, we use control theoretic tools to compare the predictions of the neuromechanical black box with experimental data and examine if a linear transfer function suffices for various preferred positions. Finally, based on known contributions of the sensory and motor system, we tease out the contributions of the neural network (section 1.4). Based on this, we propose a minimalistic model neural network that integrates fast feedback from Böhm's bristles to generate reflexive responses to perturbations, with slower feedback from JO modulating position. Thus, moths maintain antennal position over short timescales while retaining flexibility over longer durations.

Knowing the structure of the neuromechanical black box underlying antennal position allowed us to individually investigate each of its subsystems (section 1.4). In chapter 3, we focus on the neural mechanisms of airflow-dependent set-point modulation. Using behavioral experiments, we map out the flow of information from JOs to the antennal motor system, i.e. the structure of this subsystem (section 1.3). We find that sensory inputs from both JOs are required for reliable modulation of each antennal set-point, suggesting a bilateral, possibly non-linear, integration of JOs input. Next, we perform open-loop EMG experiments to characterize how activity of antennal muscles are modulated based on sensory inputs from the JOs. Using a finely calibrated stimulus setup, we deliver precise flagellar vibrations to excite the mechanosensory neurons of the Johnston's organ while simultaneously recording from the extrinsic muscles.

In chapter 4, we use computational tools to describe activation patterns of Böhm's bristles to different movements of the antenna (mechanosensory system; section 1.4). Because the activation of mechanosensory hairs depends on both the position of the hair plate on the antenna as well as the movement of the antennal joint, the sensitivity of the hair plate is different for different positions. I develop a toolbox to quantify input-output (antennal position-hair field stimulation) transformation of the hair plates. Additionally, this toolbox provides an easy way to simulate the proprioceptive feedback sent to the nervous system during active positioning of the antenna.

In addition to the above efforts, I also worked on quantifying the kinematics of pitch-up maneuvers in freely flying houseflies. This was an interlude to understanding which movements of the wing produce pitch-up torques. In effect, this study investigated part of the flight biomechanical system. However, because it was correlational in nature, and because it was a new behavior on a new model system, I have placed the results of this study in the Appendix D.

On the whole, this thesis uses the proposed framework to investigate antennal positioning in hawkmoths. It uses control theory to describe the neuromechanical black box, behavior and EMG experiments as well as computational models to delve into the underlying computations/transformations of each the constituent systems. Each chapter ends with a discussion on the insights obtained from these experiments/simulations, its applicability to other insect reflexes and the generality of the mechanisms discerned.

Bibliography

S. Agrawal, D. Grimaldi, and J. L. Fox. Haltere morphology and campaniform sensilla arrangement across Diptera. *Arthropod Structure & Development*, 46(2):215–229, Mar. 2017. ISSN 1467-8039. doi: 10.1016/j.asd.2017.01.005.

K. J. Åström and R. M. Murray. *Feedback Systems: An Introduction for Scientists and Engineers*. Princeton University Press, Apr. 2008.

S. Balebail, S. K. Raja, and S. P. Sane. Landing maneuvers of houseflies on vertical and inverted surfaces. *PLOS ONE*, 14(8):e0219861, Aug. 2019. ISSN 1932-6203. doi: 10.1371/journal.pone.0219861.

C. I. Bargmann. Beyond the connectome: How neuromodulators shape neural circuits. *BioEssays*, 34(6):458–465, 2012. ISSN 1521-1878. doi: 10.1002/bies.201100185.

C. I. Bargmann and E. Marder. From the connectome to brain function. *Nature Methods*, 10(6):483–490, June 2013. ISSN 1548-7105. doi: 10.1038/nmeth.2451.

J. Bartussek and F.-O. Lehmann. Proprioceptive feedback determines visuomotor gain in Drosophila. *Royal Society Open Science*, 3(1):150562, Jan. 2016. ISSN 2054-5703. doi: 10.1098/rsos.150562.

T. Beatus, J. M. Guckenheimer, and I. Cohen. Controlling roll perturbations in fruit flies. *Journal of The Royal Society Interface*, 12(105):20150075, Apr. 2015. ISSN 1742-5689, 1742-5662. doi: 10.1098/rsif.2015.0075.

C. C. Bell. An efference copy which is modified by reafferent input. *Science*, 214(4519): 450–453, Oct. 1981. ISSN 0036-8075, 1095-9203. doi: 10.1126/science.7291985.

L. K. Böhm. Die antennalen Sinnesorgane der Lepidopteren. *Arbeiten aus dem Zoologischen Instituten der Universität Wien und der Zoologischen Station in Triest*, 14: 219–246, 1911.

A. Borst, J. Haag, and D. F. Reiff. Fly Motion Vision. *Annual Review of Neuroscience*, 33(1):49–70, 2010. doi: 10.1146/annurev-neuro-060909-153155.

J. M. Bower and D. Beeman. *The Book of GENESIS: Exploring Realistic Neural Models with the GEneral NEural SImulation System*. Springer-Verlag, New York, 2 edition, 1998. ISBN 978-1-4612-7224-3.

E. Buchner. Behavioural Analysis of Spatial Vision in Insects. In M. A. Ali, editor, *Photoreception and Vision in Invertebrates*, NATO ASI Series, pages 561–621. Springer US, Boston, MA, 1984. ISBN 978-1-4613-2743-1. doi: 10.1007/978-1-4613-2743-1_16.

G. M. Card. Escape behaviors in insects. *Current Opinion in Neurobiology*, 22(2): 180–186, Apr. 2012. ISSN 0959-4388. doi: 10.1016/j.conb.2011.12.009.

N. T. Carnevale and M. L. Hines. *The NEURON Book*. Cambridge University Press, Cambridge, UK ; New York, 1 edition edition, Feb. 2006. ISBN 978-0-521-84321-8.

C. E. Carr. Processing of Temporal Information in the Brain. *Annual Review of Neuroscience*, 16(1):223–243, Mar. 1993. ISSN 0147-006X. doi: 10.1146/annurev.ne.16.030193.001255.

W. P. Chan and M. H. Dickinson. Position-specific central projections of mechanosensory neurons on the haltere of the blow fly, Calliphora vicina. *Journal of Comparative Neurology*, 369(3):405–418, June 1996. ISSN 0021-9967. doi: 10.1002/(SICI)1096-9861(19960603)369:3<405::AID-CNE6>3.0.CO;2-9.

S. Chang and Z. J. Wang. Predicting fruit fly's sensing rate with insect flight simulations. *Proceedings of the National Academy of Sciences*, 111(31):11246–11251, Aug. 2014. ISSN 0027-8424, 1091-6490. doi: 10.1073/pnas.1314738111.

M. E. Chiappe, J. D. Seelig, M. B. Reiser, and V. Jayaraman. Walking Modulates Speed Sensitivity in Drosophila Motion Vision. *Current Biology*, 20(16):1470–1475, Aug. 2010. ISSN 0960-9822. doi: 10.1016/j.cub.2010.06.072.

H. J. Chiel and R. D. Beer. The brain has a body: Adaptive behavior emerges from interactions of nervous system, body and environment. *Trends in Neurosciences*, 20(12):553–557, Dec. 1997. ISSN 0166-2236. doi: 10.1016/S0166-2236(97)01149-1. 00859.

D. A. Clark, L. Freifeld, and T. R. Clandinin. Mapping and Cracking Sensorimotor Circuits in Genetic Model Organisms. *Neuron*, 78(4):583–595, May 2013. ISSN 0896-6273. doi: 10.1016/j.neuron.2013.05.006. 00014.

M. Clynes. Unidirectional Rate Sensitivity: A Biocybernetic* Law of Reflex and Humoral Systems as Physiologic Channels of Control and Communication†. *Annals of the New York Academy of Sciences*, 92(3):946–969, 1961. ISSN 1749-6632. doi: 10.1111/j.1749-6632.1961.tb40968.x.

T. S. Collett and M. F. Land. Visual control of flight behaviour in the hoverflySyritta pipiens L. *Journal of comparative physiology*, 99(1):1–66, Mar. 1975. ISSN 0340-7594, 1432-1351. doi: 10.1007/BF01464710.

N. J. Cowan, J. Lee, and R. J. Full. Task-level control of rapid wall following in the American cockroach. *Journal of Experimental Biology*, 209(9):1617–1629, May 2006. ISSN 0022-0949, 1477-9145. doi: 10.1242/jeb.02166. 00105.

N. J. Cowan, M. M. Ankarali, J. P. Dyhr, M. S. Madhav, E. Roth, S. Sefati, S. Sponberg, S. A. Stamper, E. S. Fortune, and T. L. Daniel. Feedback Control as a Framework for Understanding Tradeoffs in Biology. *Integrative and Comparative Biology*, 54(2):223–237, July 2014. ISSN 1540-7063. doi: 10.1093/icb/icu050. 00053.

T. B. Crapse and M. A. Sommer. Corollary discharge across the animal kingdom. *Nature Reviews Neuroscience*, 9(8):587, Aug. 2008. ISSN 1471-0048. doi: 10.1038/nrn2457.

M. H. Dickinson. Haltere–mediated equilibrium reflexes of the fruit fly, Drosophila melanogaster. *Philosophical Transactions of the Royal Society of London B: Bio-*

logical Sciences, 354(1385):903–916, May 1999. ISSN 0962-8436, 1471-2970. doi: 10.1098/rstb.1999.0442.

M. H. Dickinson, C. T. Farley, R. J. Full, M. a. R. Koehl, R. Kram, and S. Lehman. How Animals Move: An Integrative View. *Science*, 288(5463):100–106, Apr. 2000. ISSN 0036-8075, 1095-9203. doi: 10.1126/science.288.5463.100.

R. C. Dorf and R. H. Bishop. *Modern Control Systems*. Pearson, Harlow, England London New York Boston San Francisco Toronto Sydney Dubai Singapore Hong Kong Tokyo Seoul Taipei New Delhi Cape Town São Paulo Mexico City Madrid Amsterdam Munich Paris Milan, thirteenth edition, global edition edition, 2017. ISBN 978-0-13-440762-3 978-1-292-15297-4. OCLC: 999399782.

J. P. Dyhr, K. A. Morgansen, T. L. Daniel, and N. J. Cowan. Flexible strategies for flight control: An active role for the abdomen. *Journal of Experimental Biology*, 216(9):1523–1536, May 2013. ISSN 0022-0949, 1477-9145. doi: 10.1242/jeb.077644. 00064.

J.-P. Ewert. What is Neuroethology? In J.-P. Ewert, editor, *Neuroethology: An Introduction to the Neurophysiological Fundamentals of Behavior*, pages 1–12. Springer Berlin Heidelberg, Berlin, Heidelberg, 1980. ISBN 978-3-642-67500-3. doi: 10.1007/978-3-642-67500-3_1.

W. M. Farina, D. Varjú, and Y. Zhou. The regulation of distance to dummy flowers during hovering flight in the hawk moth Macroglossum stellatarum. *Journal of Comparative Physiology A*, 174(2):239–247, Feb. 1994. ISSN 0340-7594, 1432-1351. doi: 10.1007/BF00193790. 00000.

W. M. Farina, D. Kramer, and D. Varjú. The response of the hovering hawk moth Macroglossum stellatarum to translatory pattern motion. *Journal of Comparative Physiology A*, 176(4):551–562, Apr. 1995. ISSN 1432-1351. doi: 10.1007/BF00196420.

A. Fayyazuddin and M. H. Dickinson. Haltere Afferents Provide Direct, Electrotonic Input to a Steering Motor Neuron in the Blowfly, Calliphora. *Journal of Neuroscience*, 16(16):5225–5232, Aug. 1996. ISSN 0270-6474, 1529-2401.

D. H. Fender and P. W. Nye. An investigation of the mechanisms of eye movement control. *Kybernetik*, 1(2):81–88, July 1961. ISSN 1432-0770. doi: 10.1007/BF00288819.

G. Fraenkel and J. W. S. Pringle. Biological Sciences: Halteres of Flies as Gyroscopic Organs of Equilibrium. *Nature*, 141(3577):919–920, May 1938. ISSN 1476-4687. doi: 10.1038/141919a0.

M. Gewecke. The Antennae of Insects as Air-Current Sense Organs and their Relationship to the Control of Flight. In L. Barton Browne, editor, *Experimental Analysis of Insect Behaviour*, pages 100–113. Springer, Berlin, Heidelberg, 1974. ISBN 978-3-642-86666-1. doi: 10.1007/978-3-642-86666-1_8.

D. F. M. Goodman and R. Brette. The Brian simulator. *Frontiers in Neuroscience*, 3, 2009. ISSN 1662-453X. doi: 10.3389/neuro.01.026.2009.

K. G. Götz. Flight control in Drosophila by visual perception of motion. *Kybernetik*, 4(6):199–208, June 1968. ISSN 1432-0770. doi: 10.1007/BF00272517.

K. G. Götz. The optomotor equilibrium of the Drosophila navigation system. *Journal of comparative physiology*, 99(3):187–210, Sept. 1975. ISSN 1432-1351. doi: 10.1007/BF00613835.

K. G. Götz, B. Hengstenberg, and R. Biesinger. Optomotor control of wing beat and body posture in drosophila. *Biological Cybernetics*, 35(2):101–112, Nov. 1979. ISSN 0340-1200, 1432-0770. doi: 10.1007/BF00337435.

R. Goulard, A. Julien-Laferriere, J. Fleuriet, J.-L. Vercher, and S. Viollet. Behavioural evidence for a visual and proprioceptive control of head roll in hoverflies (Episyrphus balteatus). *Journal of Experimental Biology*, 218(23):3777–3787, Dec. 2015. ISSN 0022-0949, 1477-9145. doi: 10.1242/jeb.127043. 00009.

R. J. Greenspan and J.-F. Ferveur. Courtship in drosophila. *Annual Review of Genetics*, 34(1):205–232, Dec. 2000. ISSN 0066-4197. doi: 10.1146/annurev.genet.34.1.205.

E. Gruntman, S. Romani, and M. B. Reiser. Simple integration of fast excitation and offset, delayed inhibition computes directional selectivity in Drosophila. *Nature Neuroscience*, page 1, Jan. 2018. ISSN 1546-1726. doi: 10.1038/s41593-017-0046-4.

M. Heisenberg and R. Wolf. Reafferent control of optomotor yaw torque in Drosophila melanogaster. *Journal of Comparative Physiology A*, 163(3):373–388, May 1988. ISSN 1432-1351. doi: 10.1007/BF00604013.

R. Hengstenberg. Gaze control in the blowfly Calliphora: A multisensory, two-stage integration process. *Seminars in Neuroscience*, 3(1):19–29, Feb. 1991. ISSN 1044-5765. doi: 10.1016/1044-5765(91)90063-T.

R. Hengstenberg. Multisensory control in insect oculomotor systems. *Visual Motion and its Role in the Stabilization of Gaze*, 5:285–298, 1993.

R. Hengstenberg, D. C. Sandeman, and B. Hengstenberg. Compensatory head roll in the blowfly Calliphora during flight. *Proc. R. Soc. Lond. B*, 227(1249):455–482, May 1986. ISSN 0080-4649, 2053-9193. doi: 10.1098/rspb.1986.0034.

H. Heran. Wahrnehmung und Regelung der Flugeigengeschwindigkeit bei Apis mellifica L. *Zeitschrift für vergleichende Physiologie*, 42(2):103–163, Mar. 1959. ISSN 0044-362x, 1432-1351. doi: 10.1007/BF00298733.

H.-W. Honegger. A preliminary note on a new optomotor response in crickets: Antennal tracking of moving targets. *Journal of comparative physiology*, 142(3):419–421, Sept. 1981. ISSN 0340-7594, 1432-1351. doi: 10.1007/BF00605454.

L. A. Jeffress. A place theory of sound localization. *Journal of Comparative and Physiological Psychology*, 41(1):35–39, 1948. ISSN 0021-9940(Print). doi: 10.1037/h0061495.

R. K. Josephson. Dissecting muscle power output. *Journal of Experimental Biology*, 202(23):3369–3375, Dec. 1999. ISSN 0022-0949, 1477-9145. 00125.

K.-E. Kaissling. Insect Olfaction. In J. E. Amoore, M. G. J. Beets, J. T. Davies, T. Engen, J. Garcia, R. C. Gesteland, P. P. C. Graziadei, K.-E. Kaissling, R. A. Koelling, J. LeMagnen, P. MacLeod, D. G. Moulton, M. M. Mozell, D. Ottoson, T. S. Parsons, S. F. Takagi, D. Tucker, B. M. Wenzel, and L. M. Beidler, editors, *Olfaction*, Handbook of Sensory Physiology, pages 351–431. Springer Berlin Heidelberg, Berlin, Heidelberg, 1971. ISBN 978-3-642-65126-7. doi: 10.1007/978-3-642-65126-7_14.

J. S. Kennedy. Zigzagging and casting as a programmed response to wind-borne odour: A review. *Physiological Entomology*, 8(2):109–120, June 1983. ISSN 1365-3032. doi: 10.1111/j.1365-3032.1983.tb00340.x.

R. Kern and D. Varjú. Visual position stabilization in the hummingbird hawk moth, Macroglossum stellatarum L. I. Behavioural analysis. *Journal of Comparative Physiology A*, 182(2):225–237, Jan. 1998. ISSN 1432-1351. doi: 10.1007/s003590050173.

T. R. Khurana and S. P. Sane. Airflow and optic flow mediate antennal positioning in flying honeybees. *eLife*, 5:e14449, Apr. 2016. ISSN 2050-084X. doi: 10.7554/eLife.14449.

A. J. Kim, J. K. Fitzgerald, and G. Maimon. Cellular evidence for efference copy in *Drosophila* visuomotor processing. *Nature Neuroscience*, 18(9):1247, Sept. 2015. ISSN 1546-1726. doi: 10.1038/nn.4083.

J. W. Krakauer, A. A. Ghazanfar, A. Gomez-Marin, M. A. MacIver, and D. Poeppel. Neuroscience Needs Behavior: Correcting a Reductionist Bias. *Neuron*, 93(3): 480–490, Feb. 2017. ISSN 0896-6273. doi: 10.1016/j.neuron.2016.12.041.

A. F. Krause, A. Winkler, and V. Dürr. Central drive and proprioceptive control of antennal movements in the walking stick insect. *Journal of Physiology-Paris*, 107 (1):116–129, Jan. 2013. ISSN 0928-4257. doi: 10.1016/j.jphysparis.2012.06.001.

A. Krishnan and S. P. Sane. Visual feedback influences antennal positioning in flying hawk moths. *Journal of Experimental Biology*, 217(6):908–917, Mar. 2014. ISSN 0022-0949, 1477-9145. doi: 10.1242/jeb.094276.

A. Krishnan, S. Prabhakar, S. Sudarsan, and S. P. Sane. The neural mechanisms of antennal positioning in flying moths. *Journal of Experimental Biology*, 215(17): 3096–3105, Sept. 2012. ISSN 0022-0949, 1477-9145. doi: 10.1242/jeb.071704.

M. Lambin, P. Déglise, and M. Gauthier. Antennal movements as indicators of odor detection by worker honeybees. *Apidologie*, 36(1):119–126, Jan. 2005. ISSN 0044-8435, 1297-9678. doi: 10.1051/apido:2004076.

M. F. Land and T. S. Collett. Chasing behaviour of houseflies (Fannia canicularis). *Journal of comparative physiology*, 89(4):331–357, Dec. 1974. ISSN 1432-1351. doi: 10.1007/BF00695351.

C. Linssen, M. E. Lepperød, J. Mitchell, J. Pronold, J. M. Eppler, C. Keup, A. Peyser, S. Kunkel, P. Weidel, Y. Nodem, D. Terhorst, R. Deepu, M. Deger, J. Hahne, A. Sinha, A. Antonietti, M. Schmidt, L. Paz, J. Garrido, T. Ippen, L. Riquelme, A. Serenko, T. Kühn, I. Kitayama, H. Mørk, S. Spreizer, J. Jordan, J. Krishnan,

M. Senden, E. Hagen, A. Shusharin, S. B. Vennemo, D. Rodarie, A. Morrison, S. Graber, J. Schuecker, S. Diaz, B. Zajzon, and H. E. Plesser. NEST 2.16.0. Zenodo, Aug. 2018.

K. Lorenz and P. Leyhausen. *Motivation of Human and Animal Behavior; an Ethological View.* Van Nostrand Reinhold Co., New York, 1973. ISBN 978-0-442-24885-7. OCLC: 572903.

D. M. MacKay. Visual Stability and Voluntary Eye Movements. In H. Autrum, P. O. Bishop, V. Braitenberg, K. L. Chow, R. L. De Valois, R. B. Freeman, W. A. van de Grind, O.-J. Grüsser, U. Grüsser-Cornehls, R. Jung, W. R. Levick, H.-U. Lunkenheimer, D. M. MacKay, M. Snyder, J. Stone, N. J. Strausfeld, I. Thomas, and R. Jung, editors, *Central Processing of Visual Information A: Integrative Functions and Comparative Data*, Handbook of Sensory Physiology, pages 307–331. Springer, Berlin, Heidelberg, 1973. ISBN 978-3-642-65352-0. doi: 10.1007/978-3-642-65352-0_5.

M. S. Madhav, S. A. Stamper, E. S. Fortune, and N. J. Cowan. Closed-loop stabilization of the Jamming Avoidance Response reveals its locally unstable and globally nonlinear dynamics. *Journal of Experimental Biology*, 216(22):4272–4284, Nov. 2013. ISSN 0022-0949, 1477-9145. doi: 10.1242/jeb.088922. 00018.

A. Mamiya and M. H. Dickinson. Antennal Mechanosensory Neurons Mediate Wing Motor Reflexes in Flying Drosophila. *Journal of Neuroscience*, 35(20):7977–7991, May 2015. ISSN 0270-6474, 1529-2401. doi: 10.1523/JNEUROSCI.0034-15.2015.

V. Marmarelis. *Analysis of Physiological Systems: The White-Noise Approach.* Computers in Biology and Medicine. Springer US, 1978. ISBN 978-1-4613-3972-4.

D. Marr and T. Poggio. From Understanding Computation to Understanding Neural Circuitry. May 1976. 00607.

J. McIntyre and E. Bizzi. Servo Hypotheses for the Biological Control of Movement. *Journal of Motor Behavior*, 25(3):193–202, Sept. 1993. ISSN 0022-2895. doi: 10.1080/00222895.1993.9942049.

J. B. Messenger. The visual attack of the cuttlefish, Sepia officinalis. *Animal Behaviour*, 16(2):342–357, Apr. 1968. ISSN 0003-3472. doi: 10.1016/0003-3472(68)90020-1.

H. Mittelstaedt. Prey capture in mantids. In *Recent Advances in Invertebrate Physiology*, pages 51–71. University of Oregon Publications, 1957.

H. Mittelstaedt. Control Systems of Orientation in Insects. *Annual Review of Entomology*, 7(1):177–198, 1962. doi: 10.1146/annurev.en.07.010162.001141. 00132.

J.-M. Mongeau, A. Demir, J. Lee, N. J. Cowan, and R. J. Full. Locomotion- and mechanics-mediated tactile sensing: Antenna reconfiguration simplifies control during high-speed navigation in cockroaches. *Journal of Experimental Biology*, 216(24): 4530–4541, Dec. 2013. ISSN 0022-0949, 1477-9145. doi: 10.1242/jeb.083477. 00020.

J.-M. Mongeau, S. N. Sponberg, J. P. Miller, and R. J. Full. Sensory processing within cockroach antenna enables rapid implementation of feedback control for high-speed running maneuvers. *Journal of Experimental Biology*, 218(15):2344–2354, Aug. 2015. ISSN 0022-0949, 1477-9145. doi: 10.1242/jeb.118604.

S. Mureli and J. L. Fox. Haltere mechanosensory influence on tethered flight behavior in Drosophila. *Journal of Experimental Biology*, 218(16):2528–2537, Aug. 2015. ISSN 0022-0949, 1477-9145. doi: 10.1242/jeb.121863.

G. Nalbach. The halteres of the blowfly Calliphora. *Journal of Comparative Physiology A*, 173(3):293–300, Sept. 1993. ISSN 1432-1351. doi: 10.1007/BF00212693.

G. Nalbach. Extremely non-orthogonal axes in a sense organ for rotation: Behavioural analysis of the dipteran haltere system. *Neuroscience*, 61(1):149–163, July 1994. ISSN 0306-4522. doi: 10.1016/0306-4522(94)90068-X.

D. Natesan, N. Saxena, Ö. Ekeberg, and S. P. Sane. Tuneable reflexes control antennal positioning in flying hawkmoths. *Nature Communications*, 10(1):1–15, Dec. 2019. ISSN 2041-1723. doi: 10.1038/s41467-019-13595-3.

J. Okada and Y. Toh. The role of antennal hair plates in object-guided tactile orientation of the cockroach (Periplaneta americana). *Journal of Comparative Physiology A*, 186(9):849–857, Sept. 2000. ISSN 0340-7594, 1432-1351. doi: 10.1007/s003590000137.

J. Okada and Y. Toh. Active tactile sensing for localization of objects by the cockroach antenna. *Journal of Comparative Physiology A*, 192(7):715–726, July 2006. ISSN 0340-7594, 1432-1351. doi: 10.1007/s00359-006-0106-9.

A. V. Oppenheim, A. S. Willsky, and w. S. Hamid. *Signals and Systems*. Pearson, Upper Saddle River, N.J, 2 edition edition, Aug. 1996. ISBN 978-0-13-814757-0.

K. Pearson, Ö. Ekeberg, and A. Büschges. Assessing sensory function in locomotor systems using neuro-mechanical simulations. *Trends in Neurosciences*, 29(11):625–631, Nov. 2006. ISSN 0166-2236. doi: 10.1016/j.tins.2006.08.007. 00147.

J. F. A. Poulet and B. Hedwig. A corollary discharge maintains auditory sensitivity during sound production. *Nature*, 418(6900):872–876, Aug. 2002. ISSN 1476-4687. doi: 10.1038/nature00919.

J. F. A. Poulet and B. Hedwig. The Cellular Basis of a Corollary Discharge. *Science*, 311(5760):518–522, Jan. 2006. ISSN 0036-8075, 1095-9203. doi: 10.1126/science.1120847.

J. W. S. Pringle. The gyroscopic mechanism of the halteres of Diptera. *Phil. Trans. R. Soc. Lond. B*, 233(602):347–384, Nov. 1948. ISSN 0080-4622, 2054-0280. doi: 10.1098/rstb.1948.0007.

V. Ramaswamy. An Algorithmic Barrier to Neural Circuit Understanding. *bioRxiv*, page 639724, May 2019. doi: 10.1101/639724.

S. Ray and U. S. Bhalla. PyMOOSE: Interoperable scripting in Python for MOOSE.

Frontiers in Neuroinformatics, 2, 2008. ISSN 1662-5196. doi: 10.3389/neuro.11.006.2008.

W. Reichardt. Autocorrelation, a principle for the evaluation of sensory information by the central nervous system. *Sensory communication*, pages 303–317, 1961.

W. Reichardt and T. Poggio. Visual control of orientation behaviour in the fly: Part I. A quantitative analysis. *Quarterly reviews of biophysics*, 9(3):311–375, 1976.

W. Reichardt and H. Wenking. Optical detection and fixation of objects by fixed flying flies. *Naturwissenschaften*, 56(8):424–424, 1969.

W. E. Reichardt, F. O. Schmitt, and F. G. Worden. Functional characterization of neural interactions through an analysis of behavior. In *The Neurosciences: Fourth Study Program*, pages 81–103. MIT Press, 1979.

D. Ringach and R. Shapley. Reverse correlation in neurophysiology. *Cognitive Science*, 28(2):147–166, 2004. ISSN 1551-6709. doi: 10.1207/s15516709cog2802_2.

L. Ristroph, A. J. Bergou, G. Ristroph, K. Coumes, G. J. Berman, J. Guckenheimer, Z. J. Wang, and I. Cohen. Discovering the flight autostabilizer of fruit flies by inducing aerial stumbles. *Proceedings of the National Academy of Sciences*, 107(11): 4820–4824, Mar. 2010. ISSN 0027-8424, 1091-6490. doi: 10.1073/pnas.1000615107. 00116.

R. E. Ritzmann and A. Büschges. Adaptive motor behavior in insects. *Current Opinion in Neurobiology*, 17(6):629–636, Dec. 2007. ISSN 0959-4388. doi: 10.1016/j.conb.2008.01.001.

R. E. Ritzmann, C. M. Harley, K. A. Daltorio, B. R. Tietz, A. J. Pollack, J. A. Bender, P. Guo, A. L. Horomanski, N. D. Kathman, C. Nieuwoudt, A. E. Brown, and R. D. Quinn. Deciding Which Way to Go: How Do Insects Alter Movements to Negotiate Barriers? *Frontiers in Neuroscience*, 6, 2012. ISSN 1662-453X. doi: 10.3389/fnins.2012.00097.

D. A. Robinson. The Use of Control Systems Analysis in the Neurophysiology of Eye Movements. *Annual Review of Neuroscience*, 4(1):463–503, Mar. 1981. ISSN 0147-006X. doi: 10.1146/annurev.ne.04.030181.002335.

A. Rosenblueth and N. Wiener. The Role of Models in Science. *Philosophy of Science*, 12(4):316–321, 1945. ISSN 0031-8248. 00540.

A. Rosenblueth, N. Wiener, and J. Bigelow. Behavior, Purpose and Teleology. *Philosophy of Science*, 10(1):18–24, Jan. 1943. ISSN 0031-8248. doi: 10.1086/286788.

E. Roth, K. Zhuang, S. A. Stamper, E. S. Fortune, and N. J. Cowan. Stimulus predictability mediates a switch in locomotor smooth pursuit performance for Eigenmannia virescens. *Journal of Experimental Biology*, 214(7):1170–1180, Apr. 2011. ISSN 0022-0949, 1477-9145. doi: 10.1242/jeb.048124. 00029.

E. Roth, S. Sponberg, and N. Cowan. A comparative approach to closed-loop computation. *Current Opinion in Neurobiology*, 25:54–62, Apr. 2014. ISSN 0959-4388. doi: 10.1016/j.conb.2013.11.005. 00060.

E. Roth, R. W. Hall, T. L. Daniel, and S. Sponberg. Integration of parallel mechanosensory and visual pathways resolved through sensory conflict. *Proceedings of the National Academy of Sciences*, 113(45):12832–12837, Aug. 2016. ISSN 0027-8424, 1091-6490. doi: 10.1073/pnas.1522419113. 00010.

J. E. Roy and K. E. Cullen. Dissociating Self-Generated from Passively Applied Head Motion: Neural Mechanisms in the Vestibular Nuclei. *Journal of Neuroscience*, 24 (9):2102–2111, Mar. 2004. ISSN 0270-6474, 1529-2401. doi: 10.1523/JNEUROSCI.3988-03.2004.

S. P. Sane and M. J. McHenry. The biomechanics of sensory organs. *Integrative and Comparative Biology*, 49(6):i8–i23, Dec. 2009. ISSN 1540-7063. doi: 10.1093/icb/icp112.

S. P. Sane, A. Dieudonné, M. A. Willis, and T. L. Daniel. Antennal Mechanosensors Mediate Flight Control in Moths. *Science*, 315(5813):863–866, Feb. 2007. ISSN 0036-8075, 1095-9203. doi: 10.1126/science.1133598.

H. H. Sant and S. P. Sane. Conserved mechanosensory-motor circuits in insect antennae. In *International Congress for Neuroethology*, Uruguay, Feb. 2016.

H. H. Sant and S. P. Sane. The mechanosensory-motor apparatus of antennae in the Oleander hawk moth (Daphnis nerii, Lepidoptera). *Journal of Comparative Neurology*, 526(14):2215–2230, June 2018. ISSN 0021-9967. doi: 10.1002/cne.24477.

N. Saxena, D. Natesan, and S. P. Sane. Odor source localization in complex visual environments by fruit flies. *The Journal of Experimental Biology*, 221(2):jeb172023, Jan. 2018. ISSN 0022-0949, 1477-9145. doi: 10.1242/jeb.172023.

A. Sherman and M. H. Dickinson. Summation of visual and mechanosensory feedback in Drosophila flight control. *Journal of Experimental Biology*, 207(1):133–142, Jan. 2004. ISSN 0022-0949, 1477-9145. doi: 10.1242/jeb.00731.

D. S. Smith. The fine structure of haltere sensilla in the blowfly Calliphora erythrocephala (Meig.), with scanning electron microscopic observations on the haltere surface. *Tissue and Cell*, 1(3):443–484, Jan. 1969. ISSN 0040-8166. doi: 10.1016/S0040-8166(69)80016-9.

R. W. Sperry. Neural basis of the spontaneous optokinetic response produced by visual inversion. *Journal of Comparative and Physiological Psychology*, 43(6):482–489, 1950. ISSN 0021-9940(Print). doi: 10.1037/h0055479. 01660.

S. Sponberg, T. Libby, C. H. Mullens, and R. J. Full. Shifts in a single muscle's control potential of body dynamics are determined by mechanical feedback. *Philosophical Transactions of the Royal Society of London B: Biological Sciences*, 366(1570): 1606–1620, May 2011a. ISSN 0962-8436, 1471-2970. doi: 10.1098/rstb.2010.0368. 00024.

S. Sponberg, A. J. Spence, C. H. Mullens, and R. J. Full. A single muscle's multifunctional control potential of body dynamics for postural control and running. *Philosophical Transactions of the Royal Society of London B: Biological Sciences*, 366(1570):1592–1605, May 2011b. ISSN 0962-8436, 1471-2970. doi: 10.1098/rstb.2010.0367. 00035.

S. Sponberg, J. P. Dyhr, R. W. Hall, and T. L. Daniel. Luminance-dependent visual processing enables moth flight in low light. *Science*, 348(6240):1245–1248, June 2015. ISSN 0036-8075, 1095-9203. doi: 10.1126/science.aaa3042.

M. V. Srinivasan and S. Zhang. Visual Motor Computations in Insects. *Annual Review of Neuroscience*, 27(1):679–696, 2004. doi: 10.1146/annurev.neuro.27.070203.144343.

L. Stark. *Neurological Control Systems: Studies in Bioengineering.* Basic Books, New York, 1968. ISBN 978-0-306-30325-8. OCLC: 1012468879.

L. Stark and P. M. Sherman. A servoanalytic study of consensual pupil reflex to light. *Journal of Neurophysiology*, 20(1):17–26, Jan. 1957. ISSN 0022-3077. doi: 10.1152/jn.1957.20.1.17.

E. M. Staudacher, M. Gebhardt, and V. Dürr. Antennal Movements and Mechanoreception: Neurobiology of Active Tactile Sensors. In S. J. Simpson, editor, *Advances in Insect Physiology*, volume 32, pages 49–205. Academic Press, Jan. 2005. doi: 10.1016/S0065-2806(05)32002-9.

G. J. Stephens, B. Johnson-Kerner, W. Bialek, and W. S. Ryu. Dimensionality and Dynamics in the Behavior of C. elegans. *PLOS Computational Biology*, 4(4):e1000028, Apr. 2008. ISSN 1553-7358. doi: 10.1371/journal.pcbi.1000028.

S. S. Stevens and E. B. Newman. The Localization of Actual Sources of Sound. *The American Journal of Psychology*, 48(2):297–306, 1936. ISSN 0002-9556. doi: 10.2307/1415748.

M. Stimberg, D. F. M. Goodman, V. Benichoux, and R. Brette. Equation-oriented specification of neural models for simulations. *Frontiers in Neuroinformatics*, 8, 2014. ISSN 1662-5196. doi: 10.3389/fninf.2014.00006.

J. A. Strother, S.-T. Wu, E. M. Rogers, J. L. M. Eliason, A. M. Wong, A. Nern, and M. B. Reiser. Behavioral state modulates the ON visual motion pathway of Drosophila. *Proceedings of the National Academy of Sciences*, 115(1):E102–E111, Jan. 2018. ISSN 0027-8424, 1091-6490. doi: 10.1073/pnas.1703090115.

G. J. Taylor, T. Luu, D. Ball, and M. V. Srinivasan. Vision and air flow combine to streamline flying honeybees. *Scientific Reports*, 3, Sept. 2013. ISSN 2045-2322. doi: 10.1038/srep02614.

J. C. Theobald, D. L. Ringach, and M. A. Frye. Dynamics of optomotor responses in Drosophila to perturbations in optic flow. *Journal of Experimental Biology*, 213(8): 1366–1375, Apr. 2010a. ISSN 0022-0949, 1477-9145. doi: 10.1242/jeb.037945.

J. C. Theobald, D. L. Ringach, and M. A. Frye. Visual stabilization dynamics are enhanced by standing flight velocity. *Biology Letters*, 6(3):410–413, June 2010b. ISSN 1744-9561, 1744-957X. doi: 10.1098/rsbl.2009.0845. 00011.

J. Thorson. Dynamics of Motion Perception in the Desert Locust. *Science*, 145(3627): 69–71, July 1964. ISSN 0036-8075, 1095-9203. doi: 10.1126/science.145.3627.69.

N. Tinbergen. *The Study of Instinct*. The Study of Instinct. Clarendon Press/Oxford University Press, New York, NY, US, 1951.

N. Tinbergen. On aims and methods of Ethology. *Zeitschrift für Tierpsychologie*, 20 (4):410–433, Jan. 1963. ISSN 1439-0310. doi: 10.1111/j.1439-0310.1963.tb01161.x.

E. Tytell, P. Holmes, and A. Cohen. Spikes alone do not behavior make: Why neuroscience needs biomechanics. *Current Opinion in Neurobiology*, 21(5):816–822, Oct. 2011. ISSN 0959-4388. doi: 10.1016/j.conb.2011.05.017. 00056.

F. van Breugel and M. H. Dickinson. The visual control of landing and obstacle avoidance in the fruit fly Drosophila melanogaster. *Journal of Experimental Biology*, 215(11):1783–1798, June 2012. ISSN 0022-0949, 1477-9145. doi: 10.1242/jeb.066498. 00075.

F. van Breugel and M. H. Dickinson. Plume-Tracking Behavior of Flying Drosophila Emerges from a Set of Distinct Sensory-Motor Reflexes. *Current Biology*, 24(3): 274–286, Feb. 2014. ISSN 0960-9822. doi: 10.1016/j.cub.2013.12.023.

D. Varju. Stationary and dynamic responses during visual edge fixation by walking insects. *Nature*, 255(5506):330–332, May 1975. ISSN 1476-4687. doi: 10.1038/255330a0.

D. Varjú. Visual edge fixation and negative phototaxis in the mealworm beetle Tenebrio molitor. *Biological Cybernetics*, 25(1):17–26, Mar. 1976. ISSN 1432-0770. doi: 10.1007/BF00337045.

D. Varjú. *Systemtheorie: für Biologen und Mediziner*. 1977. ISBN 978-3-642-66567-7 978-3-540-08086-2. OCLC: 913684259.

D. Varjú. A note on the reafference principle. *Biological Cybernetics*, 63(4):315–323, Aug. 1990. ISSN 1432-0770. doi: 10.1007/BF00203455.

M. Vergassola, E. Villermaux, and B. I. Shraiman. ‘Infotaxis’ as a strategy for searching without gradients. *Nature*, 445(7126):406–409, Jan. 2007. ISSN 1476-4687. doi: 10.1038/nature05464.

S. Viollet and J. Zeil. Feed-forward and visual feedback control of head roll orientation in wasps (Polistes humilis, Vespidae, Hymenoptera). *Journal of Experimental Biology*, 216(7):1280–1291, Apr. 2013. ISSN 0022-0949, 1477-9145. doi: 10.1242/jeb.074773.

H. von Helmholtz. *Handbuch der physiologischen Optik*. Voss, 1867.

H. von Helmholtz and J. P. C. Southall. *Helmholtz’s treatise on physiological optics.*

Thoemmes, Bristol, England; Sterling, VA, 2000. ISBN 978-1-85506-831-5. OCLC: 81243490.

E. von Holst and R. D. Martin. *The Behavioral Physiology of Animals and Man Volume 1*. University of Miami Press, Place of publication not identified, 1973. ISBN 978-0-87024-261-8. OCLC: 798386219.

E. von Holst and H. Mittelstaedt. Das reafferenzprinzip. *Naturwissenschaften*, 37(20): 464–476, 1950.

H. Wagner. Flow-field variables trigger landing in flies. *Nature*, 297(5862):147–148, May 1982. ISSN 0028-0836, 1476-4687. doi: 10.1038/297147a0.

J. Wessnitzer and B. Webb. Multimodal sensory integration in insects—towards insect brain control architectures. *Bioinspiration & Biomimetics*, 1(3):63–75, Sept. 2006. ISSN 1748-3190. doi: 10.1088/1748-3182/1/3/001.

S. C. Whitehead, T. Beatus, L. Canale, and I. Cohen. Pitch perfect: How fruit flies control their body pitch angle. *Journal of Experimental Biology*, 218(21):3508–3519, Nov. 2015. ISSN 0022-0949, 1477-9145. doi: 10.1242/jeb.122622.

N. Wiener. *Cybernetics Or Control and Communication in the Animal and the Machine*. MIT Press, 1961. ISBN 978-0-262-73009-9. 00233.

Y. Yamawaki and W. Ishibashi. Antennal pointing at a looming object in the cricket Acheta domesticus. *Journal of Insect Physiology*, 60(Supplement C):80–91, Jan. 2014. ISSN 0022-1910. doi: 10.1016/j.jinsphys.2013.11.006.

Chapter 2

Airflow-dependent modulation of antennal positioning reflex

2.1 Introduction

Animal locomotion depends on the acquisition and reliable encoding of sensory information from their surroundings. This task is particularly challenging for control of fast movements, such as those that drive flight in insects. On stroke-to-stroke timescales, insect flight relies heavily on rapid mechanosensory feedback from antennae and visual feedback from their compound eyes (Sane et al., 2007; Warrant and Dacke, 2011). They actively move and position their antennae and heads via fine feedback control of antennal muscles and head movements, thereby optimizing acquisition of sensory information required for robust flight control (Hengstenberg, 1993; Staudacher et al., 2005). In addition to the dynamics of movements of sensory organs, the activity of sensory neurons is also inherently dependent on the internal state of the animal. For instance, the activity of visual interneurons has been shown to be different in active vs. quiescent insects (Chiappe et al., 2010; Maimon et al., 2010). Such state-dependent modulation vastly enhances the functionality of the antennae and eyes by greatly widening the range of their sensory acquisition.

From a controls perspective, how state-modulated sensory-feedback influences movements of sensory organs for optimal acquisition of information poses a fascinating neurobiological question. Specifically, the insect antenna provides an excellent study system to address this question for several reasons. First, antennae are multi-modal sensory probes; they are used to acquire both olfactory and mechanosensory information (Schneider, 1964). Thus, their movements may strongly depend on the cues the insects are trying to maximize. Second, the movements of antennae are guided by multi-sensory inputs (Erber et al., 1993; Khurana and Sane, 2016). Antennal movements therefore provide a convenient readout for understanding how the nervous system combines sensory feedback from diverse modalities. Third, such movements are context-specific and depend on whether the insect is walking, flying, foraging, escaping, etc. (Staudacher et al., 2005). State-dependent neuromodulation therefore plays an important role in the control of antennal movements.

State-based and context-specific modulations of antennal position likely optimize sensory input acquisition on long timescales. On shorter, stroke-to-stroke timescales the antennae should be held in a stable position to reliably obtain information. For instance, drifts in position on these timescales would alter antennal mechanosensory feedback from the Johnston's organ (JO), which is required for controlled flight (Sane et al., 2007). The smooth mobility of the antennae must therefore be balanced against the need for maintaining them in a stable, unambiguous position. Here, we investigate this trade-off using the Oleander hawkmoth, Daphnis nerii, as our model system.

Stable positioning of the antennae requires mechanosensory feedback from antennal hair plates (also called Böhm's bristles in moths). These are located at the base of the antennae and they encode the instantaneous position of the antenna with respect to the head (Böhm, 1911; Krause et al., 2013; Krishnan et al., 2012; Okada and Toh, 2000). Across a variety of insects, including hawkmoths, the axons of these mechanosensors spatially overlap with the dendritic arbors of antennal motor neurons in the Antennal Mechanosensory and Motor Centre (AMMC) (Schneider and Kaissling, 1956; Krishnan et al., 2012; Sant and Sane, 2018, 2019). Information about instantaneous antennal position is therefore rapidly fed back into the antennal muscles, likely stabilizing position. Indeed, ablating these mechanosensors destroys stable positioning of the antenna in various insects (Krause et al., 2013; Krishnan et al., 2012; Okada and Toh, 2000).

Modulation of antennal position is guided by multiple sensory cues. Flying insects respond to increasing airflow by bringing their antennae progressively and symmetrically forward (Gewecke, 1974; Heran, 1959; Khurana and Sane, 2016). Optic flow, on the other hand, induces antennae to move in the opposite direction (Khurana and Sane, 2016; Krishnan and Sane, 2014; Mamiya et al., 2011). Walking insects also respond to visual motion by tracking moving objects with their antennae, but this behavior is not bilaterally symmetric (Honegger, 1981; Okada and Toh, 2006; Yamawaki and Ishibashi, 2014). In addition to these inputs, odor, too, has been shown to modulate antennal position (Erber et al., 1993; Lambin et al., 2005). Although the effect of these cues on antennal position has been quantified, the mechanistic basis underlying this modulation remains largely unknown.

The above studies suggest that the antennal motor system combines information from several sources with disparate latencies ranging from fast mechanosensory feedback from the Böhm's bristles ($< 10\,\mathrm{ms}$) to slower visual input from the eyes (approx. $35\,\mathrm{ms}$ to $60\,\mathrm{ms}$) (Krishnan et al., 2012; Krishnan and Sane, 2014). How does the antennal motor system integrate proprioceptive feedback at rapid (stroke-to-stroke) timescales with relatively slower multi-sensory input to produce stable antennal positioning? Here, we address this question by investigating the neural principles underlying airflow-dependent antennal positioning in the oleander hawkmoth, Daphnis nerii. Because both stable positioning of antennae and airflow-dependent changes occur while preparing for or during flight, our experiments were performed on tethered flying hawkmoths. We use the framework described in chapter 1 to perform experiments, describe the behavior, derive the structure of the neuromechanical black box and infer the computation performed by the underlying circuits. Finally, based on this, we construct a minimalistic neural circuit that can position the antennae in a robust, yet flexible manner.

2.2 Methods

2.2.1 Moth breeding and treatment procedures

The experiments described in this paper were performed on 1-2 day old adult oleander hawkmoths, Daphnis nerii. The moths used were either laboratory-bred or obtained from wild pupae. Moth eggs were obtained by placing 2 male and 2 female moths in a large meshed chamber (approximately $8\,\mathrm{m}^3$) along with their host plants, Nerium oleander, and Tabernaemontana divaricata. Additional flowering plants placed in the meshed chamber provided nectar for the adult moths. Moth larvae were placed in mesh-topped boxes and reared on a natural diet of Nerium oleander leaves. Post-pupation, they were placed in sawdust till the moths emerged. The emerged adults were placed in cloth cages and exposed to natural day-night cycles until they were used for experiments.

Airflow stimulus

A wind tunnel was used to provide moths with different airflow cues. The working section of the wind tunnel had a cross-section of $0.28\,\mathrm{m} \times 0.28\,\mathrm{m}$ and a length of 1.2 m (Figure 2.1A). The floor and the walls of the working section were covered with white paper to minimize visual cues. Moths were tethered such that their heads lay approximately at the center of the wind tunnel. The airflow speed in the wind tunnel was monitored using a constant temperature mini-anemometer (Kurz 490S, Kurz Instruments Inc., Monterey, CA, USA).

Dorsal magnetic tether

Moths were first cold anesthetized by placing them in $-20\,^{\circ}\mathrm{C}$ for 7 min to 9 min. The anesthetized moths were placed on an aluminum block maintained at $0\,^{\circ}\mathrm{C}$, the dorsal thorax descaled and a neodymium magnet (3 mm diameter, 1.5 mm) attached to the area (Figure A.1A). The total duration of the tethering process, including the cold anesthesia, did not exceed 20 min. For the antennal perturbation experiments (described below), a small piece of a minutien pin (Austerlitz insect pins) was glued to the tip of the left antenna using UV-cure glue (Loctite-352). Moths were allowed to recover from the process for at least an hour. After recovery, moths were tethered using the dorsally glued magnet and placed in a wind tunnel. This method of tethering is similar to that used in Hinterwirth and Daniel (2010).

Restricting Johnston's organs

Moths were cold anesthetized and placed on an aluminum block maintained at $0\,^{\circ}\mathrm{C}$ throughout the procedure. The area around the base of the antenna was carefully

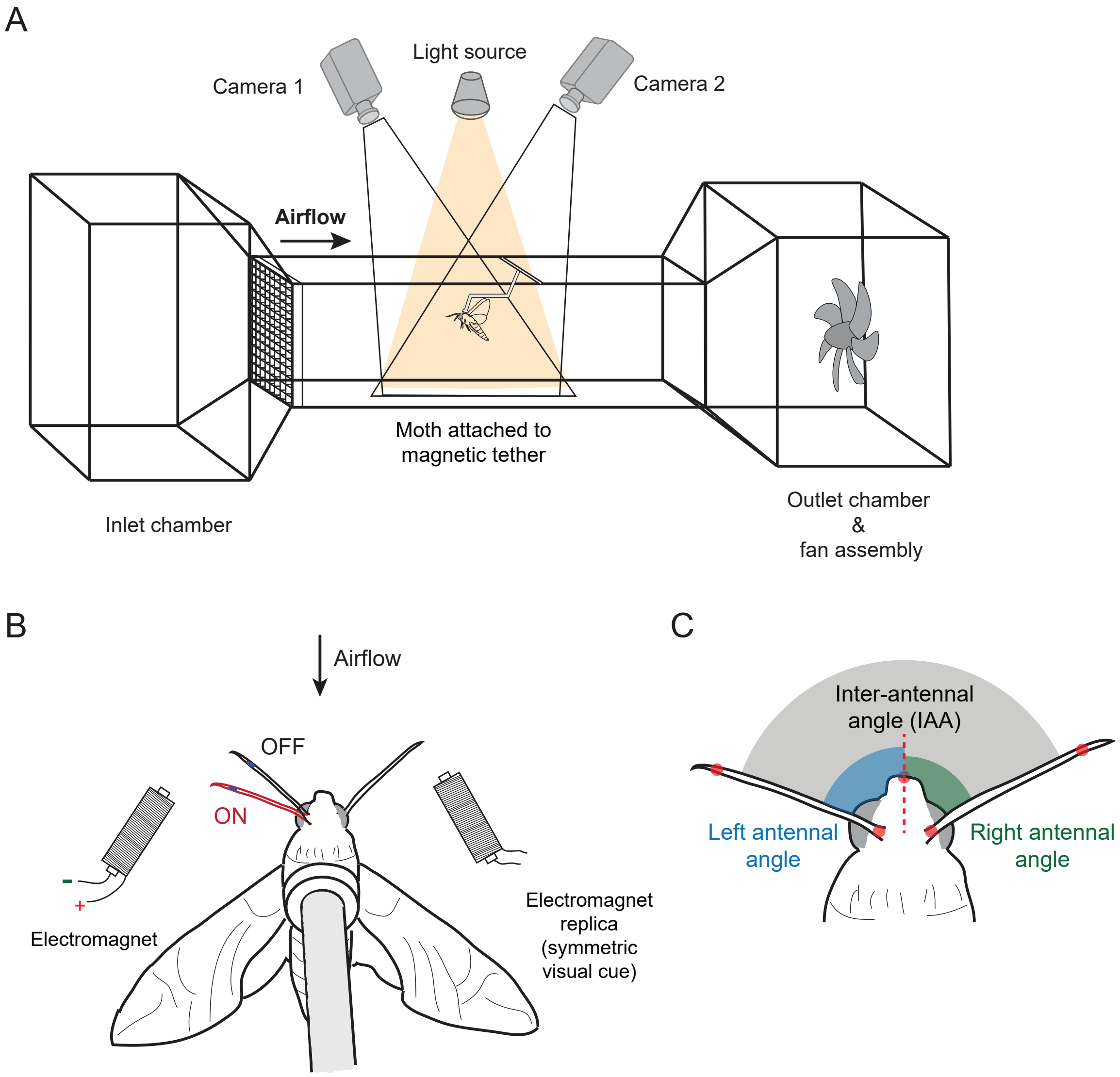

Fig. 2.1 : Experimental apparatus
(A) Experiments were performed in a 1.2 m × 0.28 m × 0.28 m wind tunnel. The moth was tethered to the wind tunnel through a neodymium magnet glued to the thorax. Two high speed cameras filming at 100 fps captured the antennal responses during tethered flight. **(B)** Electromagnets were used to perturb the antennae in order to quantify stability at different airflows. Iron filings were glued to the left antenna and perturbed during tethered flight using the left electromagnet (the right electromagnet was retained for visual symmetry but otherwise not used). The response was filmed at 1000 fps for four different airflows. **(C)** IAA was computed as angle between antennae (grey). Head vector (dashed red line) was defined using head point and midpoint of antennal bases. Left and right antennal angle (blue, green) was computed as angle between respective antenna and head vector.

descaled using a fine brush. This ensured that the Böhm's bristles present at the base of the antenna remained intact (Figure A.1B,C,E). Next, the pedicel-flagellum joint was carefully descaled under the microscope. A small drop of cyanoacrylate glue was placed on the pedicel-flagellum joint and spread around the joint using an insect minutien pin (Austerlitz insect pins) (Figure 2.2, Figure A.1F). For sham-treated moths, the glue was placed on the third/fourth annulus of the antenna instead of the pedicel-flagellum joint (Figure 2.2, Figure A.1D). After both the antennae were treated, a neodymium magnet was glued to the thorax of the moth (described above). The entire duration of this procedure for both the sham and the JO-restricted moths was around 20 min to 40 min.

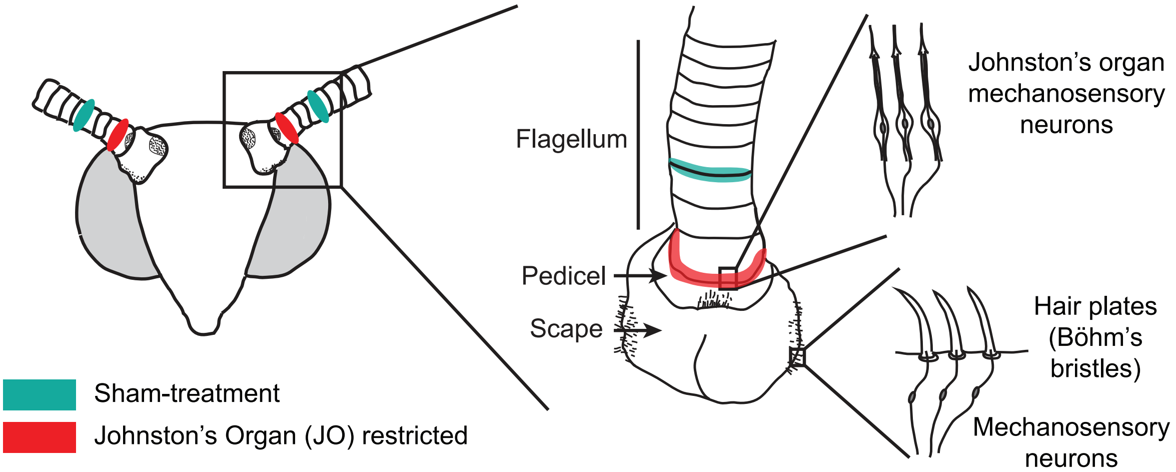

Fig. 2.2 : Treatment groups
JO-restricted: mechanosensory feedback from JO was restricted in a subset of moths by gluing the pedicel-flagellar joint (red). Sham-treated: To control for the effect of glue, annuli on the flagellum some distance from the pedicel-flagellar joint were restricted in another subset of moths (green). Note that active joints of the antenna were not glued, allowing full antennal mobility.

2.2.2 Behavior experiments

The below described behavior experiments were performed alongside with Nitesh Saxena, a graduate student from Sanjay P. Sane's lab. We together performed the experiments and digitized the data. I performed the subsequent data analysis and developed the computational models.

Antennal response to airflow

Tethered moths (control, sham and JO-restricted) were presented with frontal airflow ranging from $0\,\mathrm{m\,s^{-1}}$ to $5\,\mathrm{m\,s^{-1}}$ in increments of $0.5\,\mathrm{m\,s^{-1}}$. The antennal response to airflow was filmed at 100 fps using two Phantom v7.3 high-speed cameras (Vision Research, Wayne, NJ, USA; Figure 2.1A). To ease digitization, a black spot was marked at ~5 mm from the tip of each antenna for all the treatments (control, sham and JO-restricted). We recorded at 100 frames for each windspeed, which corresponds to about 35 wingbeats of antennal position data per windspeed. Most moths initiated flight immediately after tethering. In the few cases when flight was not automatically initiated, flight was elicited either by giving it a brief airflow of 0.5-1 $\mathrm{m\,s^{-1}}$ or by a tactile stimulus to the abdomen. Once a flight bout was initiated, the moth was given increasing airflow from $0\,\mathrm{m\,s^{-1}}$ to $5\,\mathrm{m\,s^{-1}}$ and the antennal response was continuously recorded. In general, the antennal response was obtained in one continuous flight bout of the moth. After every experiment, the filming area was calibrated using a custom-made 3D calibration object. The recorded videos were sub-divided into antennal responses for individual airflow speeds, then calibrated, digitized and analyzed.

Antennal perturbation at different airflows

In this experiment, tethered moths were given 4 values of airspeed – $0\,\mathrm{m\,s^{-1}}$ $1.5\,\mathrm{m\,s^{-1}}$ $2.5\,\mathrm{m\,s^{-1}}$ and $4\,\mathrm{m\,s^{-1}}$. The values were chosen such that they represented the entire curve obtained from the above experiment (Figure 2.3A). Two custom electromagnets were used to perturb the antennae of either control or JO-restricted moths, at the above four airflow speeds (Figure 2.1B). The electromagnets were positioned above and behind the tethered moth such that, when switched on, they pulled the antenna backward and slightly upward. Only the left electromagnet was used for perturbation, whereas the right was placed symmetrically to avoid differential visual inputs to the moth. The antennal responses to perturbations at different airflows were recorded at 1000 fps using two Phantom v7.3 high-speed cameras (Vision Research, Wayne, NJ, USA). An Arduino mega 2560 was used to switch on and off the electromagnet five times per trial, at a frequency of 1 Hz. The perturbation protocols were flanked by quiet zones to record the resting position of the antennae. The total duration of perturbation for each airflow was ~7.122 s. To ensure consistent ratios of quiet zones and perturbations, the camera was triggered by the Arduino before beginning a protocol. The data was usually obtained from one flight bout for each protocol.

2.2.3 Data analysis

Almost all the data analysis and statistics used in this paper were done in MATLAB (The MathWorks, Natick, MA, USA). Regression fits, on the other hand, were all performed in R (Team, 2017).

Antennal response to airflow

Using two different calibrated camera views, we reconstructed the three-dimensional (3D) Cartesian coordinates of the tip and base of both antennae. Digitization of the antennae and reconstruction of the digitized points were done in MATLAB using a custom written code (DLTdv5; Hedrick (2008)). Antennal vectors were calculated using the Cartesian coordinates of the tip and base of each antenna. The angle between the antennae, also called inter-antennal angle (IAA), was computed as the angle between the two antenna vectors (Figure 2.1C). All 100 frames of antennal position for all airflows were first digitized for a subset of the data (2 out of 8 control moths, 2 out of 5 sham moths and 5 out of 9 JO-glued moths). The mean and the standard deviation of IAA for each of these moths were then compared to 10 randomly picked frames from the same dataset. The mean and standard deviation of just 10 digitized frames were comparable to those from all digitized frames. Therefore, for the rest of the dataset, only 10 frames were digitized out of the 100 recorded frames.

After digitization, the IAA data was imported into R. Spearman's coefficient was computed for response to airflow in control, sham and JO-restricted moths. The coefficients for all moths were then pooled together based on treatment and tested for normality using Lilliefors test. Because the coefficients for all three treatments were not normally distributed ($p < 0.05$), Kruskal Wallis and Nemenyi tests were used to detect statistically significant differences between the three treatments.

The sensitivity of antennal movements to airflow was computed as change in IAA per $0.5\,\mathrm{m\,s^{-1}}$ step change in airflow (Figure A.2D-F). The torque on the antennal base due to aerodynamic drag was non-linear and dependent on the antennal angle and speed of frontal airflow (Gewecke and Heinzel, 1980). It was computed using the following equation (derived from Gewecke and Heinzel (1980)):

$$T_\gamma = \sin\gamma . v_a^{1.44}, \tag{2.1}$$

where,

$$\gamma = \text{antennal angle},$$
$$v_a = \text{speed of airflow}$$

T_γ was calculated for all three treatments (using data in Figure 2.3A-C, Figure A.2A-C). If feedback from JO regulates torques by changing antennal position, T_γ should remain constant for increasing airflows. Airflow-dependent changes in antennal position mitigated T_γ (Figure A.2G-I; compare control, sham with JO-restricted), but did not maintain it at a constant value.

Antennal perturbation at different airflows

Antennal responses to perturbations were recorded at 1000 fps by two high-speed cameras for ~7 s per airflow, for four different airflows. Because of this high frame rate, the number of frames to be digitized per moth was 28000 per camera view. The partially manual method of digitizing used for the above experiment was not feasible here. Therefore, an automated method of digitization was developed and used for this experiment. A custom code, henceforth called Autotracker, was written using the computer vision toolbox in MATLAB to automatically track the moth antennae and the tip of the moths' heads. Autotracker requires only the first frame (and a few problematic frames) to be manually annotated. It uses the annotated frames as templates and tracks the antennae by using a combination of template matching score maximization, error residual minimization and point drift minimization. At every frame, manually annotated templates were compared with sub-images extracted from the image. A template-matching score was computed as the distance between individual pixels in the sub-images and the templates. To minimize point drift to similar structures in the vicinity (from tips of antennae to tips of legs, for instance), we assumed a maximum velocity of the antennal movements. This method also restricted the search space of the template-matching algorithm, thereby increasing its speed.

It outputs the 3D Cartesian coordinates of the tip and base of both antennae, and the tip of the moth's head. The output was checked for mistracked frames, which were then manually corrected. The mistracked frame correction was performed using a modified version of DLTdv5 (Hedrick, 2008) which uses the same template matching algorithm as Autotracker.

By matching templates, we obtained a distribution of similarity, ideally centered around the point which was being tracked, for both camera views. Because the actual tracked point was an object in 3D, the tracked points in both camera views should correspond to the same point in 3D. This occasionally failed if we used the highest matched template for both views because of small variations in lighting which moved the position of the highest matched template in one view, but not the other. To circumvent this problem, we used the top 50 matched templates from both views to calculate the error residual, i.e. the 3D reconstruction error (Hedrick, 2008). We found a 3D point which minimized the 3D reconstruction error while simultaneously maximizing the similarity of templates in both views. The 3D reconstruction code was adapted from Hedrick (2008), and DLTdv5 was used to validate all computations. Using this approach, we were able to robustly track the points of interest in our videos and reconstruct them in 3D.

Using the Autotracker, we first completely digitized a subset of dataset (2 out of 11 control moths and 2 out of 6 JO-restricted moths; Figure A.7A,B). For the rest, we completely digitized only the regions where the electromagnets were switched off and the antennae were free to respond, as digitization of the whole dataset was not necessary (Figure A.7C,D). For instance, when the electromagnet was on, the antenna and head positions remained relatively constant. Hence, using only a few frames before the antenna release was sufficient for obtaining the perturbed location of the antenna. Additionally, the distributions of the digitized points obtained from this dataset were comparable to the distributions from the complete dataset.

After correcting for tracking errors, the Cartesian coordinates of the digitized points were used to compute the antenna vectors and the head vectors. Antennal vectors, as done above, were computed from the Cartesian coordinates of the antennal tip and the base points. The head vector, on the other hand, was computed as the unit vector along the line connecting the midpoint of the antennal bases to the head point. Individual antennal angle was defined as the angle between an antenna vector and the head vector (Figure 2.1C). Because the head is free to rotate in our experiments, a head-centric definition allowed us to compute the antennal angle independent of head rotation (Figure A.5A-D). During electromagnetic perturbations, we observed small changes in head orientation throughout our experiments (Figure A.5E-G). Despite this, the average position of the right (control) antennal angle typically remained constant throughout the trial, suggesting that the head-centric method used to compute antennal angles eliminated rotations of the head (Figure A.5A-D, Figure A.5). Additionally, both active head rotations and the ones elicited by electromagnetic perturbation seem to be too small to affect airflow-dependent antennal positioning (Figure A.5A-D).

Antennal set-point was defined as the angle the antenna was corrected to after each perturbation (steady-state angle after perturbation). Set-points were statistically compared using the same methodology as for IAA in the above experiment. After importing the corrected angle data set into R, Spearman's correlation coefficient was computed for set-point vs. airflow for every moth (control/JO). The coefficients for all moths were then pooled together based on treatment and tested for normality using Lilliefors test. Because the coefficients were not normally distributed ($p < 0.05$), Wilcoxon rank sum test was used to detect statistically significant differences between the two treatments.

Next, the antennal return trajectory was extracted from the left (perturbed) antennal angle. The return trajectory, however, was influenced by the wingbeat (Figure A.6A), likely due to transmission of wing motion via the head to the antennae and due to induced airflow produced by the beating wings (Sane et al., 2007; Sane and Jacobson, 2006). Such wingbeat-induced noise is typically removed using a simple notch filter about the undesired frequency. However, this approach would have filtered nearby frequencies and/or added ringing effects, thereby modifying the characteristics of the return trajectory. We circumvented this problem by subtracting the wingbeat frequency from the return trajectory. To do this, we first obtained the Fourier transform of the first derivative of the antennal trajectory, where the wingbeat frequency was most prominent. Generally, we found two dominant frequencies in the wingbeat frequency range (35 Hz to 40 Hz). These two frequencies might arise due to slight drifts in wingbeat frequencies due to the long recording duration (the separation between these frequencies were generally around 1 Hz). These two dominant wingbeat frequencies, along with their first harmonics, were selected and used to fit sine waves (amplitude and phase were the two free parameters for the fitting algorithm). These were then subtracted from the first derivative of the antennal return trajectory, and the resultant was integrated to obtain the wingbeat frequency-free return trajectory. To validate this approach, we compared the effect of notch filtering vs. sine subtraction on raw data (Figure A.6A). We used a fourth-order notch filter with a bandwidth of 5 Hz around the wingbeat frequency, which was determined as the highest power sinusoid with frequency from 35 Hz to 45 Hz (wingbeat frequency of moths). The sine subtraction method produced very similar trajectories to the notch filtered one even for antennal trajectories with greater wingbeat-induced noise, which illustrates its effectiveness (Figure A.6A). Sine subtraction ensured that only a particular frequency of a specific phase and amplitude was removed, ensuring that the characteristics of the return trajectory remain more or less unaltered.

After subtracting the wingbeat frequency from antennal kinematics, we calculated antennal set-points from the return trajectories and used these as inputs to tune the control theoretic models. After the electromagnetic perturbation was turned off, the antenna initiated the return to its set-point. The switching off of the electromagnetic field itself, as measured using a Hall effect sensor (DRV5053), was not a precise step function and took about ~75 ms to reach zero (Figure A.6C,D). Hence, the point at which the electromagnet stopped did not provide an accurate indication of the end of perturbation. The onset of antennal return movement was inherently variable from trial to trial because it was dependent on many factors including the distance of the electromagnet, the differences in antennal inertia, etc. (Figure A.6A,B). Instead, we determined the angular difference between the angle at which the antenna was held by the electromagnet to the angle at which it finally settled (set-point), and arbitrarily defined 25% of this difference as the start of the return trajectory (Figure A.6A). The set-point, the start point and the return trajectories were stored for further analysis (control theoretic model described below).

2.2.4 Computational Models

Control theory model of antennal response to perturbation

To analyze the return characteristics of the antennae, we modeled the antennal circuit as a closed loop feedback system with set-point as the input and the measured antennal position as the output (Figure 2.7). The transfer function of the complete system depends on the transfer function of the antennal circuit $L(s)$. We systematically increased the number of poles (n_p) and zeros (n_z) in $L(s)$ from zero to two (similar approach to Madhav et al. (2013)), as shown below:

1. $[n_p = 0, n_z = 0]$ Proportional (P) system
2. $[n_p = 1, n_z = 0]$ Integral (I) system
3. $[n_p = 1, n_z = 1]$ Proportional Integral (PI) system
4. $[n_p = 1, n_z = 1]$ Proportional Differential (PD) system
5. $[n_p = 2, n_z = 0]$ Double integral (II) system
6. $[n_p = 2, n_z = 2]$ Proportional Differential Integral (PID) system

We then described the transfer function for each of these models (Figure 2.7) and converted them into state space models with the constants as free parameters, set-point as the input and the antennal return trajectory after release as the output. We found the best parameter fits for each model for the given input and output using the System Identification Toolbox in MATLAB. The coefficient of determination (R^2) and normalized akaike information criterion (nAIC) were computed for each of these models to estimate the goodness-of-fit. R^2 quantifies the amount of variation in the raw data explained by the model. The nAIC, on the other hand, quantifies how much information is lost if one uses the model instead of the raw data. Both estimates, when combined, provide a measure of the goodness-of-fit for each model. Additionally, both these coefficients were statistically compared across models using Kruskal-Wallis and Nemenyi tests (not normally distributed, Lilliefors test, $p < 0.001$).

To test the predictive capabilities of all the models, we computed the model constants based on the measurements from one single airflow and used it to predict the return trajectories of the antennae for another airflow. We performed this analysis repeatedly for all airflows and computed the R^2 and the nAIC values for all the fits. These coefficients were also not normally distributed (Lilliefors test, $p < 0.001$). We, therefore, compared them statistically using Kruskal-Wallis and Nemenyi tests.

Spiking neural network circuit of the antennal circuit

The parameters of the components of the minimal neural circuit were set based on the integral (I) system model. Overall, we kept the spiking neural circuit model extremely simple, with the number of assumptions at a bare minimum, and used it as a feasibility test to check if such a neural circuit can produce behavior similar to that seen in experiments.

The minimal spiking neural circuit model incorporated the equivalent components of a simple linear integral model and had four components:

1. Mechanosensory neurons of the Böhm's bristles were assumed to be simple on-off neurons which encoded antennal position at the population level. Firing rates of individual neurons were dependent on activation (On: 50 Hz Poisson firing, Off: 10 Hz). Recruitment of the sensory neurons were proportional to activation of the hair plates (Böhm's bristles), i.e. the antennal angle.
2. Interneurons modulated the set-point of individual motor neurons based on activity of JO, which in turn depended on airflow. To break symmetry and cause the antenna to move forward with increasing airflow, the interneuron activated one of the motor neurons preferentially more than the other (Figure 2.9).
3. The motor neuron was a simple integrate-and-fire neuron whose output firing rate was proportional to synaptic input. Thus, it effectively acted as an activity summator in the control theoretic model (Figure 2.9). The negative feedback arises from the connectivity between motor neurons and the muscles they activate; motor neurons activate muscles which, upon contraction, reduce the mechanosensory feedback from the hair plates, in turn decreasing their own activity (Figure 2.9).
4. Muscles, due to their slow calcium dynamics, integrate the error signal (the time constant of the integral system is in the same range as calcium integration times (Chapman, 2012; Staudacher et al., 2005)). The combined activity of all antennal muscles determine change in antennal position. For the simple scape–pedicel joint, changes in position depend of on the difference in activity between the two muscles (Figure 2.9) and reach equilibrium when the activities are equal.

The sensory neurons model mechanosensory neurons that innervate hair plates (Böhm's bristles). The activation of the hair plates is binary - the mechanosensory hairs are either active (bent) or inactive (Krishnan et al., 2012). The interneuron in the model was an excitatory neuron whose firing rate changed with airflow (set-point). The motor neuron was approximated by an integrate-and-fire neuron which received inputs from sensory neurons and the interneuron (generic integrate-and-fire parameters Kunkel et al. (2017)). Every spike from the motor neuron elicited a calcium spike in the muscle, which decayed exponentially with a time constant of 50 ms (based on the integral system from the control theoretic analysis). The contraction of the muscle, at every time step, was determined by the level of calcium in the muscle. Two such circuits were used to model the pedicel segment of the antenna (Figure 2.9). The time step for the neural circuit and the associated calcium dynamics of the muscles was 0.1 ms. The change in antennal position, which was determined from the contraction of the antennal muscles, was updated every 10 ms. The model was simulated using NEST (Kunkel et al., 2017) and the antennal position was analysed in MATLAB. To compare the performance of the neural circuit with behavioral data, we ran the simulated data through the same control theoretic analysis. Because the sampling rate was 1000 fps for the model, the simulated position was upsampled using a cubic spline interpolation. The simulated position was then run through the same control theoretic framework described above. The exact same analysis, including statistics, was also used on the simulated data.

2.3 Results

Tethered flying moths were placed in a wind tunnel and presented with airflow stimuli of different magnitudes to measure their effect on antennal position. Using two high-speed cameras mounted on the wind tunnel (Figure 2.1A, see section 2.2), we recorded the changes in inter-antennal angle (IAA) for a range of airflows (Figure 2.1C) for a normal (Control) group which was left untreated, followed by moths in which the antennal mechanosensory feedback was restricted, as described below.

Two sets of mechanosensory structures – the antennal hair plates (Böhm's bristles) and the JOs are located in the basal scape and pedicel segments of the antenna (Figure 2.2). Both scape and pedicel are active joints, deformations in which are sensed by Böhm's bristles (Böhm, 1911; Krishnan et al., 2012). In contrast, the JO, composed of ca. 140 scolopidial sensory neurons, senses the passive vibrations in pedicel-flagellum joint (Sant and Sane, 2018). Previous studies have shown that the JO senses flagellar vibrations over a wide range of frequencies, from low-frequency vibrations due to airflow and gravity (Dieudonné et al., 2014; Kamikouchi et al., 2009; Mamiya and Dickinson, 2015; Yorozu et al., 2009) to high-frequency vibrations due to flight-related strains in the antennal base (Dieudonné et al., 2014; Sane et al., 2007). Based on these observations, we hypothesized that the mechanosensory inputs from JO modulate antennal position in response to airflow. To test this hypothesis, we restricted motion in the pedicel-flagellar joint of the antenna, and monitored its response to variable frontal airflow. This attenuated the passive vibrations of the flagellum that activate the JO (Figure 2.2, see section 2.2), thereby disrupting its mechanosensory feedback. Specifically, the moths were divided into three groups. In the control group, the moths were left unmanipulated. In the sham-treated group, we glued the annuli on the flagellum at some distance from the pedicel-flagellar joint. Finally, in the JO-restricted group, we glued the pedicel-flagellar joint thereby reducing or eliminating mechanosensory feedback from the JO.

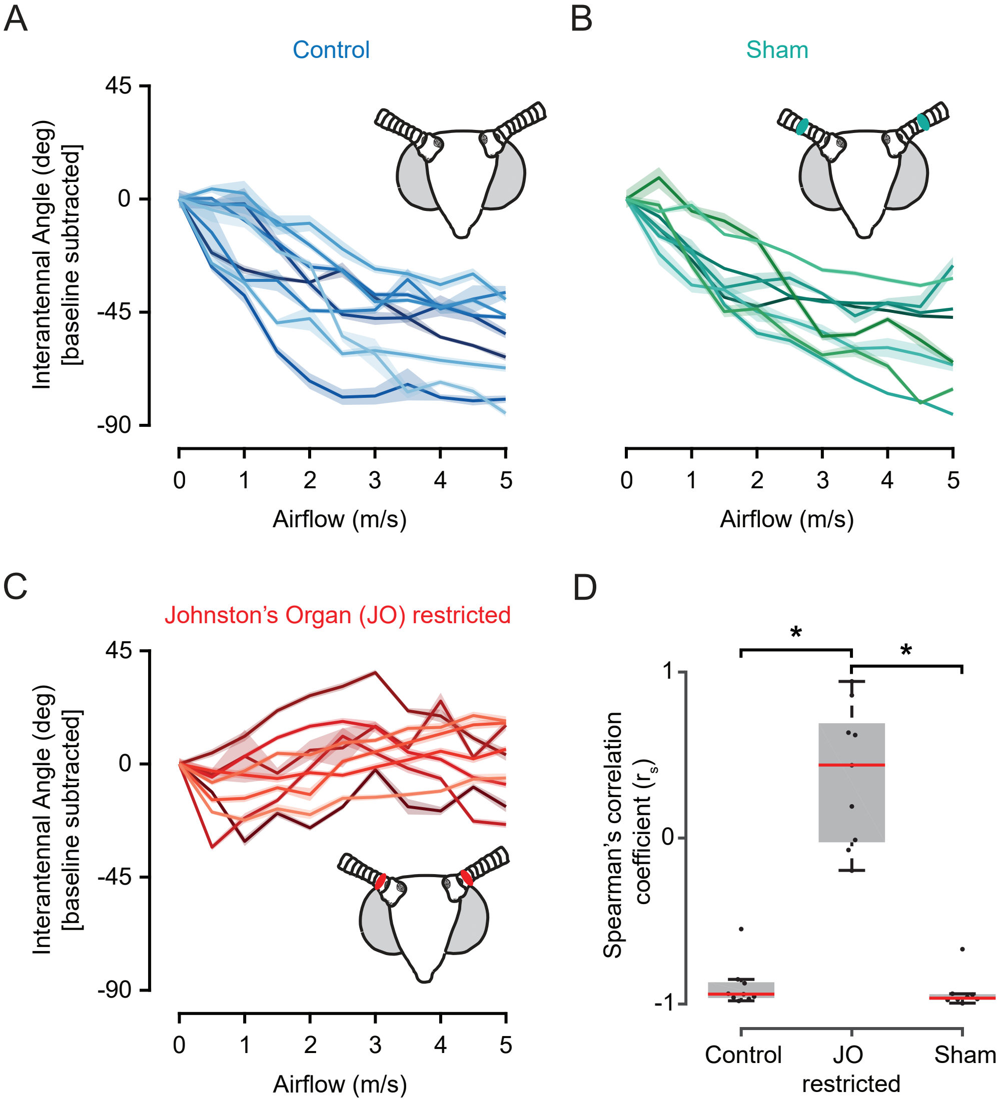

Fig. 2.3 : Antennal response to airflow
IAA of **(A)** Control (blue, n=9), **(B)** Sham-treated (green, n=8), and **(C)** JO-restricted moths (red, n=9). The initial IAA was subtracted from the rest (baseline subtraction) to clearly visualize the response to airflow. Different shades represent different individuals. Overlay around each line represents the standard error of the mean (s.e.m). **(D)** Box-and-whisker plots of Spearman's correlation coefficient (r_s) of IAA response to airflow for all treatments. The coefficient quantifies the monotonicity of IAA vs. airflow ($+1/-1$ perfect monotonic increase/decrease; median – Control: -0.94, JO: 0.44, Sham: -0.96). The grey box represents the central 50% data around the median (red line). The whiskers represent 1.5 times the interquartile range. Asterisks represent statistically different comparisons (Kruskal–Wallis, Nemenyi test, $p < 0.01$).

2.3.1 Johnston's organ mediate airflow-dependent antennal positioning

During tethered flight, control moths decreased their IAA with increasing frontal airflow (Figure 2.3A, Figure A.2A). This active modulation of antennae in response to airflow is henceforth termed as airflow-dependent antennal positioning. Although the initial IAA was different for each individual, in all cases it decreased monotonously as airflow varied from approximately 0 to 3 m/s, and stabilized when airflow exceeded about 3 m/s (Figure 2.3A, Figure A.2A). In sham-treated moths, for whom the third or the fourth annulus of the antenna was glued instead of the pedicel-flagellum joint, we observed a reduction in IAA with increasing airflow, similar to the control set (Figure 2.3B, Figure A.2B).

In moths with restricted pedicel-flagellar joints, airflow-dependent antennal positioning was abolished (Figure 2.3C, Figure A.2C) although these moths were still capable of moving their antennae. The IAA of these moths remained unchanged at the low airflow values, increasing slightly at higher airflows, perhaps due to aerodynamic drag (Figure 2.3C, Figure A.2C).

The Spearman's rank correlation coefficient (r_s) between IAA and airflow (Figure 2.3D, see section 2.2) was close to -1 for both control and sham-treated moths, implying a decrease in IAA with increasing airflow. In contrast, in the pedicel-flagellum restricted moths, mean r_s is close to 0, suggesting that their antennal position remains relatively unchanged with airflow (Figure 2.3D, $p < 0.01$, Kruskal Wallis test, Nemenyi test). Thus, only specific restriction of the pedicel-flagellum joint causes cessation of airflow-dependent antennal positioning, implying that mechanosensory inputs from the JO are required for this behavior to occur.

2.3.2 Conceptual model of airflow-dependent antennal positioning

The results described above are also consistent with previous data in honeybees (Khurana and Sane, 2016), indicating an evolutionarily conserved mechanism. Although mechanosensory inputs from JO control antennal responses to airflow, restricting these inputs by gluing pedicel-flagellar joint does not affect the ability of the animal to position antennae at flight-onset. Additionally, in honeybees, antennal response to other modalities, e.g. vision, is not affected upon JO-restriction (Khurana and Sane, 2016). Thus, initiation and maintenance of antennal position is independent of JO-mediated changes.

Along with sensory inputs from the JO, the antennal motor system receives proprioceptive inputs from Böhm's bristles (Krishnan et al., 2012; Sant and Sane, 2018). Antennal movement stimulates neurons underlying these sensory hairs, in turn activating antennal motor neurons and associated muscles with latencies of ~10 ms (Krishnan et al., 2012). Antennae are rendered immobile upon Böhm's bristles ablation, underscoring their importance in initiation and maintenance of antennal position (Krause et al., 2013; Krishnan et al., 2012; Okada and Toh, 2000). Thus, mechanosensory inputs from

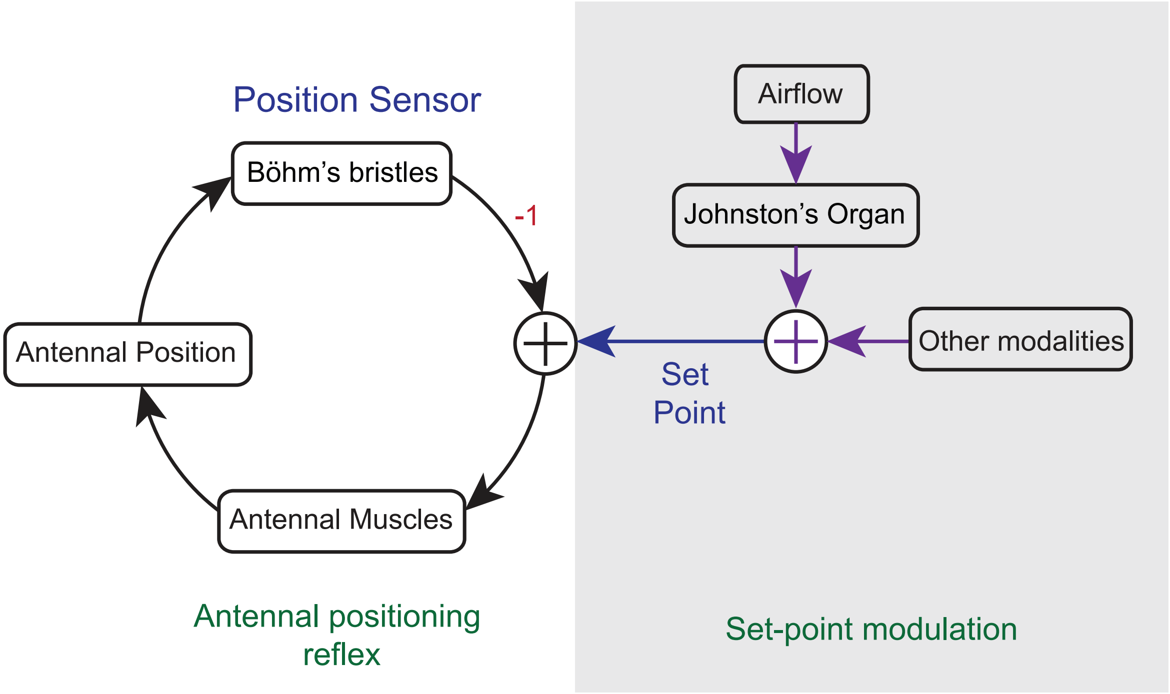

Fig. 2.4 : Conceptual model for airflow-dependent antennal positioning The model comprises two sub-circuits. "Antennal positioning reflex" is a fast sub-circuit that maintains antennal position at set-point (preferred position) using proprioceptive feedback from Böhm's bristles. "Set-point modulation circuit" continually modulates the set-point based on airflow, via the JO.

Böhm's bristles are essential for maintaining stable antennal position. On the other hand, restricting inputs from JO by gluing the pedicel-flagellar joint does not affect the ability to position antennae, but disrupts airflow-dependent antennal movements (Figure 2.3C, Figure A.2C).

These and previous results suggested a conceptual model of antennal positioning behavior (Figure 2.4), where antennal position is encoded by Böhm's bristles which activate antennal muscles via a reflex arc (Krishnan et al., 2012). This reflex operates as a negative feedback loop to ensure initiation and maintenance of antennal position during flight. JO-mediated airflow-dependent changes are achieved by modulation of the set-point (equilibrium position) of this negative feedback loop. Ablation of Böhm's bristles would break the feedback loop, disabling antennal positioning. On the other hand, restriction of JO inputs would cease airflow-dependent movements while still allowing initiation and maintenance of antennal position.

We propose that the antennal positioning behavior comprises two hierarchically arranged sub-circuits (Figure 2.4); one that maintains antennae at a preferred position or set-point using proprioceptive feedback from Böhm's bristles (antennal positioning reflex) and another that modulates the set-point using sensory inputs from multiple modalities (set-point modulation circuit). Using an electromagnet set-up, we altered proprioceptive feedback from the Böhm's bristles by perturbing antennal position (Figure 2.1B, see section 2.2). We could not ablate Böhm's bristles because removal of proprioceptive inputs renders the antennae immobile (Krishnan et al., 2012). Inputs to the set-point modulation circuit were experimentally altered by changing airflow and restricting the JO (Figure 2.1A, Figure 2.2). Therefore, using both experiments and computational simulations, we tested the hypothesis that airflow-dependent antennal positioning results from these two components working in concert, allowing its set-point to be tunable.

2.3.3 Airflow modulates set-point of antennal positioning reflex

To test the hypothesis that airflow-dependent mechanosensory feedback from the JO alters the set-point at which the antenna is maintained, we asymmetrically perturbed the left antenna with an electromagnet at different values of frontal airflow (Figure 2.1B, see section 2.2). In these experiments, the right unperturbed antenna served as internal control. The position of both antennae were separately monitored, and the angle of each antenna was calculated with respect to the head vector to quantify the magnitude of electromagnet perturbation (Figure 2.1C, see section 2.2). The average position of the right (unperturbed) antenna remained unaffected by magnetic perturbations delivered to the contralateral antenna (Figure 2.5A,C). Thus, the reflex loop on each side of the antenna was independent of the contralateral antenna, consistent with previous findings that the anatomical projections of the Böhm's bristles do not cross the midline (Krishnan et al., 2012; Sant and Sane, 2018). After perturbation was removed by switching off the electromagnet, the left (perturbed) antenna returned to the set-point corresponding to the airflow value (Figure 2.5B,D). For greater values of frontal airflow,

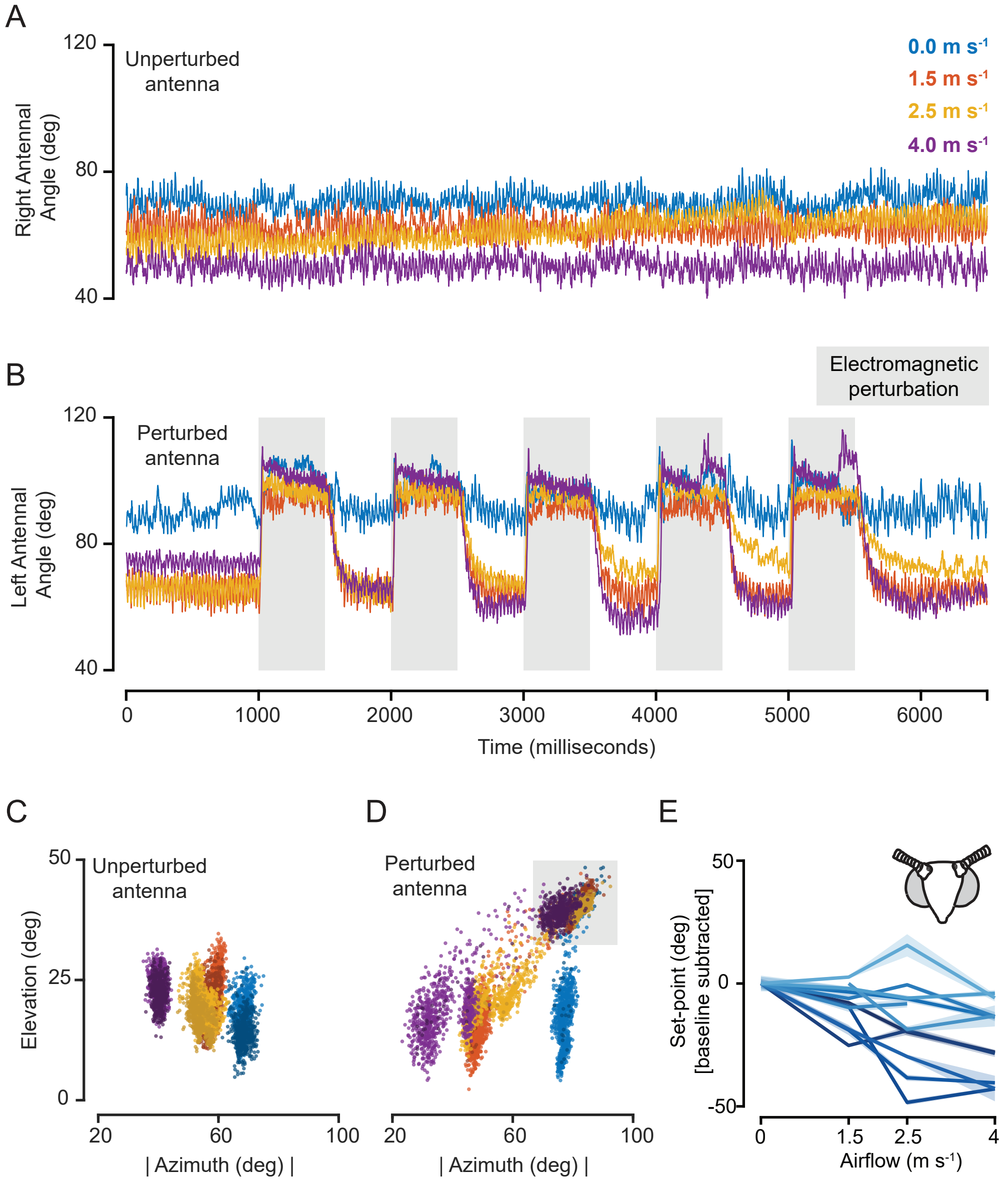

Fig. 2.5 : Antennal response to perturbations in control moths
(A) Right antenna (internal control) was unaffected by left antennal perturbations (depends only on frontal airflows). **(B)** Left antenna actively corrected position upon electromagnet release (perturbations in grey). Corrected angle depended on frontal airflow. Sometimes moths varied their corrected positions during trials (example response - 1.5 $\mathrm{m\,s^{-1}}$), perhaps due to set-point modulations by other modalities (Figure 2.4). **(C)** Azimuth-elevation plots show airflow based clustering of right antennal position. **(D)** Left antenna formed five clusters (four airflows, perturbed location). **(E)** Set-points of control moths decreased with increasing airflow. Different shades indicate different trials (n=11 trials from 9 moths). The overlay indicates s.e.m.

the antennae moved forward to smaller set-points (Figure 2.5E). Thus, the presence of airflow causes the state of the antennal motor neurons to change, thereby altering the motor commands to the antennal muscles and hence the set-point of the antennal position.

2.3.4 Antennal positioning reflex is unaffected by absence of sensory inputs from Johnston's organs

If mechanosensory inputs from the JO only modulates the internal state (set-point) of the antennal motor neurons, we hypothesized that restricting it should not affect the antennal positioning reflex (Figure 2.4). To test this, we perturbed the antennae of moths in which the pedicel-flagellar joint was glued, thereby restricting the input from the JOs. Such moths could consistently correct for perturbations of the antennae (Figure 2.6A-D), but their set-points did not decrease in response to airflow (Figure 2.6E). Spearman's rank correlation coefficients (r_s) between set-points and airflow were significantly different for control and JO-restricted moths (Figure 2.6F, $p < 0.01$, Wilcoxon rank sum test). JO restriction, therefore, only alters set-point modulation due to airflow and not the ability to maintain antennal position.

2.3.5 Simple linear models approximate antennal positioning reflex

Next, we used a control theoretic framework to compare the dynamics of the antennal positioning reflex at different set-points. We first expressed the conceptual model (Figure 2.4) as a linear control theory model, with the transfer function $L(s)$ representing the error correction dynamics of the antennal positioning reflex (Figure 2.7). $L(s)$ was represented as a standard set of transfer functions ranging from Proportional (P), Integral (I), Proportional-Integral (PI), Proportional-Differential (PD), Double-integral (II) and Proportional-Integral-Differential (PID) systems (Figure 2.7, see section 2.2). These models were fit to the return trajectory of a perturbed antenna using the System Identification Toolbox in MATLAB.

We used two measures to quantify the goodness of fit of transfer functions - adjusted coefficient of determination R^2 and normalized akaike's information criterion (nAIC). R^2 estimates the percentage of variation in the raw data explained by a model. nAIC, on the other hand, quantifies the information lost when a model is used instead of raw data. Both measures penalize models with a high number of parameters (i.e. complex models). The most parsimonious model, therefore, would have a high adjusted R^2 and a low nAIC. These two measures, when combined, provide a reliable way of estimating the goodness of fit of transfer functions.

Transfer functions I, PI, PD and PID best fit the error correction dynamics underlying antennal return trajectories based on both measures (control: Figure 2.8A-D, JO-restricted: Figure A.3A-D; parameters given in Table 2.1). Goodness-of-fits of these models were statistically different from other models (P, II), but not from one another (control: Figure 2.8C,D, JO-restricted: Figure A.3C,D). Simple linear models, such as

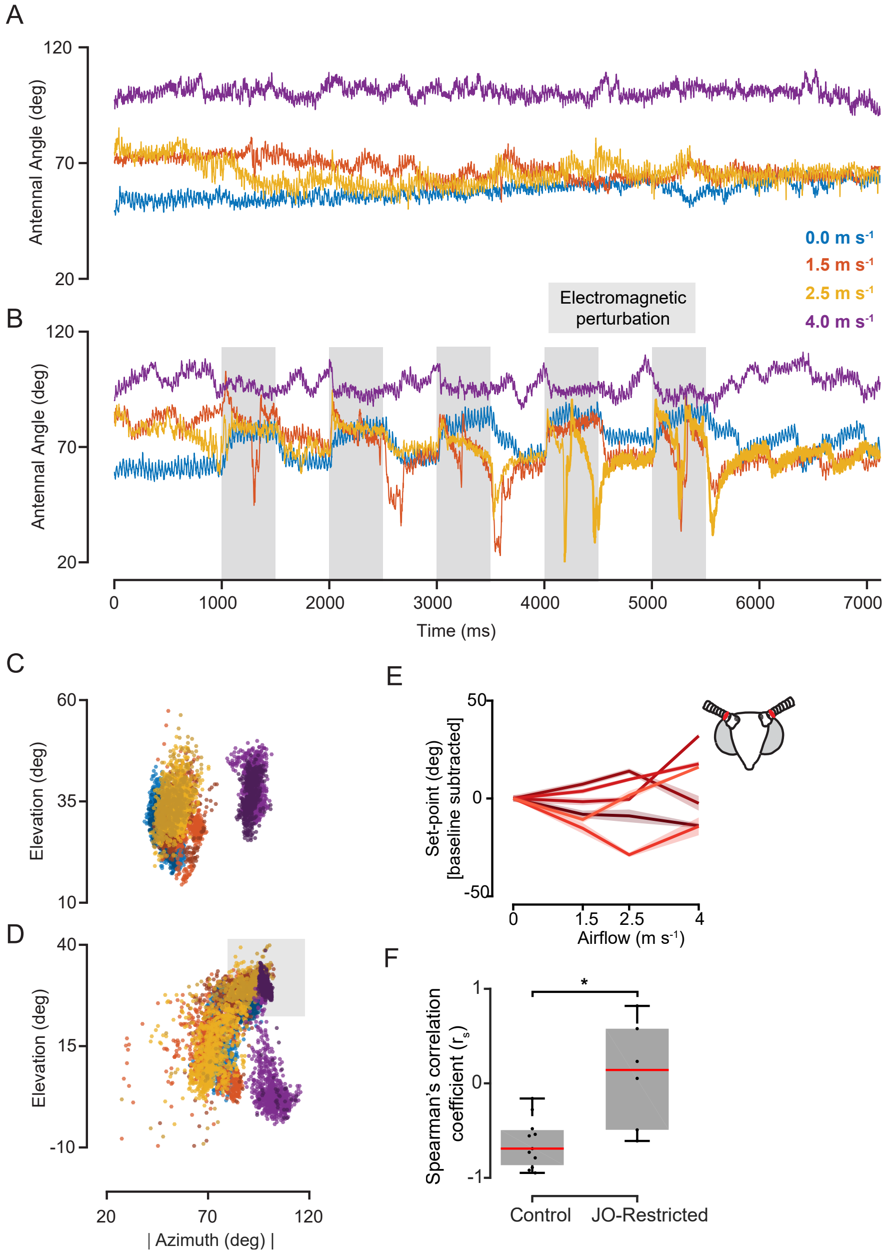

Fig. 2.6 : Antennal response to perturbations in JO-restricted moths
(A) Right antenna was unaffected by perturbations. **(B)** Left antenna was actively corrected to the same position regardless of airflow in JO-restricted moths (except for $4\,\mathrm{m\,s^{-1}}$). Spikes in position were caused by antennal movement due to ipsilateral front leg. **(C-D)** Azimuth-elevation plots of **(C)** right and **(D)** left antennal position. At $4\,\mathrm{m\,s^{-1}}$, the antenna was unable to maintain position and drifted backward. **(E)** Set-points of JO-restricted moths were airflow independent (n=6). **(F)** Box plots of r_s for set-points vs. airflow (Control: n=11 trials, 9 moths; JO: n=6 trials, 6 moths; Wilcoxon rank sum test, $p<0.01$; median—Control: −0.69, JO: 0.14).

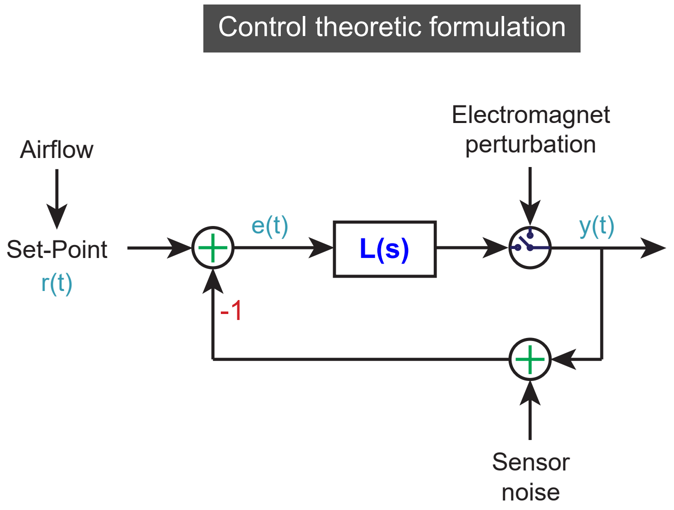

System model	Transfer function $L(s)$	Graphical representation
(1) Proportional (**P**)	K_p	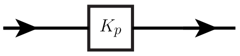
(2) Integral (**I**)	$\frac{K_i}{s}$	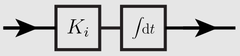
(3) Proportional-Integral (**PI**)	$K_p + \frac{K_i}{s}$	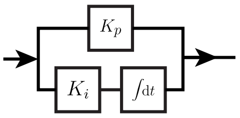
(4) Proportional-Differential (**PD**)	$K_p + K_d.s$	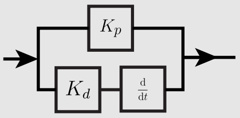
(5) Double Integral (**II**)	$\frac{K_i}{s^2}$	
(6) Proportional-Integral-Differential (**PID**)	$K_p + \frac{K_i}{s} + K_d.s$	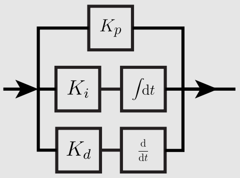

Fig. 2.7 : Control theoretic formulation
To analyze the return characteristics of the antenna, we reformulated Figure 2.4 using a control theoretic framework. The model takes in set-point as input, which is modulated by airflow via JO. Output is antennal position, which is sensed and fed back by Böhm's bristles. The error in position is convolved with a transfer function to obtain the output. We used six transfer functions—Proportional (P), Integral (I), Proportional-Integral (PI), Proportional-Differential (PD), Double-Integral (II) and Proportional-Integral-Differential (PID).

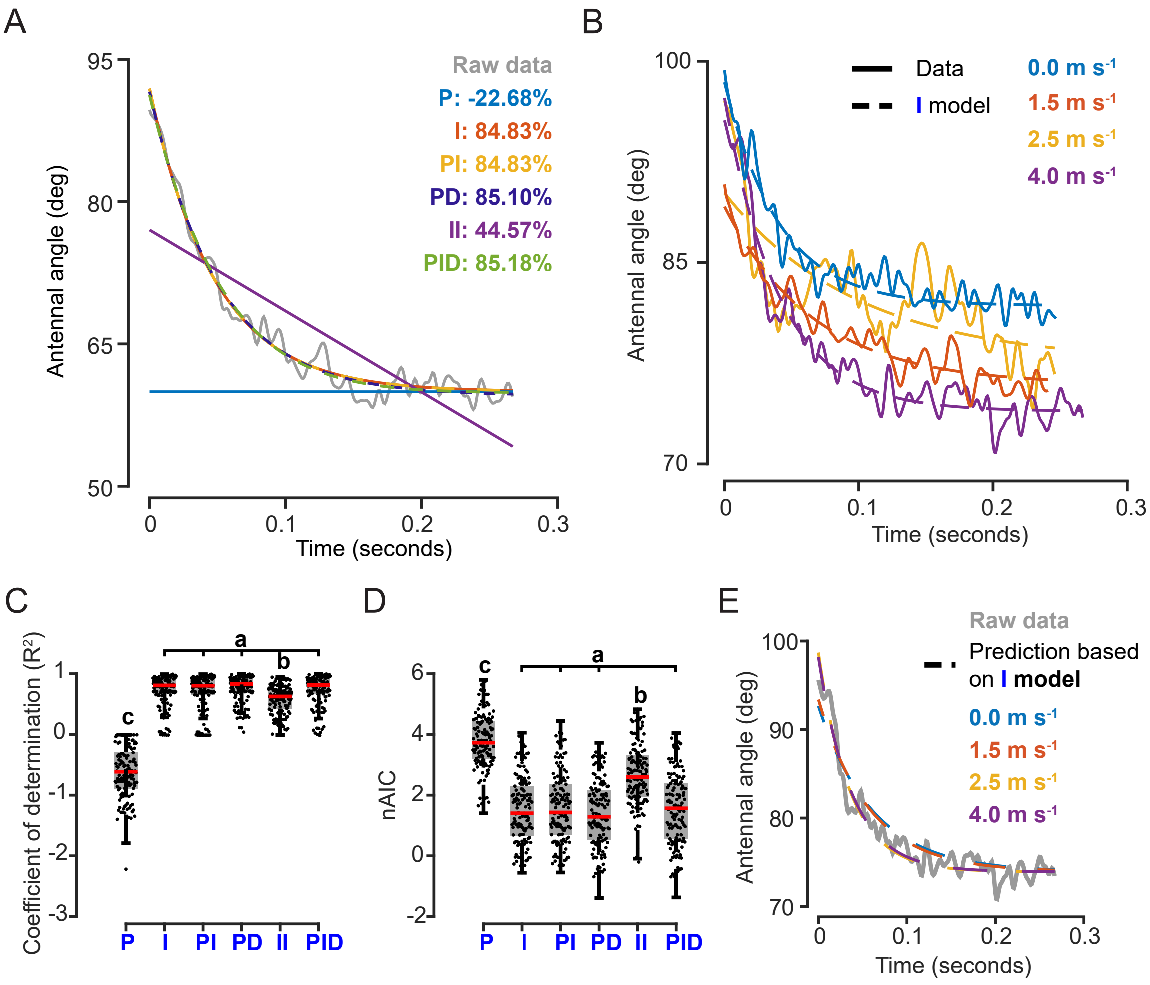

Fig. 2.8 : System model fits on antenna return trajectories
(A) A representative antennal return trajectory is plotted in grey, and model fits are plotted in color. I, PI, PD and PID fit the representative antennal return trajectory well (>80% fit). The integral model (I) was most parsimonious based on system components. **(B)** The integral model fits return trajectories of all airflows (shown for one representative dataset). Solid line represents raw data and its color represents airflow for the return trajectory. Dashed lines represent integral model estimations. **(C,D)** Box plots of **(C)** coefficient of determination (R^2) and **(D)** normalized Akaike information criterion (nAIC) for all system models. Fits based on I, PI, PD, PID models were significantly different from the rest (a, b, c represent statistically different groups, Kruskal Wallis, Nemenyi test, $p<0.01$; $n = 133$ trajectories; median R^2—P: -0.61, I: 0.81, PI: 0.80, PD: 0.83, II: 0.63, PID: 0.81; median nAIC—P: 3.73, I: 1.40, PI: 1.43, PD: 1.29, II: 2.59, PID: 1.56). **(E)** Predictive capabilities of the integral model. A representative return trajectory of the antenna at 4 $\mathrm{m\,s^{-1}}$ is plotted in grey. Dashed lines represent integral model predictions based on one airflow (indicated by their colors).

the integral system (Figure 2.8B, Figure A.3B), can hence closely fit the error correction dynamics of the antennal positioning reflex.

2.3.6 Error correction dynamics of antennal positioning reflex is independent of set-point

The antennal positioning reflex is operational even as antennal set-point varies with different frontal airflows, and it is also active when feedback from the JO is severely reduced. This suggests that the error correction dynamics of the antennal positioning reflex are independent of set-point (Figure 2.4). We tested this by quantifying our ability to predict the return trajectory of the antenna at different airflows based on the dynamics from one airflow value. Transfer functions I, PI, PD and PID with constants based on single airflow values reliably predicted the dynamics of all airflow values (control: Figure 2.8E, Figure A.3E,F; JO-restricted: Figure A.3G-I). The goodness-of-fits of these predictions were equivalent to fitting the transfer function on experimental data (compare Figure 2.8C,D Figure A.3E,F; Figure A.3C,D,H,I). Simple linear models can thus closely predict the error correction dynamics of the antennal positioning reflex for all antennal set-points. Additionally, the consistent dynamics in error correction, irrespective of set-point, suggest an active rather than passive mechanism. These results support a simple linear feedback loop with an adjustable set-point as the underlying neural circuit for antennal positioning.

2.3.7 A simple model neural network reproduces core characteristics of airflow-dependent antennal positioning behavior

The above experiments and control theoretic analysis showed that airflow-dependent antennal positioning arises from an interplay between the antennal positioning reflex and a circuit that modulates the set-point. Additionally, the antennal positioning reflex can be modeled as simple linear models which both fit and predict their return dynamics irrespective of set-point. These models formally describe and characterize the computations underlying airflow-dependent antennal positioning, but do not provide a mechanistic explanation of how neural circuits perform these computations. We therefore proposed a minimal neural circuit that incorporates the simple linear models described above and simulated it as a feasibility test. Because a group of linear models (I, PI, PD, PID) fit and predict the antennal return dynamics equally well, we modelled the minimal neural circuit as an integral model on the basis of parsimony (Figure 2.7).

The minimal neural circuit is based on electrophysiological and neuroanatomical data from previous studies, which showed that mechanosensory neurons underlying Böhm's bristles activate antennal motor neurons, likely via direct connections (Krishnan et al., 2012; Sant and Sane, 2018). Therefore, in the minimal circuit, mechanosensory neurons were treated as simple on–off neurons that monosynaptically activate antennal motor neurons (Figure 2.9, see section 2.2). On the other hand, mechanosensory inputs from JO do not appear to form synapses with motor neurons (Sant and Sane, 2018). Hence, in our minimal circuit model, we assumed that they connected via interneurons

Table 2.1 : Fitted parameters of control theoretic models.
Mean fitted parameter values for each of the control theoretic models along with the standard error of the mean (s.e.m.)

Model	Parameter	Control	JO-restricted	Neural circuit with intrinsic setpoint	Neural circuit with modulated setpoint
P	K_p	277,183.36 ± 12,165.88	183,833.13 ± 17,525.61	184,733.75 ± 19,417.91	458,754.41 ± 5584.12
I	K_i	22.50 ± 1.71	21.80 ± 2.70	13.88 ± 0.27	11.91 ± 0.11
PI	K_p	40.60 ± 5.45	33.16 ± 3.43	15.47 ± 1.44	36.24 ± 1.34
	K_i	543.07 ± 27.75	485.98 ± 48.47	218.90 ± 19.20	440.92 ± 15.44
PD	K_p	81,856.67 ± 15,559.45	67,682.04 ± 20,216.36	66,715.73 ± 7703.52	7.97 ± 1.06
	K_d	3363.48 ± 510.77	3175.06 ± 733.58	4677.09 ± 503.23	1.16 ± 0.09
II	K_i	31.65 ± 7.62	97.59 ± 28.30	0.04 ± 0.00	0.09 ± 0.01
PID	K_p	12.32 ± 1.22	10.27 ± 1.42	4.05 ± 0.55	3.39 ± 0.41
	K_i	50.15 ± 15.91	89.32 ± 45.05	55.32 ± 9.30	22.45 ± 3.47
	K_d	1.84 ± 0.39	3.16 ± 1.61	0.22 ± 0.02	0.40 ± 0.04

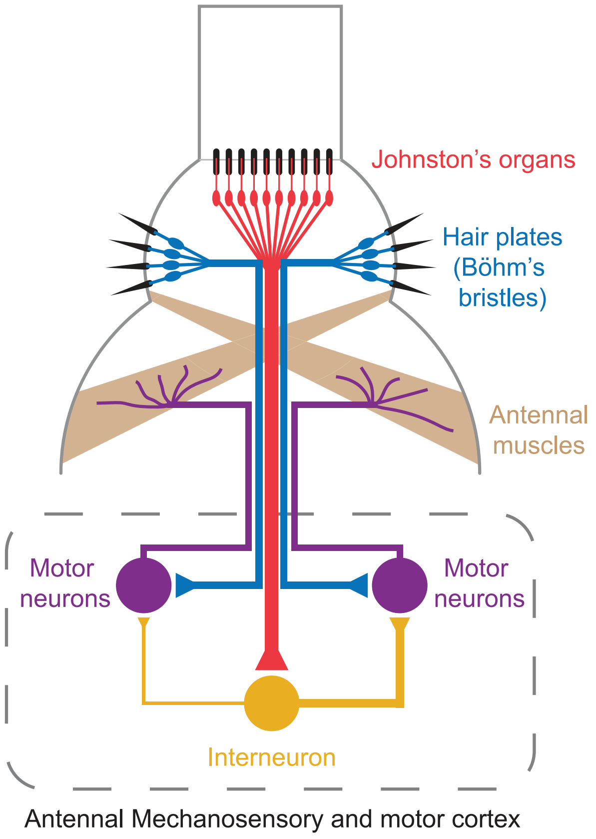

Fig. 2.9 : Model neural circuit
Motor neurons summate activity from mechanosensory neurons from Böhm's bristles and interneurons transmitting sensory inputs from the JO. The connectivity between the motor neuron and the muscles give rise to the negative feedback in Figure 2.4; motor neurons activate muscles which, upon contraction, reduce feedback from the hair plates, thereby decreasing their own activity. Muscles, due to the slow calcium integration times, integrate error in position. Sensory inputs from JO asymmetrically activate the motor neurons, thereby modulating antennal set-point.

(Figure 2.9). Finally, we modeled motor neurons as simple integrate-and-fire neurons that pool incoming activity and control antennal muscles, and thus also the antennal position (Figure 2.9).

As a template for the above neural circuit, we used the scape–pedicel joint with only one degree of freedom to simplify the model mechanics. As in the actual case, the model pedicel has two proprioceptive Böhm's bristles fields that sense its movement relative to the scape, and two muscles that control this motion (Figure 2.1C, Figure 2.9) (Kloppenburg et al., 1997; Sant and Sane, 2018). This minimal circuit can correct position and maintain it in response to simulated antennal perturbation (Figure 2.10A, Figure A.4A,B). The set-point of this circuit could also be modulated by changing firing rates of the interneuron carrying information from JO (Figure 2.10B, Figure A.4A,B). It maintained position at the modulated set-point despite external perturbations (Figure 2.10B, qualitatively similar to Figure 2.5B).

We further analyzed the neural circuit using an identical control framework as in the behavioral data, and found that its dynamics were recapitulated by I, PI, PD and PID systems (Figure 2.10C-D, Figure A.4C; parameters given in Table 2.1). PID fit the data better than I (median: 1.00, 0.97, respectively), possibly because it also fit the noise due to the Poissonian nature of model neurons (Figure 2.10E, see section 2.2). Both models captured the return dynamics for all simulated set-points (Figure 2.10E, Figure A.4C). Moreover, they predicted the return dynamics at all set-points based on the dynamics of any one (Figure A.4D-F). Thus, the realized neural circuit maps onto the control theoretic model, providing a mechanistic basis for airflow-dependent antennal positioning.

2.4 Discussion

2.4.1 A tunable set-point enables multisensory modulation of the antennal positioning reflex

Antennal positioning behavior in moths consists of two behaviors that operate at different timescales. The first is antennal deployment at the onset of flight and the subsequent maintenance of this position during flight; this requires rapid, wingbeat timescale error corrections in antennal position (antennal positioning reflex). The second behavior of stimulus-dependent antennal positioning involves slower modulation of position based on multisensory inputs like optic flow, airflow and odor. Whereas the latency of the antennal positioning reflex is typically $< 10\,\mathrm{ms}$ (Krishnan et al., 2012), the latencies of the modulatory inputs are much longer (ex. optic flow: 35 ms to 60 ms Krishnan and Sane (2014)). Because antennae are crucial in sensing olfactory, mechanosensory, hygrosensory and thermosensory stimuli, control and maintenance of their position is critical.

Antennal positioning at flight onset and its airflow-dependent modulation have been observed in diverse insects (honeybees, locusts, flies (Gewecke, 1974; Heran, 1959; Mamiya and Dickinson, 2015). Airflow-dependent modulation is mediated by the JO,

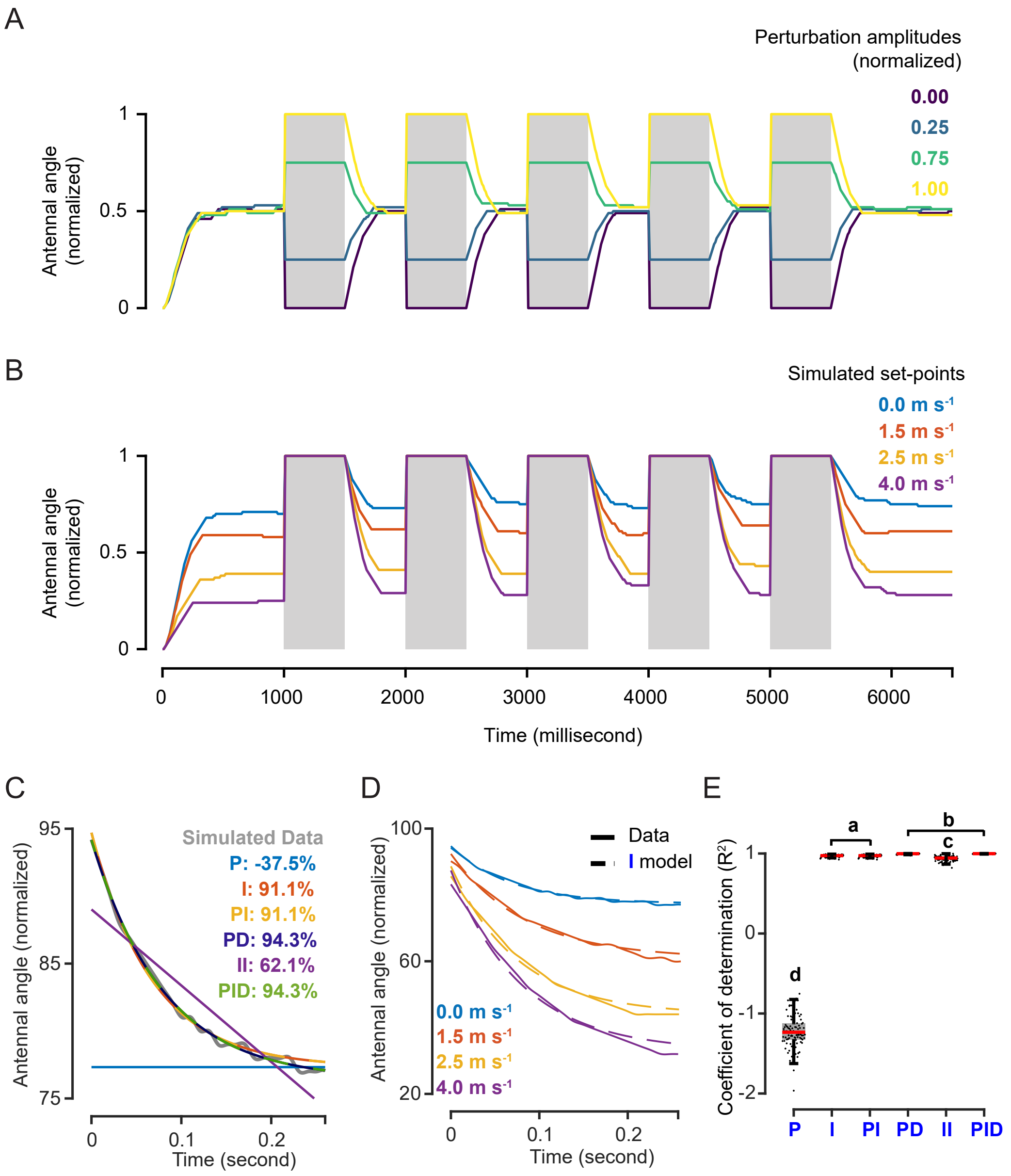

Fig. 2.10 : Simulated airflow-dependent antennal positioning
(A-B) Simulated perturbation of model in Figure 2.9. **(A)** Without set-point modulation, simulated antennae maintained position at an intrinsic set-point. Colors represent levels of perturbation. **(B)** Set-point was modulated by asymmetric excitation of the motor neurons. Simulated antennae corrected and maintained position based on set-point. Colors represent set-points. **(C)** I, PI, PD, PID fit representative simulated antennal trajectory well (>80% fit). Integral model (I) was most parsimonious. **(D)** Fits of integral model on return trajectories for different set-points. **(E)** Box plots of R^2 (a–d represent statistically different groups, Kruskal–Wallis, Nemenyi test, p<0.01; n = 100 trajectories; median R^2—P: -1.23, I: 0.97, PI: 0.97, PD: 1.0, II: 0.94, PID: 1.0)

which likely senses antennal deflections due to aerodynamic torques (Gewecke and Heinzel, 1980; Heinzel and Gewecke, 1987; Staudacher et al., 2005). How this behavior aids in sensory acquisition is as yet unclear; airflow-dependent modulation does not seem to maintain aerodynamic torques (Figure A.2G-I, also Gewecke and Heinzel (1980); Heinzel and Gewecke (1987)), and depends on multiple sensory inputs including optic flow (Khurana and Sane, 2016).

We investigated the mechanisms underlying control and maintenance of antennal position and developed a control theoretic and neural circuit model to account for the observed behavior based on the framework described in chapter 1. At the core of these models is a fast, linear, negative feedback loop that reflexively maintains antennae at a fixed set-point on stroke-to-stroke timescales. Overlying this feedback loop are slower, modulatory influences due to frontal airflow, and presumably other modalities that alter this set-point in proportion to the appropriate sensory input. When these modulatory inputs are reduced (e.g. by restricting JO), moths retain their ability to maintain antennal position at an arbitrary set-point, but do not alter the set-point at which the antennae are held (Figure 2.6). For instance, JO-restricted honeybees retain the ability to modulate antennal position based on optic flow (Khurana and Sane, 2016). This suggests the existence of an intrinsic set-point for antennal position in the absence of other sensory cues. In the presence of other sensory cues however, the set-point is modulated to a new value (Figure 2.5, also Khurana and Sane (2016)). Although airflow-dependent changes appear to symmetrically modulate set-points of both antennae (further investigated in chapter 3), this may not be true for other modalities. Indeed, asymmetric responses of antennae have been observed in previous studies on optic flow and odor (Erber et al., 1993; Honegger, 1981; Krishnan and Sane, 2014; Lambin et al., 2005; Mamiya et al., 2011; Okada and Toh, 2006; Yamawaki and Ishibashi, 2014), perhaps due to unequal modulation of the set-points of local reflex loops.

2.4.2 Linear response characteristics of antennal positioning reflex

To further illustrate the effect of set-point modulation on the antennal positioning reflex, we modeled the error correction dynamics of the perturbed antenna using control theoretic methods. Because the precise details of the muscle and the biomechanical properties of the antennal motor system were not known to us, we modeled the whole antennal circuit as a single system, which includes both the neural controller and the biomechanical plant (chapter 1). The names of the system models are abbreviations for the mathematical transfer functions. Although our model nomenclature resembles neural controller models in literature (Beatus et al., 2015; Cowan et al., 2006; Whitehead et al., 2015), these are in fact systems-level transfer functions.

We used standard linear models to fit error correction dynamics and found that they depended only on the error between current position and set-point. Dependence on error in current position instead of absolute position indicates an underlying mechanism of active error correction rather than passive mechanical rebound. The linear control theoretic model L(s) captures dependence of output position with respect to this error, with the integral model being mathematically equivalent to a decaying error exponential. Other higher-order models (PI, PD, PID) can capture more complex dependencies between output and error. We provided different amplitudes of step perturbations, but this disturbance was insufficient to distinguish differences in performances of higher-order models. Other stimuli (e.g. sum of sines, white noise or chirps) may provide better resolution on which of the four models (I, PI, PD, PID) best approximates error correction dynamics of the antennae for a variety of disturbances [section 1.2; Madhav et al. (2013); Roth et al. (2016); Roth et al. (2011)].

Our alternate hypothesis was a non-linear model in which error correction dynamics depend on antennal set-point. Such dynamics could occur if modulatory inputs like optic flow or airflow alter not just the set-point, but also the time constants of control models. Such a system can maintain the antenna at set-point, but the error correction dynamics would change as the set-point changes. In such scenarios, predicting antennal return dynamics at different set-points would not be possible based on just one set-point. To differentiate the above scenario from the linear model (Figure 2.4, Figure 2.7), we quantified how well these models could predict antennal dynamics in other airflows based on dynamics of just one case. Such predictions were only possible in the linear case, for which the underlying dynamics did not alter based on set-point. The predictions explained a large range of return trajectories in all airflows (median of 0.76 for I model, Figure A.3), suggesting that the linear model was sufficient.

In our control model, set-point was assumed to be fixed for each value of airflow. This allowed us to isolate and characterize the inner loop dynamics, thereby identifying its stereotypic error correction (Figure 2.7). Because goodness-of-fits for these models were high (Figure 2.8C,D), we inferred that inner loop timescales were faster than those of the set-point modulation circuit. We concluded that the Böhm's bristle-mediated reflex loop rapidly maintains antennal position, whereas feedback from JO slowly modulates set-point based on airflow. However, airflow sensing by JO and resulting set-point modulation have their own temporal dynamics, which may interact with those of the inner feedback loop during flight. This may be especially true in variable airspeed conditions, e.g. rapid flight maneuvers or a sudden wind gust. This motivates the need for experiments and modeling specifically targeted towards understanding how insect nervous systems disambiguate the interacting timescales of these two circuits.

2.4.3 Model neural circuit for stimulus-dependent antennal positioning

Based on the linear models and existing anatomical and physiological data (Krishnan et al., 2012; Sant and Sane, 2018), we proposed a minimal neural circuit model that could maintain and modulate position based on sensory stimuli. Because a whole group of models were able to fit and predict the error correction dynamics of the antennal positioning reflex, several neural circuits are possible. The integral model was used based on parsimony of components and formed the basic framework for higher order models. We used this control theoretic approach to generate mechanistic hypotheses of underlying neural circuits that perform this computation.

We decoupled contributions of the neural circuit (controller) from the biomechanical system (plant), based on the time constant of the integral system (unpacking the neuromechanical black box; section 1.4). The integration constants of the I model were in the same range as those of muscle calcium dynamics [Table 2.1; Chapman (2012); Staudacher et al. (2005)]. We therefore assumed that muscles perform this integration in the neural circuit model, making them the biomechanical plant. Estimating the error between set-point and current position was the only remaining computation, which could be performed by the neural controller. Computing the error requires a difference operation, either due to inhibition or antagonistic excitation. We chose antagonistic excitation over inhibition due to the prevalence of excitatory neurons in the antennal motor system (Staudacher et al., 2005). Output of a neural circuit with the above architecture matched observed behaviors (compare Figure 2.10B with Figure 2.5B).

The model neural circuit captures the information flow from Böhm's bristles and JO to the antennal muscles. Böhm's bristles control motor neuronal activity via negative feedback (inhibition/antagonistic excitation), whereas JO modulates its set-point. The specific set-point modulation can happen in multiple ways, including activation of antennal motor neurons by JO either via interneurons or by direct synapses onto them. However, the latter possibility is not supported by neuroanatomical data, which show very little co-localization between axonal arbors of JO and dendritic fields of Böhm's bristles (Sant and Sane, 2018). This modulation translates to asymmetric activation of antennal motor neurons by JO, which is a key feature of information flow from JO in the model neural circuit (Figure 2.9).

Here, the only major computation performed by the neural controller is summation. The motor neuron was modeled as an integrate-and-fire neuron that integrates synaptic inputs (excitatory post-synaptic potentials - EPSPs) to fire spikes. Because of this membrane voltage integration at fast timescales, the output firing rate is proportional to input firing rate. Mathematically, the computation performed by the motor neuron is equivalent to summation of all its inputs and multiplication by a gain. This linear computation makes the neural controller extremely fast. Such linear response characteristics are a feature of higher order fast behaviors, such as flower tracking in moths (Roth et al., 2016; Sponberg et al., 2015) and wall-following in cockroaches (Cowan et al., 2006) suggesting that this may be a general feature for fast behaviors.

The intrinsic set-point of our model neural circuit (i.e. position in the absence of any modulatory sensory inputs) results from both the mechanical placement of bristles and muscles, and the underlying sensory to motor neuron connectivity. In absence of modulation, equal activation of both Böhm's bristles results in simultaneous muscle activation on both sides (Figure 2.9, Figure 2.10A). JO feedback can modulate this set-point by asymmetrically activating the motor neurons without changing error correction dynamics (Figure 2.10B). Altering error correction dynamics requires changing the overall excitability of both muscles, which in turn requires symmetric excitation/inhibition of all motor neurons/muscles. For example, in crickets, inhibitory or excitatory dorsal unpaired median (DUM) neurons symmetrically innervate antennal muscles on both sides (Allgäuer and Honegger, 1993; Bräunig et al., 1990; Honegger et al., 1990; Staudacher et al., 2005). Activity in these neurons may change dynamics without altering set-point. Such changes might explain the slow return to baseline seen in a few trials (Figure 2.5B, Figure A.7).

Can this model be extended to other systems? The reflexive activation of motor neurons due to mechanosensory feedback, the basis of the model neural circuit for the antennal motor system, is also observed in other systems. For example, wing stretch receptors in locusts monosynaptically activate wing depressor motor neurons while simultaneously inhibiting wing elevator motor neurons (Burrows, 1975). Stretching the wing during an upstroke activates muscles that initiate a downstroke, thereby indirectly reducing wing stretch. Similarly, hair plates in certain segments of insect legs, which are likely precursors of the Böhm's bristles (Krishnan and Sane, 2015), sense changes in joint angles and directly activate muscles that reduce these angles (Kuenzi and Burrows, 1995; Pearson et al., 1976; Trimarchi et al., 1999; Wong and Pearson, 1976). These examples are analogous to activity of Böhm's bristles in the model proposed here (Figure 2.9), in which antennal position is stabilized via antennal muscles, but with the additional attribute that it is tunable. In such feedback loops, the intrinsic set-points depend on mechanosensory feedback and its influence on the associated motor neuron, whereas modulation of the set-point may be controlled by interneurons synapsing onto this motor neuron (Figure 2.9). The model neural circuit, therefore, provides a functional hypothesis for modulation of rapid reflexes with similar connectivity (chapter 1).

2.4.4 State based modulation of antennal movements

Antennal positioning, as examined in this study, is an example of state-dependent behavior in flying insects. Antennal position impacts acquisition of both mechanosensory and olfactory cues. For instance, active forward movement of the antennae with increasing airflow may potentially help restrict the flagellum to operate in the linear range of the pedicel-flagellar joint, thus enabling reliable acquisition of airflow-related and other flagellar vibrations (Gewecke and Heinzel, 1980; Heinzel and Gewecke, 1987). However, this may diminish the ability of the antenna to sample the odor space around the insect. On the other hand, if the antennae are held at a large angle for maximal odor sampling, the resultant increase in the aerodynamic drag may affect its mechanosensory function. This sets up a potential trade-off in which increasing sensitivity of one (olfactory) cue compromises sensitivity of the other (mechanosensory). In addition to mechanosensory and olfactory cues, antennal position is also influenced by visual feedback (Khurana and Sane, 2016; Krishnan and Sane, 2014; Mamiya and Dickinson, 2015), with consequences on obtaining both olfactory and mechanosensory feedback. Such trade-offs for optimal acquisition of sensory stimuli have received very little attention.

The linear integration model proposed here suggests a specific mechanism by which such multiple cues may be integrated by the antennal motor neurons. A tunable reflex (Figure 2.9) would ensure that the antenna has both the necessary flexibility to integrate and optimize the acquisition of diverse cues, while ensuring that its position is sufficiently stable to reliably acquire information. The intensity or requirement of each cue would then determine the new set-points for the antennae, while the Böhm's bristles mediated antennal positioning reflex would ensure that the set-point is maintained in face of external perturbations. Because the antennal positioning system and the associated neural circuits are fairly conserved (Sant and Sane, 2016), it seems likely that the tunable reflex proposed here can be used to understand antennal movements in diverse insects.

Bibliography

C. Allgäuer and H. W. Honegger. The antennal motor system of crickets: Modulation of muscle contractions by a common inhibitor, DUM neurons, and proctolin. *Journal of Comparative Physiology A*, 173(4):485–494, Oct. 1993. ISSN 1432-1351. doi: 10.1007/BF00193521. 00025.

T. Beatus, J. M. Guckenheimer, and I. Cohen. Controlling roll perturbations in fruit flies. *Journal of The Royal Society Interface*, 12(105):20150075, Apr. 2015. ISSN 1742-5689, 1742-5662. doi: 10.1098/rsif.2015.0075.

L. K. Böhm. Die antennalen Sinnesorgane der Lepidopteren. *Arbeiten aus dem Zoologischen Instituten der Universität Wien und der Zoologischen Station in Triest*, 14: 219–246, 1911.

P. Bräunig, C. Allgäuer, and H. W. Honegger. Suboesophageal DUM neurones are part of the antennal motor system of locusts and crickets. *Experientia*, 46(3):259–261, Mar. 1990. ISSN 1420-9071. doi: 10.1007/BF01951758.

M. Burrows. Monosynaptic connexions between wing stretch receptors and flight motoneurones of the locust. *Journal of Experimental Biology*, 62(1):189–219, Feb. 1975. ISSN 0022-0949, 1477-9145.

R. F. Chapman. *The Insects: Structure and Function.* Cambridge University Press, New York, 5 edition edition, Nov. 2012. ISBN 978-0-521-11389-2.

M. E. Chiappe, J. D. Seelig, M. B. Reiser, and V. Jayaraman. Walking Modulates Speed Sensitivity in Drosophila Motion Vision. *Current Biology*, 20(16):1470–1475, Aug. 2010. ISSN 0960-9822. doi: 10.1016/j.cub.2010.06.072.

N. J. Cowan, J. Lee, and R. J. Full. Task-level control of rapid wall following in the American cockroach. *Journal of Experimental Biology*, 209(9):1617–1629, May 2006. ISSN 0022-0949, 1477-9145. doi: 10.1242/jeb.02166. 00105.

A. Dieudonné, T. L. Daniel, and S. P. Sane. Encoding properties of the mechanosensory neurons in the Johnston's organ of the hawk moth, Manduca sexta. *Journal of Experimental Biology*, 217(17):3045–3056, Sept. 2014. ISSN 0022-0949, 1477-9145. doi: 10.1242/jeb.101568.

J. Erber, B. Pribbenow, A. Bauer, and P. Kloppenburg. Antennal reflexes in the honeybee: Tools for studying the nervous system. *Apidologie*, 24(3):283–296, 1993. ISSN 0044-8435. doi: 10.1051/apido:19930308.

M. Gewecke. The Antennae of Insects as Air-Current Sense Organs and their Relationship to the Control of Flight. In L. Barton Browne, editor, *Experimental Analysis of Insect Behaviour*, pages 100–113. Springer, Berlin, Heidelberg, 1974. ISBN 978-3-642-86666-1. doi: 10.1007/978-3-642-86666-1_8.

M. Gewecke and H.-G. Heinzel. Aerodynamic and mechanical properties of the antennae as air-current sense organs inLocusta migratoria. *Journal of compar-*

ative physiology, 139(4):357–366, Dec. 1980. ISSN 0340-7594, 1432-1351. doi: 10.1007/BF00610466.

T. L. Hedrick. Software techniques for two- and three-dimensional kinematic measurements of biological and biomimetic systems. *Bioinspiration & Biomimetics*, 3(3): 034001, 2008. ISSN 1748-3190. doi: 10.1088/1748-3182/3/3/034001.

H.-G. Heinzel and M. Gewecke. Aerodynamic and mechanical properties of the antennae as air-current sense organs inLocusta migratoria. *Journal of Comparative Physiology A*, 161(5):671–680, Sept. 1987. ISSN 0340-7594, 1432-1351. doi: 10.1007/BF00605008.

R. Hengstenberg. Multisensory control in insect oculomotor systems. *Visual Motion and its Role in the Stabilization of Gaze*, 5:285–298, 1993.

H. Heran. Wahrnehmung und Regelung der Flugeigengeschwindigkeit bei Apis mellifica L. *Zeitschrift für vergleichende Physiologie*, 42(2):103–163, Mar. 1959. ISSN 0044-362x, 1432-1351. doi: 10.1007/BF00298733.

A. J. Hinterwirth and T. L. Daniel. Antennae in the hawkmoth Manduca sexta (Lepidoptera, Sphingidae) mediate abdominal flexion in response to mechanical stimuli. *Journal of Comparative Physiology A*, 196(12):947–956, Dec. 2010. ISSN 0340-7594, 1432-1351. doi: 10.1007/s00359-010-0578-5. 00053.

H.-W. Honegger. A preliminary note on a new optomotor response in crickets: Antennal tracking of moving targets. *Journal of comparative physiology*, 142(3):419–421, Sept. 1981. ISSN 0340-7594, 1432-1351. doi: 10.1007/BF00605454.

H.-W. Honegger, B. Brunninger, P. Bräunig, and K. Elekes. GABA-like immunoreactivity in a common inhibitory neuron of the antennal motor system of crickets. *Cell and Tissue Research*, 260(2):349–354, May 1990. ISSN 1432-0878. doi: 10.1007/BF00318637. 00018.

A. Kamikouchi, H. K. Inagaki, T. Effertz, O. Hendrich, A. Fiala, M. C. Göpfert, and K. Ito. The neural basis of Drosophila gravity-sensing and hearing. *Nature*, 458 (7235):165–171, Mar. 2009. ISSN 1476-4687. doi: 10.1038/nature07810.

T. R. Khurana and S. P. Sane. Airflow and optic flow mediate antennal positioning in flying honeybees. *eLife*, 5:e14449, Apr. 2016. ISSN 2050-084X. doi: 10.7554/eLife.14449.

P. Kloppenburg, S. M. Camazine, X. J. Sun, P. Randolph, and J. G. Hildebrand. Organization of the antennal motor system in the sphinx moth Manduca sexta. *Cell and Tissue Research*, 287(2):425–433, Jan. 1997. ISSN 0302-766X, 1432-0878. doi: 10.1007/s004410050767.

A. F. Krause, A. Winkler, and V. Dürr. Central drive and proprioceptive control of antennal movements in the walking stick insect. *Journal of Physiology-Paris*, 107 (1):116–129, Jan. 2013. ISSN 0928-4257. doi: 10.1016/j.jphysparis.2012.06.001.

A. Krishnan and S. P. Sane. Visual feedback influences antennal positioning in flying hawk moths. *Journal of Experimental Biology*, 217(6):908–917, Mar. 2014. ISSN 0022-0949, 1477-9145. doi: 10.1242/jeb.094276.

A. Krishnan and S. P. Sane. Chapter Three - Antennal Mechanosensors and Their Evolutionary Antecedents. In R. Jurenka, editor, *Advances in Insect Physiology*, volume 49, pages 59–99. Academic Press, Jan. 2015. doi: 10.1016/bs.aiip.2015.06.003.

A. Krishnan, S. Prabhakar, S. Sudarsan, and S. P. Sane. The neural mechanisms of antennal positioning in flying moths. *Journal of Experimental Biology*, 215(17): 3096–3105, Sept. 2012. ISSN 0022-0949, 1477-9145. doi: 10.1242/jeb.071704.

F. Kuenzi and M. Burrows. Central connections of sensory neurones from a hair plate proprioceptor in the thoraco-coxal joint of the locust. *Journal of Experimental Biology*, 198(7):1589–1601, July 1995. ISSN 0022-0949, 1477-9145. 00019.

S. Kunkel, A. Morrison, P. Weidel, J. M. Eppler, A. Sinha, W. Schenck, M. Schmidt, S. B. Vennemo, J. Jordan, A. Peyser, D. Plotnikov, S. Graber, T. Fardet, D. Terhorst, H. Mørk, G. Trensch, A. Seeholzer, R. Deepu, J. Hahne, I. Blundell, T. Ippen, J. Schuecker, H. Bos, S. Diaz, E. Hagen, S. Mahmoudian, C. Bachmann, M. E. Lepperød, O. Breitwieser, B. Golosio, H. Rothe, H. Setareh, M. Djurfeldt, T. Schumann, A. Shusharin, J. Garrido, E. B. Muller, A. Rao, J. H. Vieites, and H. E. Plesser. NEST 2.12.0. Technical report, Zenodo, Mar. 2017.

M. Lambin, P. Déglise, and M. Gauthier. Antennal movements as indicators of odor detection by worker honeybees. *Apidologie*, 36(1):119–126, Jan. 2005. ISSN 0044-8435, 1297-9678. doi: 10.1051/apido:2004076.

M. S. Madhav, S. A. Stamper, E. S. Fortune, and N. J. Cowan. Closed-loop stabilization of the Jamming Avoidance Response reveals its locally unstable and globally nonlinear dynamics. *Journal of Experimental Biology*, 216(22):4272–4284, Nov. 2013. ISSN 0022-0949, 1477-9145. doi: 10.1242/jeb.088922. 00018.

G. Maimon, A. D. Straw, and M. H. Dickinson. Active flight increases the gain of visual motion processing in *Drosophila*. *Nature Neuroscience*, 13(3):393–399, Mar. 2010. ISSN 1546-1726. doi: 10.1038/nn.2492. 00000.

A. Mamiya and M. H. Dickinson. Antennal Mechanosensory Neurons Mediate Wing Motor Reflexes in Flying Drosophila. *Journal of Neuroscience*, 35(20):7977–7991, May 2015. ISSN 0270-6474, 1529-2401. doi: 10.1523/JNEUROSCI.0034-15.2015.

A. Mamiya, A. D. Straw, E. Tómasson, and M. H. Dickinson. Active and Passive Antennal Movements during Visually Guided Steering in Flying Drosophila. *Journal of Neuroscience*, 31(18):6900–6914, May 2011. ISSN 0270-6474, 1529-2401. doi: 10.1523/JNEUROSCI.0498-11.2011.

J. Okada and Y. Toh. The role of antennal hair plates in object-guided tactile orientation of the cockroach (Periplaneta americana). *Journal of Comparative Physiology A*, 186(9):849–857, Sept. 2000. ISSN 0340-7594, 1432-1351. doi: 10.1007/s003590000137.

J. Okada and Y. Toh. Active tactile sensing for localization of objects by the cockroach antenna. *Journal of Comparative Physiology A*, 192(7):715–726, July 2006. ISSN 0340-7594, 1432-1351. doi: 10.1007/s00359-006-0106-9.

K. G. Pearson, R. K. Wong, and C. R. Fourtner. Connexions between hair-plate afferents and motoneurones in the cockroach leg. *Journal of Experimental Biology*, 64(1):251–266, Feb. 1976. ISSN 0022-0949, 1477-9145.

E. Roth, K. Zhuang, S. A. Stamper, E. S. Fortune, and N. J. Cowan. Stimulus predictability mediates a switch in locomotor smooth pursuit performance for Eigenmannia virescens. *Journal of Experimental Biology*, 214(7):1170–1180, Apr. 2011. ISSN 0022-0949, 1477-9145. doi: 10.1242/jeb.048124. 00029.

E. Roth, R. W. Hall, T. L. Daniel, and S. Sponberg. Integration of parallel mechanosensory and visual pathways resolved through sensory conflict. *Proceedings of the National Academy of Sciences*, 113(45):12832–12837, Aug. 2016. ISSN 0027-8424, 1091-6490. doi: 10.1073/pnas.1522419113. 00010.

S. P. Sane and N. P. Jacobson. Induced airflow in flying insects II. Measurement of induced flow. *Journal of Experimental Biology*, 209(1):43–56, Jan. 2006. ISSN 0022-0949, 1477-9145. doi: 10.1242/jeb.01958.

S. P. Sane, A. Dieudonné, M. A. Willis, and T. L. Daniel. Antennal Mechanosensors Mediate Flight Control in Moths. *Science*, 315(5813):863–866, Feb. 2007. ISSN 0036-8075, 1095-9203. doi: 10.1126/science.1133598.

H. H. Sant and S. P. Sane. Conserved mechanosensory-motor circuits in insect antennae. In *International Congress for Neuroethology*, Uruguay, Feb. 2016.

H. H. Sant and S. P. Sane. The mechanosensory-motor apparatus of antennae in the Oleander hawk moth (Daphnis nerii, Lepidoptera). *Journal of Comparative Neurology*, 526(14):2215–2230, June 2018. ISSN 0021-9967. doi: 10.1002/cne.24477.

H. H. Sant and S. P. Sane. Chapter 19: A Comparative Study Of Antennal Mechanosensors In Insects. In *Indian Insects: Diversity and Science*, pages 389–399. Taylor & Francis, 2019. ISBN 978-0-429-06140-0.

D. Schneider. Insect Antennae. *Annual Review of Entomology*, 9(1):103–122, Jan. 1964. ISSN 0066-4170. doi: 10.1146/annurev.en.09.010164.000535.

D. Schneider and K.-E. Kaissling. Der Bau der Antenne des Seidenspinners Bombyx mori LI Architektur und Bewegungsapparat der Antenne sowie Struktur der Cuticula. *Zoologische Jahrbücher/Abteilung für Anatomie und Ontogenie der Tiere*, 75: 287–310, 1956.

S. Sponberg, J. P. Dyhr, R. W. Hall, and T. L. Daniel. Luminance-dependent visual processing enables moth flight in low light. *Science*, 348(6240):1245–1248, June 2015. ISSN 0036-8075, 1095-9203. doi: 10.1126/science.aaa3042.

E. M. Staudacher, M. Gebhardt, and V. Dürr. Antennal Movements and Mechanoreception: Neurobiology of Active Tactile Sensors. In S. J. Simpson, editor, *Advances* *in Insect Physiology*, volume 32, pages 49–205. Academic Press, Jan. 2005. doi: 10.1016/S0065-2806(05)32002-9.

R. C. Team. *R: A Language and Environment for Statistical Computing [Internet]. Vienna, Austria; 2014*. 2017.

J. R. Trimarchi, P. Jin, and R. K. Murphey. Controlling the Motor Neuron. In R. J. Bradley, R. A. Harris, and P. Jenner, editors, *International Review of Neurobiology*, volume 43 of *Neuromuscular Junctions in Drosophila*, pages 241–264. Academic Press, Jan. 1999. doi: 10.1016/S0074-7742(08)60548-6. 00018.

E. Warrant and M. Dacke. Vision and Visual Navigation in Nocturnal Insects. *Annual Review of Entomology*, 56(1):239–254, 2011. doi: 10.1146/annurev-ento-120709-144852.

S. C. Whitehead, T. Beatus, L. Canale, and I. Cohen. Pitch perfect: How fruit flies control their body pitch angle. *Journal of Experimental Biology*, 218(21):3508–3519, Nov. 2015. ISSN 0022-0949, 1477-9145. doi: 10.1242/jeb.122622.

R. K. Wong and K. G. Pearson. Properties of the trochanteral hair plate and its function in the control of walking in the cockroach. *The Journal of Experimental Biology*, 64(1):233–249, Feb. 1976. ISSN 0022-0949.

Y. Yamawaki and W. Ishibashi. Antennal pointing at a looming object in the cricket Acheta domesticus. *Journal of Insect Physiology*, 60(Supplement C):80–91, Jan. 2014. ISSN 0022-1910. doi: 10.1016/j.jinsphys.2013.11.006.

S. Yorozu, A. Wong, B. J. Fischer, H. Dankert, M. J. Kernan, A. Kamikouchi, K. Ito, and D. J. Anderson. Distinct sensory representations of wind and near-field sound in the Drosophila brain. *Nature*, 458(7235):201–205, Mar. 2009. ISSN 1476-4687. doi: 10.1038/nature07843.

Chapter 3

Modulation of set-point by the Johnston's organ

3.1 Introduction

The fast yet controlled flight exhibited by jet-fighters and insects alike requires closed loop control (chapter 1). Insects rely on heavily on mechanosensory feedback from the antennae for fast proprioceptive feedback (Sane et al., 2007). This is then coupled with slower visual feedback from compound eyes to stabilize flight on a stroke-to-stroke basis (Warrant and Dacke, 2011). Additionally, insect antennae are multimodal probes; apart from detecting inertial forces required for flight stability (Sane et al., 2007), the antennae house olfactory receptors and are critical for sensing food and mates (Schneider, 1964). Positioning of antennae is therefore essential for both stroke-to-stroke flight stability, as well as for longer timescale behaviors like odor tracking.

In the previous chapter (chapter 2), we showed that moths achieve stable antennal positioning with slower, context-specific modulation using a tunable feedback loop. Stable positioning at short timescales is reliably maintained by a local sensory-motor reflex which depends on rapid, continuous proprioceptive feedback from the Böhm's bristles. Flexible positioning on longer timescales relies on modulation of the set-point of this rapid feedback loop. In moths, we also showed that airflow-dependent modulation is mediated by the Johnston's organ (JO), a mechanosensory organ that senses passive vibrations of the antenna. Similar modulation of set-points perhaps underlies other context-based antennal positioning seen in insects (Erber et al., 1993; Gewecke, 1974; Heran, 1959; Honegger, 1981; Khurana and Sane, 2016; Krishnan and Sane, 2014; Lambin et al., 2005; Mamiya et al., 2011; Okada and Toh, 2006; Staudacher et al., 2005; Yamawaki and Ishibashi, 2014).

How does this context-specific set-point modulation affect acquisition of sensory information by the antennae? Investigating this requires us to methodically characterize the modulation of set-point by each individual modality as well as combinations of them. This would allow us to generate and test out multi-modal hypotheses, as single-modal hypotheses typically fail. For instance, one can hypothesize that airflow-dependent antennal positioning (chapter 2) counteracts increases in aerodynamic drag by reducing the interantennal angle (IAA). Decreases in IAA should therefore result in a constant torque (drag) on the antenna irrespective of frontal airflow. However, this is not the case; the drag on the antenna increases with airflow despite the decreases in IAA (Figure A.2G-I; Gewecke and Heinzel (1980), Heinzel and Gewecke (1987)). Additionally, antennae hold different positions for the same airflow when given different optic flow cues (Khurana and Sane, 2016). Thus, the modulation of set-point, and its effect on sensory acquisition, depends on a combination of cues. To test multi-modal hypotheses, we require fine characterization of set-point modulation at a mechanistic level, using electrophysiology and neuroanatomy (unpacking the neuromechanical blackbox, section 1.4). These data would enable us understand the functional role of these sensory inputs in maintaining antennal position and their effects on set-point.

Specifically, we investigate how sensory inputs from both JOs control the set-point of each antenna. In addition to sensing airflow (chapter 2), JO senses flagellar vibrations over a wide frequency spectrum (Dieudonné et al., 2014; Kamikouchi et al., 2009; Patella and Wilson, 2018; Sane et al., 2007; Yorozu et al., 2009). This suggests the necessity of an additional filtering step to ensure that only airflow-related vibrations sensed by the JO are used to modulate antennal set-point. A recent study has shown that sensory afferents from the JO extend into the AMMC but do not directly arborize on the motor neurons (Sant and Sane, 2018), and are likely carried by interneurons. Additionally, regions in fruitfly brains have been shown to contain tonotopic maps of flagellar vibrations; the maps are generated by pooling mechanosensory inputs from both JOs (Patella and Wilson, 2018; Suver et al., 2019). These tonotopic maps also depend on the amplitude and phase of the input (Patella and Wilson, 2018). The specific facets of this information that are relayed to the AMMC, and how they are used to modulate the set-point of both antennae, are largely unknown.

What is the nature of JO mediated set-point modulation? We address this question in the oleander hawkmoth, Daphnis nerii, using a combination of behavior and electrophysiology (chapter 1). By restricting JOs unilaterally or bilaterally and measuring its response to increasing frontal airflow, we map the flow of information from both the JOs to the antennal motor system (structure of the set-point modulation circuit, section 1.3). Next, we use a finely calibrated stimulus setup to deliver precise flagellar vibrations while simultaneously recording from the extrinsic muscles of both antennae. This allowed us to characterize how sensory inputs from the JOs modulate the activity of antennal muscles (unpacking the neuromechanical black box, section 1.4). By pooling behavioral and electrophysiological data, we draw inferences about the underlying connectivity between the JO and antennal motor system.

3.2 Methods

Moth breeding

All experiments described in this chapter were performed on adult oleander hawkmoths, Daphnis nerii. The moths used were mostly laboratory-bred, with a few moths obtained from wild pupae. Larvae were fed with Nerium oleander till they pupated, and placed in saw-dust. Upon eclosion, the hawkmoths were placed in cloth cages and exposed to natural day-night cycles. Typically, one to three day old moths were used for experiments.

3.2.1 Behavior experiments

The below described behavior experiments were performed alongside with Nitesh Saxena, a graduate student from Sanjay P. Sane's lab. We performed the experiment and digitized the videos together. I performed the subsequent data analysis.

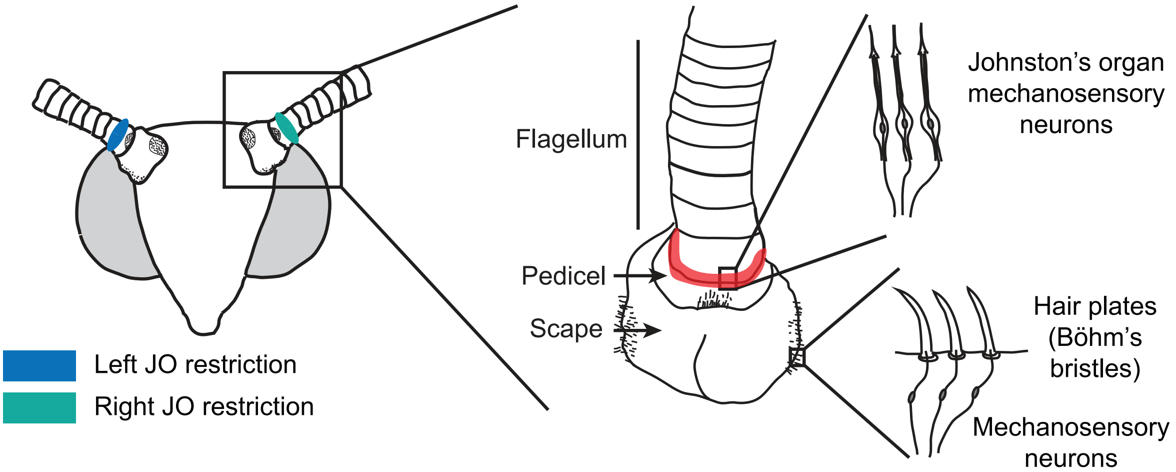

Fig. 3.1 : Unilateral JO-restriction experiments
Sensory inputs to the JOs are restricted by gluing the pedicel-flagellum joint. Two unilateral restriction treatments were performed in a subset of moths (left restricted in blue; right restricted in green). This was compared with antennal responses from control and bilateral JO restriction treatments (chapter 2).

Experiment design

All behavioral experiments were carried out in a wind tunnel with a cross-section of $0.28\,\mathrm{m} \times 0.28\,\mathrm{m}$ and a length of $1.2\,\mathrm{m}$ (Figure 2.1A). Moths were tethered to the wind tunnel using a dorsal magnetic tether and presented with a range of airflow speeds from $0\,\mathrm{m\,s^{-1}}$ to $5\,\mathrm{m\,s^{-1}}$ in steps of $0.5\,\mathrm{m\,s^{-1}}$. The antennal response of the moth at every airflow was recorded using two Phantom v7.3 high-speed cameras (Vision Research, Wayne, NJ, USA) at 100 fps.

Before presenting airflow, either the left or the right pedicel-flagellum joint of the moths was restricted using cyanoacrylate glue (Figure 3.1). Moths were kept under anesthesia during this procedure and a neodymium magnet was attached to dorsal thorax (refer to section 2.2 for more details). The duration of the entire procedure was 20 min to 30 min. After this, the moths were allowed to recover from the process for at least an hour. Post recovery, moths were tethered using the dorsally glued magnet and placed in the wind tunnel.

Tethering the moths and placing them in the wind tunnel initiated flight in most moths. Moths that did not actively elicit flight were given a brief airflow pulse of $0.5\,\mathrm{m\,s^{-1}}$ to $1\,\mathrm{m\,s^{-1}}$ or a tactile stimulus to the abdomen. Both these stimuli immediately triggered a flight bout in moths. Once a flight bout was initiated, we presented the moth with a series of airflow values. Images were acquired for one second from both cameras for each value of airflow, which gave us approximately 30-35 wingbeats per airflow. Both the cameras were calibrated before and after every experiment. In general, the airflow response for each moth was obtained from one continuous flight bout.

Analysis of behavior

After each experiment, antennal responses for individual airflow speeds were extracted from the recorded videos. Individual antennal positions were reconstructed from the two camera views using Direct Linear Transformation (DLT) approach. Calibration of the filming space and digitization of the antennae were done in MATLAB using custom software (Hedrick, 2008). Initially, all 100 frames were digitized. The mean and standard deviation of antennal angles obtained from the complete dataset were comparable to those computed from 10 randomly digitized frames in the dataset. Therefore, only 10 frames per airflow were digitized for the rest of the dataset.

Antennal angles were computed from the digitized antennal vectors (Figure 2.1C). All antennal vectors were first projected onto the XY plane (ground plane), which roughly corresponded to the head plane of the moth. The inter-antennal angle (IAA) was defined as the angle between the left and the right antennal projections. To compute left and the right antennal angles, a reference vector across the median (sagittal) plane of the moth was required. This was computed as the vector orthogonal to a line joining antennal bases. Left and right antennal angles were computed as the angle between the respective antennal projections and the reference projection.

Spearman's correlation coefficients were used to quantify the degree of correlated changes in airflow and antennal angles. Because not all the coefficients for the three treatments were not normally distributed (Lilliefors test, $p < 0.01$), non-parametric tests were used to quantify statistically significant differences. Mann-Whitney U test was used for two sample comparisons, and Kruskal Wallis and Nemenyi tests were used for multiple sample comparisons.

All computations and statistical analysis were performed in MATLAB (The MathWorks, Natick, MA, USA).

3.2.2 Electromyograms

The below described electromyograms were performed alongside Shivansh D. Dave, a junior research fellow in Sanjay P. Sane's lab. I developed the first version of the stimulus setup based on methods from Mohan et al. (2017) (described below), and wrote the associated computer programs. Shivansh joined in later, helped me improve both the stimulus setup and the experiment, and performed the final set of experiments. I wrote the necessary codes to perform the data analysis presented in this chapter.

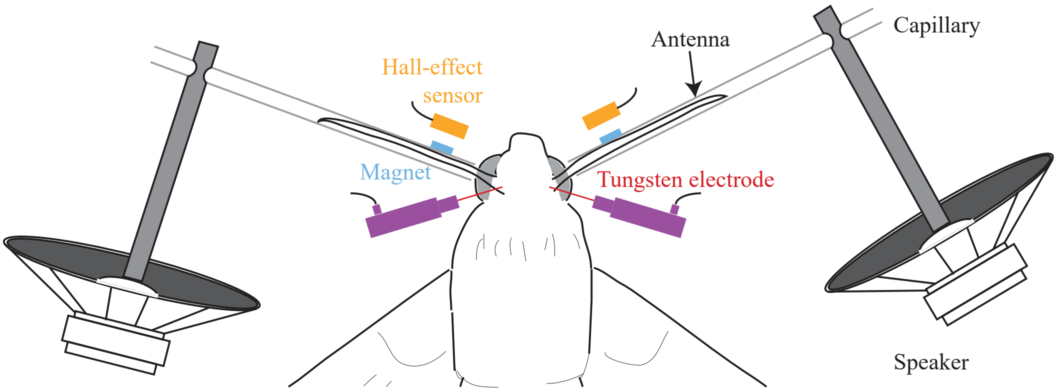

Fig. 3.2 : Apparatus for electromyograms of antennal muscles
The antennae were oscillated by a pair of speakers via glass capillaries. To ensure that only the JO is stimulated, the other antennal joints were restricted using wax. The final motion of the antenna was captured using a pair of Hall effect sensors which sensed the motion of a neodymium magnet attached to the antennal end of the capillary (Mohan et al., 2017). The activity of the muscles was recorded using a pair of custom made tungsten electrodes.

Preparation of the moth

To record the response of extrinsic antennal muscles to JO stimulation, we immobilized the moth in a sawed-off syringe. The moth was first anesthetized by placing it in −20 °C for 12 minutes. After anesthesia, its leg joints, wing joints, neck and labial palp were immobilized using wax. The moth was then attached to the sawed-off syringe. The immobilization procedure prevented movement of the antennae due to wing, leg or head movements, thereby increasing the stability of the recording. The whole procedure took about 5-7 minutes, during which the moth was kept under cold anesthesia.

The immobilized moth was placed under a microscope and two small windows were cut below the antennae (Figure B.5A). Through the window, two of the three antennal muscles could be seen (ALM, PLM and PDM; Kloppenburg et al. (1997), Sant and Sane (2018)). We recorded from the anterior levator muscle (ALM), which was most readily accessible. We pitched the head slightly downwards and restricted it, making the muscle accessible for recording. Because the region where the window was cut has very few hemolymph vessels and no proboscis muscles, we did not have to cut through any tissue, making our preparation minimally invasive (Figure B.5B).

After making the window openings, the moth was mounted on to the stimulus setup described below. The active antennal joints, i.e., the head-scape and the scape-pedicel joints, were immobilized using wax. The antennae were inserted in and glued to capillaries attached to the stimulus setup (Figure 3.2, Figure B.5C,D). This allowed us to move only the pedicel-flagellar joint, thus stimulating only JO.

Stimulus setup

The JOs were stimulated by vibrating the capillaries inside which the antennae were inserted. Each capillary (Kimble #73811 - outer diameter 1.5 mm, inner diameter 0.85 mm) was affixed to the shaft which was directly mounted on the voice coil of two stripped-down sub-woofer speakers (SAMCON, 4 Ω, 25 W; Figure 3.2, Figure B.5C). The speaker mount was reinforced by a 3D-printed rectangular plate that doubled as a cover for the speaker. A small neodymium magnet (3 mm diameter, 1.5 mm thick) was attached at the free end of each capillary (approx. 5 mm from the tip; Figure 3.2; Figure B.5C,D). The first few annuli of the antennae were inserted into the free end of the capillary and glued using a resin-based adhesive (Fevibond, Pidilite Industries Ltd., India). The movement of the capillary, and consequently the antenna tip, was measured using a Hall effect sensor which recorded the change in magnetic field due to the moving neodymium magnet (Figure 3.2; Figure B.5C,D). The stimulus setup described here is very similar to the one used in Mohan et al. (2017).

Stimulus generation and data acquisition were done using a data acquisition device (National instruments, USB 6229). Stimuli were generated using custom written codes in MATLAB and sent to the DAQ using the data acquisition toolbox. Custom-made circuits were used to power the speakers and move them based on the voltage signal from the DAQ. Voltage outputs from the Hall effect sensors were also amplified to a range of -5 V to 5 V using custom-made circuits and acquired using the same data acquisition system.

Recording setup

Tungsten rods (diameter: 0.004 inch , AM systems #719200) were sharpened by etching them in a 10 M sodium hydroxide (NaOH) solution. Two sharpened tungsten electrodes were inserted into the ALM (Kloppenburg et al. (1997); Sant and Sane (2018)), which could be seen through the two windows (Figure B.5A,B). An insulated silver electrode, with the insulating layer removed only at the very tip, was inserted in left compound eye, near the eye-rim region. It served as a stable reference for both the tungsten electrodes. The voltages from the electrodes were amplified by a dual channel extracellular amplifier in differential mode (1000x amplification, 1 Hz-1 kHz analog bandpass filter; Model 1800 2-channel microelectrode AC amplifier, A-M systems). The amplified signal was then acquired using the same data acquisition system described above.

Experiment design

Before each experiment, the moth was prepared as described above and mounted on to the stimulus setup. Next, the electrodes were inserted into the left and the right ALMs. Finally, the Hall effect sensor and stimuli were calibrated (Appendix B).

In each experiment, the following types of stimuli were provided to the moth while simultaneously recording from the antennal muscle:

1. **Impulse:** A short (<50 ms) movement of the antennal tip was termed as an

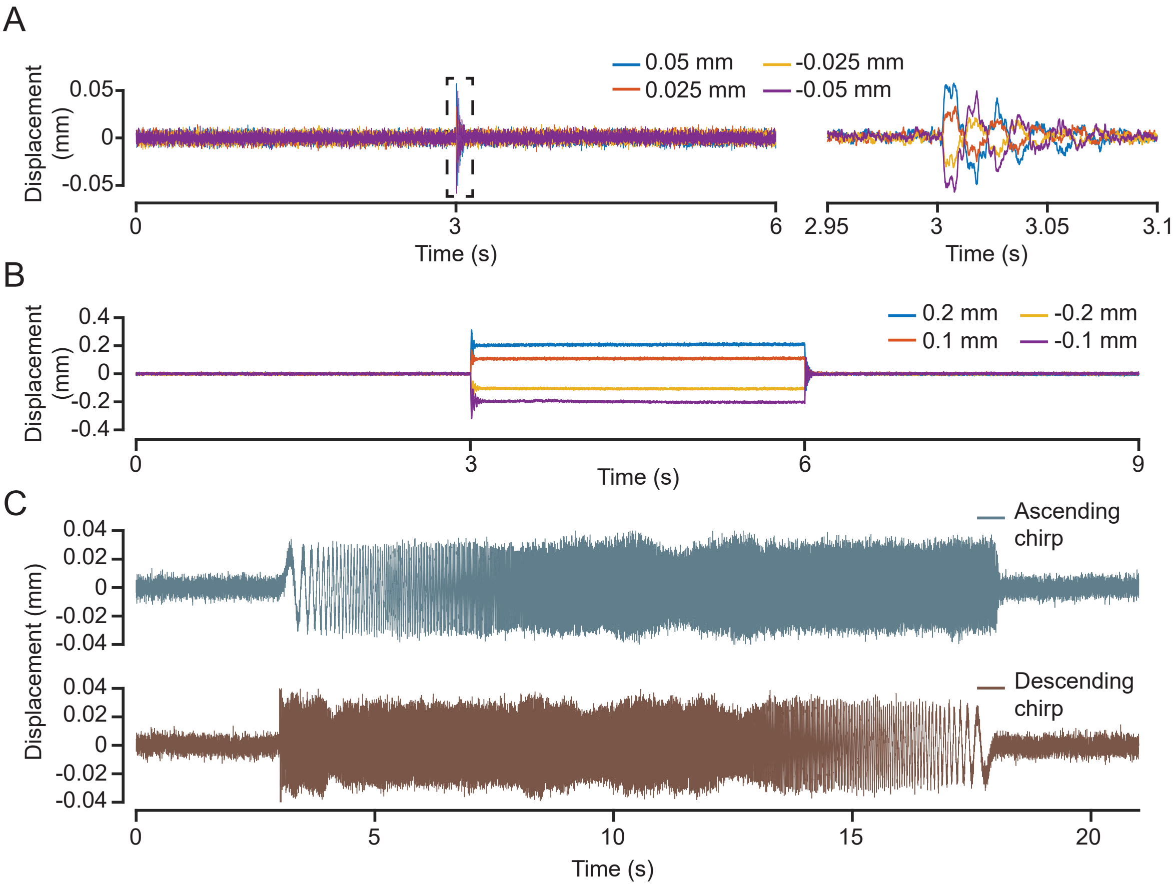

Fig. 3.3 : Vibration stimulus to the antennae
(A) Impulse stimulus (four displacements, indicated by different colors). **(B)** Step stimulus (Duration - 3 s, four displacements). **(C)** Ascending (blue-grey) and descending (brown) chirp stimulus (Duration - 3 s; start frequency - 0 Hz; end frequency - 150 Hz; peak-to-peak displacement - 0.08 mm).

impulse stimulus (Figure 3.3A). The maximum amplitude of stimulation was ~0.05 mm, which translated to ~0.05° angular displacement for an average antenna (~5 cm long). The antennae were stimulated both separately (only left, only right) and together (both same direction, both different direction). These combinations were repeated for four amplitudes - 0.05 mm, 0.025 mm, −0.025 mm and −0.05 mm (Figure 3.3A) - providing 16 different impulse stimuli.

2. **Step:** A sustained (3 s) displacement of the antenna was termed as a step stimulus (Figure 3.3B). The maximum displacement was ~0.2 mm which translated to ~0.2° angular displacement of the pedicel-flagellum joint. Similar to the impulse stimulus, the antennae were stimulated both separately and together, with four different amplitudes (0.2 mm, 0.1 mm, −0.1 mm and −0.2 mm), (Figure 3.3B) giving rise to 16 combinations of step stimuli.
3. **Chirp:** A sinusoid whose frequency linearly increased (or decreased) with time was termed as a chirp stimulus (Figure 3.3C). In our experiments, the sinusoid had a peak-to-peak amplitude of ~0.08 mm (~0.08° angular displacement) and its frequency changed from 0 Hz to 150 Hz in 15 s (Figure 3.3C). Both increasing and decreasing chirps were provided to the antenna separately (only left and only right) and together, giving rise to 6 different types of chirp stimuli.

Each experiment consisted of a maximum of 15 trials, with every stimulus repeating twice per trial. The stimuli were generated and the amplified voltage from the muscles was recorded at a sampling rate of 10 kHz. Typically, multiple experiments were performed on the same moth, each containing multiple trials. Only trials which were completed without interruption and lacked motion artifacts were accepted and further analyzed. At the end of each experiment, the raw data from valid trials from every experiment were pooled, compressed and stored as an hdf file for further analysis.

Data analysis

The raw data were loaded and a spike detection algorithm was run on every stimulus trial. The spike detection algorithm performed the following steps:

1. **Bandpass filter:** EMG voltage from both the electrodes were bandpass filtered to only allow frequencies between 10 Hz to 1000 Hz (4 pole). This retained the frequencies typically associated with a spike while removing baseline fluctuations and high-frequency noise (Figure 3.4A,B).
2. **Threshold-based spike detection:** Threshold was estimated from the dataset to detect spikes. First, the standard deviation of noise was estimated by Equation 3.1 (Donoho and Johnstone, 1994; Quiroga et al., 2004). The spike threshold was defined as four times the noise standard deviation (Figure 3.4B,C). Local maxima/minima for signals above the threshold were categorized as spikes (Figure 3.4C). To ensure that the same spike is not detected twice, a refractory period of 2 ms was used. Although this sometimes caused two or more valid spikes from multiple units to be detected as one spike (false negatives), this scenario was rare. It was more frequent for one spike to be detected as multiple ones (false posi-

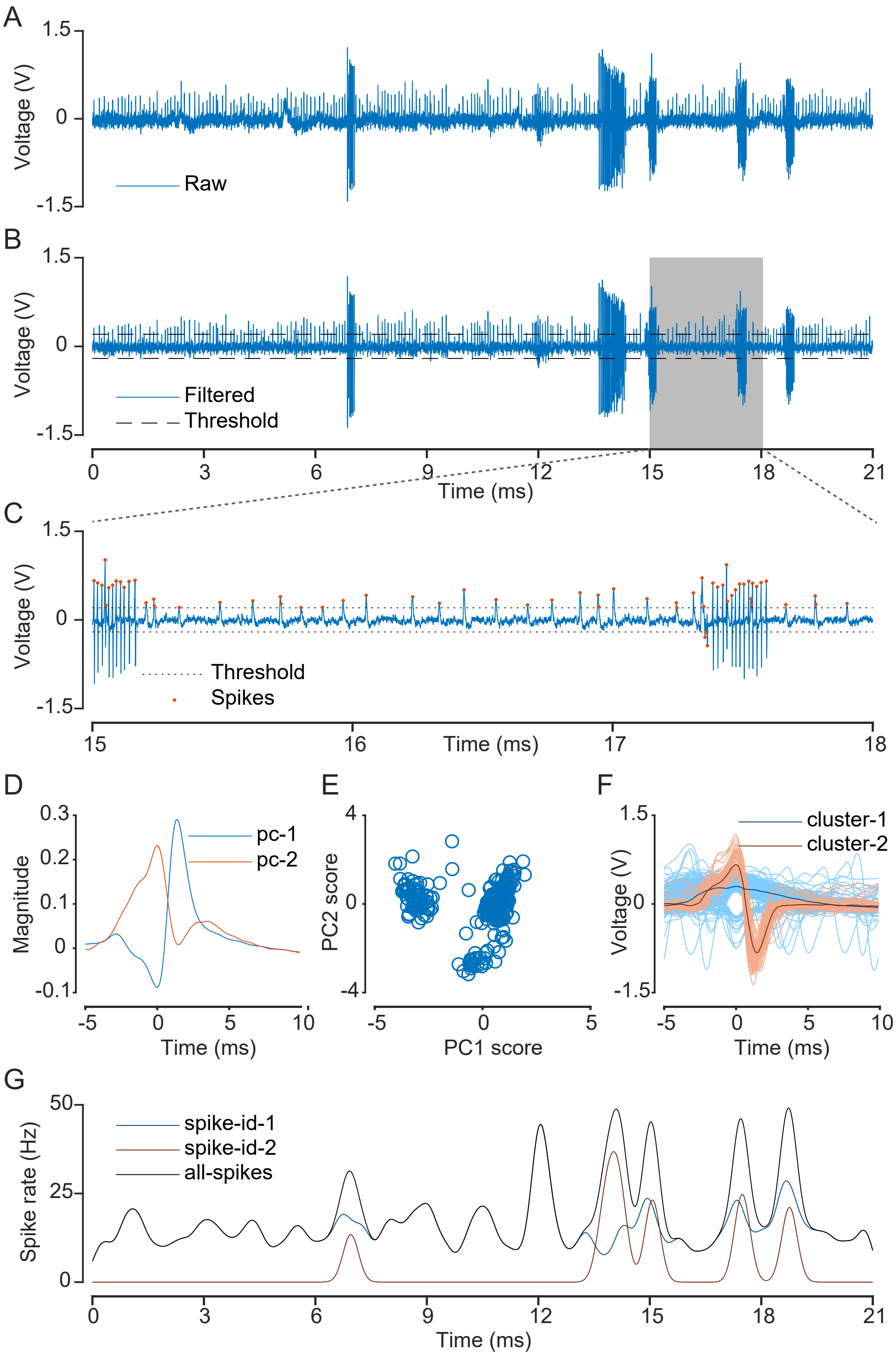

Fig. 3.4 : Spike detection and sorting from raw EMG data
(A) Representative raw EMG, **(B)** filtered using a bandpass filter (10 Hz to 1000 Hz, 4 pole). Spike threshold from Equation 3.1. **(C)** Spike detection. Data from the grey overlay in B is expanded and shown here. **(D)**, **(E)** Principal component analysis (PCA) of spikes. **(F)** Detected spikes based on clusters from PCA. **(G)** Gaussian convoluted spike rate (GCSR).

tives). The threshold + refractory period was sufficient to capture most spikes, while ensuring that the same spike was not detected multiple times.

$$\sigma_n = median(\frac{|x|}{0.6745}) \qquad [3.1]$$

$$s_t = 4\sigma_n \qquad [3.2]$$

where,

σ_n = standard deviation of background noise

x = voltage signal from electrode

s_t = spike threshold

3. **Spike identity detection:** Once the spikes were classified, principal component analysis (PCA) was used to find the optimum set of basis vectors that allowed easy clustering. A spike profile was generated around the maxima/minima of the spike - 5 ms before the maxima/minima and 10 ms after it (Figure 3.4F). This gave rise to 150 sample points (sampling rate of 10 kHz), which resulted in 150 dimensions after PCA. Of these, the first few principal components explained 99% of the variance, and were used for the cluster analysis. Typically, the first two dimensions were sufficient to visually spot the clusters (Figure 3.4D,E). Calinski-Harabasz method was used to detect the number of spike clusters (Caliński and Harabasz, 1974). Kmedoids clustering was used to cluster and identify spikes based on the first few principal components (Figure 3.4F). The cluster analysis was done using the statistical and machine learning toolbox in MATLAB.
4. **Gaussian convoluted spike rate (GCSR):** Once the spikes were detected, a Gaussian window with a standard deviation of 200 ms was used to convert the individual spiketimes into a continuous spike rate (Dayan et al., 2005). This was done for all the spikes as well as for the individually identified clusters (Figure 3.4G). Both the spikes and the GCSR were used for data visualization and further analysis.

Experiments were performed on a total of n=11 individuals. However, only three of these had sufficiently high signal-to-noise (SNR); most of them had a low SNR. Thus, they were not used for this analysis, and the preliminary results and inferences described below are based on n=3 individuals (with 22 trials, 4 trials and 6 trials respectively).

3.3 Results

3.3.1 Unilateral Johnston's organ restriction affects airflow response of both antennae

To quantify the extent of set-point modulation by individual JO we unilaterally restricted the left or the right JO in a group of moths. Left/right JO-restricted moths were tethered and placed in a wind tunnel and presented with windspeeds ranging

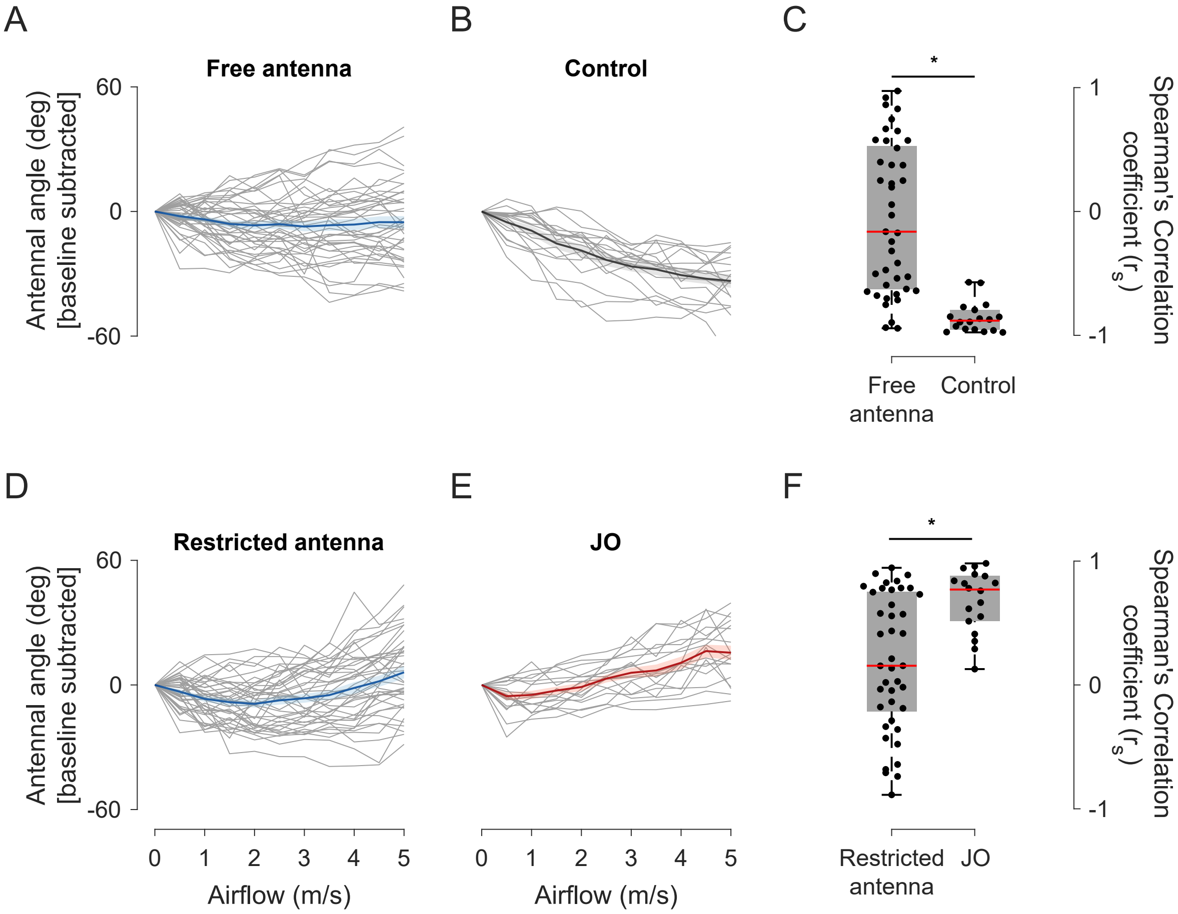

Fig. 3.5 : Effect of unilateral JO-restriction

(A) Antennal angle (baseline subtracted) of the free antenna pooled from both unilateral restriction treatments. Individual responses of moths are shown in grey, overlaid by the mean (blue) and the standard error margin (s.e.m; light blue overlay). **(B)** Antennal angle seen in control moths (Individuals: grey, mean: black, s.e.m: grey overlay). **(C)** Box-and-whisker plots of Spearman's correlation coefficients (r_s) for the free antennal angles from unilateral restriction and control treatments. **(D)** Antennal angle of the JO-restricted antenna pooled from both unilateral restriction treatments (Individuals: grey, mean: blue, s.e.m: light blue overlay). **(E)** Antennal angle of restricted antenna seen in bilateral JO restricted moths (Individuals: grey, mean: red, s.e.m: light red overlay). **(F)** Box-and-whisker plots of Spearman's correlation coefficients (r_s) for the restricted antenna from unilateral restriction and bilateral JO-restricted treatments. The boxes represent the central 50% of the data around the median (red line). Whiskers indicate 1.5 times the interquartile range. Individual data points are additionally shown as black spheres. Statistically different groups are shown by an asterisk (Mann-Whitney ranksum test, $p < 0.01$).

from 0 m s^{-1} to 5 m s^{-1}. The antennal responses of these moths were filmed using two high-speed cameras at 100 fps (Figure 2.1A, see section 3.2). The behavioral responses of these moths were compared with control moths and moths in which both JO were restricted (data from chapter 2).

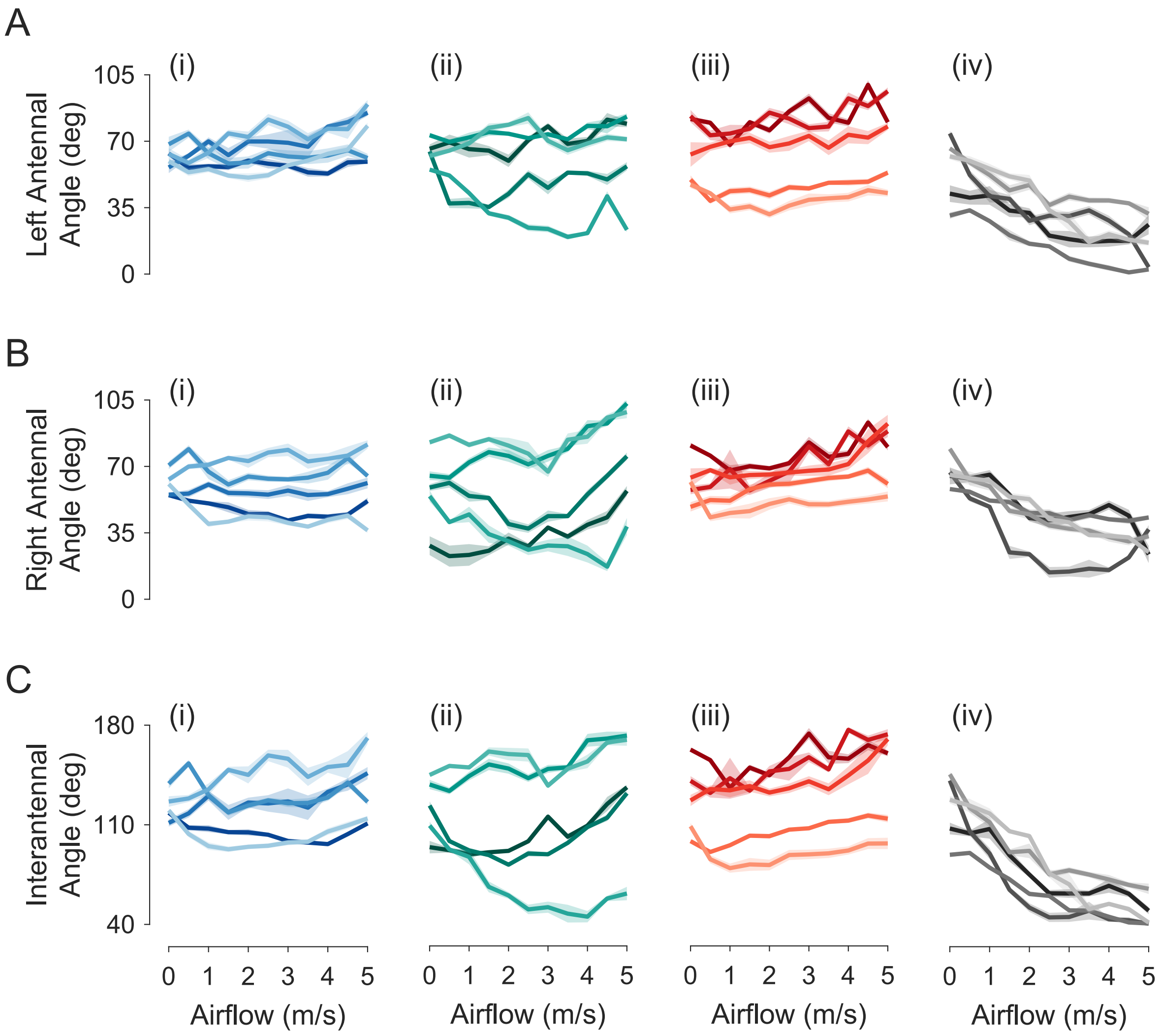

Fig. 3.6 : Antennal angles of control and JO-restriction treatments **(A)** left, **(B)** right and **(C)** inter-antennal angle for **(i) left) (ii) right (iii) both** JO-restricted and **(iv) control** moths. The dark line represents the mean, with the light overlay representing the standard error margin. Only five moths are shown out of a sample of 21, 20, 9 and 9 for the respective treatments (rest shown in Figure B.8, Figure B.9).

Because the antennal positioning reflex is ipsilateral (chapter 2; Krishnan et al. (2012); Sant and Sane (2018)) and because the primary JO afferents only extend into the ipsilateral AMMC (Sant and Sane, 2018), we hypothesized that the sensory inputs from JO that modulate this reflex should also be ipsilateral. Unilateral JO restriction should only alter the airflow response of the restricted antenna, leaving the response of the unrestricted one unaffected.

To test this, we computed the left and right antennal angles from moths for all treatments (Figure 2.1B). From this, we quantified the change in antennal angle of individual antennae at different airflows. The change was measured with respect to the angle of the antenna in still air ($0\,\mathrm{m\,s^{-1}}$). This avoided confounding effects due to the natural differences seen in the initial antennal position among moths. Spearman's rank correlation coefficient, a measure of monotonicity of antennal angles vs airflow (+1/-1 perfect monotonic increase/decrease respectively), was used to compare the observed angles between different treatments.

Based on the null hypothesis, we expected the free antenna of the unilateral JO-restricted moths to behave similarly to a control moth. We pooled the data from the free antennae of both the unilateral treatments, and compared it with controls (Figure 3.5A,B). The mean antennal angle of the free antenna from these treatments was significantly different from the control moths (Figure 3.5A-C). Furthermore, analyzing the unilateral treatments separately did not change this result (Figure B.6, Figure B.7). Because the free antenna was not experimentally manipulated, this indicates that the change in behavior was due to restriction of the contralateral JO.

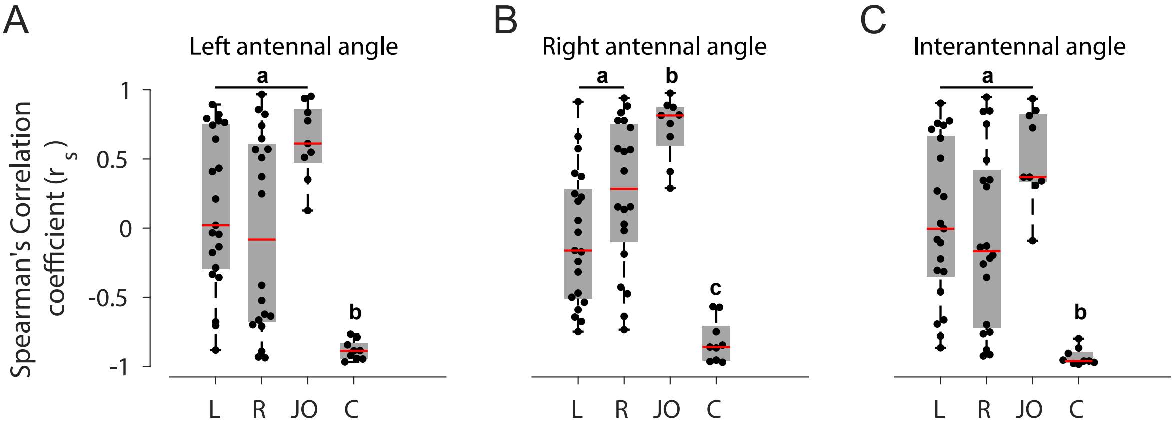

Fig. 3.7 : Statistical comparisons of restriction and control treatments
Box plots of Spearman's correlation coefficients (r_s) for **(A)** left antennal angle, **(B)** right antennal angle and **(C)** inter-antennal angle for left (*L*), right (*R*) and both (*JO*) JO-restricted treatments, and control (*C*). (a,b,c) represent statistically different groups (Kruskal Wallis, Nemenyi test, $p < 0.01$).

Next, we compared the antennal angles from the restricted antennae of the unilateral restriction treatments with those of the bilaterally restricted ones. Although the mean antennal angle of the restricted antennae look qualitatively similar to the bilaterally restricted ones (Figure 3.5D,E, Figure B.6, Figure B.7), the variance in behavior is significantly larger (Figure 3.5F, Figure B.6, Figure B.7).

To further characterize the effect of unilateral restriction, we compared the antennal angles of the unilateral and bilateral restriction treatments. The strong decrease in all three antennal angles seen in control moths is not observed in the unilateral JO-restricted moths (Figure 3.6, Figure B.8, Figure B.9). Additionally, the correlation coefficients of both unilateral and bilateral JO-restricted moths are statistically different from controls (Figure 3.7). However, the variability in unilateral JO-restricted moths is greater than the bilaterally restricted ones (Figure 3.7). This suggests that reliable antennal response to airflow requires sensory inputs from both JOs. Hence, sensory inputs from both JOs likely modulate the set-points of the antennal positioning reflex of individual antennae.

3.3.2 Sustained high frequency vibrations alter antennal muscle activity

The behavioral data described above suggests that the activity of antennal muscles of an individual antenna is modulated by both JOs. To examine the influence of both JOs on antennal muscles, we recorded EMGs from the anterior levator antennal muscles (ALMs, Kloppenburg et al. (1997); Sant and Sane (2018)) while simultaneously subjecting both the antennae to controlled displacements (see section 3.2 for details). We carefully glued all antennal joints except the pedicel-flagellum joint. This allowed the controlled displacements provided to the antenna to be directly transferred to the pedicel-flagellum joint, which in turn activated the JO. By recording antennal muscle activity during controlled antenna movements, we could record the modulation of muscle activity by the JO.

We first quantified how bilateral activation of the JO affects both the ALMs using three types of stimuli - an impulse, a step and a chirp (frequency from 0 Hz to 150 Hz, see section 3.2). Recorded muscle activity was run through spike sorting algorithms to extract spikes (Figure 3.4). These were used to compute Gaussian convoluted firing rate (GCSR), a measure of how the spike rate of muscles changed in response to these stimuli (Figure 3.4). Multiple rounds of experiments, each with several stimulus trials, were performed with the same individual to increase the stimulus-response data points per moth. Each trial was then inspected to ensure that the recording was reliable (no motion artifacts, changes in SNR, etc.) and then pooled for data analysis (see section 3.2 for details). Although a total of 11 individual moths were recorded from, only 3 of them had sufficiently high SNR for spike detection. The preliminary results shown here are based on this data.

Spike rate of the ALMs did not consistently change in response to step and impulse stimuli (Figure 3.8, Figure B.10). Two out of the three moths did not respond to the stimuli, whereas the third one weakly changed its spike-rate (Figure 3.9, Figure B.11). This was consistent over several different forms of bilateral step and impulse stimuli (Figure 3.9, Figure B.11), indicating that instantaneous (impulse) or sustained offsets (step) of the flagellum do not change antennal muscle activity.

When provided with a chirp stimulus, however, the spike rate sharply increased for high frequency vibrations of the antenna (Figure 3.10), which was consistent across all three moths (Figure 3.11). Additionally, the frequency regime during which muscle activity increased remained similar between ascending and descending chirp stimuli (Figure 3.11). This suggests that sustained high frequency vibrations, such as those that occur during flight (like wingbeat frequency and its harmonics), maybe sensed by

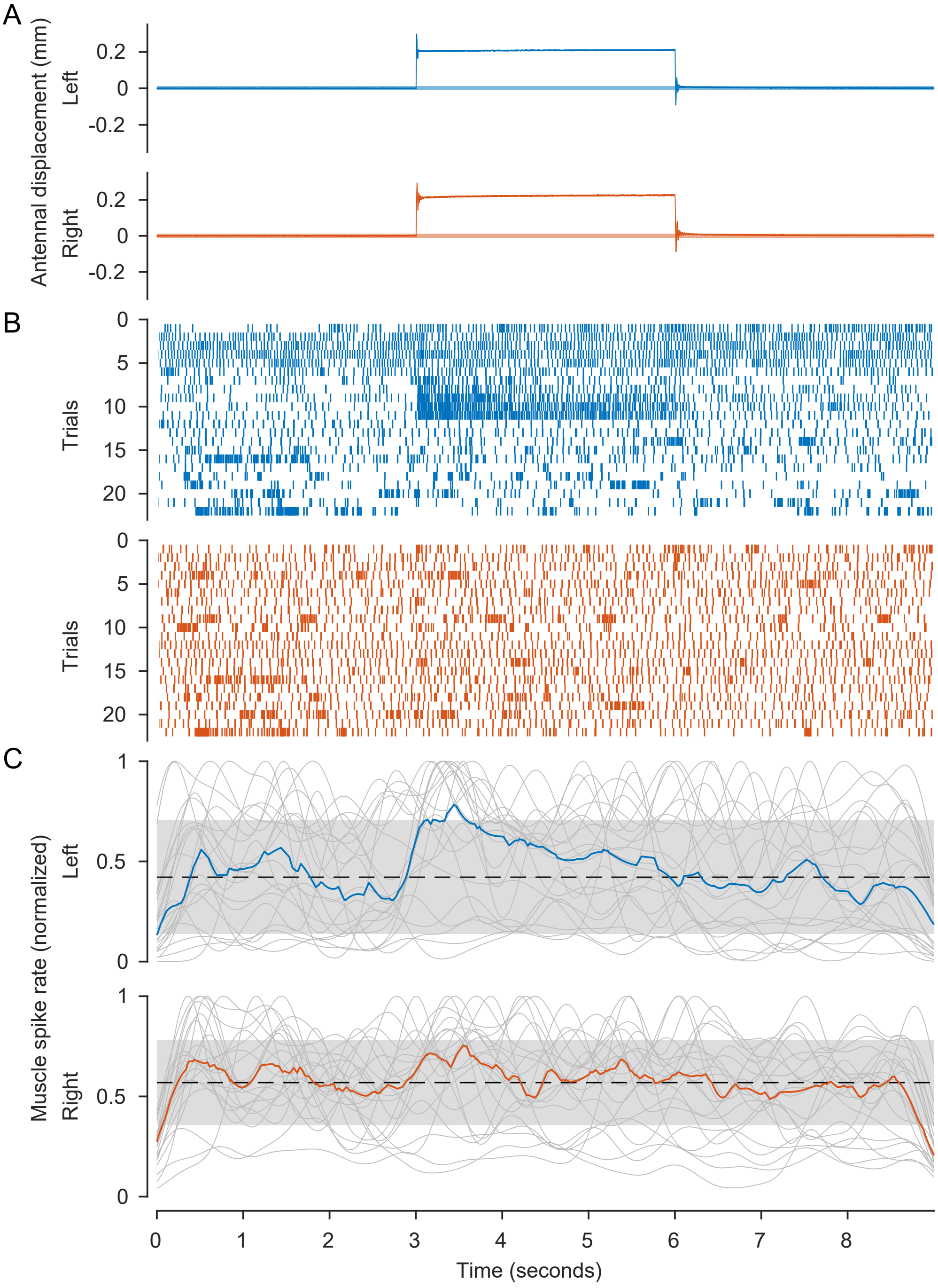

Fig. 3.8 : Representative response to a bilateral step
(A) Displacement of left (blue), right (red) antenna respectively. **(B)** Raster plots of spikes in left (blue), right (red) anterior levator muscle, respectively. **(C)** Normalized GCSR of left (blue), right (red) muscles, respectively. Grey lines represent rates from individual trials, with median response shown in blue/red. Dashed black line denotes median baseline spike rate and grey overlay represents three standard deviations around the median.

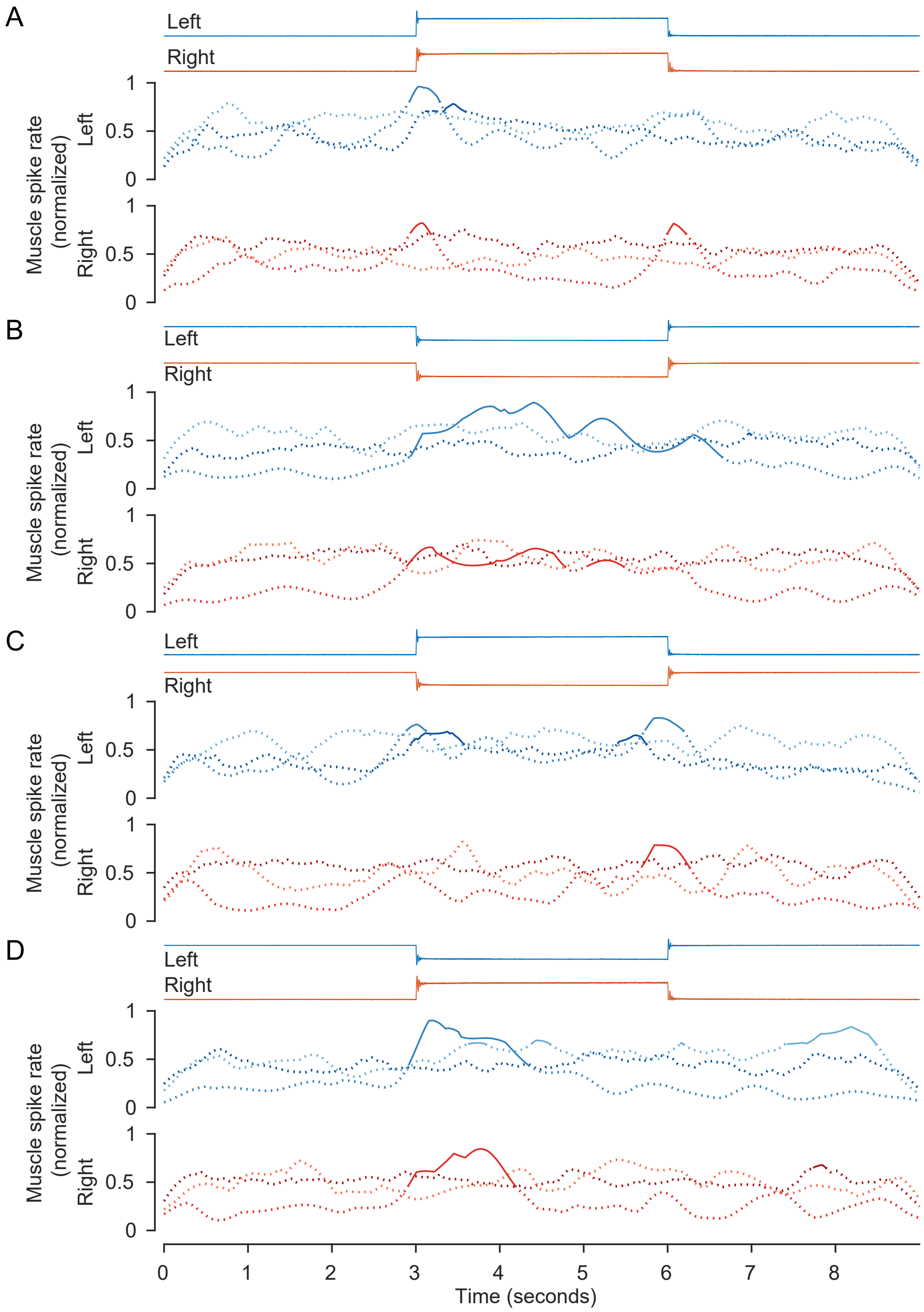

Fig. 3.9 : Muscle activity in response to bilateral step
Four types of step stimuli were given (shown at the top of each panel) - **(A)** bilateral forward, **(B)** bilateral backward, **(C)** clockwise (left forward, right backward) and **(D)** anticlockwise (right forward, left backward). Solid lines denote spike rates that are at least three standard deviations away from baseline; dotted lines are indistinguishable from baseline (n=3 individuals).

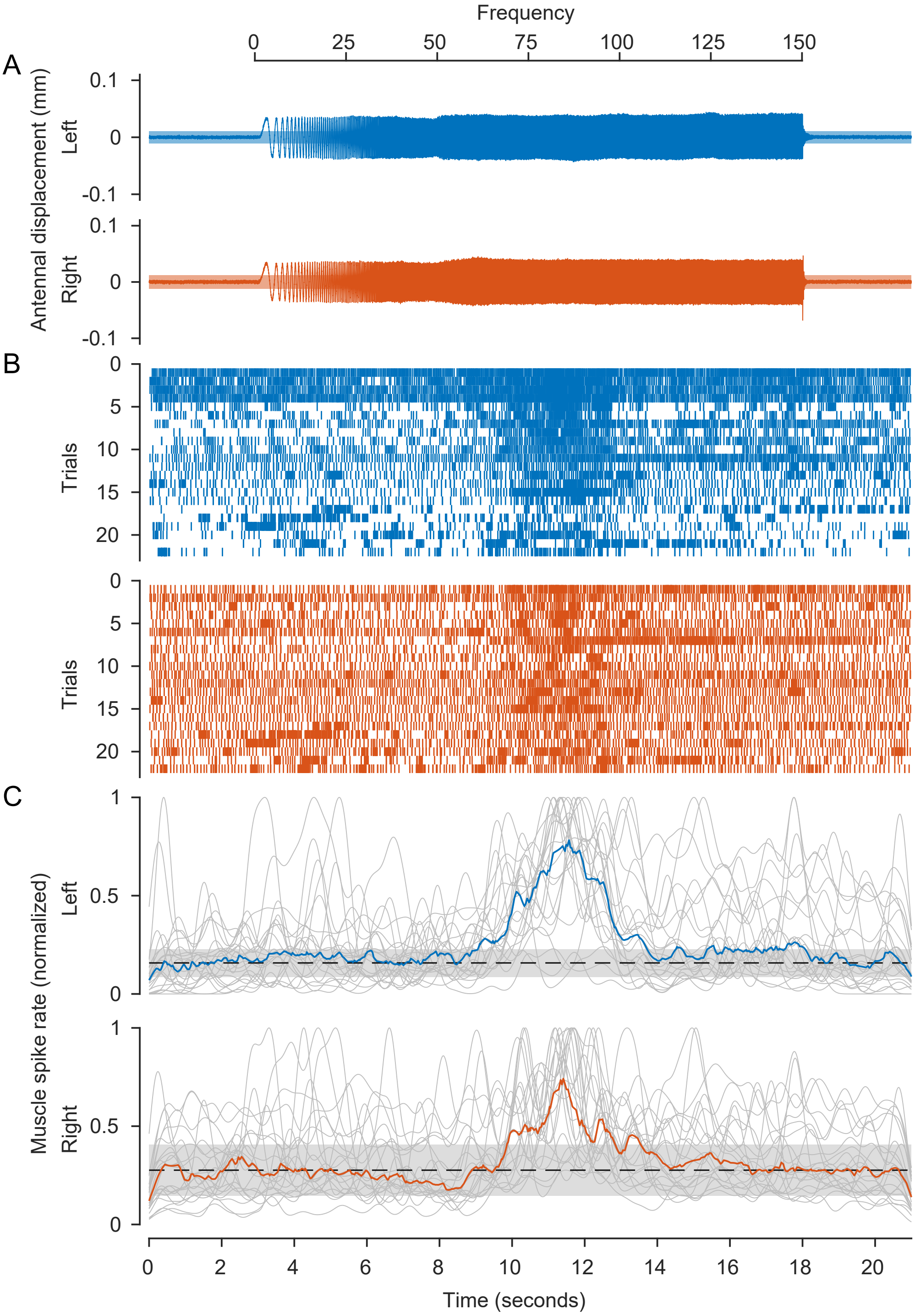

Fig. 3.10 : Representative response to a bilateral chirp
(A) Frequency increases from 0 Hz to 150 Hz. Blue, red overlay denotes noise around baseline (three standard deviations). **(B)** Spike raster for left (blue), right (red) muscles, respectively. **(C)** A noticeable increase in spike-rate is visible in both muscles during high frequency vibrations. Colors correspond to the same entities as in Figure 3.8.

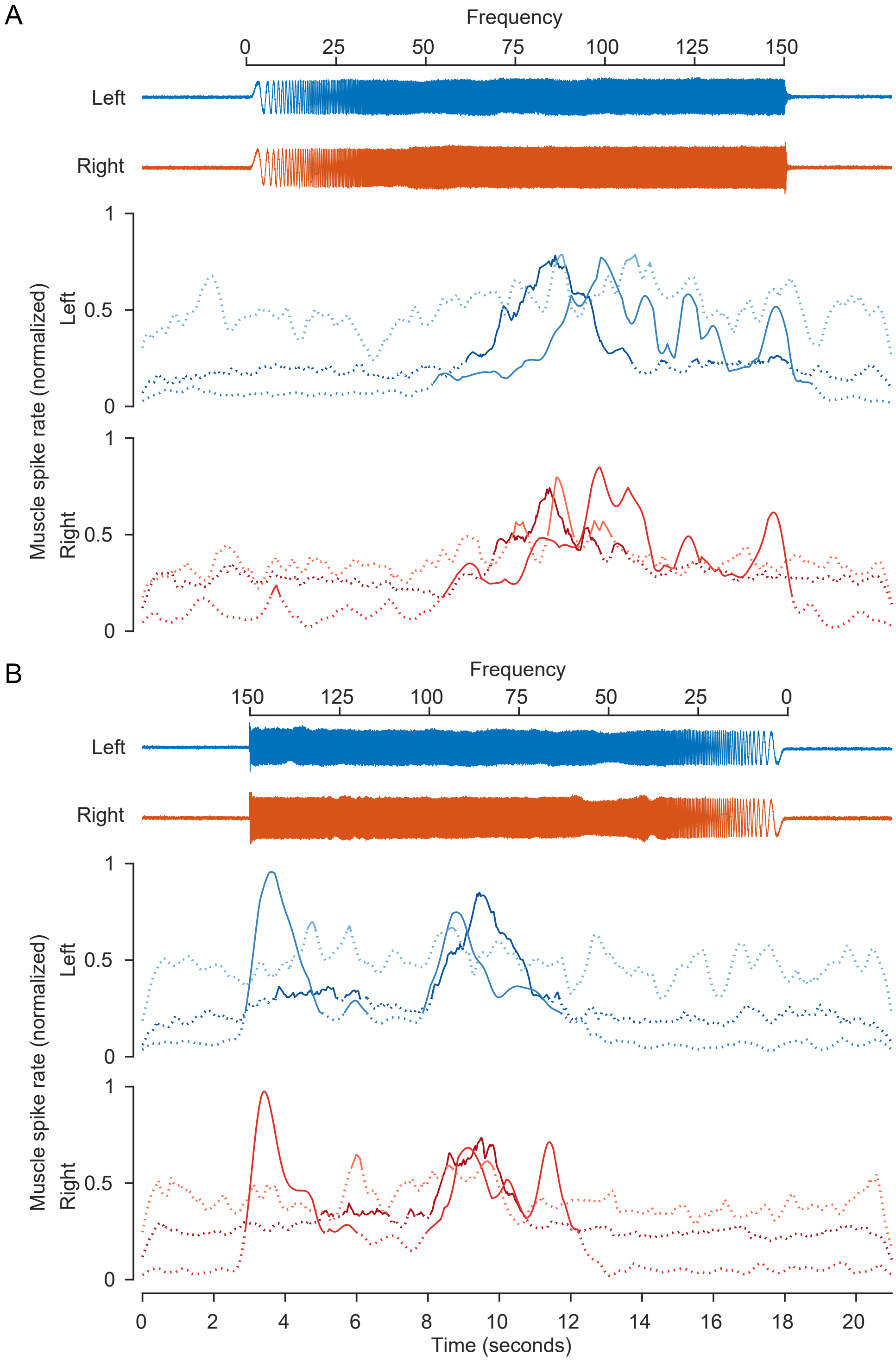

Fig. 3.11 : Muscle activity in response to bilateral chirp
Two types of chirp were given (shown at the top of each panel) **(A)** ascending and **(B)** descending. Muscle activity significantly changed in response to high frequency vibrations in both chirp stimuli (n=3). Colors correspond to the same entities as in Figure 3.9.

the JO and used to modulate antennal position.

3.3.3 Unilateral antennal stimulation bilaterally changes muscle activity

Next, we quantified how unilateral movements of the flagellum (pedicel-flagellum joint) affects the activity of both the ALMs. When provided with a chirp stimulus to just one antenna, the spike rate in both the antennal muscles increased (Figure 3.12). This was consistent across all three moths, and the frequency regime where muscle activity increased was similar for both ascending and descending chirp stimuli (Figure 3.13). Hence, it is likely that the vibrations transduced by the JO on one side is sent bilaterally to both antennae.

On the other hand, unilateral step and impulse stimuli barely changed the spike rates of either muscle (Figure B.12, Figure B.13). The weak response seen in one of the moths decreased when the antennae were stimulated unilaterally (Figure B.12, Figure B.13).

All the electrophysiological results are based on a small sample size (n=3 moths, with multiple trials each), and needs to be increased to provide a conclusive result. However, these data provide preliminary evidence of bilateral control of antennal muscle activity by both JOs.

3.4 Discussion

Antennal positioning in insects is an example of a fast yet flexible reflex (Khurana and Sane (2016); Natesan et al. (2019)). In chapter 2, we showed that this behavior has two components - one, a fast reflexive action that keeps the antenna at set-point on short timescales, the other, a slower modulation of the set-point by multisensory cues to keep the antenna flexible on longer timescales. We also showed that the JO senses airflow and continually modulates the antennal set-point based on airflow. In this chapter, we investigated one of the subsystems of the behavior - the set-point modulation circuit (unpacking the neuromechanical black box, section 1.4).

JOs can potentially modulate the set-point of the antennae in two ways - unilaterally and bilaterally. In the unilateral case, each JO senses the deflection due to airflow and uses it to modulate the position of the corresponding antenna. This would make individual antennae independent not just with respect to maintaining antennal position [chapter 2; Krishnan et al. (2012)], but also with respect to responding to airflow. In the bilateral case, sensory inputs from both the JOs maybe pooled to determine the set-point of each antenna.

To test if JO modulates set-point unilaterally, we used airflow-dependent antennal positioning as a behavioral readout (Figure 2.3A). By unilaterally restricting JOs, we showed that the antennal response to airflow in the free (unrestricted) antenna is substantially decreased (Figure 3.5A-C). Furthermore, the JO-restricted antennae weakly respond to airflow as well (Figure 3.5D-F). This provides evidence against

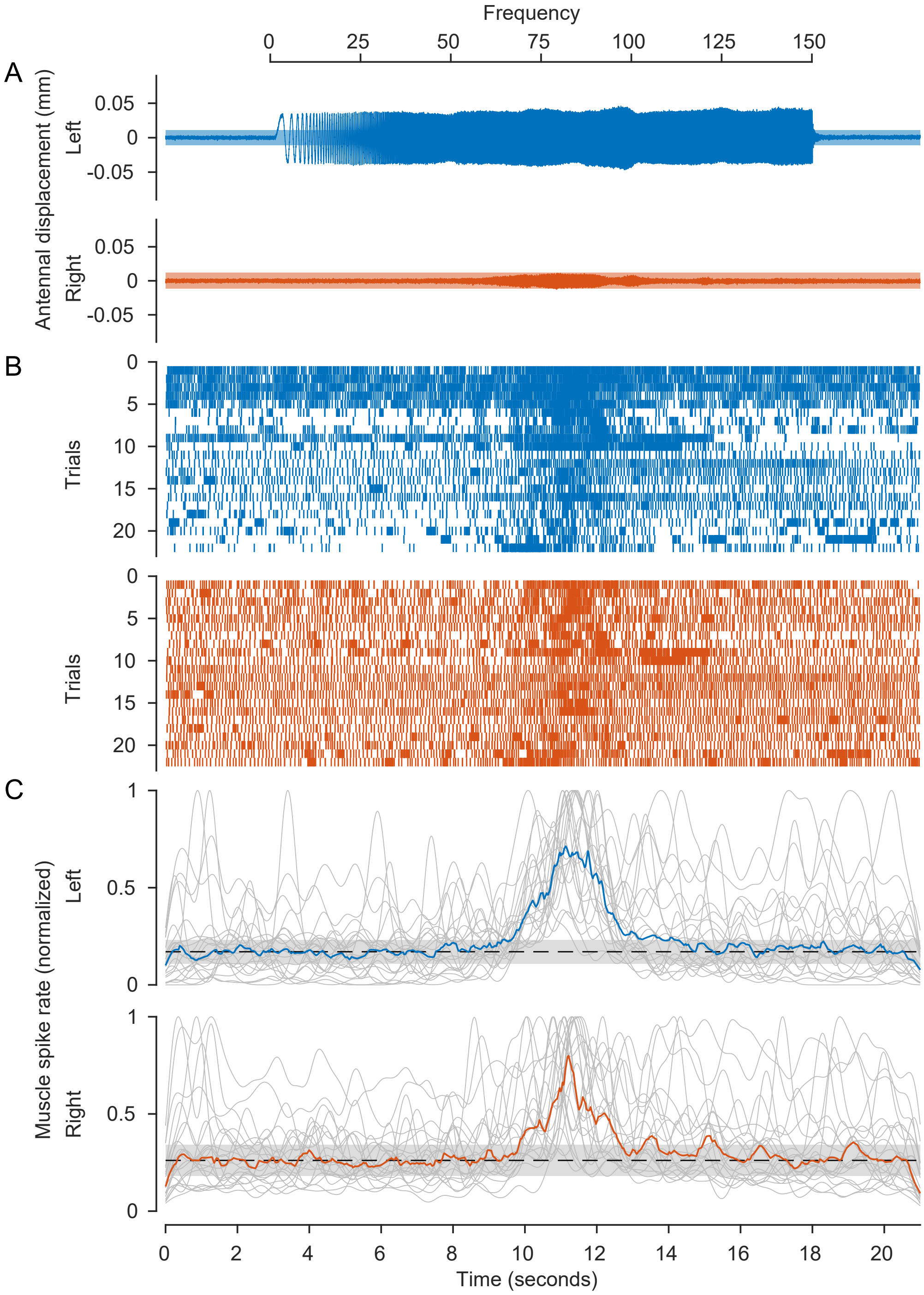

Fig. 3.12 : Representative response to a unilateral chirp
(A) Left antenna frequency increases from 0 Hz to 150 Hz (top x-axis). **(B)** Spike raster for left (blue), right (red) muscles, respectively. **(C)** A noticeable increase in spike-rate visible in both muscles during high frequency vibrations of the left pedicel-flagellum joint, suggesting bilateral transfer of information from the left JO. Colors correspond to the same entities as in Figure 3.8.

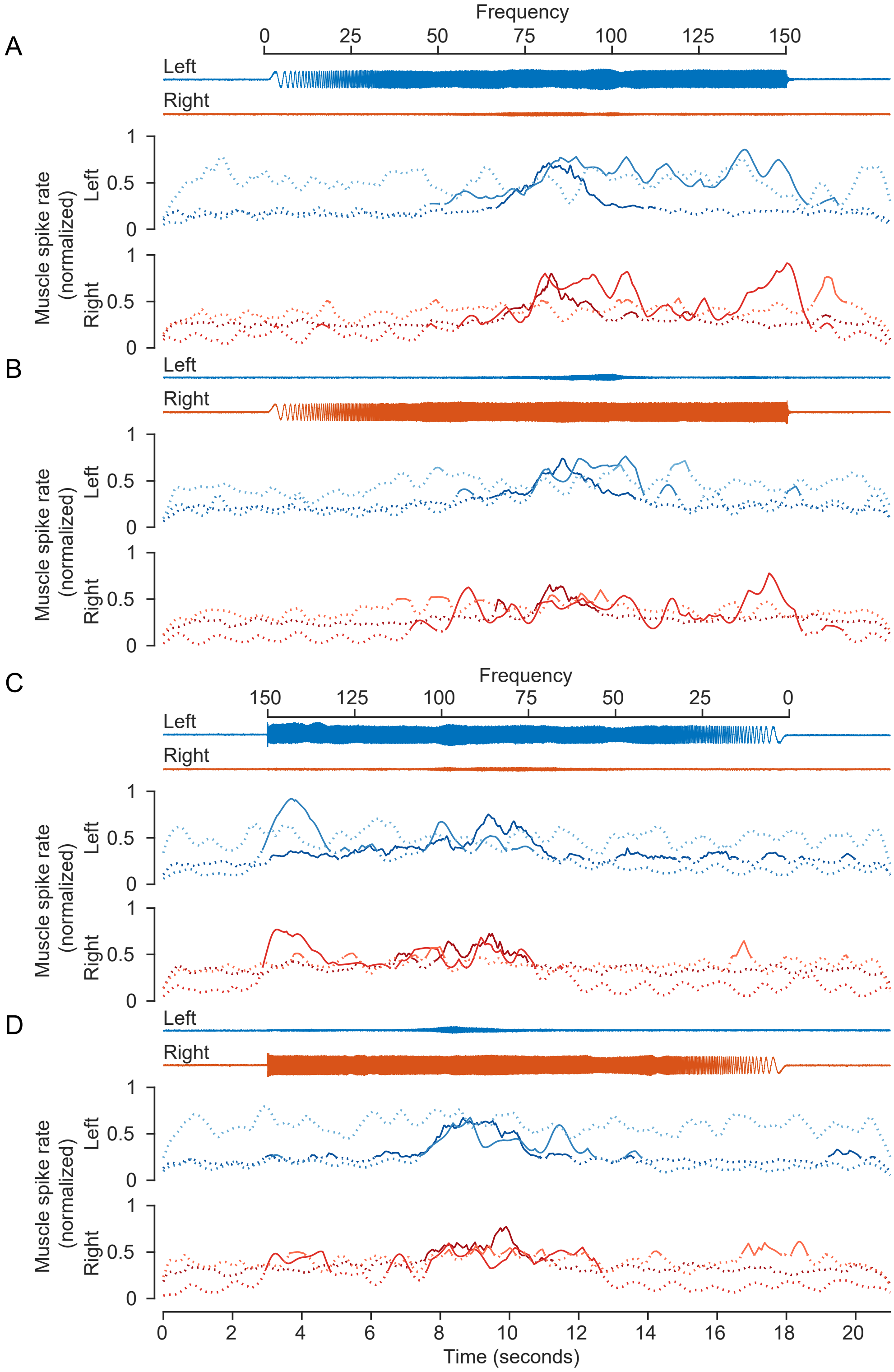

Fig. 3.13 : Muscle activity in response to unilateral chirp
Muscle activity changed bilaterally in response to both ascending and descending unilateral chirp (n=3 individuals). Colors correspond to the same entities as in Figure 3.9.

the hypothesis that set-point is unilaterally modulated and suggests the likelihood of bilateral pooling of sensory inputs from the JOs.

To capture the mechanism of bilateral pooling, we needed a readout of the set-point of each antenna. Activity of either the antennal motor neurons or the muscles would serve as a good proxy of set-point (spiking neuron model in chapter 2). The extrinsic muscles that move the head-scape joint and position the antennae consist of five muscles innervated by atleast seven motor neurons (Kloppenburg et al., 1997; Sant and Sane, 2018). We recorded simultaneously from both the ALMs, one of the larger muscles out of the five extrinsic muscles (Kloppenburg et al., 1997; Sant and Sane, 2018). We chose these muscles both due to their size as well as the ease of accessibility. Next, we custom designed our stimulus setup (based on Mohan et al., 2017) to allow us to move the flagellum of each antenna independently and in a controlled manner. By restricting all antennal joints except the pedicel-flagellum joint, we tried to ensure that movements of the flagellum activated only the JO. Hence, our setup enabled us to simultaneously stimulate both the JOs while recording the activity of both the ALMs.

JO has been shown to sense flagellar vibrations over a wide range of frequencies, ranging from low frequency movements arising due to airflow and gravity to high-frequency movements to due wingbeat and inertia forces during flight (Dieudonné et al., 2014; Kamikouchi et al., 2009; Mamiya and Dickinson, 2015; Sane et al., 2007; Yorozu et al., 2009). Based on these studies, we hypothesized that airflow is sensed by the JO as sustained displacements of the flagellum. To test this, we provided step stimuli to both flagella while recording antennal muscle activity. Surprisingly, the step stimuli did not evoke a consistent change in activity of either muscle (Figure 3.8). Chirp stimuli, on the other hand, evoked a strong increase in firing rate in both muscles (Figure 3.10). This suggests that, in hawkmoths, airflow-dependent modulation by the JO likely utilizes characteristics of high-frequency vibrations and not sustained (low-frequency) displacements of the flagellum. This is in contrast to observations in fruitflies, where airflow detection arises from sustained displacements detected by the JO (Yorozu et al., 2009).

Next, we stimulated only one of the flagella while recording from both the antennal muscles. Whereas unilateral step and impulse stimuli did not change the firing rate of both muscles, unilateral chirp stimulus increased the firing rate of both ALMs. These results are preliminary as we have only few sample points at present. Increasing the sample size by performing more experiments or using better spike detection techniques, such as template-matching and deconvolution (Clements and Bekkers, 1997; Lewicki, 1998; Pernía-Andrade et al., 2012), on the low SNR dataset would provide more conclusive evidence for bilateral pooling.

Bilateral pooling of flagellar vibrations sensed by the JOs has been observed in different brain regions of insects (Homberg, 1985; Patella and Wilson, 2018; Ritzmann et al., 2008; Suver et al., 2019). In cockroaches and bees, the neurons in the central complex respond to mechanical stimuli from both antennae, often responding to other modalities as well (Homberg, 1985; Ritzmann et al., 2008). In fruitflies, sensory inputs from the ipsilateral JO forms a coarse tonotopic map in the corresponding AMMC (Patella and

Wilson, 2018). Feedback from these ipsilateral tonotopic maps are carried downstream from the AMMC to the wedge regions of the fruitfly brain where they combine to form fine, bilateral tonotopic maps (Patella and Wilson, 2018). These wedge projection neurons integrate information from both the antennae to generate a linear response to wind direction (Suver et al., 2019). Such neurons could provide feedback to the AMMC and modulate set-point, giving rise to airflow-dependent antennal positioning.

Modification of antennal set-point occurs via modulation of antennal motor neuron activity at the AMMC (chapter 2). Therefore, the airflow information, along with other inputs from modalities such as vision and odor, must eventually modulate activity of antennal motor neurons (chapter 1). Apart from this, antennal mechanosensory information is important for control of flight, abdominal flexion and leg movements [modularity of sensory systems, chapter 1; Budick et al. (2007); Cowan et al. (2006); Dürr et al. (2001); Hinterwirth and Daniel (2010); Sane et al. (2007); Staudacher et al. (2005); Taylor et al. (2013)]. The AMMC thus merits further investigation to understand state-modulated antennal movements and the role of the antennae in controlling insect behavior in different contexts.

Bibliography

S. A. Budick, M. B. Reiser, and M. H. Dickinson. The role of visual and mechanosensory cues in structuring forward flight in Drosophila melanogaster. *Journal of Experimental Biology*, 210(23):4092–4103, Dec. 2007. ISSN 0022-0949, 1477-9145. doi: 10.1242/jeb.006502.

T. Caliński and J. Harabasz. A dendrite method for cluster analysis. *Communications in Statistics*, 3(1):1–27, Jan. 1974. ISSN 0090-3272. doi: 10.1080/03610927408827101.

J. D. Clements and J. M. Bekkers. Detection of spontaneous synaptic events with an optimally scaled template. *Biophysical Journal*, 73(1):220–229, July 1997. ISSN 0006-3495. doi: 10.1016/S0006-3495(97)78062-7.

N. J. Cowan, J. Lee, and R. J. Full. Task-level control of rapid wall following in the American cockroach. *Journal of Experimental Biology*, 209(9):1617–1629, May 2006. ISSN 0022-0949, 1477-9145. doi: 10.1242/jeb.02166. 00105.

P. Dayan, L. F. Abbott, T. J. Sejnowski, and T. A. Poggio. *Theoretical Neuroscience: Computational and Mathematical Modeling of Neural Systems*. The MIT Press, Cambridge, Mass., revised ed. edition edition, Sept. 2005. ISBN 978-0-262-54185-5.

A. Dieudonné, T. L. Daniel, and S. P. Sane. Encoding properties of the mechanosensory neurons in the Johnston's organ of the hawk moth, Manduca sexta. *Journal of Experimental Biology*, 217(17):3045–3056, Sept. 2014. ISSN 0022-0949, 1477-9145. doi: 10.1242/jeb.101568.

D. L. Donoho and I. M. Johnstone. Ideal spatial adaptation by wavelet shrinkage. *Biometrika*, 81(3):425–455, Sept. 1994. ISSN 0006-3444. doi: 10.1093/biomet/81.3.425.

V. Dürr, Y. König, and R. Kittmann. The antennal motor system of the stick insect Carausius morosus: Anatomy and antennal movement pattern during walking. *Journal of Comparative Physiology A*, 187(2):131–144, Mar. 2001. ISSN 0340-7594, 1432-1351. doi: 10.1007/s003590100183.

J. Erber, B. Pribbenow, A. Bauer, and P. Kloppenburg. Antennal reflexes in the honeybee: Tools for studying the nervous system. *Apidologie*, 24(3):283–296, 1993. ISSN 0044-8435. doi: 10.1051/apido:19930308.

M. Gewecke. The Antennae of Insects as Air-Current Sense Organs and their Relationship to the Control of Flight. In L. Barton Browne, editor, *Experimental Analysis of Insect Behaviour*, pages 100–113. Springer, Berlin, Heidelberg, 1974. ISBN 978-3-642-86666-1. doi: 10.1007/978-3-642-86666-1_8.

M. Gewecke and H.-G. Heinzel. Aerodynamic and mechanical properties of the antennae as air-current sense organs inLocusta migratoria. *Journal of comparative physiology*, 139(4):357–366, Dec. 1980. ISSN 0340-7594, 1432-1351. doi: 10.1007/BF00610466.

T. L. Hedrick. Software techniques for two- and three-dimensional kinematic measurements of biological and biomimetic systems. *Bioinspiration & Biomimetics*, 3(3): 034001, 2008. ISSN 1748-3190. doi: 10.1088/1748-3182/3/3/034001.

H.-G. Heinzel and M. Gewecke. Aerodynamic and mechanical properties of the antennae as air-current sense organs inLocusta migratoria. *Journal of Comparative Physiology A*, 161(5):671–680, Sept. 1987. ISSN 0340-7594, 1432-1351. doi: 10.1007/BF00605008.

H. Heran. Wahrnehmung und Regelung der Flugeigengeschwindigkeit bei Apis mellifica L. *Zeitschrift für vergleichende Physiologie*, 42(2):103–163, Mar. 1959. ISSN 0044-362x, 1432-1351. doi: 10.1007/BF00298733.

A. J. Hinterwirth and T. L. Daniel. Antennae in the hawkmoth Manduca sexta (Lepidoptera, Sphingidae) mediate abdominal flexion in response to mechanical stimuli. *Journal of Comparative Physiology A*, 196(12):947–956, Dec. 2010. ISSN 0340-7594, 1432-1351. doi: 10.1007/s00359-010-0578-5. 00053.

U. Homberg. Interneurones of the central complex in the bee brain (Apis mellifera, L.). *Journal of Insect Physiology*, 31(3):251–264, Jan. 1985. ISSN 0022-1910. doi: 10.1016/0022-1910(85)90127-1.

H.-W. Honegger. A preliminary note on a new optomotor response in crickets: Antennal tracking of moving targets. *Journal of comparative physiology*, 142(3):419–421, Sept. 1981. ISSN 0340-7594, 1432-1351. doi: 10.1007/BF00605454.

A. Kamikouchi, H. K. Inagaki, T. Effertz, O. Hendrich, A. Fiala, M. C. Göpfert, and K. Ito. The neural basis of Drosophila gravity-sensing and hearing. *Nature*, 458 (7235):165–171, Mar. 2009. ISSN 1476-4687. doi: 10.1038/nature07810.

T. R. Khurana and S. P. Sane. Airflow and optic flow mediate antennal positioning in flying honeybees. *eLife*, 5:e14449, Apr. 2016. ISSN 2050-084X. doi: 10.7554/eLife.14449.

P. Kloppenburg, S. M. Camazine, X. J. Sun, P. Randolph, and J. G. Hildebrand. Organization of the antennal motor system in the sphinx moth Manduca sexta. *Cell and Tissue Research*, 287(2):425–433, Jan. 1997. ISSN 0302-766X, 1432-0878. doi: 10.1007/s004410050767.

A. Krishnan and S. P. Sane. Visual feedback influences antennal positioning in flying hawk moths. *Journal of Experimental Biology*, 217(6):908–917, Mar. 2014. ISSN 0022-0949, 1477-9145. doi: 10.1242/jeb.094276.

A. Krishnan, S. Prabhakar, S. Sudarsan, and S. P. Sane. The neural mechanisms of antennal positioning in flying moths. *Journal of Experimental Biology*, 215(17): 3096–3105, Sept. 2012. ISSN 0022-0949, 1477-9145. doi: 10.1242/jeb.071704.

M. Lambin, P. Déglise, and M. Gauthier. Antennal movements as indicators of odor detection by worker honeybees. *Apidologie*, 36(1):119–126, Jan. 2005. ISSN 0044-8435, 1297-9678. doi: 10.1051/apido:2004076.

M. S. Lewicki. A review of methods for spike sorting: The detection and classification of neural action potentials. *Network: Computation in Neural Systems*, 9(4):R53–R78, Jan. 1998. ISSN 0954-898X. doi: 10.1088/0954-898X_9_4_001.

A. Mamiya and M. H. Dickinson. Antennal Mechanosensory Neurons Mediate Wing Motor Reflexes in Flying Drosophila. *Journal of Neuroscience*, 35(20):7977–7991, May 2015. ISSN 0270-6474, 1529-2401. doi: 10.1523/JNEUROSCI.0034-15.2015.

A. Mamiya, A. D. Straw, E. Tómasson, and M. H. Dickinson. Active and Passive Antennal Movements during Visually Guided Steering in Flying Drosophila. *Journal of Neuroscience*, 31(18):6900–6914, May 2011. ISSN 0270-6474, 1529-2401. doi: 10.1523/JNEUROSCI.0498-11.2011.

U. Mohan, M. Maitri, and S. P. Sane. Visual and mechanosensory integration by descending interneurons in hawkmoths. In *INTEGRATIVE AND COMPARATIVE BIOLOGY*, volume 57, pages E352–E352. OXFORD UNIV PRESS INC JOURNALS DEPT, 2001 EVANS RD, CARY, NC 27513 USA, 2017.

D. Natesan, N. Saxena, Ö. Ekeberg, and S. P. Sane. Tuneable reflexes control antennal positioning in flying hawkmoths. *Nature Communications*, 10(1):1–15, Dec. 2019. ISSN 2041-1723. doi: 10.1038/s41467-019-13595-3.

J. Okada and Y. Toh. Active tactile sensing for localization of objects by the cockroach antenna. *Journal of Comparative Physiology A*, 192(7):715–726, July 2006. ISSN 0340-7594, 1432-1351. doi: 10.1007/s00359-006-0106-9.

P. Patella and R. I. Wilson. Functional Maps of Mechanosensory Features in the Drosophila Brain. *Current Biology*, 28(8):1189–1203.e5, Apr. 2018. ISSN 0960-9822. doi: 10.1016/j.cub.2018.02.074.

A. J. Pernía-Andrade, S. P. Goswami, Y. Stickler, U. Fröbe, A. Schlögl, and P. Jonas. A Deconvolution-Based Method with High Sensitivity and Temporal Resolution for Detection of Spontaneous Synaptic Currents In Vitro and In Vivo. *Biophysical Journal*, 103(7):1429–1439, Oct. 2012. ISSN 0006-3495. doi: 10.1016/j.bpj.2012.08.039.

R. Q. Quiroga, Z. Nadasdy, and Y. Ben-Shaul. Unsupervised Spike Detection and Sorting with Wavelets and Superparamagnetic Clustering. *Neural Computation*, 16 (8):1661–1687, Aug. 2004. ISSN 0899-7667. doi: 10.1162/089976604774201631.

R. E. Ritzmann, A. L. Ridgel, and A. J. Pollack. Multi-unit recording of antennal mechano-sensitive units in the central complex of the cockroach, Blaberus discoidalis. *Journal of Comparative Physiology A*, 194(4):341, Jan. 2008. ISSN 1432-1351. doi: 10.1007/s00359-007-0310-2.

S. P. Sane, A. Dieudonné, M. A. Willis, and T. L. Daniel. Antennal Mechanosensors Mediate Flight Control in Moths. *Science*, 315(5813):863–866, Feb. 2007. ISSN 0036-8075, 1095-9203. doi: 10.1126/science.1133598.

H. H. Sant and S. P. Sane. The mechanosensory-motor apparatus of antennae in the Oleander hawk moth (Daphnis nerii, Lepidoptera). *Journal of Comparative Neurology*, 526(14):2215–2230, June 2018. ISSN 0021-9967. doi: 10.1002/cne.24477.

D. Schneider. Insect Antennae. *Annual Review of Entomology*, 9(1):103–122, Jan. 1964. ISSN 0066-4170. doi: 10.1146/annurev.en.09.010164.000535.

E. M. Staudacher, M. Gebhardt, and V. Dürr. Antennal Movements and Mechanoreception: Neurobiology of Active Tactile Sensors. In S. J. Simpson, editor, *Advances in Insect Physiology*, volume 32, pages 49–205. Academic Press, Jan. 2005. doi: 10.1016/S0065-2806(05)32002-9.

M. P. Suver, A. M. M. Matheson, S. Sarkar, M. Damiata, D. Schoppik, and K. I. Nagel. Encoding of Wind Direction by Central Neurons in Drosophila. *Neuron*, 102 (4):828–842.e7, May 2019. ISSN 0896-6273. doi: 10.1016/j.neuron.2019.03.012.

G. J. Taylor, T. Luu, D. Ball, and M. V. Srinivasan. Vision and air flow combine to streamline flying honeybees. *Scientific Reports*, 3, Sept. 2013. ISSN 2045-2322. doi: 10.1038/srep02614.

E. Warrant and M. Dacke. Vision and Visual Navigation in Nocturnal Insects. *Annual Review of Entomology*, 56(1):239–254, 2011. doi: 10.1146/annurev-ento-120709-144852.

Y. Yamawaki and W. Ishibashi. Antennal pointing at a looming object in the cricket Acheta domesticus. *Journal of Insect Physiology*, 60(Supplement C):80–91, Jan. 2014. ISSN 0022-1910. doi: 10.1016/j.jinsphys.2013.11.006.

S. Yorozu, A. Wong, B. J. Fischer, H. Dankert, M. J. Kernan, A. Kamikouchi, K. Ito, and D. J. Anderson. Distinct sensory representations of wind and near-field sound in the Drosophila brain. *Nature*, 458(7235):201–205, Mar. 2009. ISSN 1476-4687. doi: 10.1038/nature07843.

Chapter 4

Modeling Böhm's bristle sensitivity to antennal movements

4.1 Introduction

Control and proper execution of fast behaviors, such as flight in insects, require proprioceptive feedback on short timescales (Dickinson, 1999; Sane et al., 2007). In addition to being fast, this feedback needs to be precise, which often requires the noise to be pre-filtered from the signal by the physical structure of the sensor. Mechanosensors, such as campaniform sensillae on halteres, have varied geometric and material properties, allowing them to specifically amplify and detect certain types of cuticular strains (Sane and McHenry, 2009). Such biomechanical filtering enables them to achieve both speed and precision (chapter 1).

As described in the previous chapters, insects rely heavily on mechanosensory hair plates for proprioceptive information. These hair plates are found on the active joints of several body parts including the antennae (Böhm, 1911; Schneider, 1964; Toh, 1981), neck (Haskell, 1959; Liske, 1982; Thurm, 1963) and legs (Cruse et al., 1984; Kuenzi and Burrows, 1995). In each of these cases, ablating the hair plates severely affects positioning of the respective appendage (Cruse et al., 1984; Krishnan et al., 2012; Mittelstaedt, 1962). Proprioceptive feedback from the hair plates is therefore critical for stable positioning of these appendages.

Mechanosensory hair plates are organized as fields of bristles which sense proprioceptive information. Biomechanical filtering in individual mechanosensory hairs has been well studied. For instance, ease of stimulation of an individual mechanosensory hair depends on the length of the hair, with longer hairs being more sensitive, i.e. they are stimulated by smaller torques (Camhi, 1969, 1980). Additionally, hairs with hardened cuticular distortions at the base bend preferentially in one direction, making them directionally sensitive (Thurm, 1965, 1963). Although the filtering properties of individual hairs are known, the mechanisms by which collections of such hairs can selectively filter information are not well understood.

Here, we investigate how Böhm's bristles transform antennal position into proprioceptive feedback that encodes position. By virtue of the mechanical properties of the joint and location of the hair plates, antennal movements undergo a first level of biomechanical filtering (Sane and McHenry, 2009). Compounded onto this are the filtering properties of individual sensory bristles (Sane and McHenry, 2009). The proprioceptive feedback provided by these hair plates therefore encompasses both these levels of filtering (chapter 2). Additionally, the nature of this transformation dictates the type of control the neural system has to exert to dictate antennal movements (chapter 1). Presumably, the proprioceptive inputs from the head and legs also undergo similar transformations before being used by the respective neural systems to control movements (chapter 1), making them quite important for understanding insect behavior.

In this chapter, we create a computational toolbox to investigate the biomechanical filtering properties of hair plates. By developing a numerical method to determine stimulation of a hair plate, we determine the sensitivity of an arbitrarily shaped bristle field. By using simple biomechanical models, we then quantify the effect of hair plate location on movement sensitivity. Together, the toolbox presented here could be used to describe the input-output transformation of the hair plate mechanosensory system (chapter 1, chapter 2) and to understand their roles in proprioception.

4.2 Methods

4.2.1 Assumptions

The biomechanical model presented here aims to quantify the stimulation of hair plates as a function of both antennal movements, and the shape and position of the hair plates. To simplify the model, we assumed the following:

1. Stimulation of sensory hairs is binary. When there is relative movement between basal antennal joints between head capsule-scape and scape-pedicel, the sensory bristles are covered by cuticular edge and thus stimulated (Figure 4.1A). We assume that a sensory bristle is completely active when it is covered by the cuticular edge at the joint, and not active when it is exposed. This is based on experimental data that suggests that the clearance between the cuticle and the base of the sensory bristle is very small [Figure 4.1B; Pringle (1938); Thurm (1963); Krishnan et al. (2012); Sant and Sane (2018)]. Therefore, once the bristle is covered by the cuticle, it invariably bends and is stimulated (Figure 4.1C).

2. Density of bristles within a field is uniform. This assumption allows us to relate the area stimulated by the cuticular edge instead of counting the number of bristles at a particular position. To obtain the number of stimulated bristles, we multiplied the stimulated area with the density and rounded it off to the nearest integer less than the obtained fraction (based on assumption 1).

3. Hair plates are two dimensional structures. Because the hair plates are structures on the surface of the antenna (or other joints), their shape is automatically two-dimensional. Variations in heights of bristles may arise from surface contortions

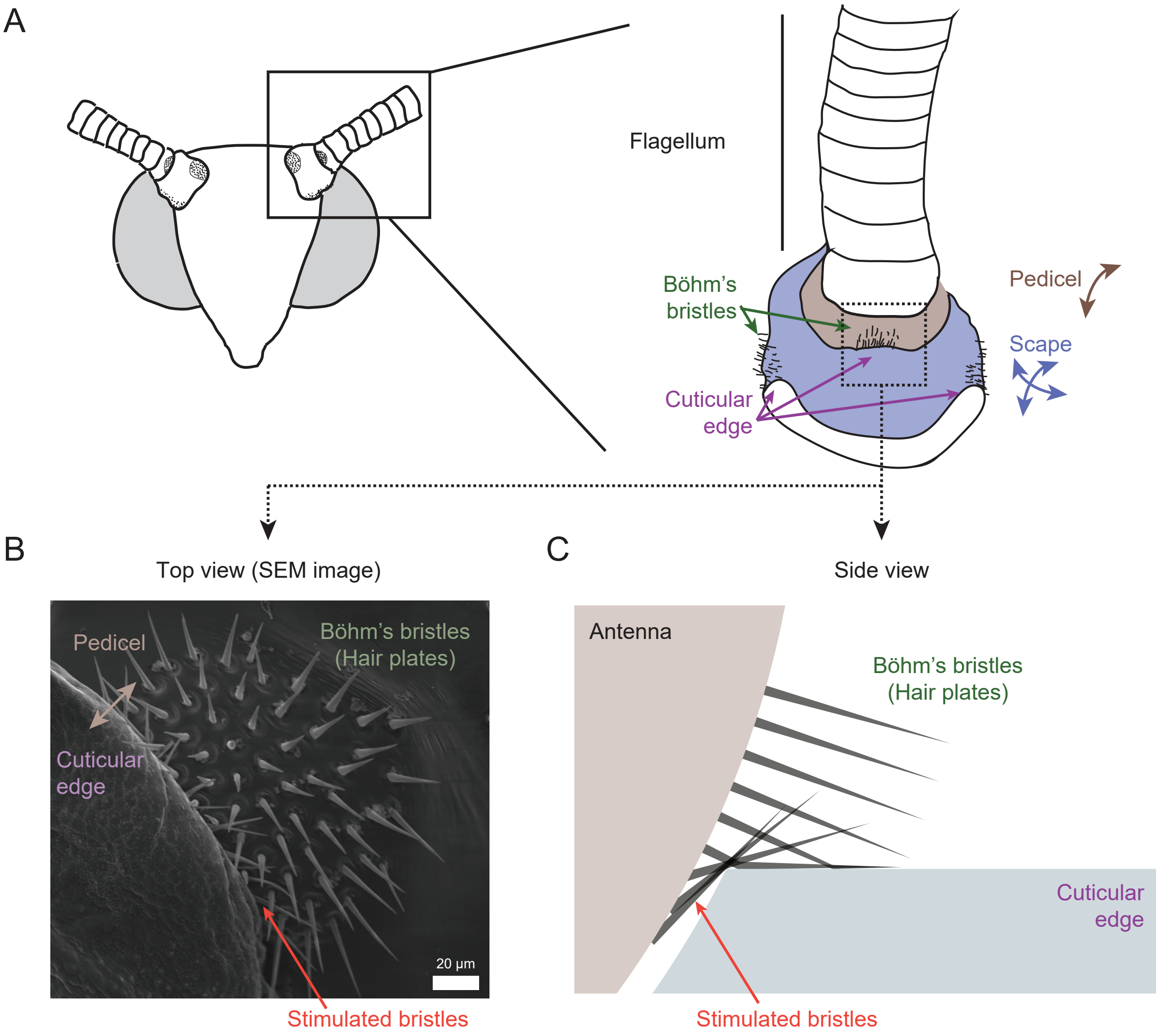

Fig. 4.1 : Antennal hair fields and their stimulation
(A) Each moth antenna has three fields of Böhm's bristles on the scape (two shown, one hidden from view) and two fields on the pedicel (one shown). The scape has two degrees of freedom whereas the pedicel has just one (directions illustrated). **(B)** SEM image of a pedicel bristle field stimulated by the cuticular edge (image credit: Harshada Sant). The movement of the pedicel with respect to the cuticular edge is shown by a brown arrow. Bristles stimulated by the edge is shown by a red arrow. **(C)** An illustration of how Böhm's bristles are stimulated by the cuticular edge.

of the antenna, or due to different bristle heights. Based on experimental data, we assume individual sensory bristles to have the same height (Krishnan et al., 2012; Sant and Sane, 2018).

4.2.2 Calculating hair field stimulation

Methodology

Hair plates of different insects have diverse shapes ranging from circular /elliptical fields to sparse, widely distributed fields (Krishnan et al., 2012; Kuenzi and Burrows, 1995; Pringle, 1938; Thurm, 1963; Wong and Pearson, 1976; Sant and Sane, 2019). We therefore could not assume hair plates to have a simple circular geometry. Instead, our methodology was designed to determine the stimulation of a bristle irrespective of the hair field shape, as described below.

$$\begin{aligned} F(t) &= (X(t), Y(t)), t \in [a, b] \\ F &: [a, b] \rightarrow \mathbb{R}^2 \end{aligned} \qquad [4.1]$$

where,

$F(t)$ = parametric representation of the hair field
$X(t)$ = spline representation of the x-coordinate
$Y(t)$ = spline representation of the y-coordinate
$[a, b]$ = interval over which the splines are defined

To parameterize an arbitrarily shaped hair field (example - Figure 4.2A), we used B-splines (Equation 4.1), which are a class of piecewise polynomial functions that can be used to represent smooth shapes. B-splines are basis functions in the spline function space, thereby giving them the capability to represent any spline function. Additionally, they are differentiable and continuous over the defining points, and are zero outside this defined region (Equation 4.1). This is useful as integrating/differentiating a particular spine outside the defined region is automatically zero. Thus, they are ideal for parameterizing the shape of hair fields, because they can represent any shape and yet be continuous and differentiable over the whole shape.

$$\begin{aligned} \mathrm{A} &= \oint Y\, dX = \oint X\, dY \\ &= \int_a^b Y(t)\, \frac{\mathrm{d}}{\mathrm{d}t}\big(X(t)\big)\, \mathrm{d}t \end{aligned} \qquad [4.2]$$

where,

A = area enclosed by a closed shape
(defined by X,Y; parameterized by Equation 4.1)
$[a, b]$ = interval over which the splines are defined

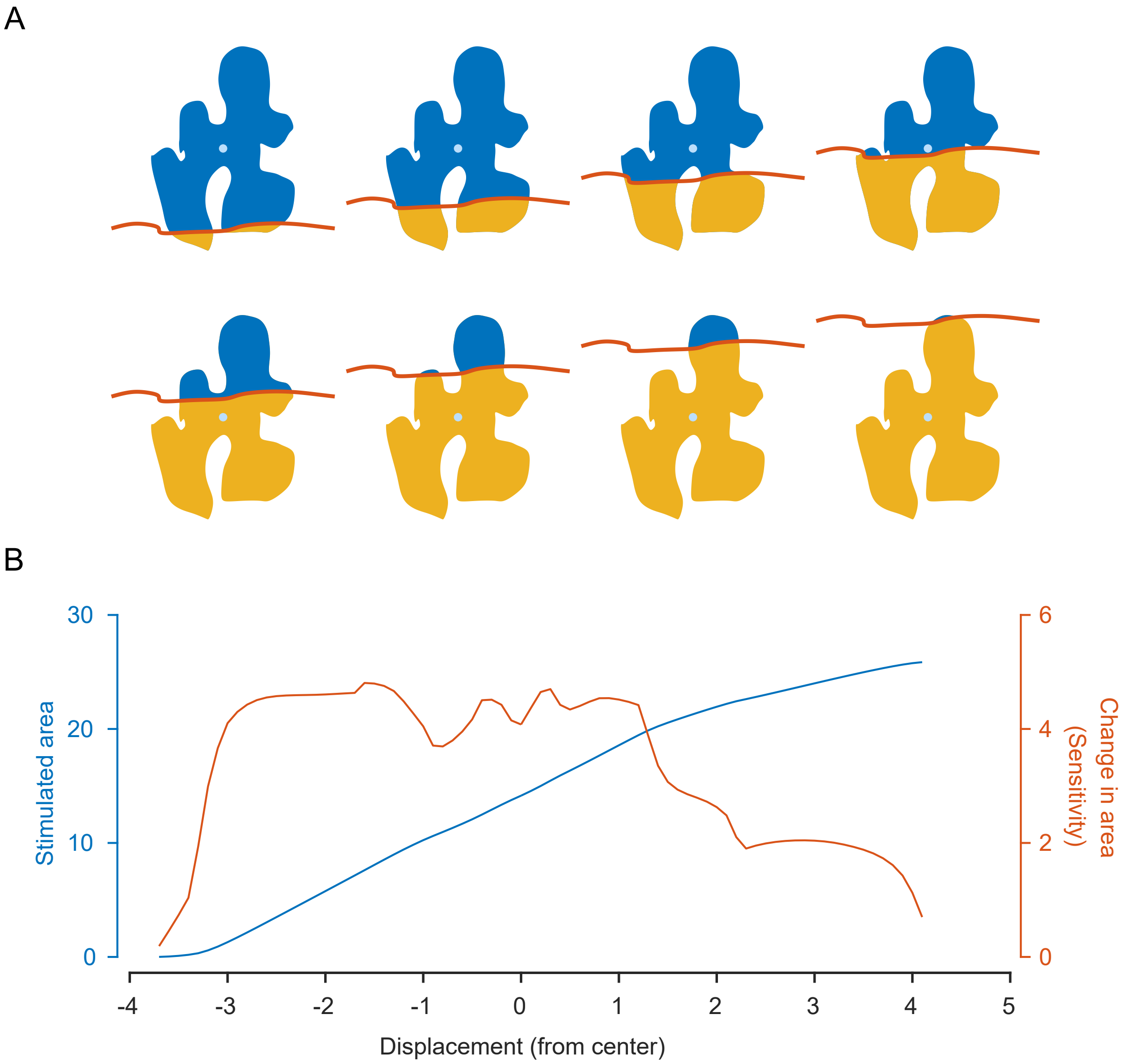

Fig. 4.2 : Numerical computation of stimulated area and sensitivity **(A)** The B-spline method used works for arbitrary closed shapes like the one shown in the figure. **(B)** The stimulated area and the sensitivity of the hair plate for different displacements (perpendicular distance of the cuticular edge) from the center (filled light blue circle).

We used the curve fitting toolbox of MATLAB (Mathworks, Natick, MA, USA) to write custom codes to represent and calculate the stimulated area of a particular hair field. We assumed the hair plates to be two dimensional (assumption 3), and used B-splines to parameterize the X and Y coordinates of the hair plates (Equation 4.1). The cuticular edge was also assumed to be two dimensional and represented in a similar fashion. Hair fields were defined as closed structures, and could take any arbitrary shape (Figure 4.2A).

The cuticle border that stimulated the bristles was an open edge that intersected with the hair-field at multiple points, forming intact and stimulated regions (Figure 4.2A). Note that the method works even for shapes with contours (Figure 4.2A), making it suitable for finding the sensitivity of any generic hair plate. To compute the area, each of these intersection regions were first converted to closed B-splines. The regions were then classified as active or inactive based on which side of the cuticle edge they lay. The areas of each of these regions were computed using Equation 4.2 (Figure 4.2B). This was then multiplied with the density of hair plates to obtain the number of stimulated bristles. Sensitivity to movements was computed as changes in area per step in movement (Figure 4.2B).

Validation

To validate our methodology, we used circular and elliptical hair fields. We simplified the cuticular edge to a line and used it to stimulate the hair field at different positions. In parallel, we analytically calculated the area for each of the different positions. The methodology described above was shown to be accurate, with the area of the intersected region identical to the one obtained analytically (circular-Figure C.1; elliptical-Figure C.2).

4.2.3 Simulation of hair plate stimulation due to appendage movement

Hair plate stimulation involves rotation and translation of the cuticle, which occur together when an appendage moves. To accurately model the hair plate stimulation we would have to model both the joint and the location of the hair plate on the joint. To weave in and out of the cuticular edge, the hair plate has to lie on a roughly spherical surface. The whole joint movement could be described as rotation on a pivot point, which lies inside the joint. By combining the two, we reasoned that the dynamics of the hair plate on a complex joint would resemble a spherical one whose center is the pivot point and whose hair plates are positioned on a sphere similar to the real joint, i.e. at same distances from the pivot point. We therefore simplified the model by modeling the whole joint as a sphere whose center was the pivot point of the joint, with the hair plate and cuticle lying on the sphere (Figure 4.5). The cuticle remained stationary while the hair plates moved in and out of the cuticle, as seen in real joints (Figure 4.1).

Next, we needed a way to describe the rotation of the sphere as translation and rotation of the cuticle surface. For points lying on the sphere, rotation of the joint is essentially addition or subtraction of a constant to their existing azimuth and elevation values.

Because both the hair plates and cuticle lie on the sphere, we represented them using azimuth and elevation. This made easy the calculation of new positions on the hair plates during every rotation. This also simplified the area calculation because the splines represented using azimuth and elevation are essentially 2D splines.

Using methods like micro-computed tomography (micro-CT) would allow us to obtain the location of hair fields, and the corresponding cuticular edge, in spherical coordinates with respect to the joint. For the purposes of this chapter, we used hair field shapes obtained from scanning electron microscopy (SEM) images. They were therefore converted from distance (in pixels) into azimuth and elevation values. Because azimuth covers a smaller circumference (distance) near the poles and a larger circumference near the equator, an arc of equal length would have a smaller azimuth difference near the equator and a larger difference near the poles. We avoided this location based inflation/deflation of the field by normalizing the azimuth to elevation. This allowed us to place the same field at different elevations and compare their sensitivities. Note that the normalization does not effect the stimulated region, which is simply the ratio of area stimulated to total area. Additionally, this step will not be necessary when the data is generated from 3D meshes (like micro-CT data).

Using this approach, we can place the hair plate at various azimuths and elevations on a joint, and characterize its sensitivity to different movements of appendages.

4.3 Results

4.3.1 Effect of hair plate shape on movement sensitivity

We first looked at how shape of a hair plate affects its sensitivity to movements. Two commonly seen hair plate shapes were studied - elliptical and circular. Using the numerical approach (B-splines, see section 4.2), we simulated the stimulation of such hair plates. We used a simple line to represent the cuticular edge, and varied the slopes of this line to obtain sensitivity of the hair plate to movements in different directions (Figure 4.3A).

We found that elliptical hair plates provide either high range or high sensitivity. Directions of movement parallel to the minor axis of the ellipse provided the most range, i.e. movements over a large displacements were detected best by the hair plates (Figure 4.3B). The sensitivity to small movements were, however, low (Figure 4.3C). Directions of movement parallel to the major axis provided low range (Figure 4.3B) but the hair plates were highly sensitive to small movements in the stimulation range (Figure 4.3C). This trade-off between sensitivity and range increased with the eccentricity of the ellipse.

Next, we looked at the sensitivity of pedicellar Böhm's bristles of antennae from the Oleander hawkmoth, Daphnis nerii. We extracted both the shape of the field as well as the cuticular edge from an SEM image (Figure 4.4A-B). The field was roughly circular in nature (Figure 4.4A-B) and had symmetric range and sensitivity for different angles of movements (Figure 4.4C). For the same area, a circular field provided symmetric

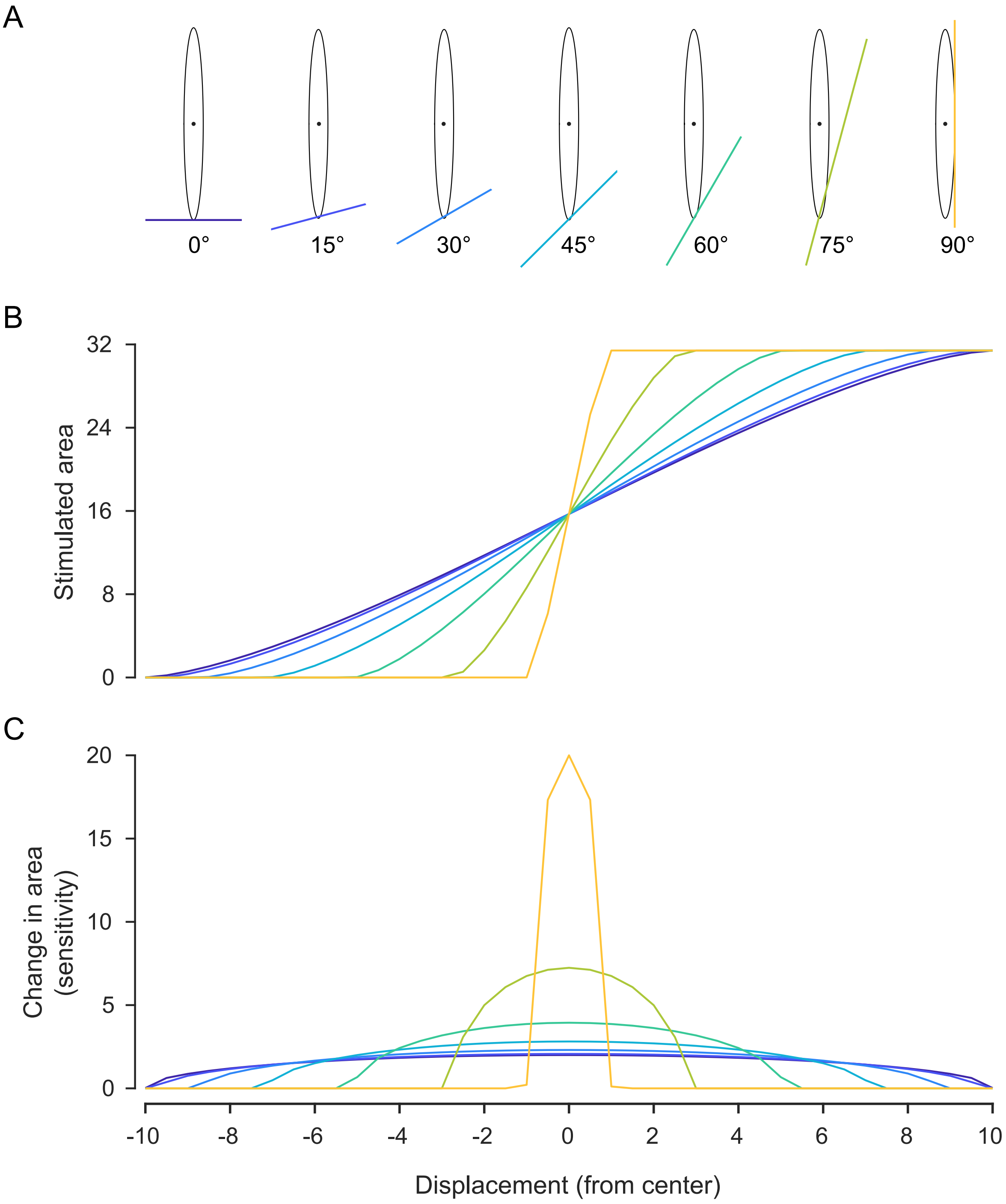

Fig. 4.3 : Sensitivity of elliptical hair plates
(A) Sensitivity of elliptical fields were computed using a simple line for the cuticular edge. The slopes of the lines were varied to determine the sensitivity of the field for different directions of movement. **(B)** Area of the hair plate stimulated by the cuticle (line). **(C)** Sensitivity of hair plate to small movements. Different colors represent different slopes of the cuticular edge. The center of the field is shown by a black filled circle.

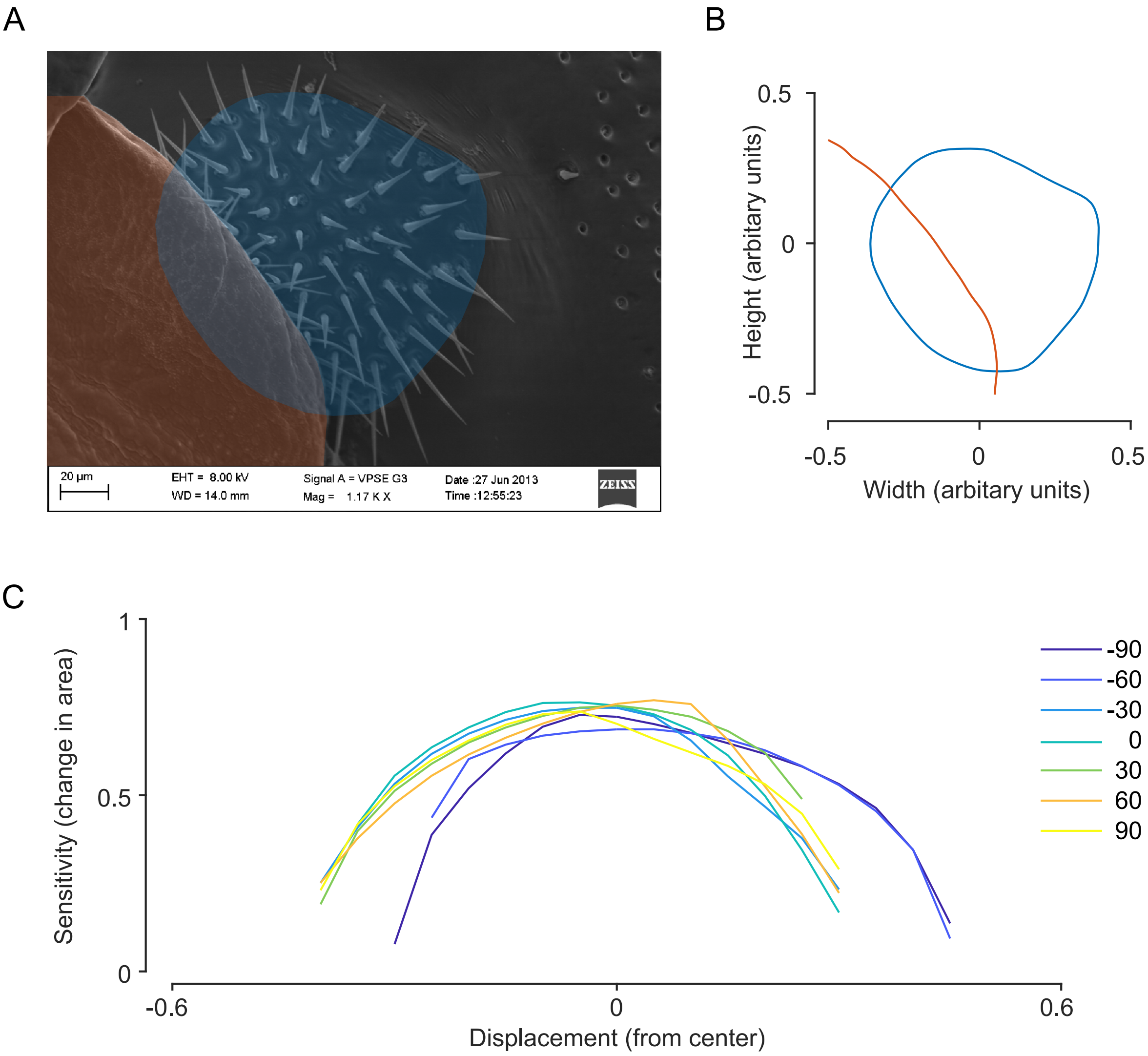

Fig. 4.4 : Sensitivity of pedicellar bristle fields
(A) The shape of the bristle field and the cuticular edge was obtained from an SEM image (credit: Harshada Sant). **(B)** Pedicellar bristle field and the corresponding cuticular edge extracted from the SEM (bristle field center marked by black filled circle). **(C)** Sensitivity of the bristle field to different directions of stimulation by the cuticular edge.

range and sensitivity (Figure 4.4C, Figure C.1), although both were lower than the range and sensitivity provided by elliptical fields in different (asymmetric) directions.

4.3.2 Effect of hair plate location on movement sensitivity

How do changes in the location of the same hair plate, i.e. its position on the antenna, change its sensitivity? To answer this, we made a spherical ball-and-stick model of the antenna (Figure 4.5). It had two degrees of freedom, one along the x-axis (pitch, Figure 4.5A) and the other along the y-axis (roll, Figure 4.5B). We placed the pedicellar bristle field at different elevations of the spherical antenna and simulated antennal movements along the pitch and the roll axis (Figure 4.5A-B).

For the same azimuth, placing the bristle field at different elevations had a stark effect on its stimulation (Figure 4.5C-E). At zero elevation, i.e. the equator, the bristle field responded strongly to movements along one axis and not the other (Figure 4.5C). As the elevation of the field decreased, it began to respond to both types of rotation (Figure 4.5D,E). Selective sensitivity to particular rotations of the antenna could only occur if the bristle field was placed at the equator of the joint - locations further away resulted in easy detection of presence or absence of movement but lack of sensitivity regarding the degree of rotation. Hence, the sensitivity of a hair plate to different movements is dependent not just on its shape, but also on its location on the joint.

4.4 Discussion

Reflexive behaviors such as antennal positioning rely on rapid proprioceptive feedback from mechanosensory structures like the Böhm's bristles (chapter 2). Böhm's bristles, and hair plates in general, consist of a collection of individual mechanosensory hairs, each responding to deflections (Böhm, 1911; Thurm, 1965). Proprioceptive feedback sent to the brain depends both on the properties of the hair, and also the biomechanical filtering due to the properties of the joint and location of the bristle fields. The brain uses this filtered information to infer antennal position and control antennal movements, via activation of antennal motor neurons and muscles (chapter 1; chapter 2).

In the pedicel, control of movements requires pooling information from two sets of bristle fields to stimulate two pairs of muscles. One possible neural circuit is conceptualized in chapter 2, where the pooled activity of one bristle field stimulates one of the muscle pairs. The bristle field to muscle connectivity encodes negative feedback; stimulation of the bristle field increases the activity of the pair of muscles that move the pedicel in the direction of decreasing bristle field stimulation (chapter 2).Because the pedicel has just one degree of freedom of movement, with two pairs of bristles and muscles to sense and actuate respectively, such one-to-one connectivity is possible. The scape, on the other hand, has two degrees of freedom, with three sets of bristle fields and five pairs of muscles sensing and controlling its movement, respectively (Kloppenburg et al., 1997; Sant and Sane, 2018). Stimulation of these bristle fields depends both on the location of the field as well as its shape, which are different for the three fields. Characterizing the hair plate mechanosensory system, i.e. how position translates to stimulation of

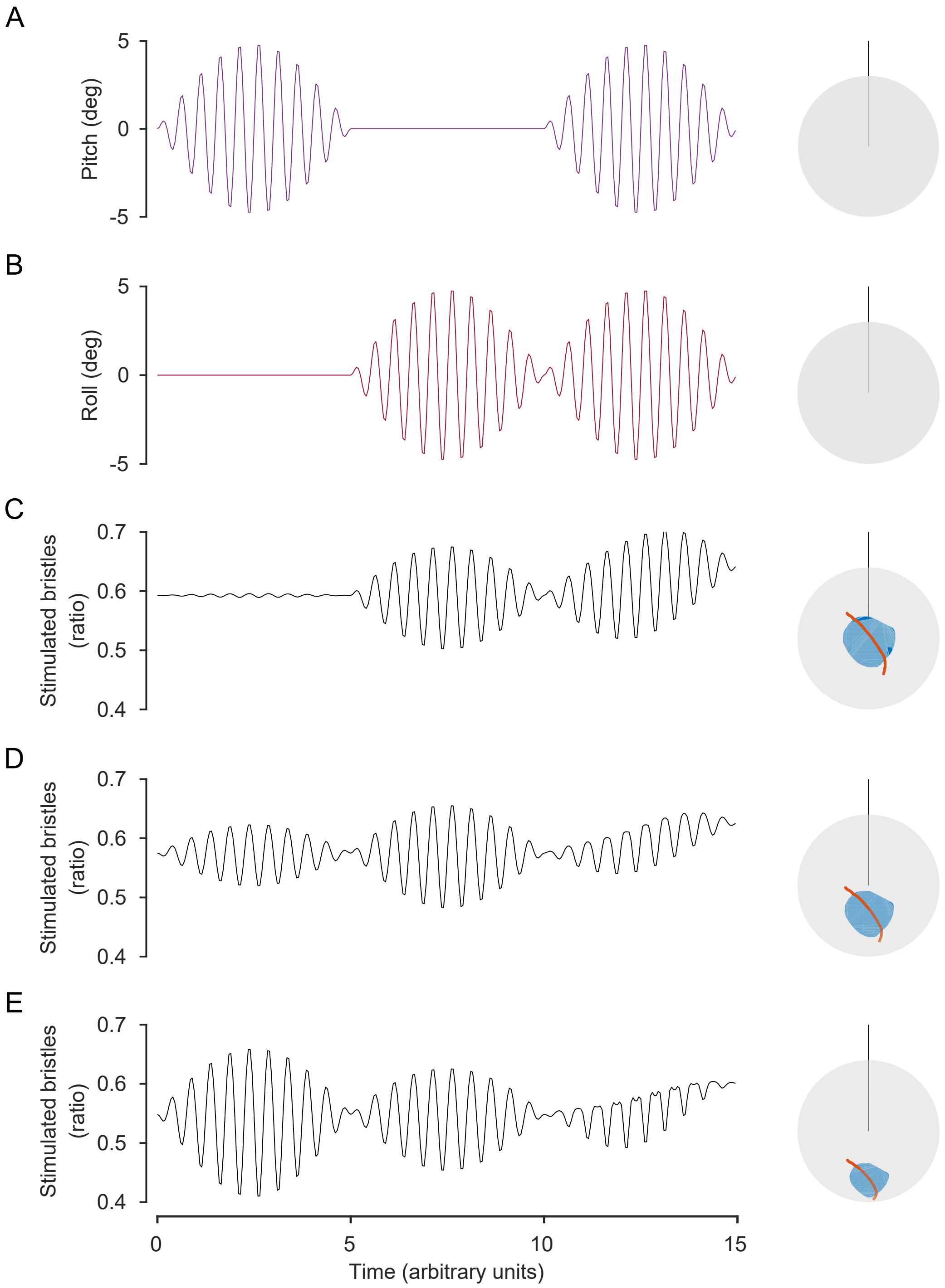

Fig. 4.5 : Location dependent changes in sensitivity
To simulate the effect on location on sensitivity to antennal movements, we used a simple ball-and-stick model of the antenna. The antenna was moved along its two degrees of freedom - **(A)** pitch and **(B)** roll. The fields were placed at a constant azimuth of 0°, whereas the elevations were **(C)** 0°, **(D)** $-22.5°$ and **(E)** $-45°$ respectively. The stimulated area of the hair plate due to small movements in each axis depends strongly on the elevation of the hair plate.

these fields, is therefore a prerequisite to understanding how the underlying neural system estimates position (chapter 1).

In this chapter, we have developed a set of tools to describe the input-output transformation of the hair fields (chapter 1). We used these tools to characterize the sensitivity of arbitrarily shaped hair plates to different types of movements. The first tool was a method to compute the stimulated area of such a bristle field. By modeling the cuticular edge as an open curve, we could compute the area stimulated for different positions of the cuticle. The second tool provided a method of placing these bristle fields on biomechanical models of antenna and simulating the stimulation of these fields as a result of the movements of the antenna. We then used these tools to understand the role of shape and location of a hair field in determining their sensitivity to small movements.

Starting with simple linear motion (one degree of freedom), we investigated the contribution of shape to sensitivity. We found that circular hair fields, such as the pedicellar Böhm's bristles, had symmetric range and sensitivity. Irrespective of direction of stimulation, these hair plates showed equal sensitivity for the same range of movements. On the other hand, elliptical hair plates had a maximum range for movements parallel to the minor axis and maximum sensitivity for movements parallel to the major axis. This informational asymmetry allowed them to preferentially pick one direction of movements.

Next, we looked at the effect of location on sensitivity to movements along two degrees of freedom. Detection of movements along either axis was easier when the fields were located away from the equator of a ball-and-stick joint. However, decoupling the movements along the axis was harder the farther away a field was from the equator. Fields right on the equator, on the other hand, were sensitive to movements along only one particular axis, making it easier to decouple different types of rotations.

Hence, we inferred that both shape and location have strong effects on sensitivity to different types of movements - certain locations or shapes can biomechanically filter particular types of movements, making it easier for the nervous system to pool information and determine position. Identifying these in insect hair plates might enable us to better understand the types of information sensed by these mechanosensory structures.

The methods used are general purpose and can be applied to a variety of data types. Data generated from techniques like X-ray tomography (micro-CT) would yield the most information, allowing one to digitize not just the shape of the field, but also its location with respect to the 3D mesh of the complete joint (Flannery et al., 1987; Friedrich and Beutel, 2008). Biomechanical models based on these data will provide accurate simulations of joint movement and stimulation of hair plates as a result of this movement. These simulations can be validated by comparing the predicted stimulations with hair plate stimulations observed in experiments.

The morphology of hair plates seen in insects is highly varied. Antennal hair plates themselves display several different morphologies for diverse insect orders, ranging from the uniform fields seen in honeybees to sparse fields seen in cockroaches and moths

(Sant and Sane, 2019). A toolbox, such as the one described in this chapter, would help generate predictions of how these fields affect sensory encoding and test them with experiments.

For sensory structures like the hair plates, it is experimentally challenging to precisely stimulate a subset of these hair plates while simultaneously recording its response. However, movements performed during behaviors will reliably and consistently stimulate subsets of individual hair plates. To understand the neural basis of such rapid reflexes, the stimulation of these bristles needs to be computed in real time and compared with the response of the nervous system (chapter 1). The computational framework used here can be used to formalize such biomechanical processes.

Bibliography

L. K. Böhm. Die antennalen Sinnesorgane der Lepidopteren. *Arbeiten aus dem Zoologischen Instituten der Universität Wien und der Zoologischen Station in Triest*, 14: 219–246, 1911.

J. M. Camhi. Locust Wind Receptors: I. Transducer Mechanics and Sensory Response. *Journal of Experimental Biology*, 50(2):335–348, Apr. 1969. ISSN 0022-0949, 1477-9145.

J. M. Camhi. The Escape System of the Cockroach. *Scientific American*, 243(6): 158–205, 1980. ISSN 0036-8733.

H. Cruse, J. Dean, and M. Suilmann. The contributions of diverse sense organs to the control of leg movement by a walking insect. *Journal of Comparative Physiology A*, 154(5):695–705, Sept. 1984. ISSN 1432-1351. doi: 10.1007/BF01350223.

M. H. Dickinson. Haltere–mediated equilibrium reflexes of the fruit fly, Drosophila melanogaster. *Philosophical Transactions of the Royal Society of London B: Biological Sciences*, 354(1385):903–916, May 1999. ISSN 0962-8436, 1471-2970. doi: 10.1098/rstb.1999.0442.

B. P. Flannery, H. W. Deckman, W. G. Roberge, and K. L. D'amico. Three-Dimensional X-ray Microtomography. *Science*, 237(4821):1439–1444, Sept. 1987. ISSN 0036-8075, 1095-9203. doi: 10.1126/science.237.4821.1439.

F. Friedrich and R. G. Beutel. Micro-computer tomography and a renaissance of insect morphology. In *Developments in X-Ray Tomography VI*, volume 7078, page 70781U. International Society for Optics and Photonics, Sept. 2008. doi: 10.1117/12.794057.

P. T. Haskell. Hair Receptors in Locusts: Function of certain Prothoracic Hair Receptors in the Desert Locust. *Nature*, 183(4668):1107, Apr. 1959. ISSN 1476-4687. doi: 10.1038/1831107a0.

P. Kloppenburg, S. M. Camazine, X. J. Sun, P. Randolph, and J. G. Hildebrand. Organization of the antennal motor system in the sphinx moth Manduca sexta. *Cell and Tissue Research*, 287(2):425–433, Jan. 1997. ISSN 0302-766X, 1432-0878. doi: 10.1007/s004410050767.

A. Krishnan, S. Prabhakar, S. Sudarsan, and S. P. Sane. The neural mechanisms of antennal positioning in flying moths. *Journal of Experimental Biology*, 215(17): 3096–3105, Sept. 2012. ISSN 0022-0949, 1477-9145. doi: 10.1242/jeb.071704.

F. Kuenzi and M. Burrows. Central connections of sensory neurones from a hair plate proprioceptor in the thoraco-coxal joint of the locust. *Journal of Experimental Biology*, 198(7):1589–1601, July 1995. ISSN 0022-0949, 1477-9145. 00019.

E. Liske. Proprioceptive control of head position and head movement in the praying mantis. *Naturwissenschaften*, 69(9):452–453, Sept. 1982. ISSN 0028-1042, 1432-1904. doi: 10.1007/BF00404773.

H. Mittelstaedt. Control Systems of Orientation in Insects. *Annual Review of Entomology*, 7(1):177–198, 1962. doi: 10.1146/annurev.en.07.010162.001141. 00132.

J. W. S. Pringle. Proprioception In Insects: III. The Function Of The Hair Sensilla At The Joints. *Journal of Experimental Biology*, 15(4):467–473, Oct. 1938. ISSN 0022-0949, 1477-9145.

S. P. Sane and M. J. McHenry. The biomechanics of sensory organs. *Integrative and Comparative Biology*, 49(6):i8–i23, Dec. 2009. ISSN 1540-7063. doi: 10.1093/icb/icp112.

S. P. Sane, A. Dieudonné, M. A. Willis, and T. L. Daniel. Antennal Mechanosensors Mediate Flight Control in Moths. *Science*, 315(5813):863–866, Feb. 2007. ISSN 0036-8075, 1095-9203. doi: 10.1126/science.1133598.

H. H. Sant and S. P. Sane. The mechanosensory-motor apparatus of antennae in the Oleander hawk moth (Daphnis nerii, Lepidoptera). *Journal of Comparative Neurology*, 526(14):2215–2230, June 2018. ISSN 0021-9967. doi: 10.1002/cne.24477.

H. H. Sant and S. P. Sane. Chapter 19: A Comparative Study Of Antennal Mechanosensors In Insects. In *Indian Insects: Diversity and Science*, pages 389–399. Taylor & Francis, 2019. ISBN 978-0-429-06140-0.

D. Schneider. Insect Antennae. *Annual Review of Entomology*, 9(1):103–122, Jan. 1964. ISSN 0066-4170. doi: 10.1146/annurev.en.09.010164.000535.

U. Thurm. Die Beziehungen zwischen mechanischen Reizgrössen und stationären Erregungszuständen bei Borstenfeld-Sensillen von Bienen. *Zeitschrift für vergleichende Physiologie*, 46(4):351–382, July 1963. ISSN 1432-1351. doi: 10.1007/BF00340465.

U. Thurm. An Insect Mechanoreceptor: Part I: Fine Structure and Adequate Stimulus. *Cold Spring Harbor Symposia on Quantitative Biology*, 30(0):75–82, Jan. 1965. ISSN 0091-7451, 1943-4456. doi: 10.1101/SQB.1965.030.01.011.

Y. Toh. Fine structure of sense organs on the antennal pedicel and scape of the male cockroach, Periplaneta americana. *Journal of Ultrastructure Research*, 77(2):119–132, Nov. 1981. ISSN 00225320. doi: 10.1016/S0022-5320(81)80036-6.

R. K. Wong and K. G. Pearson. Properties of the trochanteral hair plate and its function in the control of walking in the cockroach. *The Journal of Experimental Biology*, 64(1):233–249, Feb. 1976. ISSN 0022-0949.

Appendix A

Supplementary data for Chapter 2

The experiment and simulation data relevant for this chapter is saved in the NCBS data servers.[1]

All the codes used to analyze the data have been uploaded onto Github. Here are a list of the repositories contain codes used in this chapter:

1. Autotracker used to track the antenna.[2]
2. Analysis of experiment data, fitting control theoretic models and simulating the network model.[3]
3. Statistical analysis.[4]
4. Scatter plots.[5]

---

[1] `smb://storage.ncbs.res.in/dinesh/Archived%20Projects/2019-Antenna-paper-1`

[2] `https://github.com/AbstractGeek/Score-Based-Autotracker`

[3] `https://github.com/AbstractGeek/publication-supplementaries`

[4] `https://github.com/AbstractGeek/non-parametric-tests-toolbox`

[5] `https://github.com/AbstractGeek/CategoricalScatterplot`

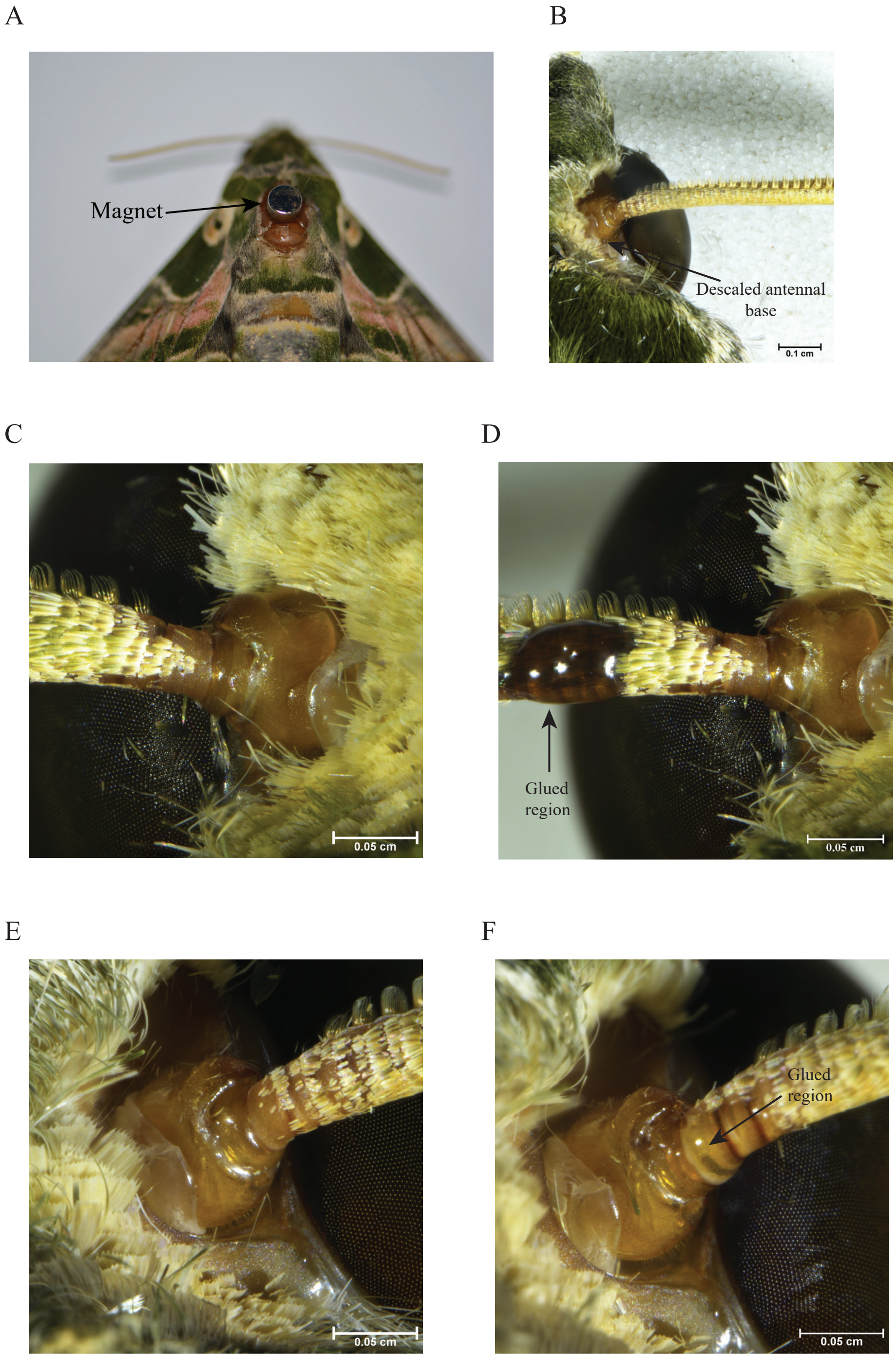

Fig. A.1 : Images of experiment manipulations

(A) *Magnetic tether.* Magnet was attached on the dorsal surface of the thorax. **(B)** *Descaled antenna base.* The antennae were carefully descaled ensuring that none of the antennal hair plates were damaged. **(C-D)** *Sham-treated moths.* **(C)** Before and **(D)** after the glue was applied to the third/fourth annulus. **(E-F)** *JO-restricted moths.* **(E)** Before and **(F)** after the pedicel-flagellar joint was glued.

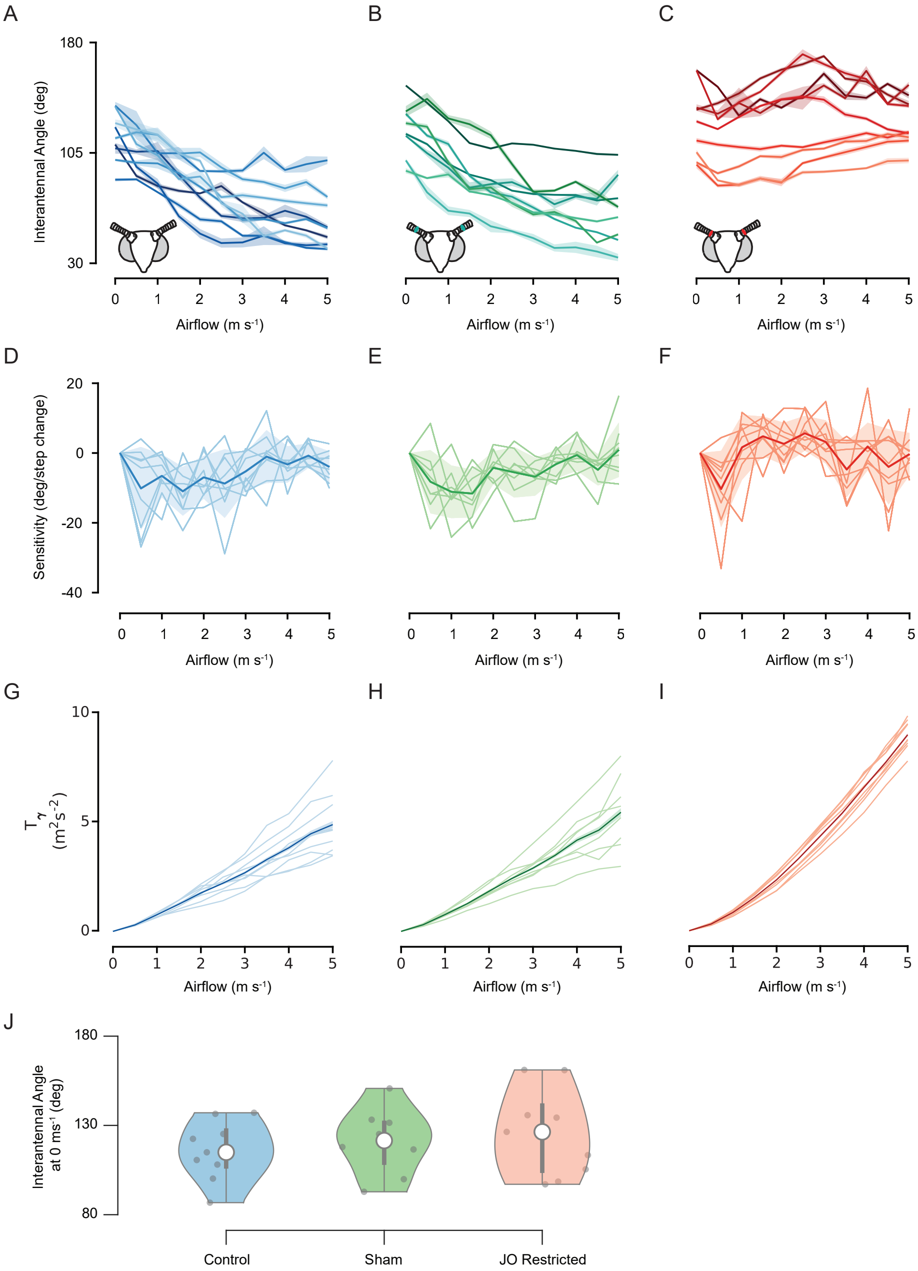

Fig. A.2 : Airflow-dependent antennal positioning

(A-C) Raw IAA without baseline shifting. **(D-F)** Sensitivity to airflow in control, sham-treated moths were correlated (ρ=0.70). JO-restricted moths were not correlated to control (ρ=-0.21), sham (ρ=-0.09) or airflow (ρ=0.04). **(G-I)** IAA changes in control, sham-treated moths reduced slope of T_γ for increases in airflow, in comparison to JO-restricted moths. However, T_γ increased for all treatments (Slopes from linear fits (adj R^2) for control: 45°, sham: 47°, JO-restricted: 62°. **(J)** IAA for no airflow (not statistically different; KW-test, p=0.78). Mean + standard deviation shown as dark line, overlay (individuals denoted by light lines).

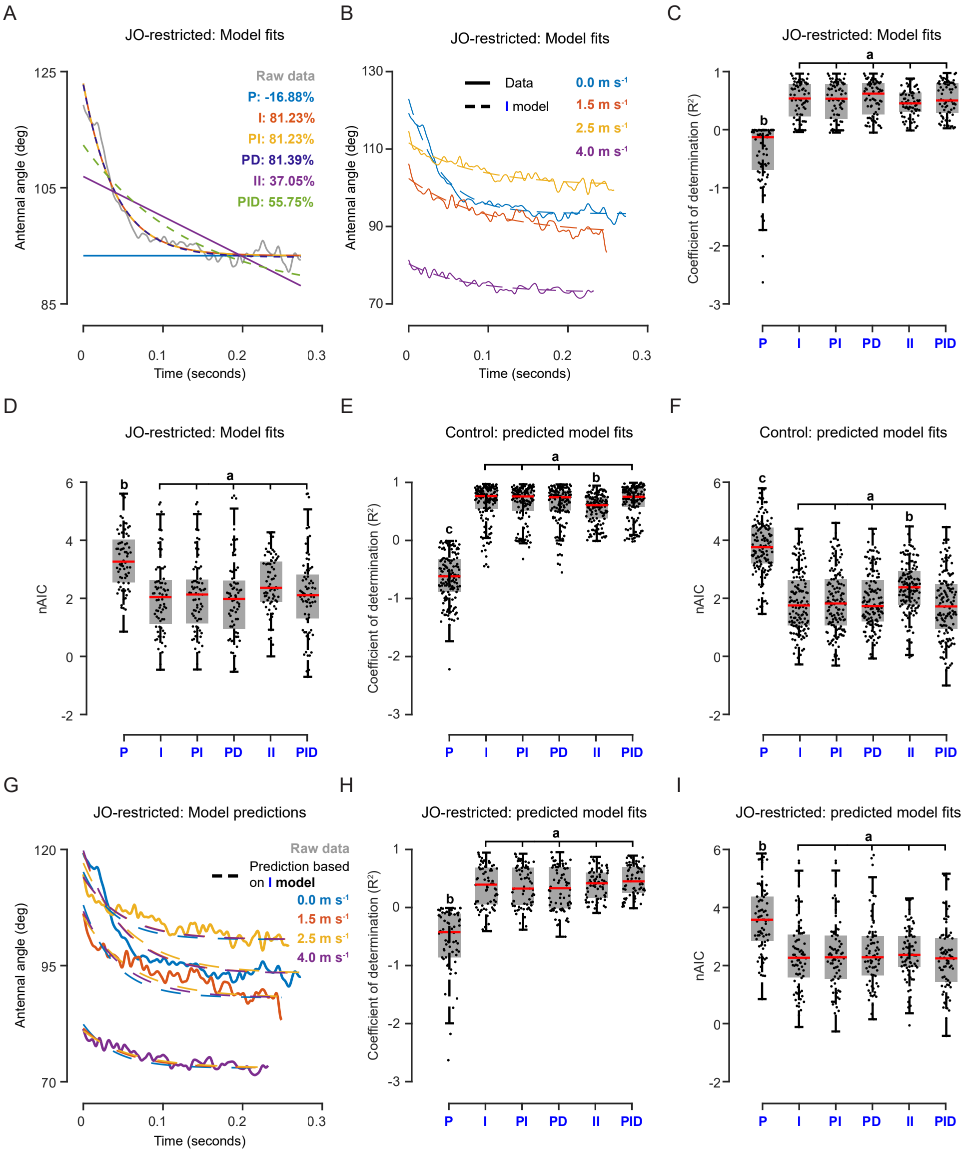

Fig. A.3 : Model fits and predictions of antennal response

(A-D) JO-restricted moth dataset. **(A)** All models, **(B)** Integral model fits for a representative dataset. **(C-D)** Goodness-of-fit (n=72 trajectories; median R^2 - P: -0.13, I: 0.54, PI: 0.53, PD: 0.62, II: 0.45, PID: 0.50; median nAIC - P: 3.26, I: 2.04, PI: 2.13, PD: 1.98, II: 2.36, PID: 2.11). **(E-F)** Goodness-of-fit for control moth predictions (n=133; median R^2 - P: -0.62, I: 0.76, PI: 0.76, PD: 0.74, II: 0.61, PID: 0.75; median nAIC - P: 3.76, I: 1.75, PI: 1.82, PD: 1.73, II:2.38, PID: 1.72). **(G)** Integral model predictions for a representative dataset. **(H-I)** Goodness-of-fit for predictions (n=72; median R^2 - P: -0.42, I: 0.39, PI: 0.33, PD: 0.33, II:0.42, PID: 0.45; median nAIC - P: 3.58, I: 2.27, PI: 2.28, PD: 2.29, II: 2.37, PID: 2.25). Kruskal Wallis, Nemenyi test (p<0.01) was used to test statistical significance (a, b, c represent statistically different groups).

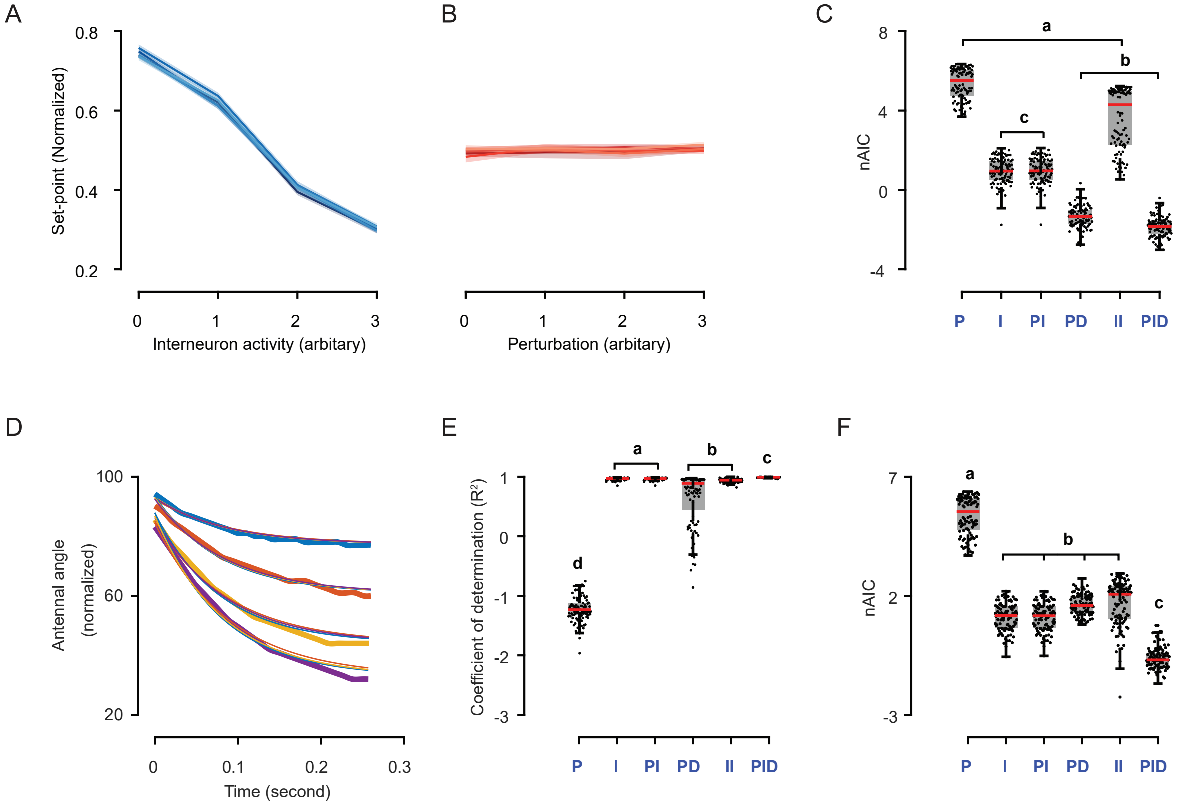

Fig. A.4 : Integral model predictions for neural circuit simulation

(A-B) Set-points of neural circuit simulation. Interneuron activity **(A)** modulated the set-point of the simulated neural circuit, which was **(B)** robustly kept constant regardless of the amplitude of perturbations. **(C)** Goodness-of-fit for model predictions for all the models (Kruskal Wallis, Nemenyi test, $p<0.01$; n=100 trajectories; median nAIC - P: 5.51, I: 0.95, PI: 0.96, PD: -1.34, II: 4.29, PID: -1.84). **(D-F)** Model predictions for neural circuit simulation. **(D)** Integral model predictions for a representative dataset from the simulated neural circuit. **(E-F)** Goodness-of-fit for model predictions for all the models (Kruskal Wallis, Nemenyi test, $p<0.01$; n=100 trajectories; median R^2 – P: -1.23, I: 0.97, PI: 0.97, PD: 0.94, II: 0.94, PID: 1.00; median nAIC - P: 5.50, I: 1.16, PI: 1.16, PD: 1.71, II: 2.05, PID: -0.81)

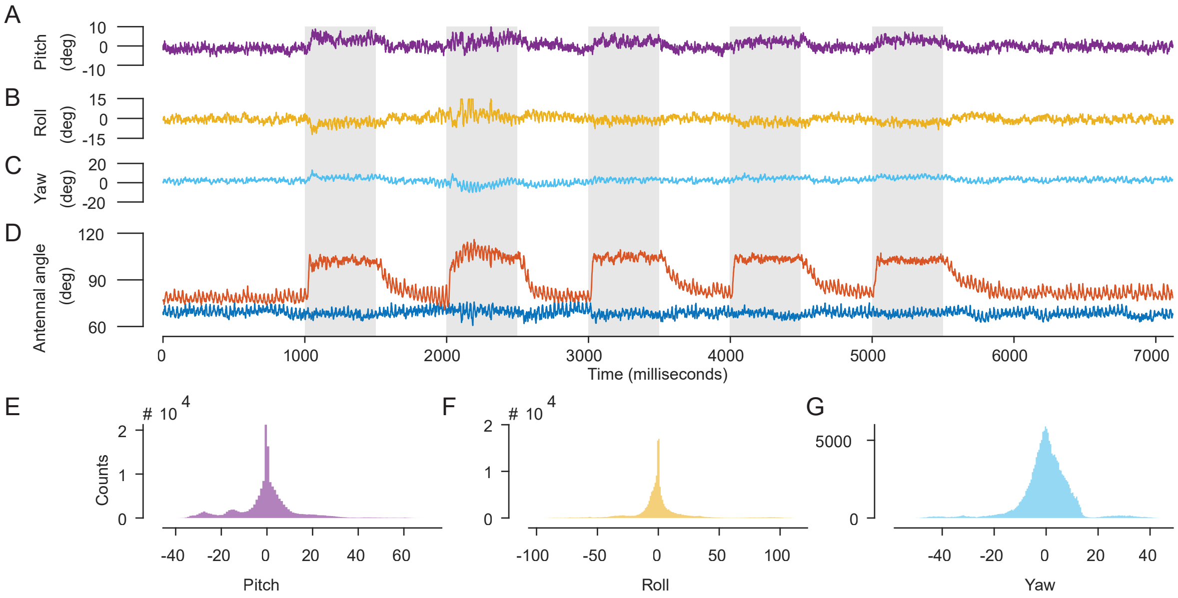

Fig. A.5 : Head rotations during electromagnet perturbations.

(A) Pitch, **(B)** Roll and **(C)** Yaw of the head. Grey boxes indicate electromagnet "on". The moth rotated its head slightly in response to left antenna perturbation, but because of the head-centric-system, **(D)** the right antennal angle (internal control, blue) did not change. The left antennal angle (red) changed as expected. Distributions of **(E)** Pitch, **(F)** Roll and **(G)** Yaw in all experiments.

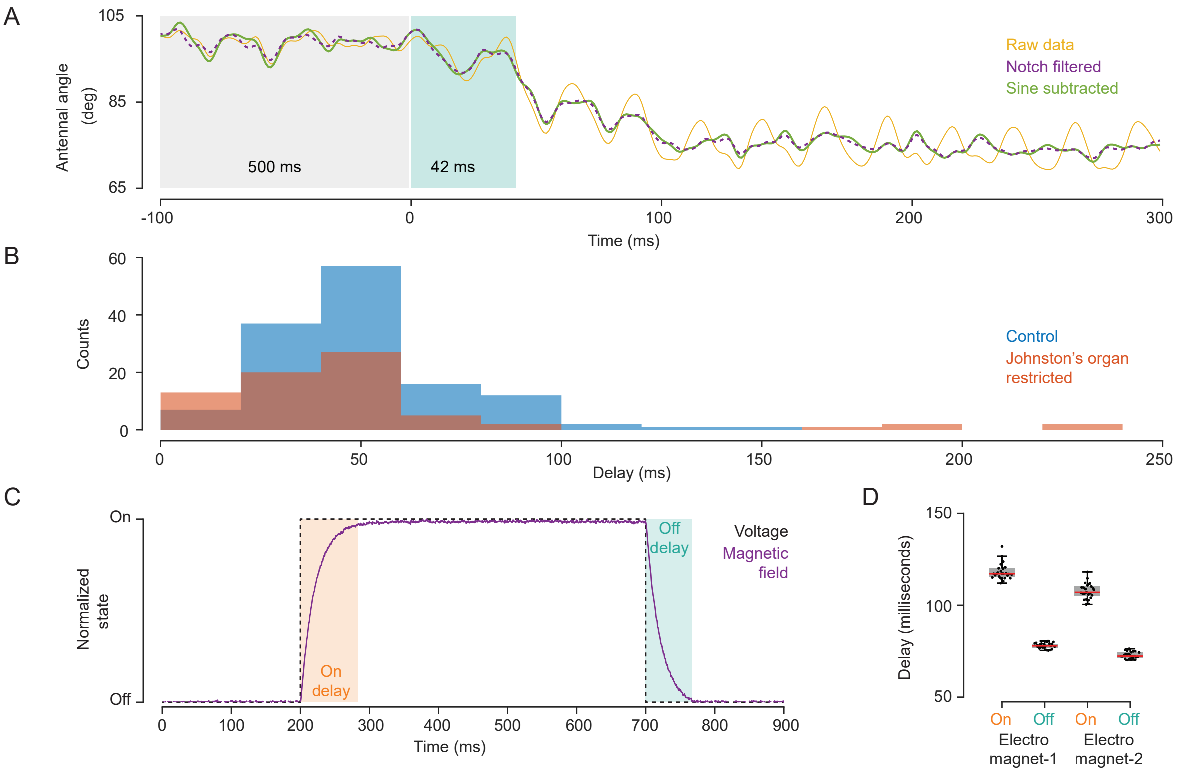

Fig. A.6 : Estimating electromagnet release delays

(A-B) Filtering of raw antennal angle and estimating release point. **(A)** Raw antennal angle (yellow) was filtered by estimating and subtracting wing beat frequencies [green, see methods, akin to using a notch filter (dotted purple line)]. Release point was estimated as point where the antenna crossed 25% of the difference between perturbed and final settled angles (set-point). Delay depended on many factors: distance of electromagnet, differences in antennal inertia, etc. and was **(B)** centered around 50 ms for both control and JO-restricted moths. **(C-D)** Characterization of the electromagnet. On-off delay was characterized by measuring the magnetic fields using a Hall effect sensor (DRV5053). The electromagnet was placed 2 cm from the sensor, roughly the same distance as for the antenna. **(C)** Normalized voltage inputs to the electromagnet (black) and measured voltage output from Hall effect sensor (purple). On- (red overlay) and off-delay (blue overlay) were computed as time taken for magnetic fields to stabilize to 99% CI of the mean on and off voltages, respectively. **(D)** Box plot of on- and off-delays of both electromagnets used (median: E1- 117.1 ms on, 77.0 ms off; E2- 107 ms on, 72.3 ms off; overall median: 113.3 ms on, 76.1 ms off).

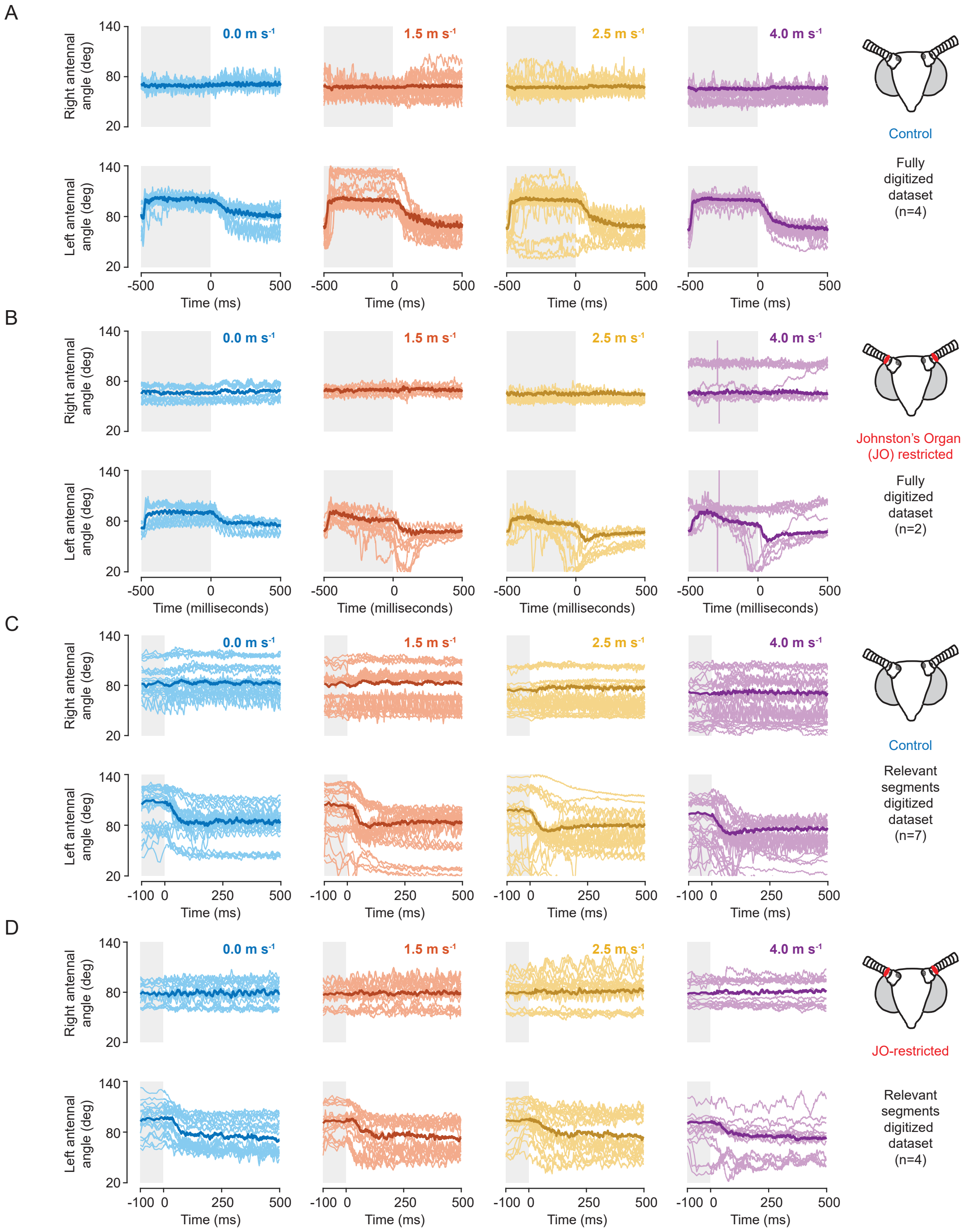

Fig. A.7 : Raw data traces of antennal response to perturbation

(A-B) Fully digitized data of control (n=4) and JO-restricted (n=2) moth trials. Color indicates airflow (light traces -individuals; dark - average response). Note that right antennal angle is typically constant and unaffected by left antennal perturbations. **(C-D)** Remaining data set [Control(n=7), JO-restricted(n=4)]. Only frames 100 ms before and 500 ms after perturbation was digitized as it was sufficient to characterize the response (see Methods).

Appendix B

Supplementary data for Chapter 3

B.1 Calibration of stimulus setup

B.1.1 Hall effect sensor calibration

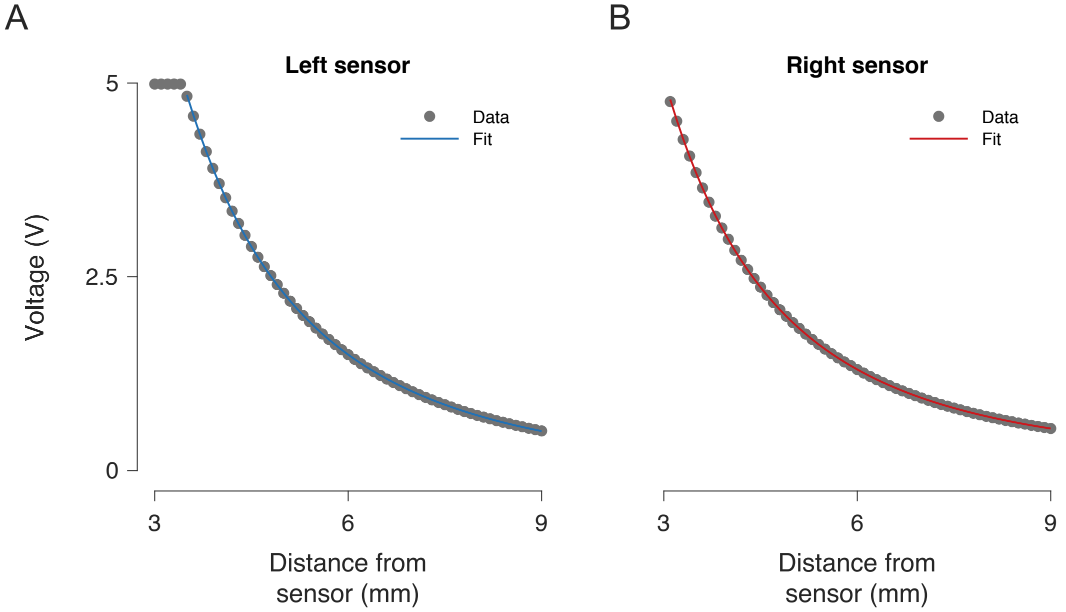

Fig. B.1 : Hall effect sensor calibration

Sensor-magnet pairs were calibrated by moving the magnet at steps of 0.1 mm away from the sensor. Average voltage output for individual distances for **(A) left** and **(B) right** sensor is shown as filled circles. Equation [B.1] was fit to the data for both the sensors; the fit output is shown are blue and red line respectively. Using the fitted constants, Equation [B.2] was used to calculate distance between the magnet and sensor from output voltage.

Hall effect sensors were used to measure the movement of the antenna during the presentation of a stimulus. A neodymium magnet attached to the end capillary generated changes in the magnetic field that were measured by the Hall effect sensor. The magnetic field at the Hall effect sensor, due to the neodymium magnet, is proportional to the inverse cubed distance between them (equation [B.1]). This can be used to back calculate the distance when the voltage at the sensor is known (equation [B.2]). However, due to differences in both the sensors and the magnets, the constants in the equation can vary. Therefore, we calibrated every sensor-magnet pair before using them to back calculate distance from voltage.

$$V = a + \frac{b}{(x+c)^3}, \qquad \text{[B.1]}$$

where,

$$\begin{aligned} V &= \text{Voltage output of the Hall effect sensor,} \\ x &= \text{distance of the magnet from the sensor,} \\ a, b, c &= \text{free parameters (fit to the calibration data)} \end{aligned}$$

For every sensor-magnet pair, we moved the magnet away from the sensor at steps of 0.1 mm using a micromanipulator (Figure B.1) (Narishige). At every step, the voltage output of the Hall effect sensor was acquired for one second using the DAQ. The free parameters in equation [B.1] were fit to the average voltage at every distance step using the curve fitting toolbox in MATLAB. The fitted equations for all the sensor-magnet pairs had adjusted $R^2 > 0.99$ (Figure B.1). Using the fitted parameters and equation [B.2] the distance of the capillary from the Hall effect sensor was computed from the voltage output of the sensor. Changes in distance when the stimulus was presented was later computed from this.

$$X = \sqrt[3]{\frac{b}{V-a}} - c, \qquad \text{[B.2]}$$

where,

$$\begin{aligned} x &= \text{distance of the magnet from the sensor,} \\ V &= \text{Voltage output of the Hall effect sensor,} \\ a, b, c &= \text{parameters fitted to calibration data} \end{aligned}$$

B.1.2 Stimulus calibration

The sub-woofer based stimulus setup described above did not provide linear movement along all frequency and amplitude ranges. Both sub-woofers had a resonance close to 35 Hz and a fall off after 50 Hz (Bode plot, Figure B.2). Each of the provided stimuli were therefore calibrated to ensure that the desired output was achieved. All the calibration was done in MATLAB using custom written codes.

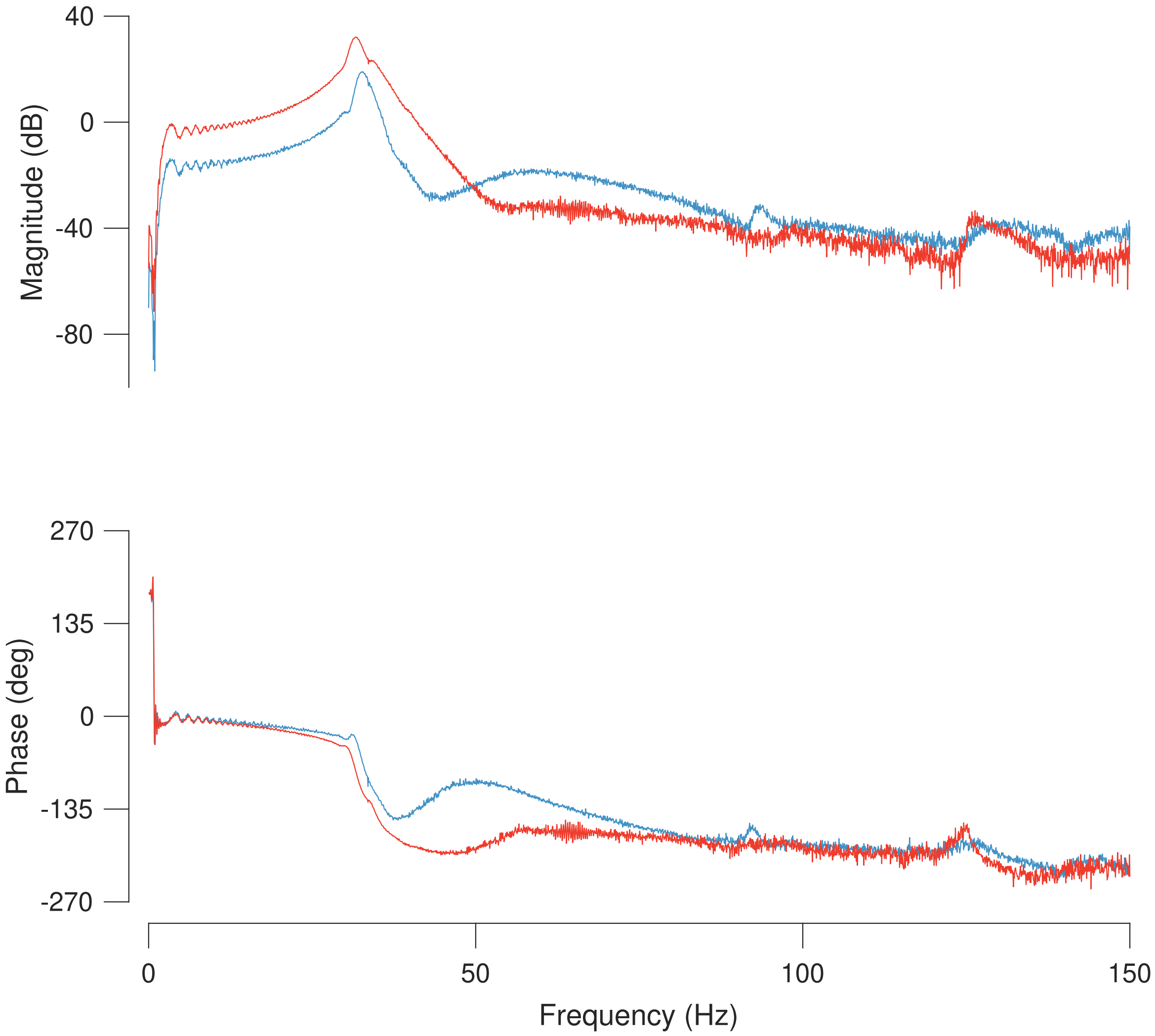

Fig. B.2 : Frequency response of stimulus speakers

Bode plot illustrating the frequency response of **left** and **right** speakers. (A) and (B) show the gain (magnitude) and the phase of the output w.r.t to the input frequency. Both speakers show a resonance peak close to 35 Hz, after which the gain drops.

Step stimulus

The sub-woofer based stimulus setup did not provide linear displacement output for input voltage (Figure B.3A,B). To provide steps of varying amplitude, we had to calibrate the input voltage - output displacement relationship. To do this, we first ran a train of steps with varying input amplitude on both the speakers. The output displacement was speaker specific and were different for the left and the right speaker.(Figure B.3E,F). However, the input-output relationship for both speakers followed a power law (equation [B.3]). The free parameters in the equation were therefore fit for both speakers separately (Figure B.3E,F). Using this fit, the input voltage was computed from the desired output displacement. The displacement outputs of the calibrated speakers were very close to the desired outputs (Figure B.3C,D).

$$V = ax^b + c; \qquad \text{[B.3]}$$

where,

$x =$ desired output displacement in mm,

$V =$ Input voltage to obtain the desired output,

$a, b, c =$ parameters fitted to input-output characteristics of the speaker

Chirp stimulus

To calibrate the chirp, we first computed the frequency dependent gain for each speaker (bode plot, Figure B.2). This was done using a chirp with peak-to-peak amplitude of 0.4 V Figure B.4A,B). The inverse of this gain was used to find the amplitude for every frequency in the chirp. However, due to the non-linearity of the speaker, we were unable to generate a constant displacement output at the very first pass of calibration. Instead, we started from a constant amplitude input and ran multiple calibration passes (generally five). At each pass, we successively multiplied the input with the inverse of the output amplitude obtained at every frequency. This iterative multiplication molded the input to produce the desired output chirp (Figure B.4C). The final speaker input was a multiplication of the constant amplitude input with the inverse amplitudes from all steps (Figure B.4C,D). This gave rise to the desired peak to peak amplitude of 0.1 mm (Figure B.4E,F).

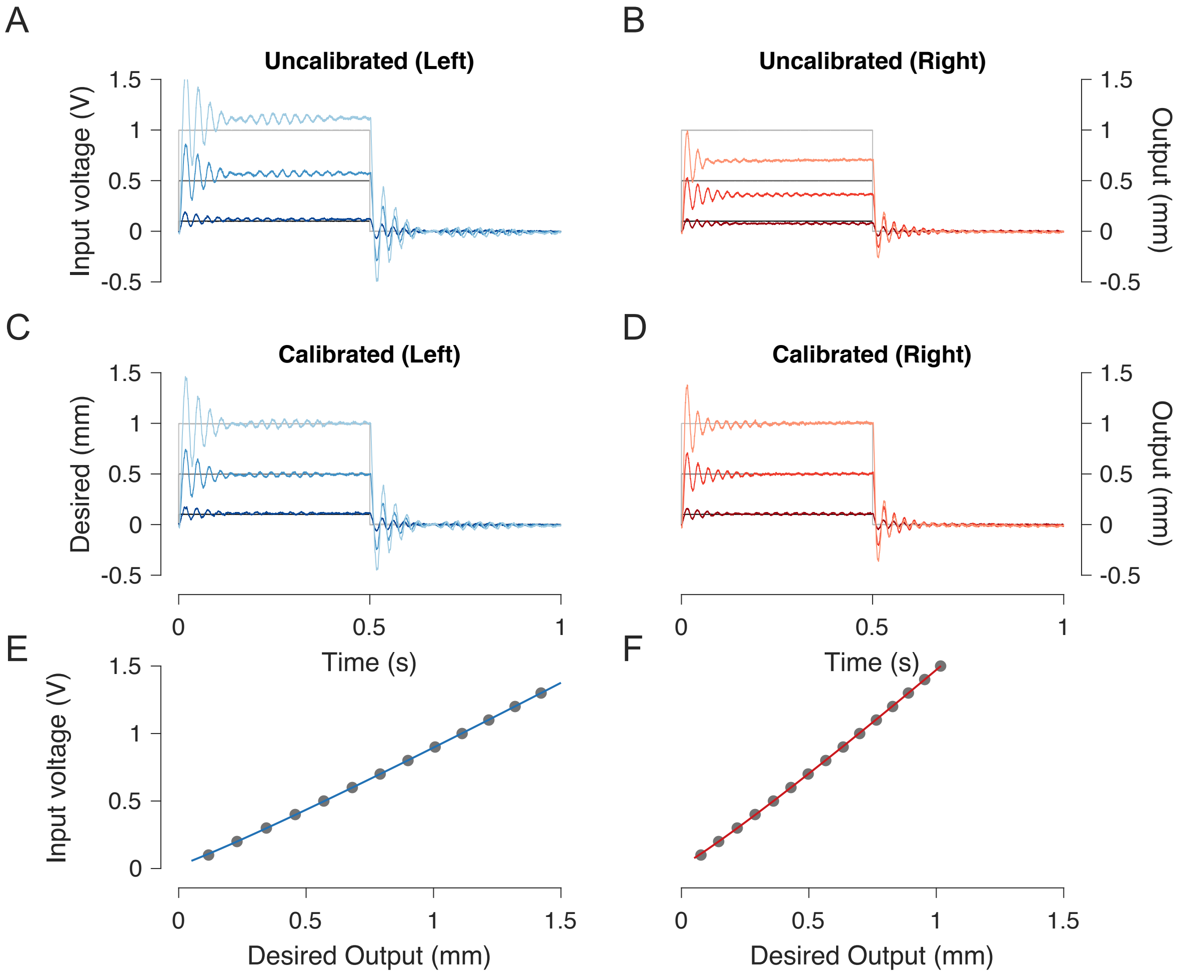

Fig. B.3 : Step stimulus calibration

Output displacement for provided input voltage was not linear for **(A) left** and **(B) right** speakers. To ensure that desired output was provided, we calibrated both the speakers **(C)**, **(D)** respectively. Using a train of different voltage amplitudes, we obtained the input-output relationship of the speaker (grey filled circles in **(E)**, **(F)**). Calibration was performed for each speaker by fitting a power law (Equation [B.3]) for this data (colored lines, **(E)**, **(F)**). The input voltage for a desired amplitude was obtained from this fit.

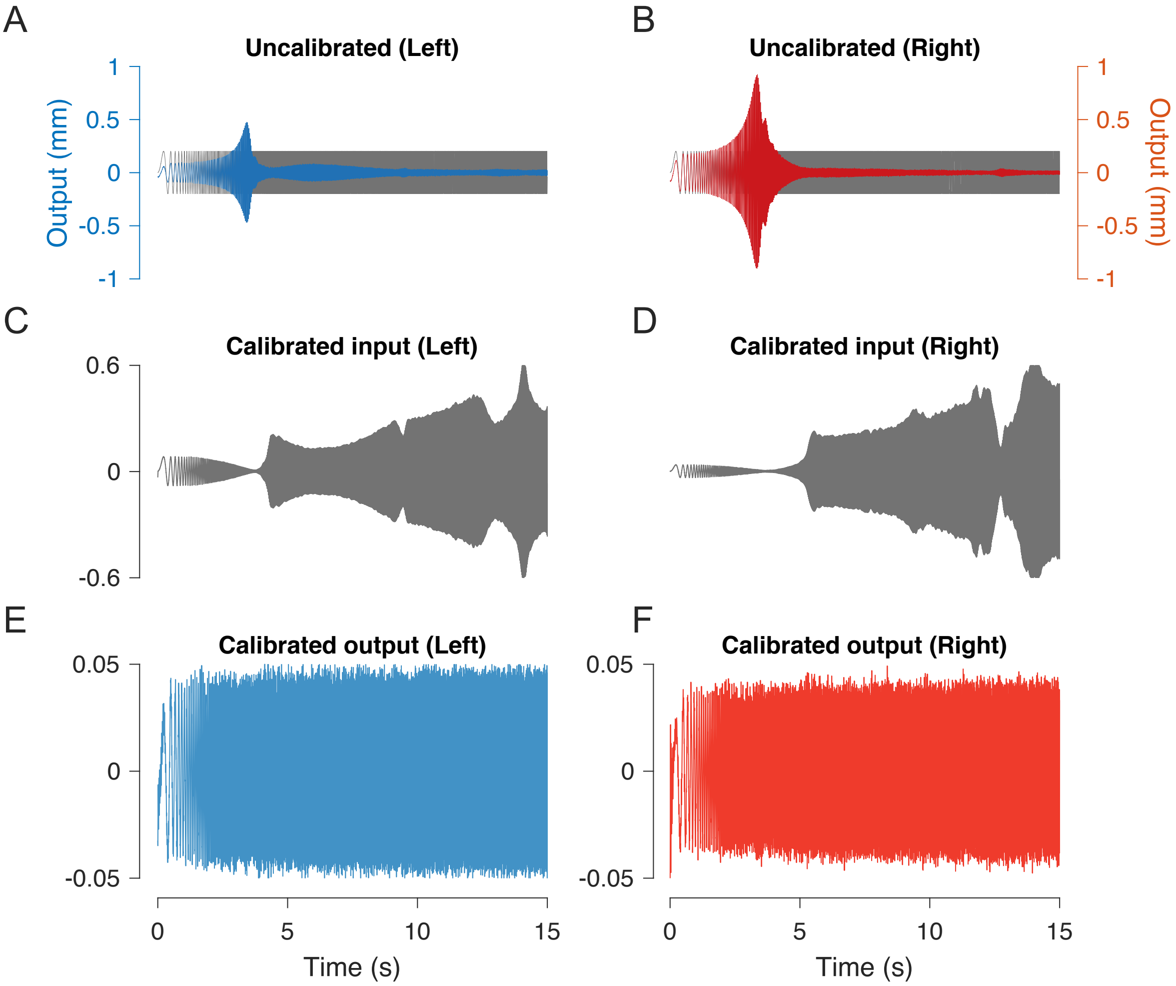

Fig. B.4 : Chirp stimulus calibration

Output displacement of **(A) left** and **(B) right** for a constant input amplitude (peak-to-peak) of 0.4 V. (C), (D) Inverse input computed from multiple calibration passes. This generated a desired peak to peak output displacement of approx. 0.1 mm in both the **(E) left** and **(F) right** speaker.

B.2 Supplementary data

The behavior and EMG experiment data relevant for this chapter is saved in the NCBS data servers (behavior data[1]; EMG data[2]).

All the codes used to analyze the data have been uploaded onto Github. Here are a list of the repositories contain codes used in this chapter:

1. GUI for data acquisition from NI DAQ.[3]
2. Analysis of behavior data, stimulus delivery for EMG experiments and analysis of EMG data.[4]
3. Statistical analysis.[5]
4. Scatter plots.[6]

---

[1] `smb://storage.ncbs.res.in/dinesh/Archived%20Projects/2019-Antenna-paper-1`

[2] `smb://storage.ncbs.res.in/dinesh/Archived%20Projects/2019-Antenna-paper-2`

[3] `https://github.com/AbstractGeek/ni-daq-acquisition-matlab`

[4] `https://github.com/AbstractGeek/publication-supplementaries`

[5] `https://github.com/AbstractGeek/non-parametric-tests-toolbox`

[6] `https://github.com/AbstractGeek/CategoricalScatterplot`

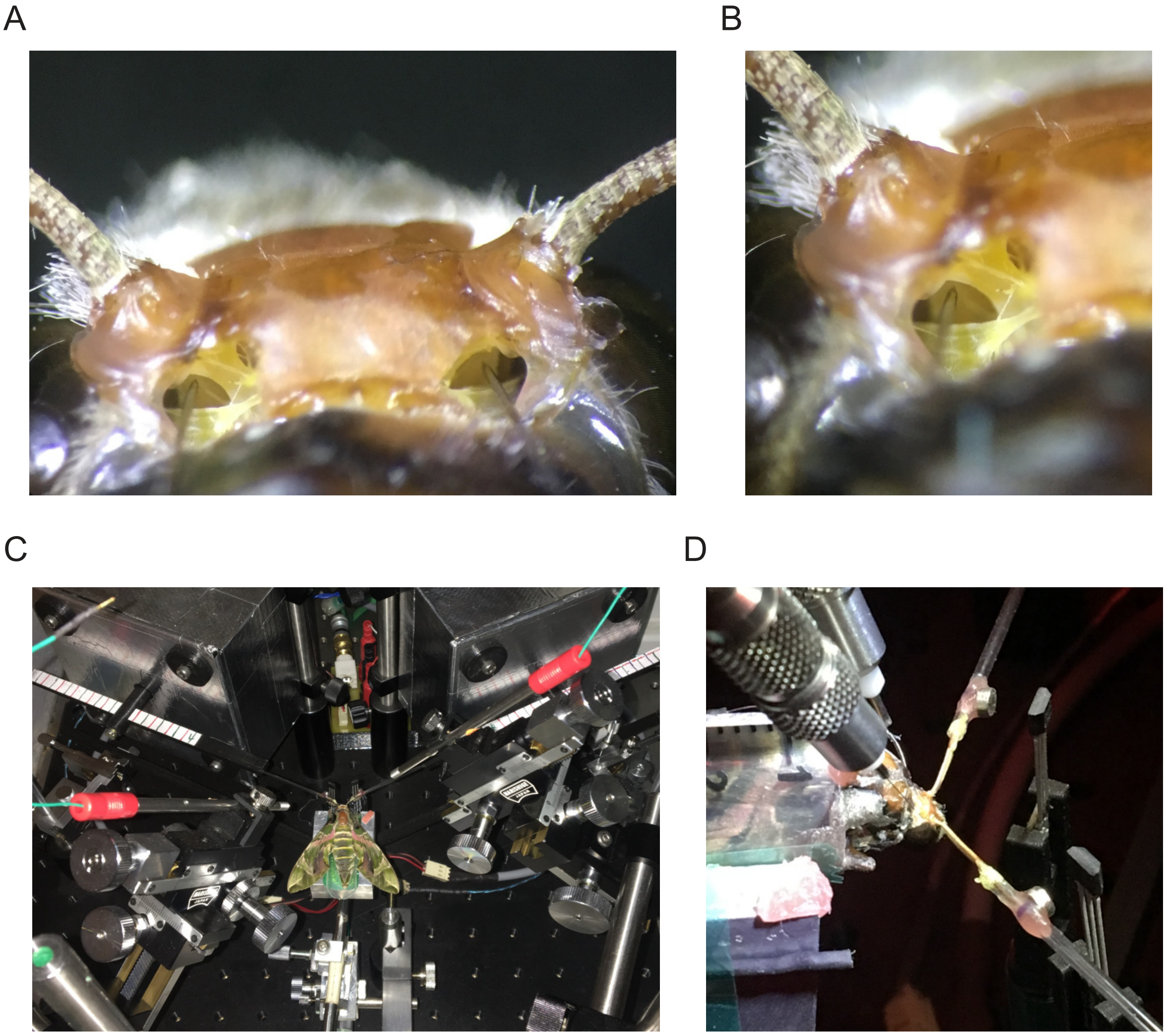

Fig. B.5 : Images of experiment setup

(A) Windows cut behind the antenna to access the antennal anterior levator muscles (ALM). **(B)** The region where the window is cut has very few hemolymph vessels and proboscis muscles, making it a simple and less invasive procedure. **(C)** Complete setup to deliver antennal vibrations using subwoofers and record activity of the muscles. **D** Closeup view of the moth, with its antennae stimulated by the capillaries and tungsten electrodes recording from both the antennal anterior levator muscles. The neodymium magnets on the capillary allow the antennal stimulation to be captured by the Hall effect sensor in front of it.

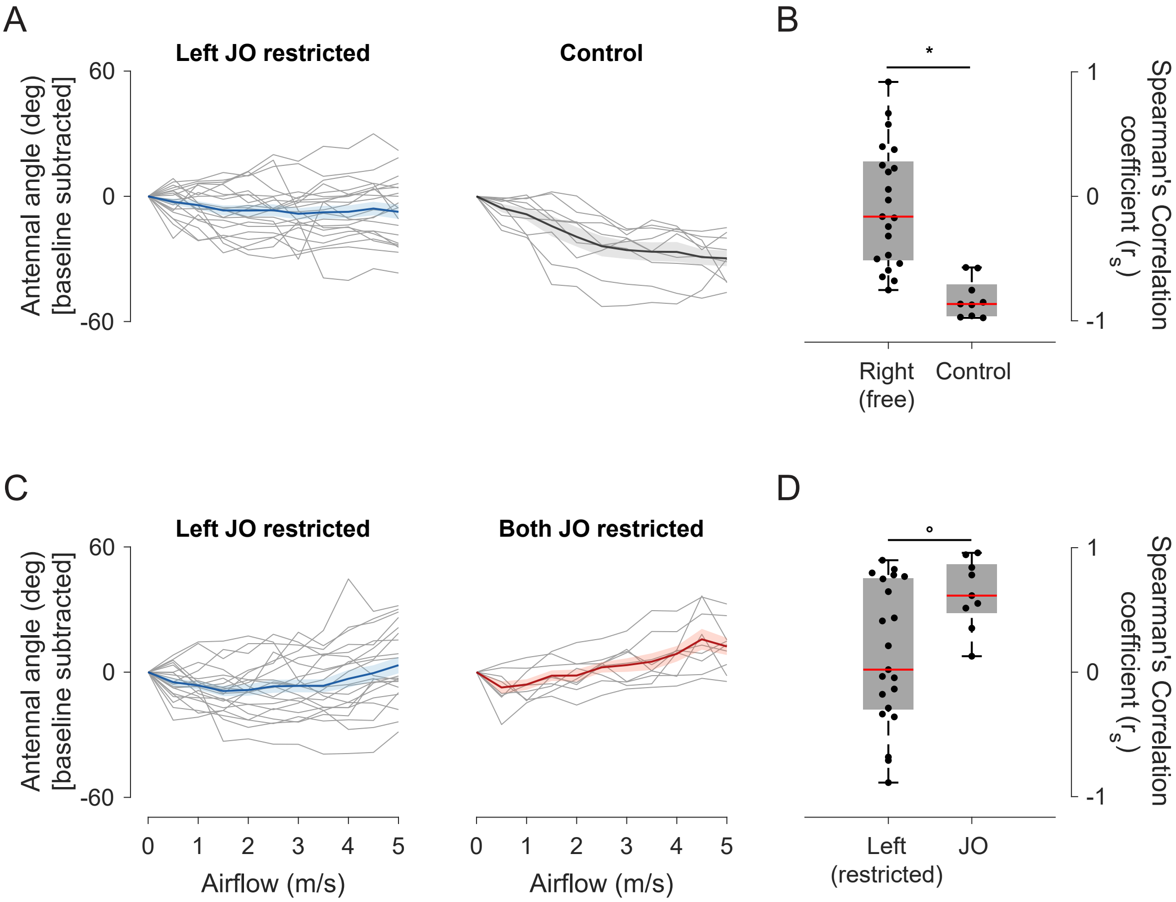

Fig. B.6 : Effect of left JO-restriction

(A) Change in antennal angle of the free (right) antenna in left JO-restricted moths (Individuals: grey, mean: blue, s.e.m: light blue). **(B)** Change in right antennal angle in control moths (Individuals: grey, mean: black, s.e.m: grey overlay). **(C)** Box-and-whisker plots of Spearman's correlation coefficients of right antennal angles in left JO-restriction and control treatments. **(D)** Change in restricted (left) angle in left JO-restricted moths (Individuals: grey, mean: blue, s.e.m: light blue). **(E)** Change in left antennal angle in bilateral JO-restricted moths (Individuals: grey, mean: red, s.e.m: light red). **(F)** Box-and-whisker plots of Spearman's correlation coefficients of left antennal antenna in left JO and both JO-restricted treatments. Statistically different groups are shown by an asterisk and an open circle (Mann-Whitney ranksum test; $p < 0.01$, $p < 0.05$ respectively).

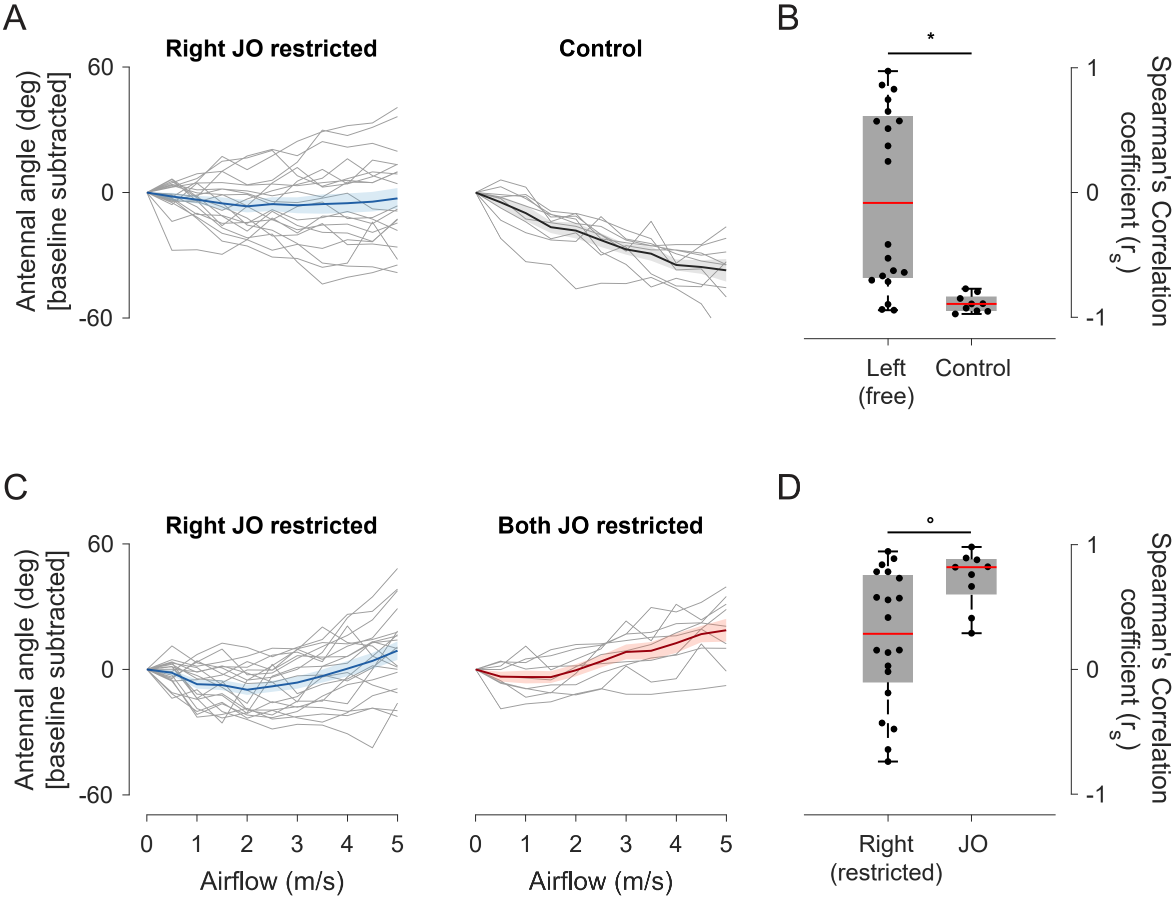

Fig. B.7 : Effect of right JO-restriction

(A) Change in antennal angle of the free (left) antenna in right JO-restricted moths (Individuals: grey, mean: blue, s.e.m: light blue). **(B)** Change in left antennal angle in control moths (Individuals: grey, mean: black, s.e.m: grey overlay). **(C)** Box-and-whisker plots of Spearman's correlation coefficients of left antennal angles in right JO-restriction and control treatments. **(D)** Change in restricted (right) angle in right JO-restricted moths (Individuals: grey, mean: blue, s.e.m: light blue). **(E)** Change in right antennal angle in bilateral JO-restricted moths (Individuals: grey, mean: red, s.e.m: light red). **(F)** Box-and-whisker plots of Spearman's correlation coefficients of right antennal antenna in right JO and both JO-restricted treatments. Statistically different groups are shown by an asterisk and an open circle (Mann-Whitney ranksum test; $p < 0.01$, $p < 0.05$ respectively).

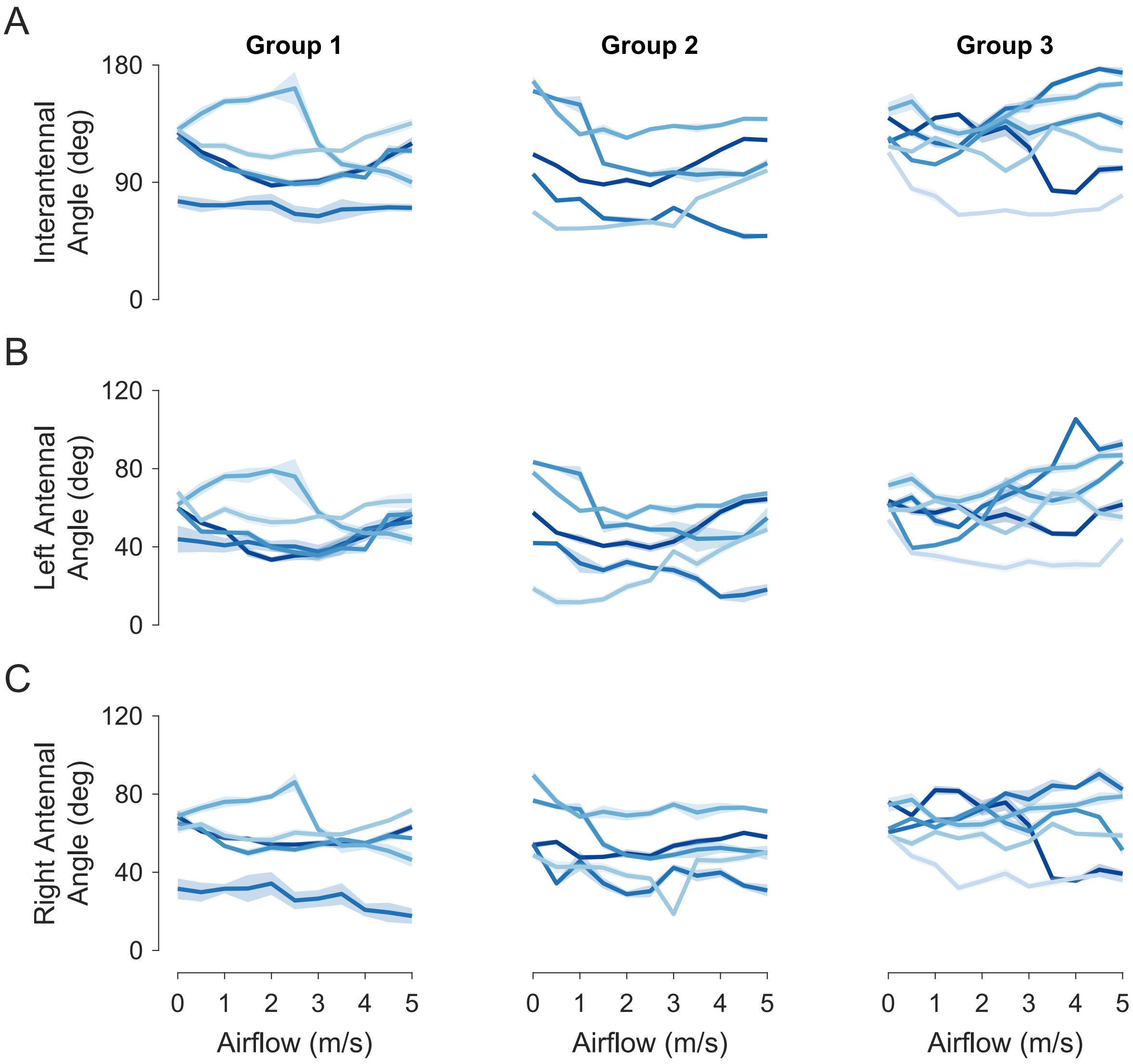

Fig. B.8 : Antennal angles of left JO-restricted moths

(A) left, (B) right and (C) inter-antennal angle for left JO-restricted moths. The dark blue line represents the mean, with the light blue overlay representing the standard error margin. Different shades represent different individuals. 16 out of 21 moths of the left JO-restriction treatments are shown here (rest in Figure 3.6). The moths are split into three groups for better visibility of individuals

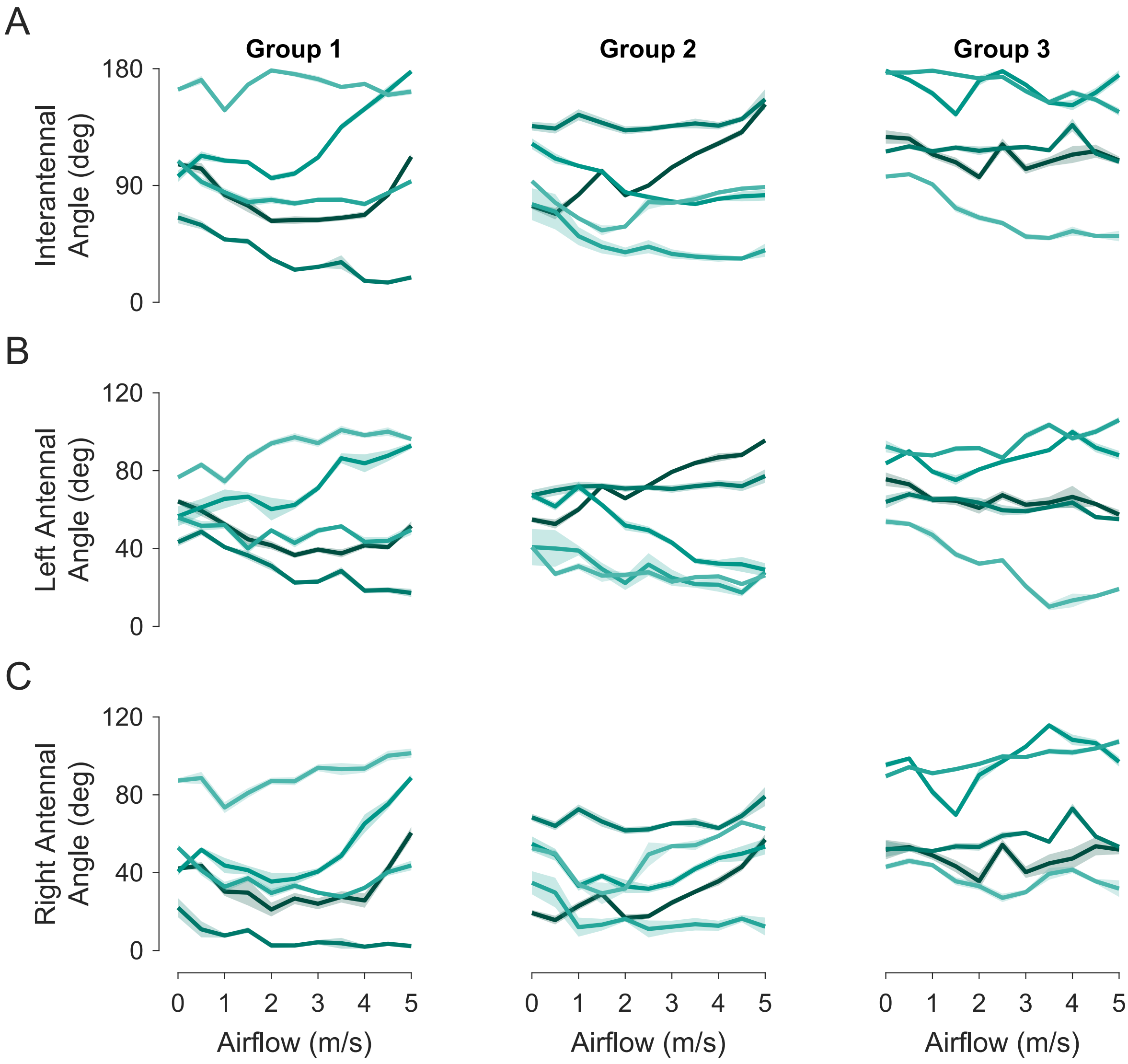

Fig. B.9 : Antennal angles of right JO-restricted moths

(A) left, (B) right and (C) inter-antennal angle for right JO-restricted moths. The dark green line represents the mean, with the light green overlay representing the standard error margin. Different shades represent different individuals. 15 out of 20 moths of the right JO-restriction treatments are shown here (rest in Figure 3.6). The moths are split into three groups for better visibility of individuals

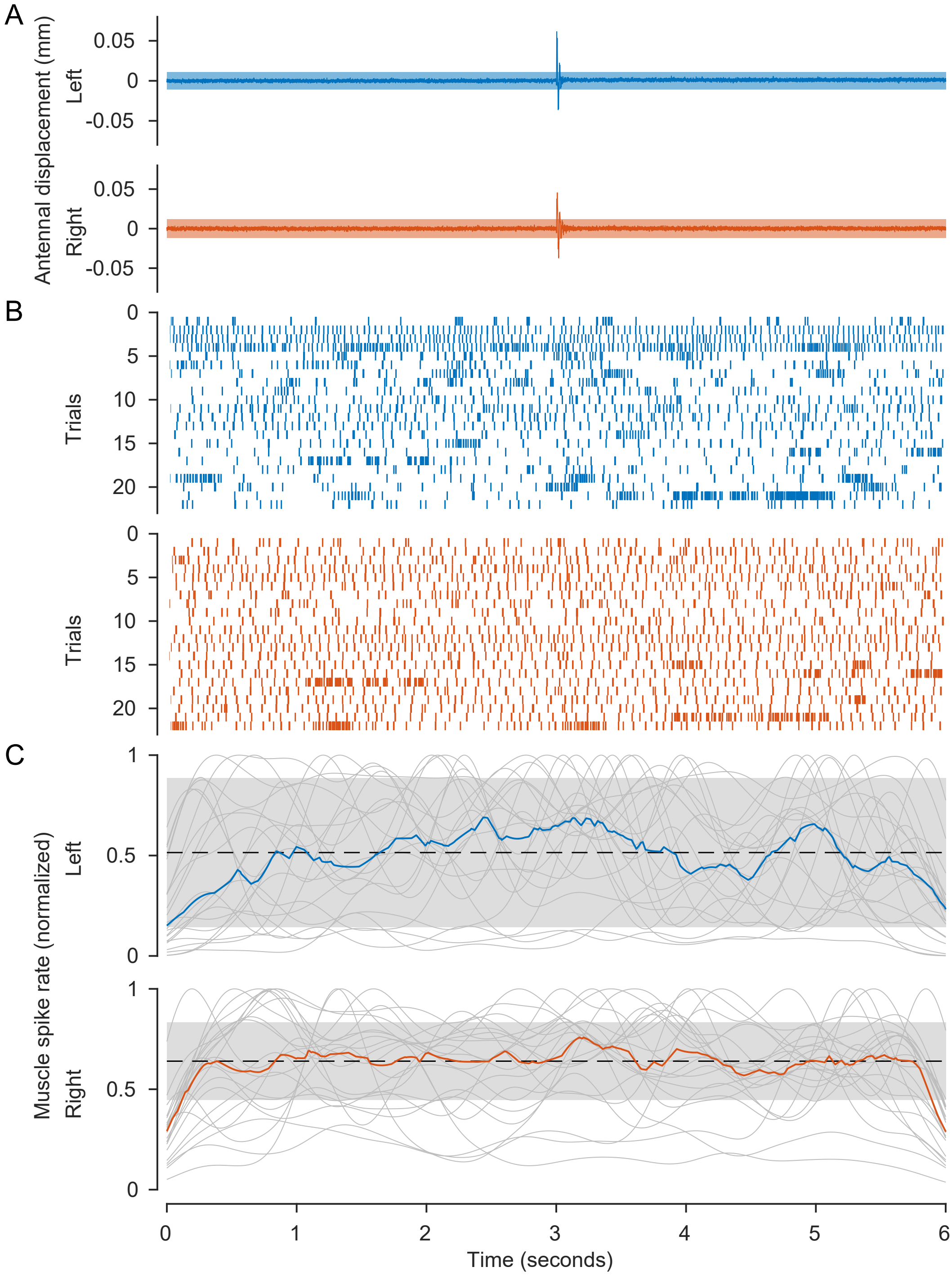

Fig. B.10 : Representative response to a bilateral impulse stimulus

(A) Displacement of left, right antenna respectively. **(B)** Spike raster for left (blue), right (red) muscles. **(C)** Muscle activity does not change in response to the impulse stimulus. Color correspond to the same entities as in Figure 3.8.

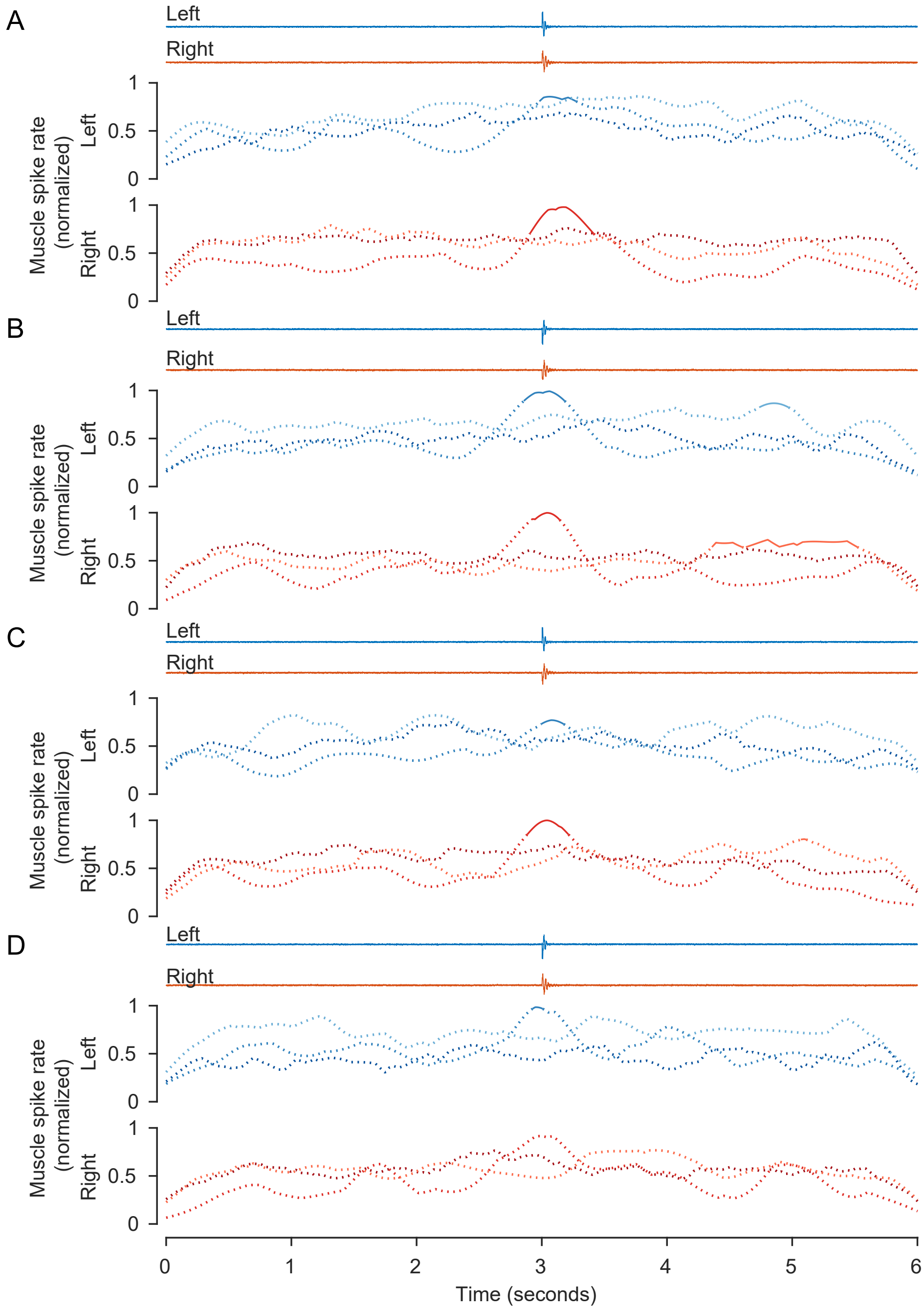

Fig. B.11 : Muscle activity in response to bilateral impulse stimuli

Four types of impulse stimuli given (shown at the top of each panel) - **(A)** bilateral forward, **(B)** bilateral backward, **(C)** clockwise (left forward, right backward) and **(D)** anticlockwise (right forward, left backward). Muscle activity does not consistently change in response to these stimuli (n=3 individuals). Color correspond to the same entities as in Figure 3.9.

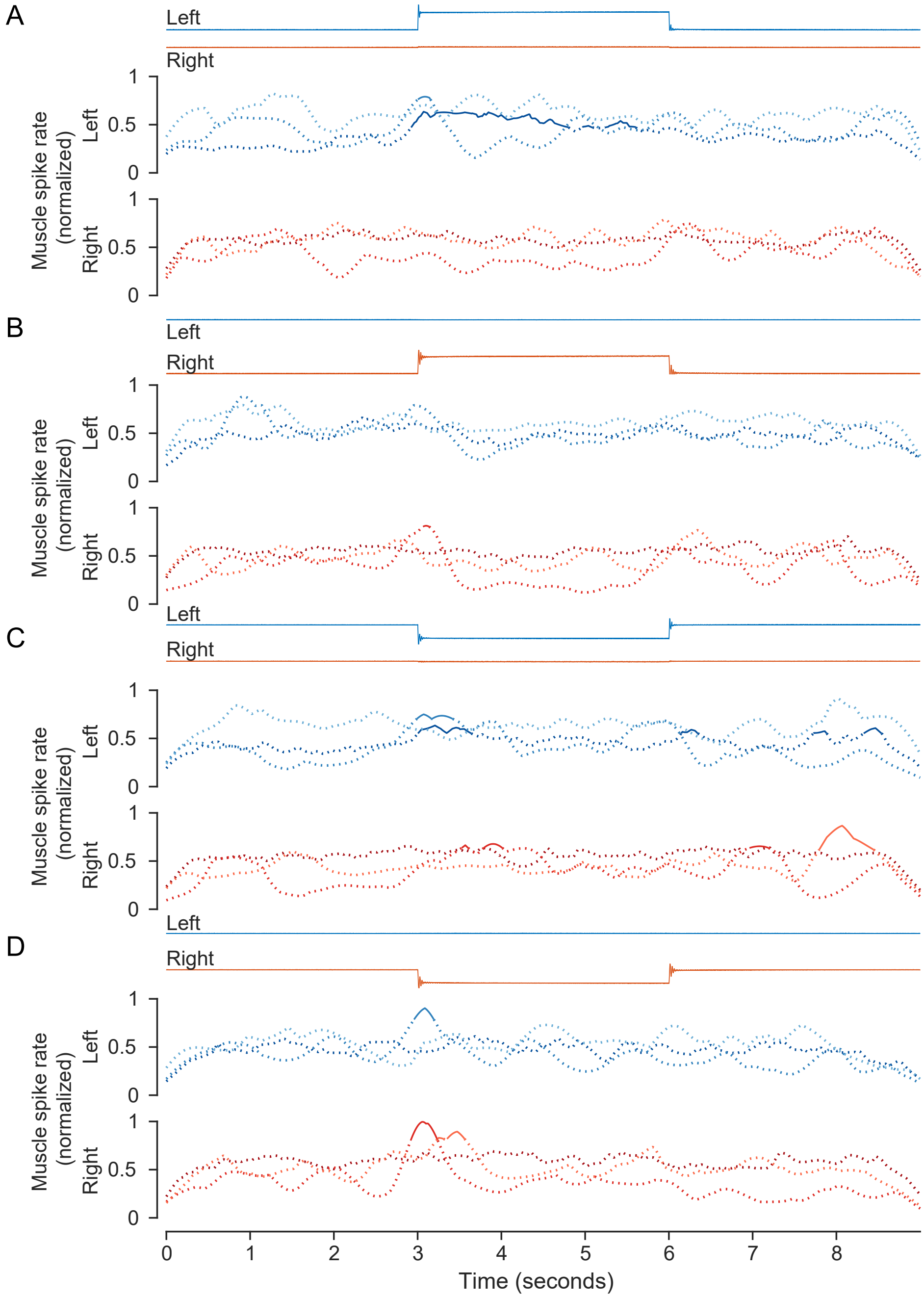

Fig. B.12 : Muscle activity in response to unilateral step stimuli

Four unilateral step stimuli were given (shown at the top of each panel) - **(A)** left forward, **(B)** right forward, **(C)** left backward and **(D)** right backward. Muscle activity does not strongly change in response to these stimuli. Color correspond to the same entities as in Figure 3.9.

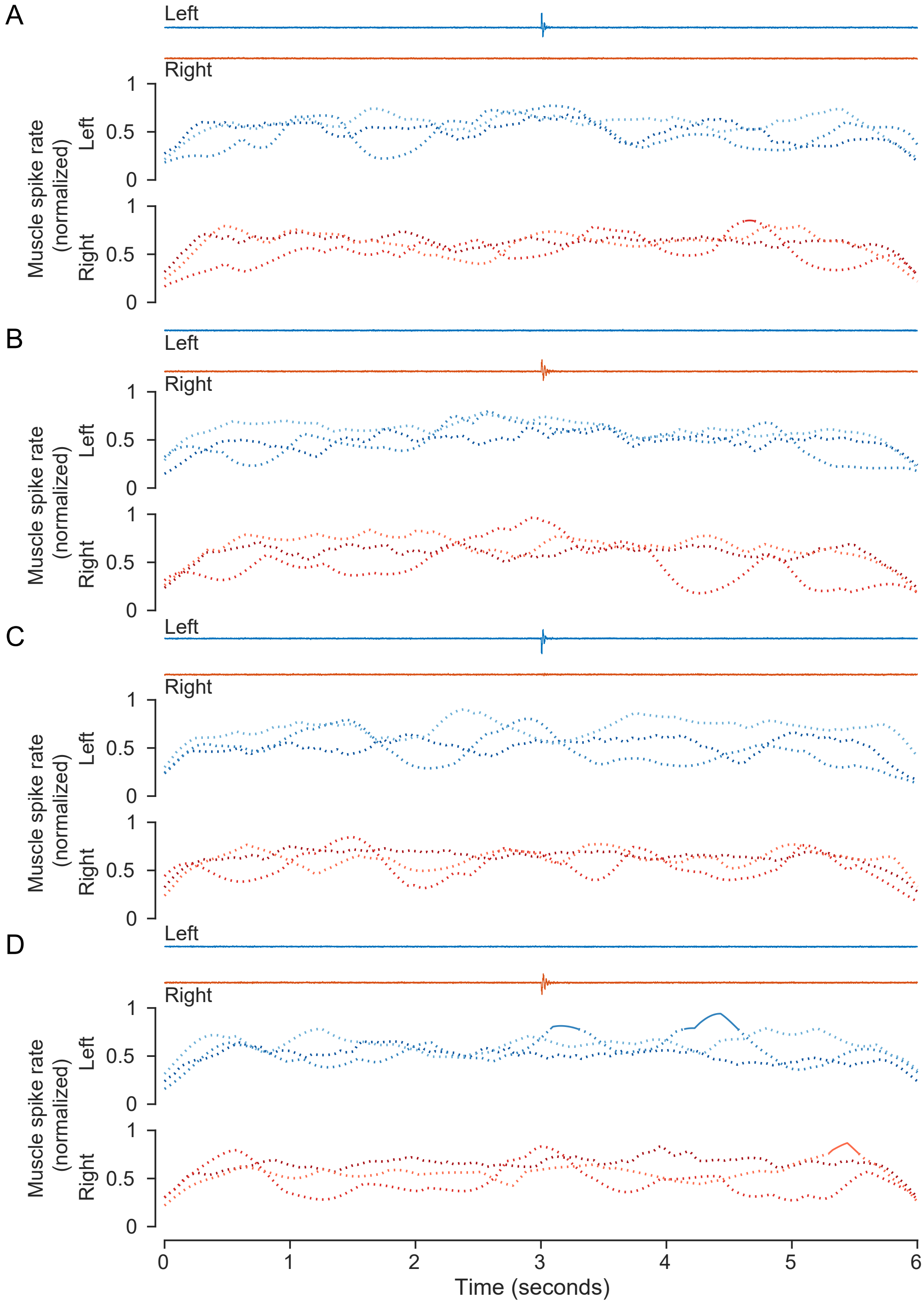

Fig. B.13 : Muscle activity in response to unilateral impulse stimuli

Four unilateral impulse stimuli were given (shown at the top of each panel) - **(A)** left forward, **(B)** right forward, **(C)** left backward and **(D)** right backward). Muscle activity does not change in response to these stimuli. Color correspond to the same entities as in Figure 3.9.

Appendix C

Supplementary data for Chapter 4

The simulation data relevant for this chapter is saved in the NCBS data servers.[1]

All the codes used to the simulations can be downloaded from my Github respository (Hair-Plate-Sensitivity[2]).

---

[1] `smb://storage.ncbs.res.in/dinesh/Archived%20Projects/2019-Hair-plate-sensitivity`

[2] `(https://github.com/AbstractGeek/Hair-Plate-Sensitivity`

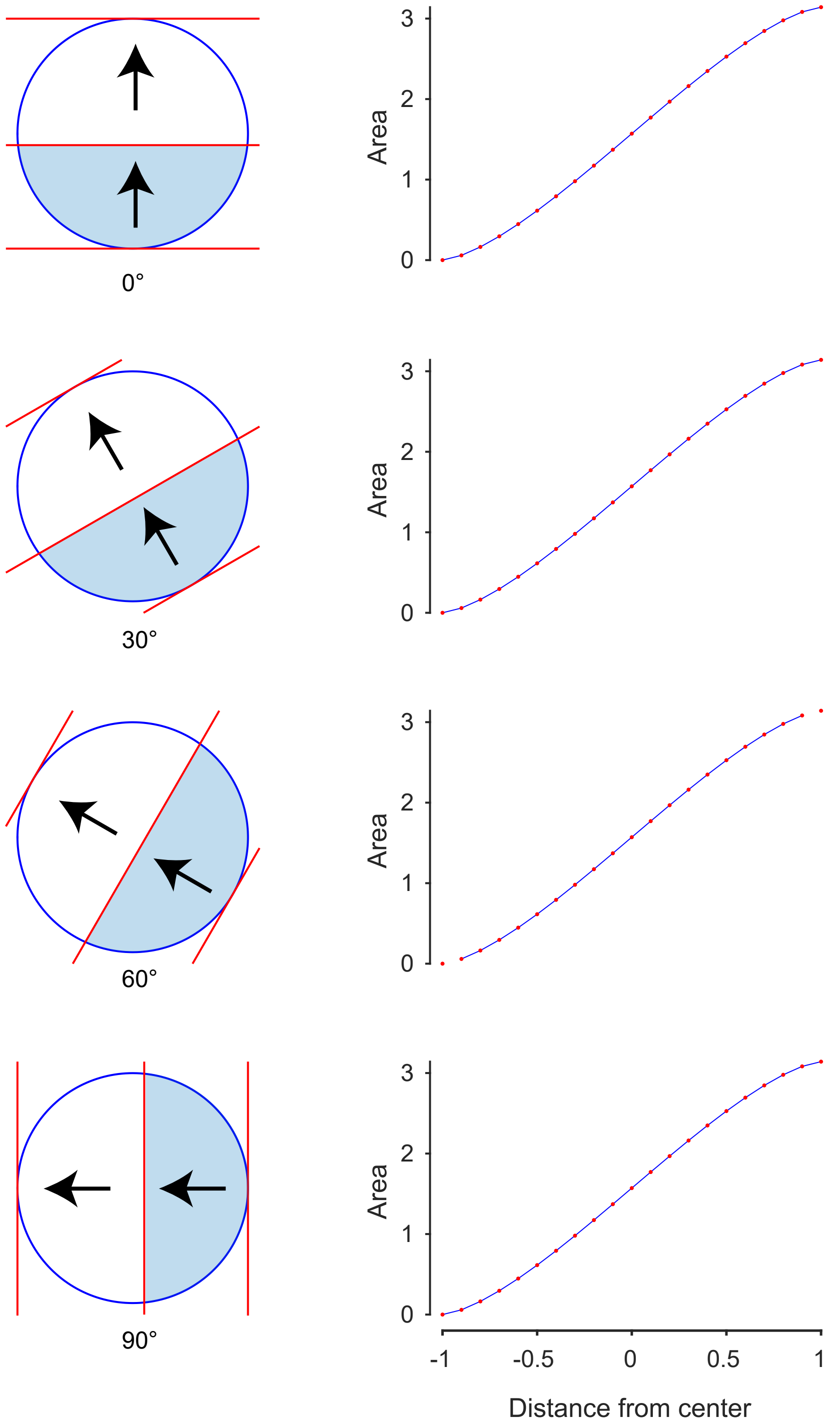

Fig. C.1 : Validation using circular hair fields

Activations of circular hair fields were computed for different slopes. Analytically computing the area, or using the numerical B-spline based approach, gave rise to identical results.

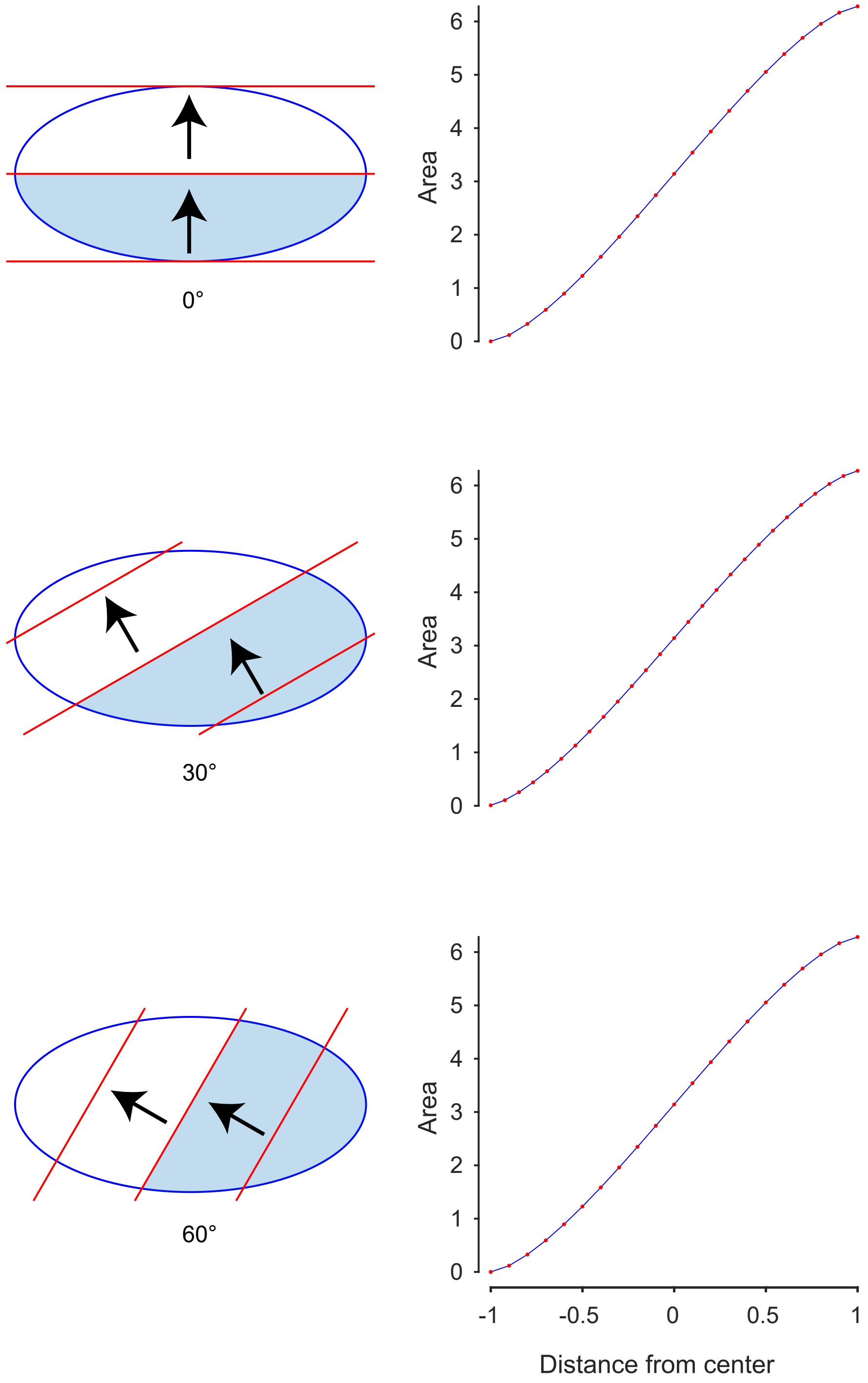

Fig. C.2 : Validation using elliptical hair fields

Activations of elliptical hair fields were computed for different slopes. Analytically computing the area, or using the numerical B-spline based approach, gave rise to identical results.

Appendix D

Kinematics of free flight pitch-up maneuvers in the housefly, *Musca domestica*

D.1 Introduction

For successful flight, animals and man-made machines should be able to perform two important tasks. First, they should be able to produce sufficient lift to counteract gravity and take off. Second, they should be able to stably alter the magnitude and direction of this lift vector to move from point A to point B without losing control and crashing. Insects are particularly good at this; they can carry loads several times their body weight, while being incredibly maneuverable (Dudley, 2002).

Miniature insects have a strict trade-off in their ability to generate lift and to control flight. Smaller insects must flap their wings at higher frequencies to generate sufficient lift, often at frequencies close to the limits of neural firing (Dudley, 2002). This puts a strain on maneuverability, which requires fast sensory feedback to precisely control wing kinematics and subsequent body position (Chang and Wang, 2014). Diptera, the true flies, are a subset of such miniature insects which are incredibly maneuverable, making them well suited for such studies. Both the aerodynamics of insect flight and the associated neural feedback control have been extensively studied in Diptera.

Flies generate lift by flapping their wings along a fixed plane with respect to the body, at high angles of attack and high wingbeat frequencies. The forces generated by flapping are due to both steady-state mechanisms during the translation phase of flapping and unsteady mechanisms during the rotation of the wing (Dickinson et al., 1999; Sane and Dickinson, 2001, 2002) (reviewed in: Chin and Lentink (2016); Sane (2003)). In flies, control of flight has been shown to be mediated by modified hindwings called halteres that detect gyroscopic forces and provide flight stabilizing feedback (Dickinson, 1999; Nalbach, 1994; Pringle, 1948). However, due to the small size of flies, and their rapid wing beat frequency, it has been hard to quantify the effect of this flight stabilizing feedback on the motion of the wing, and how it stabilizes the body. Specifically, relating minor changes in motions of the wing to changes in body trajectories has proved challenging.

Wing motions typically modify body motion in two different ways. It either causes changes in the flies' velocity by changing the magnitude of the lift vector, or it generates a torque that rotates the body. Changes in the direction of the lift-vector with respect to the body is minimal; flies have to change their lift-vector direction by rotating their body, much like a helicopter (David, 1978; Götz and Wandel, 1984). Alterations in magnitude of lift vector and generation of torque along the flies' principal axes (yaw, pitch, roll) seem to be primarily controlled by changes in the amplitude of stroke (Beatus et al., 2015; Fry et al., 2003; Muijres et al., 2014; Vogel, 1966, 1967b; Whitehead et al., 2015) (reviewed in Dickinson and Muijres (2016)). These changes are generally coupled with changes in wingbeat duration and stroke deviation that amplify the lift vector changes produced by stroke amplitude modifications (Dickinson, 1999; Muijres et al., 2014). However, subtle changes of the angle of attack in a stroke also seem to contribute to changes in forward speed and yaw rotations (Bergou et al., 2010; Dickinson et al., 1993; Muijres et al., 2015; Ristroph et al., 2011, 2010), and even pitch rotations in hawkmoths (Cheng et al., 2011).

This rich corpus of literature on flight demonstrates how wings generate lift and how changes in their kinematics can modify the body trajectories. However, in most of these experiments wing motion was correlated to changes in body trajectories by either evoking escape responses in flies or by perturbing them mid-flight. Such scenarios need not reflect the wing kinematics during active flight maneuvers. Flies indeed have been shown to perform the same maneuver in different ways depending on the context (Muijres et al., 2014). Additionally, most of these experiments were done on fruitflies, whose wing kinematics might not represent the control strategies used by the larger, more maneuverable, species of dipteran flies. Here, we performed experiments to understand the kinematics of active pitch-up maneuvers in the housefly, Musca domestica. Using an L-shaped flight area, we were able to elicit pure pitch maneuvers, which we filmed using high-speed cameras. We reconstructed the wing and the body movements in three dimensions to determine the relationship between them.

D.2 Methods

Experiments described here were performed on wildtype houseflies, Musca domestica, which were collected on the same day as the experiment.

Experimental setup and filming

Flies were introduced into an 'L'-shaped Plexiglas flight chamber with square cross-section (10 cm × 10 cm; Fig. D.1-A). A random checkerboard pattern on the walls provided visual guidance to flies during flight. The chamber was fitted with two white compact florescent lamps (CFL) at each end, which when on, attracted flies towards the ends of the 'L'. By switching on the lights in alternation, we could make flies actively fly from one end of the flight chamber to the other with high repeatability.

When the flies flew towards the top end of the L-box, they performed a sharp pitch-up at the corner of the L. This was captured using two Phantom v7.3 cameras, aligned at approximately right angles with respect to each other (Fig. D.1-A). The cameras filmed the flies' pitch-up at 4000 frames/sec, giving us approximately 16 frames per wing beat (wingbeat frequency is approx. 250Hz). A 150-watt metal halide lamp provided sufficient illumination for filming. Because flies are insensitive to wavelengths above 600 nm (Warrant and Nilsson, 2006), we placed a red filter that cuts off wavelengths under 610 nm to minimize impact of filming illumination on flight behavior. Before the start of the experiment, the cameras views were calibrated with a standard calibration object (for methodology please refer to Hedrick, 2008). Two or three flies were then released in the chamber and their flight was monitored for pitch-up events. The cameras were triggered manually when a pitch-up was observed.

Body and wing digitization

Flies' head, abdomen, wing bases and wing tips were digitized in the two camera views and the 3D position was reconstructed using software custom-written in MATLAB (Hedrick, 2008). Using these points, we were able to determine the body angles (yaw, pitch and roll), and two of the wing angles (stroke angle, stroke deviation). To determine the wing rotation angle for different frames, we adopted the approach used by Fry et al. (2003). Using a custom-written wing alignment graphical interface (adopted from Hedrick, 2008), we introduced a digital wireframe replica of the original wing in the frame and attached it to the body coordinate system defined by the head and the wing bases. Then we rotated the wireframe around to visually align it with the actual wing in every frame and measured the angular alignment of the wireframe with respect to the body coordinate system. By doing this for every frame, we digitized the wing rotation angle of the actual wing (Fig. D.1-B,C). This allowed us to completely determine all the body and wing kinematics of the fly during the pitch-up maneuver.

Body and wing angle definitions

The body coordinate system was first defined using the head and the two wing bases. The Euler angles describing the orientation of the fly's body coordinate system with respect to the global coordinate system were computed according to the Tait-Bryan convention. Such a definition allowed us to unambiguously compute the orientation of a fly on the current frame as a rotation with respect to the fly's body coordinate system from the previous frame. Yaw, pitch and roll, the flies' body angles, were defined as rotations along the flies' vertical, transverse and longitudinal axis respectively (flies' principal axes, Fig. D.1-D).

Stroke plane is the average plane which the wing tips traverse; this is generally defined over a wingbeat. To calculate this, the wing motion was first broken down into wingbeats. Within each wingbeat, we found a plane that contained both the wings for every frame. We averaged all planes in a wingbeat to compute the mean stroke plane. All wing angles were computed with respect to the stroke plane. Additionally, the angle of this plane with respect to the body plane was defined as stroke plane inclination (Fig. D.1-D).

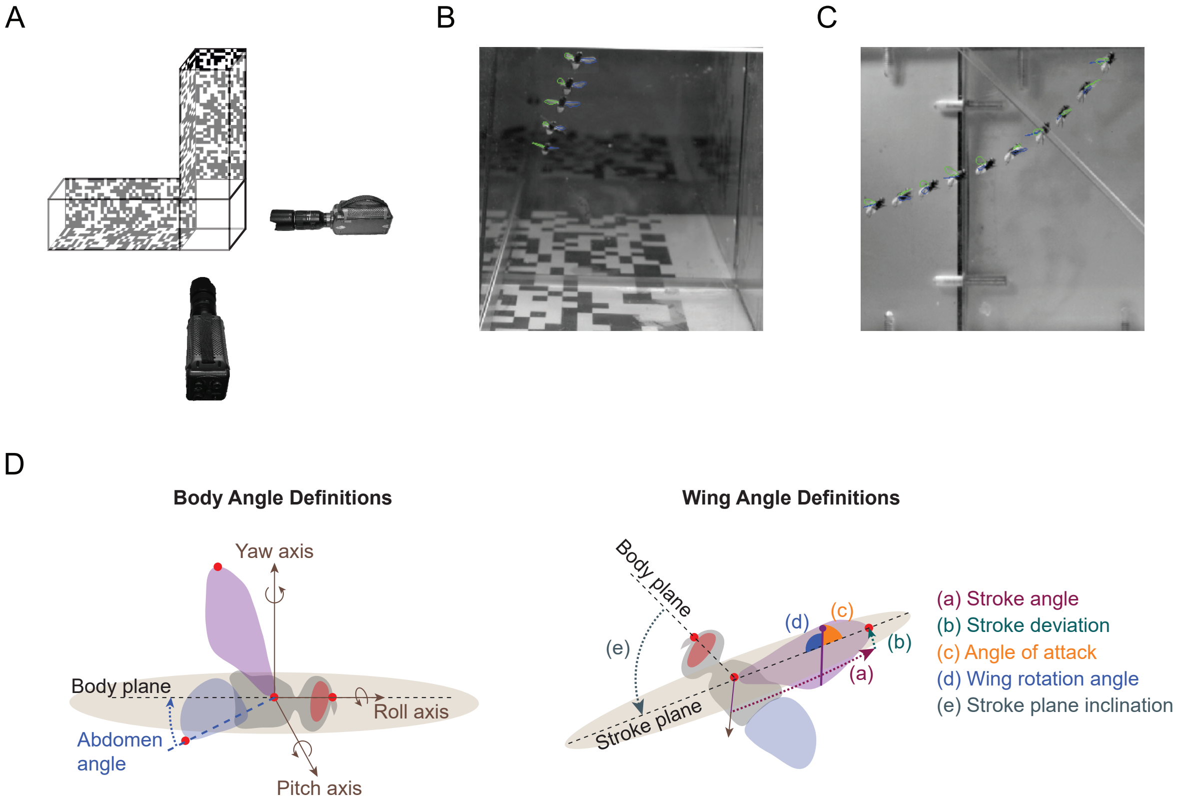

Fig. D.1 : Experimental setup and angle definitions

(A) Houseflies were introduced into the L-shaped flight chamber and motivated to fly towards the CFL lights at the two ends. Flies flying from the bottom end to the top end of the chamber performed a pitch-up maneuver at the corner of the L, which were captured by two high speed cameras filming at 4000 fps. **(B, C)** Front and side views of the pitch-up maneuvers captured by the high-speed cameras. The wing plane was digitized by fitting a digital wireframe on the wing images. **(D)** Yaw, pitch and roll were defined as rotation along the vertical, transverse and longitudinal axis of the fly (flies' principal axes). Stroke plane for every wingbeat was computed as the average plane containing both the wings. This was used to compute stroke angle, stroke deviation, and the angle of attack of the wing (see methods for definitions)

Three wing angles per wing were used to quantify wing position throughout the maneuver. The stroke angle was defined as the wing's angle of excursion within the stroke plane. It was computed by measuring the angle between the wing's projection on the stroke plane and the horizontal axis passing through the wing bases (Fig. D.1-D). The stroke deviation was defined as the angle between the wing and its projection on the stroke plane (Fig. D.1-D). Finally, the wing rotation angle was defined as the angle between the wing plane and the stroke plane (Fig. D.1-D). Additionally, we defined the angle of attack of the wing as the angle between the wing plane and the velocity vector of the wing. By this definition, the angle of attack of the wing is always between 0° and 90° during wing translation for both up and down stroke.

Apart from the wing and the body angles, we also computed the abdomen angle of the fly during the pitch-up maneuver. The abdomen angle was defined as the angle of the abdomen with respect to body plane (Fig. D.1-D). All the above computations and the subsequent data analysis was done in MATLAB (The MathWorks, Natick, MA, USA).

Data analysis

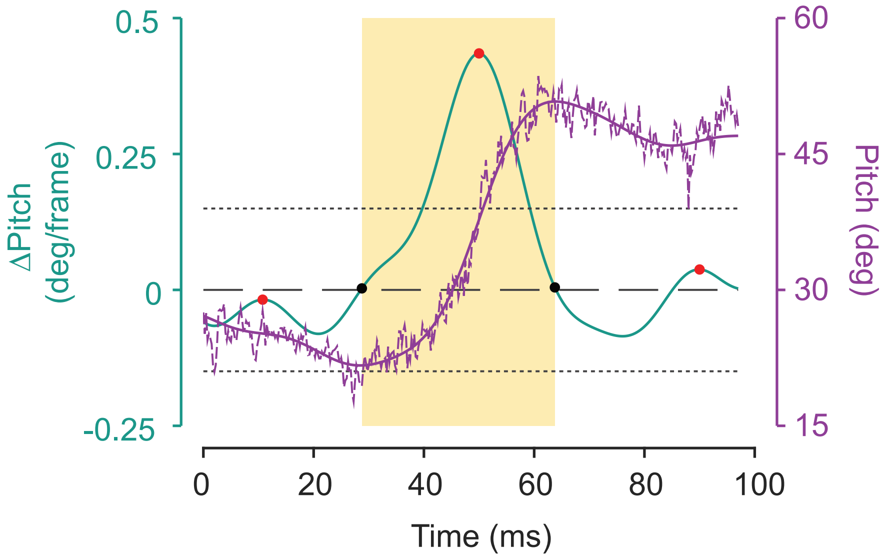

Fig. D.2 : Identification of pitch-up events

Pitch-up events were identified as instances where the local maxima (red dots) in Δpitch (change in pitch angle per frame) exceeded one standard deviation of Δpitch through the maneuver (represented by the dotted line). Zero-crossings (black dots) on both sides of such maxima marked the start and end of a pitch-up event (amber box). Sections that were not classified as pitch-up were considered to be straight flight.

For every fly, we broke down the maneuver into straight flight and pitch-up sections.

We used Δpitch, viz. change in pitch-angle per frame, for this classification. To remove body oscillations due to wingbeat, we first filtered Δpitch using a fourth order low-pass Butterworth filter with a cut-off at 50 Hz. Local maxima in Δpitch which exceeded one standard deviation of the Δpitch for the whole maneuver were then isolated. The closest zero-crossings on both sides of the maxima were found out and marked as the start and the end of the pitch-up section (Fig. D.2). Sections which weren't classified as pitch-ups were considered to be straight flight sections.

To compare straight flight and pitch-up sections, using statistical and cross-correlational methods, we first converted wing and body angle timeseries to wingbeat-based measures. Stroke amplitude was computed as the angle between the maximum and the minimum stroke angle within a wingbeat. Stroke deviation and angle of attack were averaged over the duration of the wingbeat. Other angles, such as body angles and abdomen angles, were also averaged over the wingbeat.

We compared changes between straight flight and pitch-ups in every maneuver using pairwise statistical tests. This allowed us to ignore the variability between flies and only compare changes that occurred during the maneuver. For every parameter, we calculated the average for pitch-up and compared it with average for straight flight. If a maneuver had multiple pitch-ups and/or straight flights, we simply compared all the pitch-ups with all the straight flights. Most of these parameter averages were not normally distributed (Lilliefors test, $p<0.05$). For these, we used the Wilcoxon paired-sample test to statistically compare straight and pitch-up sections. If the parameters were normally distributed, we used the paired-sample t test instead as the Wilcoxon paired-sample test has a lower power in distinguishing differences for samples from a normal distribution (Zar, 2013).

Next, we computed cross-correlation of wing angles with both pitch and Δpitch. Because the changes in wing angles generally preceded the body angles, we computed the maximum cross-correlation coefficient within a window of two wingbeats. Confidence intervals for the cross-correlation coefficients were estimated from the standard deviation of the cross-correlation coefficient obtained for two white noise timeseries (or auto-correlation for a white noise timeseries). Only cross-correlation coefficients greater than 1.645 times the white-noise standard deviation (90% confidence interval) were deemed correlated. Additionally, we used a one-sample student t-test to check if the distribution of these cross-correlation coefficients were significantly different from a distribution with zero mean. Only if the mean of cross-correlation coefficients for a parameter was significantly different from zero, we refer to it as significantly correlated. Using this method, we were able to quantify which parameters correlated with both pitch and Δpitch.

D.3 Results

We analysed a total of five pitch-up maneuvers, each of which were primarily characterized by changes along the pitch-up axis of the fly (Fig. D.3-A, see supplementary information for data). We show one representative throughout the paper, with statis-

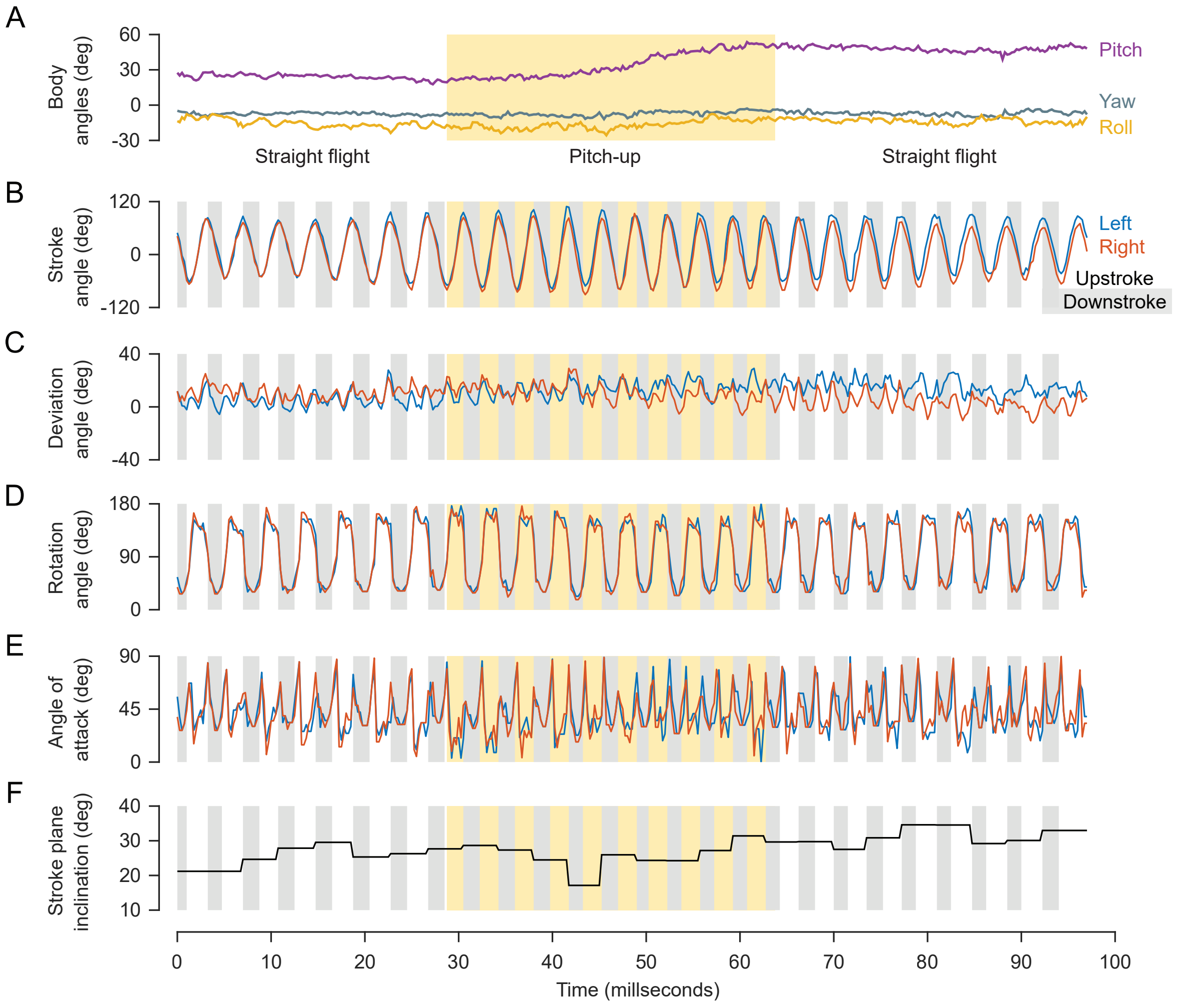

Fig. D.3 : Body and wing angles of a representative fly during a pitch-up maneuver

(A) Yaw (bluish grey), pitch (purple) and roll (yellow) of fly in Fig. D.1 performing a pitch-up maneuver. Sections classified as pitch-up were represented by an amber box. **(B-E)** Stroke angle, stroke deviation, wing rotation angle and the angle of attack of the left (blue) and right (red) wing during the pitch-up. The grey boxes and the white gaps represent the downstroke and upstroke respectively. **(F)** The angle of the stroke plane with respect to the body plane (the plane containing the head and the wing bases) during the pitch up event.

tics for all the analysed pitch up events where applicable. Fig. D.3 shows the body and wing angles of a housefly performing a pitch-up. Using change in pitch per frame, we broke down the maneuver into pitch-up and straight flight events (Fig. D.3-A, see methods). Qualitatively, stroke angle of both wings increases during the pitch-up and decreases back to normal levels after the maneuver (Fig. D.3-B). The other wing angles, on the other hand, do not change as dramatically as stroke angle, but subtle changes do occur (Fig. D.3-C-E). Interestingly, the stroke plane inclination decreases just at the initiation of pitch-up, after which it settles back to normal levels (Fig. D.3-F). To visualize these changes, we plotted the wing-tip trajectory of the representative for normal and pitch-up flight. The changes in both stroke amplitude and stroke plane are apparent in this visualization (Fig. D.4-G). Additionally, the deviation from the stroke plane also increases, i.e. wing trajectories are no longer tight around the stroke plane (Fig. D.4-G).

Fig. D.4 : Wing tip trajectories during a pitch-up manoeuvre

Wing tip trajectories of the left and right wing of the fly during straight flight (grey) and peak pitch-up (yellow). The dashed lines represent the average stroke plane during straight and pitch-up flight.

To quantify the correlation between wing angle changes and body angles, we converted the timeseries into a wingbeat-based measure (see methods). In Fig. D.5, we show the wingbeat measures of body and wing angles of the fly shown in Fig. D.4. Averages of these measures during pitch-up and straight flights were computed for every fly and compared using pairwise tests (box plots in Fig. D.5; see methods for details). The pitch-up classification was validated by comparing the change in body angles inside a pitch-up event with changes during straight flight. Only Δpitch increased significantly during a pitch-up event in all flies (Fig. D.5-A,B).

Stroke amplitude of both wings increased significantly during a pitch-up event (Fig. D.5-C,D). This increase is primarily due to an increase in the downstroke angle during a pitch-up (Fig. D.7-A,B). Although the upstroke angle also increased, it did not change symmetrically in both wings for all flies (Fig. D.7-C,D). Similarly, the two other wing angles, stroke deviation and angle of attack, did not change symmetrically during a pitch-up event (Fig. D.5-E-H).

The inclination of the stroke plane with respect to the body plane decreased consistently during pitch-up in all flies. (Fig. D.5-I,J). This decrease was accompanied by decreases in wingbeat durations (Fig. D.7-E,F). Although this decrease was prominent during the downstroke, both the stroke durations decreased during a pitch-up (Fig. D.7-G,H). Finally, the angle of the abdomen with respect to the body plane does not change significantly between normal and pitch-up events (Fig. D.5-I,J).

We next quantified the cross-correlation between wing angles and change in pitch angle (Fig. D.6, see methods). Left and right stroke amplitude, as well as mean stroke amplitude of both wings were significantly correlated with Δpitch (Fig. D.6, Fig. D.8-A). The downstroke angle, and upstroke angle to an extent, were also correlated with changes in pitch angle (Fig. D.7-A). Stroke plane inclination was negatively correlated with pitch-angle, indicating a decrease during pitch-up (Fig. D.6). Similarly, decreases in wingbeat, upstroke and downstroke durations were correlated with pitch-up (Fig. D.7-A). Other angles, like stroke deviation, angle of attack and abdomen angle do not show any significant correlations with Δpitch (Fig. D.6).

Both pitch-event based analysis and the above cross-correlation analysis look for changes correlated with Δpitch that return to normal after the pitch-up maneuver. To check if there were any body angle based changes in wing angles, we computed the cross-correlations of the wing angles with pitch, instead of Δpitch. Interestingly, abdomen angle is inversely correlated with pitch angle, i.e., it decreases with increasing pitch angle (Fig. D.7-B). The other wing angles do not show any consistently significant correlations with pitch (Fig. D.7-B,C).

D.4 Discussion

Flies perform a vast variety of behaviors ranging from rapid territorial chases (Land and Collett, 1974) to relatively slower tracking of odor sources (Saxena et al., 2018). Their capability to perform such vastly different behaviors based on the context rests critically on their ability to be stable yet maneuverable during flight (dynamic flight stability – reviewed in Sun (2014)). Although a lot is known about the aerodynamics of insect flight and the sensory control of it, it is not clear how changes in wing motion translate to complex body maneuvers that underlie this vast range of behaviors. Previous studies have outlined the role of stroke angle in pitch-up maneuvers elicited by escape responses and other perturbations (Muijres et al., 2014; Whitehead et al., 2015). In this study, we sought to correlate wing kinematics with associated body rotations during active pitch-up maneuvers in houseflies.

We find that the stroke amplitude of the housefly increases significantly when it pitches up. This is primarily due an increase in the downstroke angle, i.e. the front stroke angle, during the pitch-up maneuver (Fig. D.7-A,B, D.8-A). Additionally, wing beat

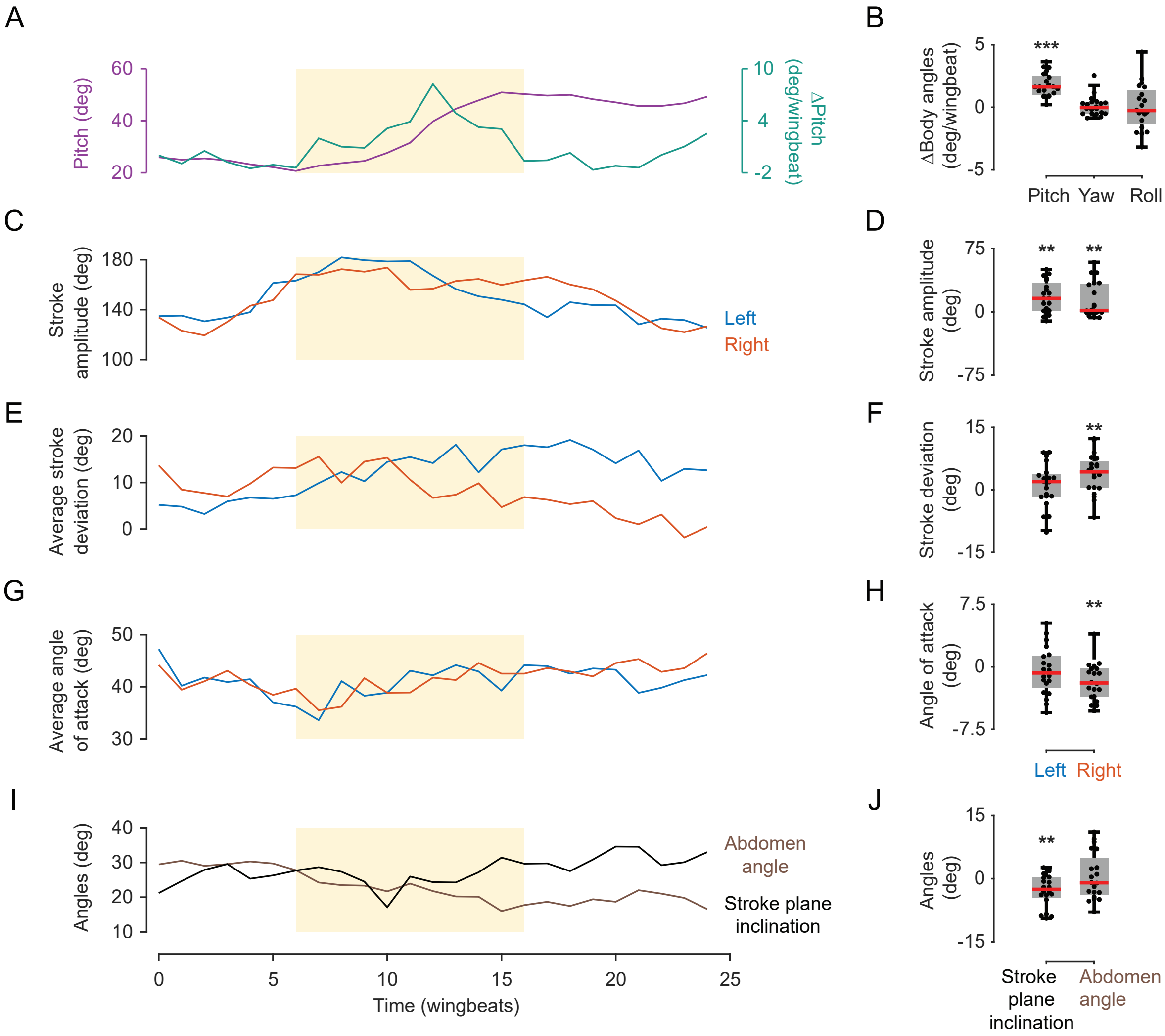

Fig. D.5 : Changes in wing-angles during a pitch-up event

(A) Pitch and change in pitch (Δpitch) of a representative fly during a pitch-up. Unlike Fig. D.4-A, the pitch angle is averaged over the duration of a wingbeat. The amber box represents a pitch-up event (see methods for details). **(B)** Pairwise difference of Δbody angles between pitch-up and straight flight sections for all flies. Only Δpitch changes significantly during a pitch-up event. **(C-J)** Changes in wingbeat-based measures for a pitch-up event is shown for a representative fly (same as Fig. D.4). The distribution of pairwise difference between pitch-up and straight flight sections, for all flies, are illustrated as box and whisker plots. The central 50% of the data around the median (red line) is represented by the box. The whiskers represent data within 1.5 times the interquartile range. Asterisks represent statistically significant comparisons (Wilcoxon/student-t paired-sample test, * - $p < 0.05$, ** - $p < 0.01$, *** - $p < 0.001$).

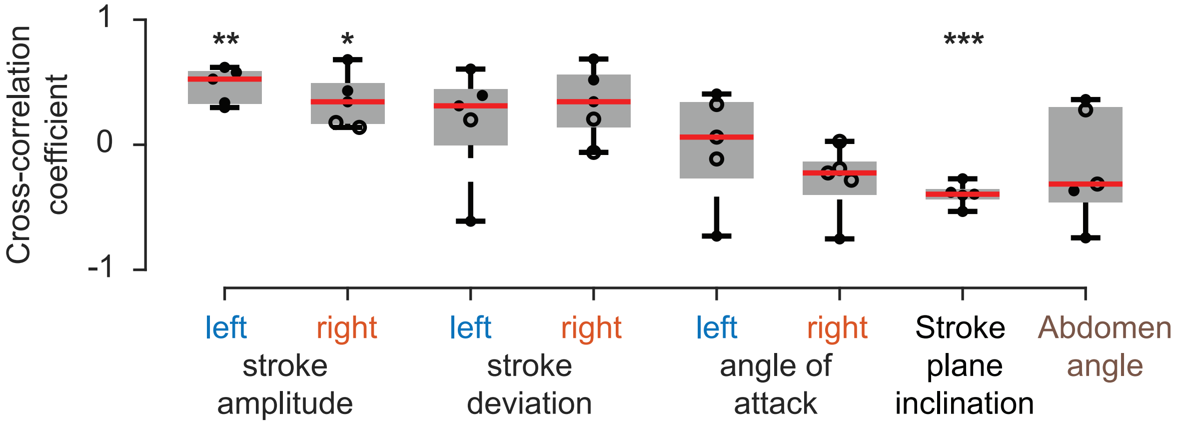

Fig. D.6 : Cross-correlation coefficients of wingbeat-based measures

Coefficient of cross-correlation between the wingbeat-based measures and Δpitch. Filled circles indicate significant correlations (90% confidence interval, see methods). Asterisks represent statistically significant comparisons.

duration decreases concurrently with increases in stroke amplitude (Fig. D.7-E,F, D.8-A). This decrease is again mainly due to a decrease in downstroke duration of the wingbeat (Fig. D.7-G,H, D.8-A). Increases in downstroke angle, and a concomitant decrease in downstroke duration, would substantially increase the wing tip velocity during the downstroke, thereby increasing the downstroke lift. As an equivalent lift is not generated during the upstroke, these changes would cause a torque that would cause the fly to pitch-up. This result is consistent with previous experiments, primarily done on fruitflies (Dickinson, 1999; Muijres et al., 2014; Whitehead et al., 2015; Zanker, 1990; reviewed in Dickinson and Muijres, 2016), suggesting that an increase in downstroke angle coupled with a decrease in downstroke duration might be one way flies generate a pitch-up torque.

However, unlike fruitflies, we find that changes in upstroke angle also contribute to the changes in stroke amplitude, albeit inconsistently (Fig. D.7-C,D, D.8-A). Upstroke duration also decreases during the pitch-up maneuver, although not to the same extent as the downstroke duration (Fig. D.7-E,F, D.8-A). Similarly, stroke deviation does not symmetrically increase in both wings during a pitch-up, although such changes are clearly seen in wing-tip trajectories (Fig. D.4, see supplementary information for all the data). Bidirectional increase in stroke angle, coupled with changes in wingbeat duration and stroke deviation, especially at the ends of a stroke (Fig. D.6), might enhance torque generation, thereby aiding rapid pitch-ups in houseflies. Subtle but distinct changes to wing trajectories, similar to the ones seen during pitch-up, have been noticed in flies presented with different airflows (Hollick, 1940).

A key finding of this study is the change in stroke plane inclination during a pitch-up maneuver. Stroke plane inclination decreases, i.e. stroke plane angle shifts towards the body plane right at the onset of pitch-up (Fig. D.6, D.5-I,J, D.6. These changes, although small, are tightly correlated with change in pitch angle. This is quite different from increases in stroke amplitude which occur well in advance of a pitch-up maneuver. The tight temporal link between the decrease in stroke plane inclination and change in pitch leads us to suggest that this event initiates the pitch-up maneuver in houseflies. However, it has been suggested that stroke plane angle and stroke amplitude are interdependent in Diptera, which might potentially explain our observed increase in stroke plane angle (Vogel, 1967a). On the other hand, independent shifts of stroke plane angle have been proposed to control free flight maneuvers in flies (Zanker, 1988b). To resolve this, we compared the correlation between stroke amplitude and stroke plane angle with change in pitch and stroke plane angle. If stroke plane inclination and stroke amplitude are indeed interdependent, their correlation should be better than the correlation between stroke plane inclination and change in pitch angle. The correlation between stroke plane inclination and change in pitch is far tighter than its correlation with stroke amplitude (Fig. D.8-D), although the difference is not statistically significant. Rigorous experiments with higher sample size of pitch-ups would be required to thoroughly quantify the extent of change in stroke plane and its interdependence on stroke amplitude during a pitch-up manoeuvre.

Angle of attack, on the other hand, does not change much on the short timescales of a pitch-up event in houseflies (Fig. D.5-G,H). This also matches observations from fruitflies (Muijres et al., 2014; Whitehead et al., 2015). However, our angle of attack resolution was limited to 0.1 radians (approx. ~5.7°) due to our wing digitization procedure (see methods). Small changes in angle of attack would therefore not be detectable in our experiments. For instance, fruitflies have been shown to change their angle of attack during fast forward flight (Ristroph et al., 2011). Additionally, hawkmoths have been shown to generate active pitch-up torque by changing their angle of attack (Cheng et al., 2011). Houseflies too might be using small changes in angle of attack to aid pitch up torque generation and possibly lift generation during vertical flight.

Abdomen angle, like stroke plane inclination, is inversely correlated with the absolute pitch angle, i.e., it streamlines with the body plane as the fly pitches up (Fig. D.5-I, D.8-B). This suggests that the sustained lift after a pitch-up requires changes in body posture. Lift-thrust ratio has indeed been shown to be dependent on body angle in flies (Vogel, 1966; Zanker, 1988b). This, combined with the changes in stroke amplitude and stroke plane angle, might give rise to the pitch-up torque as proposed by Zanker (1988b). Increasing number of recent literature suggest that the abdomen is yet another structure that insects use to control flight (Berthé and Lehmann, 2015; Dyhr et al., 2013; Hinterwirth and Daniel, 2010; Lawson and Srinivasan, 2017; Luu et al., 2011; Taylor et al., 2013; Zanker, 1988a).

As a whole, our study propose that houseflies use a combination of stroke amplitude, stroke plane inclination, wingbeat duration and abdomen angle to actively pitch-up. The next step would be to recreate the trajectories in dynamically scaled robots to tease out the relative contribution of each of these parameters (such as those used in

Dickinson et al. (1999). These robots, however, might first have to be altered to include the abdomen to untangle its influence on control of flight. Elucidating the mechanical structures that shape wing kinematics might be far more challenging. The wing-hinge is a complex biomechanical structure which combines passive cuticular linkages with an active clutch and gear system for fast yet flexible control of the wing (reviewed in Deora et al. (2017)). Using our methodology to generate repeatable active pitch-ups, one can now begin to experiment with different components of the wing hinge to quantify its effect on wing and body kinematics, thereby unraveling the role of these mechanical structures in control of flight.

Bibliography

T. Beatus, J. M. Guckenheimer, and I. Cohen. Controlling roll perturbations in fruit flies. *Journal of The Royal Society Interface*, 12(105):20150075, Apr. 2015. ISSN 1742-5689, 1742-5662. doi: 10.1098/rsif.2015.0075.

A. J. Bergou, L. Ristroph, J. Guckenheimer, I. Cohen, and Z. J. Wang. Fruit Flies Modulate Passive Wing Pitching to Generate In-Flight Turns. *Physical Review Letters*, 104(14):148101, Apr. 2010. doi: 10.1103/PhysRevLett.104.148101.

R. Berthé and F.-O. Lehmann. Body appendages fine-tune posture and moments in freely manoeuvring fruit flies. *Journal of Experimental Biology*, 218(20):3295–3307, Oct. 2015. ISSN 0022-0949, 1477-9145. doi: 10.1242/jeb.122408.

S. Chang and Z. J. Wang. Predicting fruit fly's sensing rate with insect flight simulations. *Proceedings of the National Academy of Sciences*, 111(31):11246–11251, Aug. 2014. ISSN 0027-8424, 1091-6490. doi: 10.1073/pnas.1314738111.

B. Cheng, X. Deng, and T. L. Hedrick. The mechanics and control of pitching manoeuvres in a freely flying hawkmoth (Manduca sexta). *Journal of Experimental Biology*, 214(24):4092–4106, Dec. 2011. ISSN 0022-0949, 1477-9145. doi: 10.1242/jeb.062760.

D. D. Chin and D. Lentink. Flapping wing aerodynamics: From insects to vertebrates. *Journal of Experimental Biology*, 219(7):920–932, Apr. 2016. ISSN 0022-0949, 1477-9145. doi: 10.1242/jeb.042317.

C. T. David. The relationship between body angle and flight speed in free-flying Drosophila. *Physiological Entomology*, 3(3):191–195, 1978.

T. Deora, N. Gundiah, and S. P. Sane. Mechanics of the thorax in flies. *Journal of Experimental Biology*, 220(8):1382–1395, Apr. 2017. ISSN 0022-0949, 1477-9145. doi: 10.1242/jeb.128363.

M. H. Dickinson. Haltere–mediated equilibrium reflexes of the fruit fly, Drosophila melanogaster. *Philosophical Transactions of the Royal Society of London B: Biological Sciences*, 354(1385):903–916, May 1999. ISSN 0962-8436, 1471-2970. doi: 10.1098/rstb.1999.0442.

M. H. Dickinson and F. T. Muijres. The aerodynamics and control of free flight manoeuvres in Drosophila. *Phil. Trans. R. Soc. B*, 371(1704):20150388, Sept. 2016. ISSN 0962-8436, 1471-2970. doi: 10.1098/rstb.2015.0388.

M. H. Dickinson, F. O. Lehmann, and K. G. Gotz. The active control of wing rotation by Drosophila. *Journal of Experimental Biology*, 182(1):173–189, Sept. 1993. ISSN 0022-0949, 1477-9145.

M. H. Dickinson, F.-O. Lehmann, and S. P. Sane. Wing Rotation and the Aerodynamic Basis of Insect Flight. *Science*, 284(5422):1954–1960, June 1999. ISSN 0036-8075, 1095-9203. doi: 10.1126/science.284.5422.1954.

R. Dudley. *The Biomechanics of Insect Flight – Form, Function, Evolution.* Princeton

University Press, Princeton, NJ, reprint edition edition, Oct. 2002. ISBN 978-0-691-09491-5.

J. P. Dyhr, K. A. Morgansen, T. L. Daniel, and N. J. Cowan. Flexible strategies for flight control: An active role for the abdomen. *Journal of Experimental Biology*, 216(9):1523–1536, May 2013. ISSN 0022-0949, 1477-9145. doi: 10.1242/jeb.077644. 00064.

S. N. Fry, R. Sayaman, and M. H. Dickinson. The Aerodynamics of Free-Flight Maneuvers in Drosophila. *Science*, 300(5618):495–498, Apr. 2003. ISSN 0036-8075, 1095-9203. doi: 10.1126/science.1081944.

K. G. Götz and U. Wandel. Optomotor control of the force of flight in Drosophila and Musca. *Biological Cybernetics*, 51(2):135–139, Nov. 1984. ISSN 1432-0770. doi: 10.1007/BF00357927.

T. L. Hedrick. Software techniques for two- and three-dimensional kinematic measurements of biological and biomimetic systems. *Bioinspiration & Biomimetics*, 3(3): 034001, 2008. ISSN 1748-3190. doi: 10.1088/1748-3182/3/3/034001.

A. J. Hinterwirth and T. L. Daniel. Antennae in the hawkmoth Manduca sexta (Lepidoptera, Sphingidae) mediate abdominal flexion in response to mechanical stimuli. *Journal of Comparative Physiology A*, 196(12):947–956, Dec. 2010. ISSN 0340-7594, 1432-1351. doi: 10.1007/s00359-010-0578-5. 00053.

F. S. J. Hollick. The flight of the dipterous fly Muscina stabulans Fallén. *Phil. Trans. R. Soc. Lond. B*, 230(572):357–390, Nov. 1940. ISSN 0080-4622, 2054-0280. doi: 10.1098/rstb.1940.0003.

M. F. Land and T. S. Collett. Chasing behaviour of houseflies (Fannia canicularis). *Journal of comparative physiology*, 89(4):331–357, Dec. 1974. ISSN 1432-1351. doi: 10.1007/BF00695351.

K. K. K. Lawson and M. V. Srinivasan. Flight control of fruit flies: Dynamic response to optic flow and headwind. *Journal of Experimental Biology*, 220(11):2005–2016, June 2017. ISSN 0022-0949, 1477-9145. doi: 10.1242/jeb.153056.

T. Luu, A. Cheung, D. Ball, and M. V. Srinivasan. Honeybee flight: A novel 'streamlining' response. *Journal of Experimental Biology*, 214(13):2215–2225, July 2011. ISSN 0022-0949, 1477-9145. doi: 10.1242/jeb.050310.

F. T. Muijres, M. J. Elzinga, J. M. Melis, and M. H. Dickinson. Flies Evade Looming Targets by Executing Rapid Visually Directed Banked Turns. *Science*, 344(6180): 172–177, Apr. 2014. ISSN 0036-8075, 1095-9203. doi: 10.1126/science.1248955.

F. T. Muijres, M. J. Elzinga, N. A. Iwasaki, and M. H. Dickinson. Body saccades of Drosophila consist of stereotyped banked turns. *Journal of Experimental Biology*, 218(6):864–875, Mar. 2015. ISSN 0022-0949, 1477-9145. doi: 10.1242/jeb.114280.

G. Nalbach. Extremely non-orthogonal axes in a sense organ for rotation: Behavioural analysis of the dipteran haltere system. *Neuroscience*, 61(1):149–163, July 1994. ISSN 0306-4522. doi: 10.1016/0306-4522(94)90068-X.

J. W. S. Pringle. The gyroscopic mechanism of the halteres of Diptera. *Phil. Trans. R. Soc. Lond. B*, 233(602):347–384, Nov. 1948. ISSN 0080-4622, 2054-0280. doi: 10.1098/rstb.1948.0007.

L. Ristroph, A. J. Bergou, G. Ristroph, K. Coumes, G. J. Berman, J. Guckenheimer, Z. J. Wang, and I. Cohen. Discovering the flight autostabilizer of fruit flies by inducing aerial stumbles. *Proceedings of the National Academy of Sciences*, 107(11): 4820–4824, Mar. 2010. ISSN 0027-8424, 1091-6490. doi: 10.1073/pnas.1000615107. 00116.

L. Ristroph, A. J. Bergou, J. Guckenheimer, Z. J. Wang, and I. Cohen. Paddling Mode of Forward Flight in Insects. *Physical Review Letters*, 106(17):178103, Apr. 2011. doi: 10.1103/PhysRevLett.106.178103.

S. P. Sane. The aerodynamics of insect flight. *Journal of Experimental Biology*, 206 (23):4191–4208, Dec. 2003. ISSN 0022-0949, 1477-9145. doi: 10.1242/jeb.00663.

S. P. Sane and M. H. Dickinson. The control of flight force by a flapping wing: Lift and drag production. *Journal of Experimental Biology*, 204(15):2607–2626, Aug. 2001. ISSN 0022-0949, 1477-9145.

S. P. Sane and M. H. Dickinson. The aerodynamic effects of wing rotation and a revised quasi-steady model of flapping flight. *Journal of Experimental Biology*, 205 (8):1087–1096, Apr. 2002. ISSN 0022-0949, 1477-9145.

N. Saxena, D. Natesan, and S. P. Sane. Odor source localization in complex visual environments by fruit flies. *The Journal of Experimental Biology*, 221(2):jeb172023, Jan. 2018. ISSN 0022-0949, 1477-9145. doi: 10.1242/jeb.172023.

M. Sun. Insect flight dynamics: Stability and control. *Reviews of Modern Physics*, 86 (2):615–646, May 2014. doi: 10.1103/RevModPhys.86.615.

G. J. Taylor, T. Luu, D. Ball, and M. V. Srinivasan. Vision and air flow combine to streamline flying honeybees. *Scientific Reports*, 3, Sept. 2013. ISSN 2045-2322. doi: 10.1038/srep02614.

S. Vogel. Flight in Drosophila : I. Flight Performance of Tethered Flies. *Journal of Experimental Biology*, 44(3):567–578, June 1966. ISSN 0022-0949, 1477-9145.

S. Vogel. Flight in Drosophila : II. Variations in Stroke Parameters and Wing Contour. *Journal of Experimental Biology*, 46(2):383–392, Apr. 1967a. ISSN 0022-0949, 1477-9145.

S. Vogel. Flight in Drosophila : III. Aerodynamic Characteristics of Fly Wing Sand Wing Models. *Journal of Experimental Biology*, 46(3):431–443, June 1967b. ISSN 0022-0949, 1477-9145.

E. Warrant and D.-E. Nilsson. *Invertebrate Vision.* Cambridge University Press, Oct. 2006. ISBN 978-0-521-83088-1.

S. C. Whitehead, T. Beatus, L. Canale, and I. Cohen. Pitch perfect: How fruit flies control their body pitch angle. *Journal of Experimental Biology*, 218(21):3508–3519, Nov. 2015. ISSN 0022-0949, 1477-9145. doi: 10.1242/jeb.122622.

J. M. Zanker. How does lateral abdomen deflection contribute to flight control of-Drosophila melanogaster? *Journal of Comparative Physiology A*, 162(5):581–588, Sept. 1988a. ISSN 0340-7594, 1432-1351. doi: 10.1007/BF01342633.

J. M. Zanker. On the mechanism of speed and altitude control in Drosophila melanogaster. *Physiological Entomology*, 13(3):351–361, 1988b. ISSN 1365-3032. doi: 10.1111/j.1365-3032.1988.tb00485.x.

J. M. Zanker. The wing beat of Drosophila Melanogaster. III. Control. *Phil. Trans. R. Soc. Lond. B*, 327(1238):45–64, Feb. 1990. ISSN 0080-4622, 2054-0280. doi: 10.1098/rstb.1990.0042.

D.5 Supplementary information

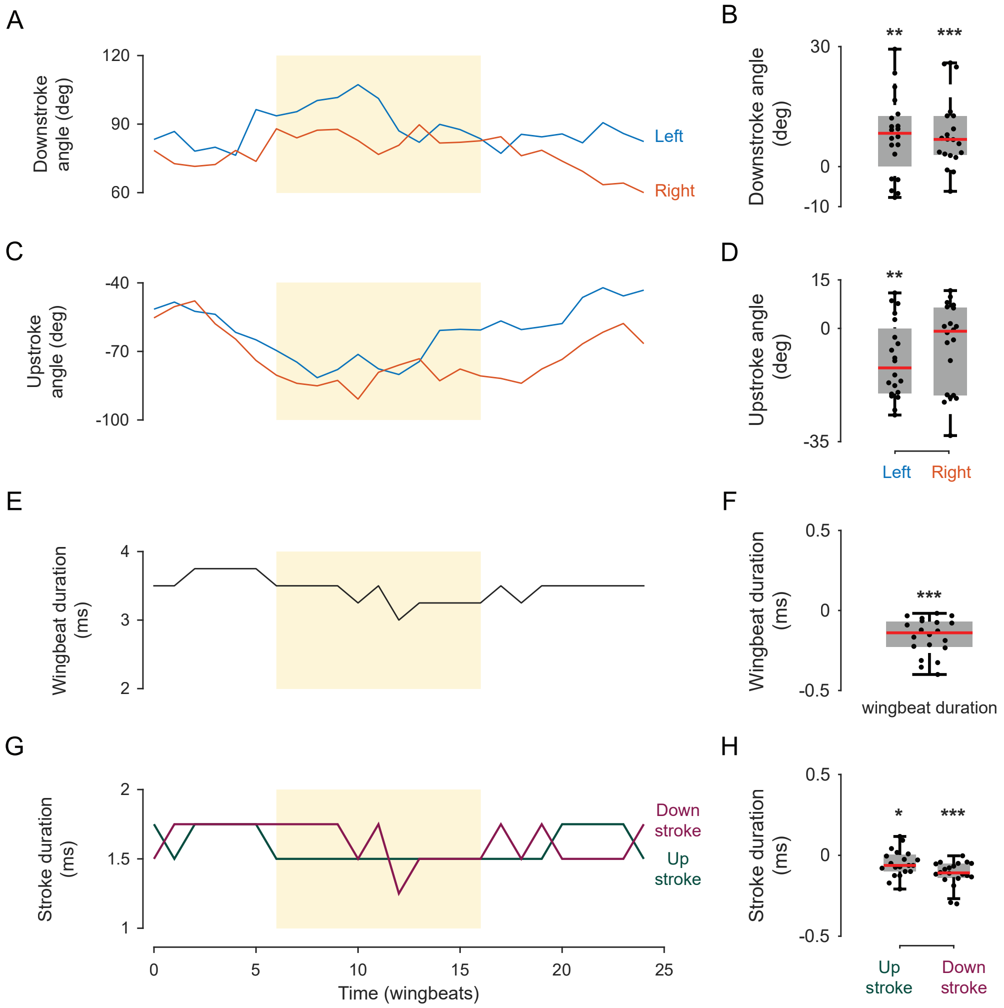

Fig. D.7 : **Changes in wing-stroke measures during pitch-up**

(A-H) Changes in stroke parameters during a pitch-up event for a representative fly (same as Fig. D.5). The distribution of pairwise difference between pitch-up and straight flight sections, for all flies, are illustrated as box and whisker plots. Asterisks represent statistically significant comparisons (Wilcoxon paired-sample test, *-$p < 0.05$,**-$p < 0.01$,***-$p < 0.001$).

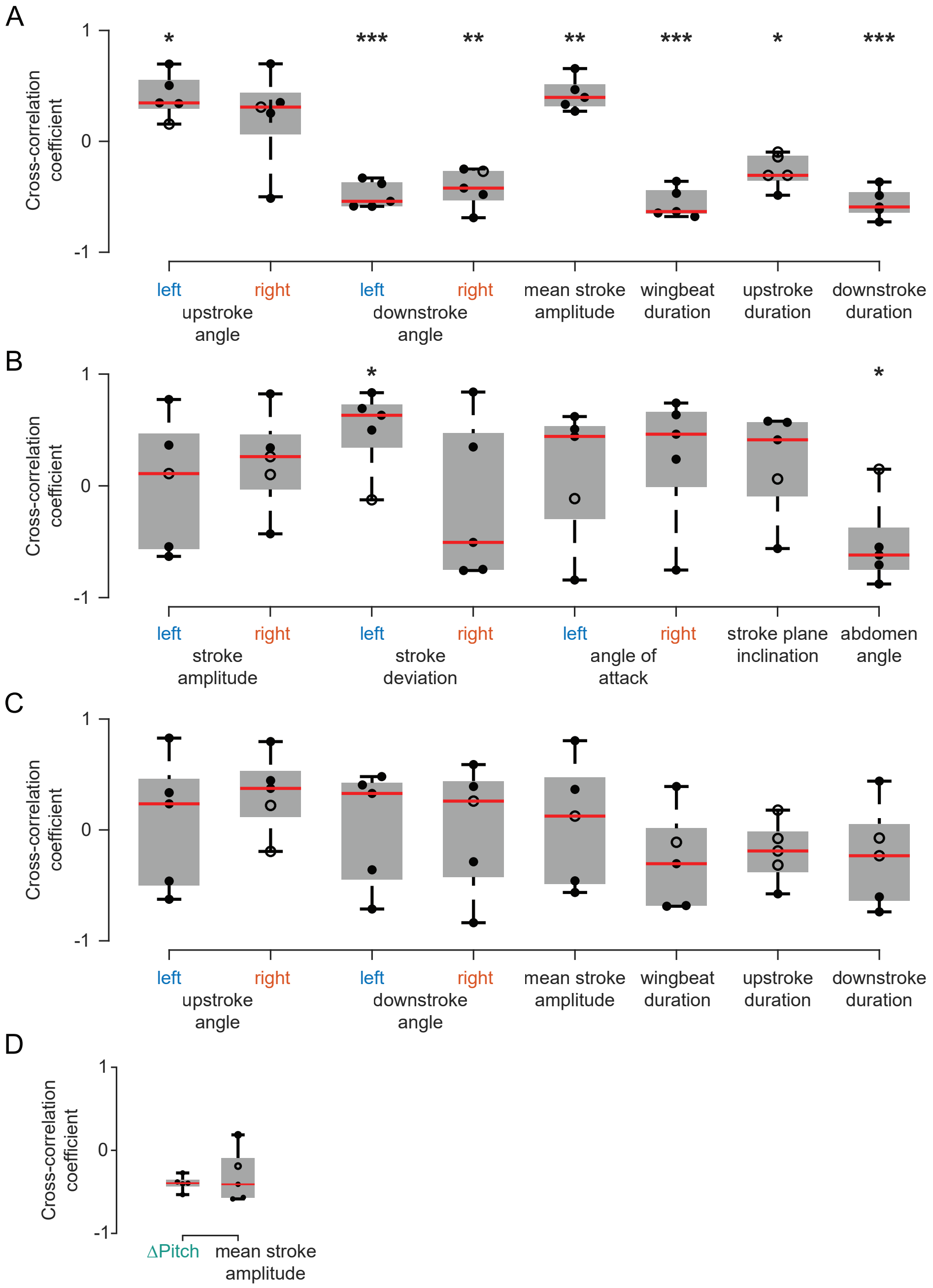

Fig. D.8 : Cross-correlation coefficients of wingbeat-based measures with pitch

(A-H) Coefficient of cross-correlation between the wingbeat-based measures and (raw) pitch angle. Filled circles indicate significant correlations (90% confidence interval, see methods). Asterisks represent statistically significant comparisons..

Raw plots (Fly-2)
Supplementary Information
Natesan, Wadhwa and Sane

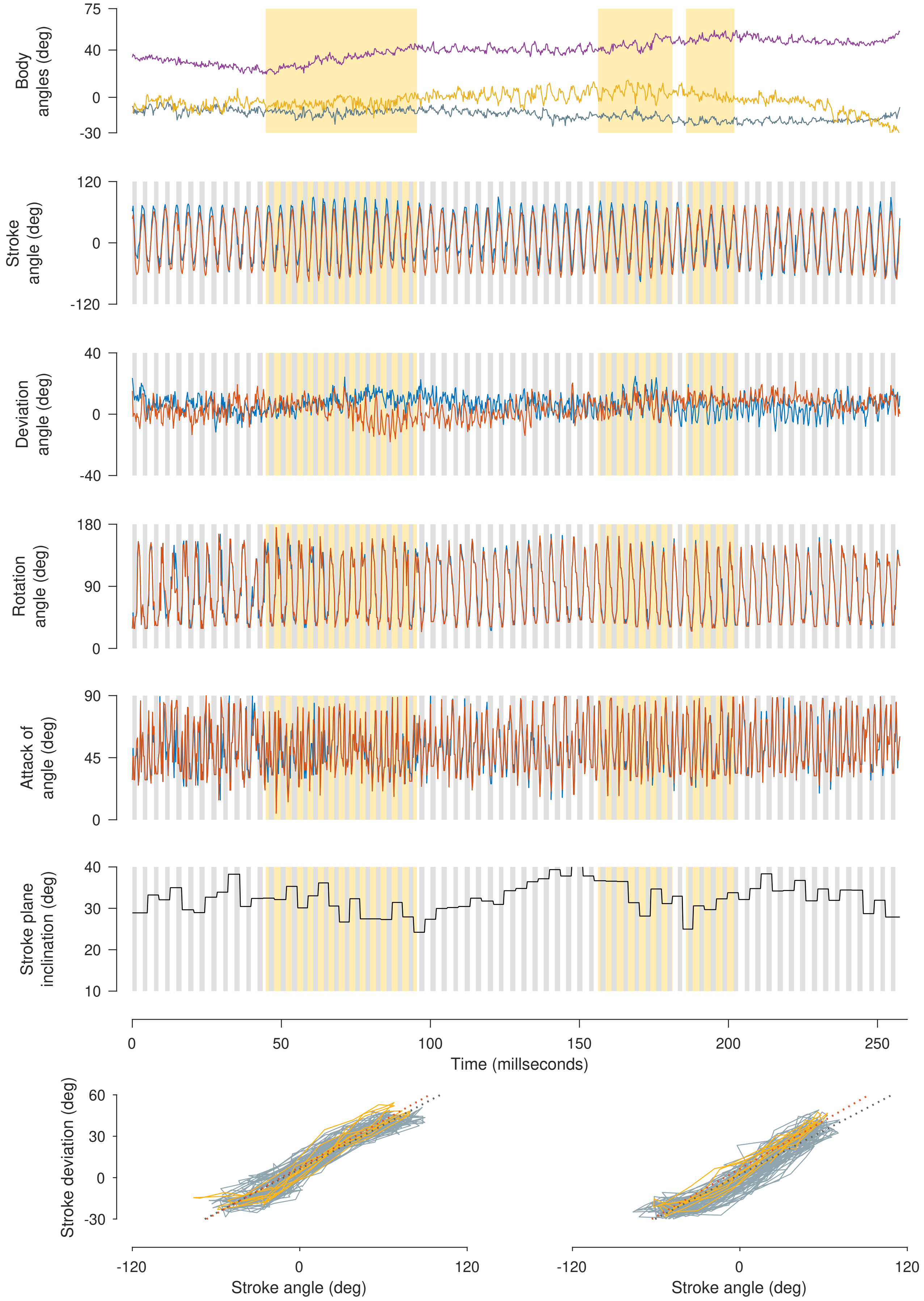

Raw plots (Fly-3)
Supplementary Information
Natesan, Wadhwa and Sane

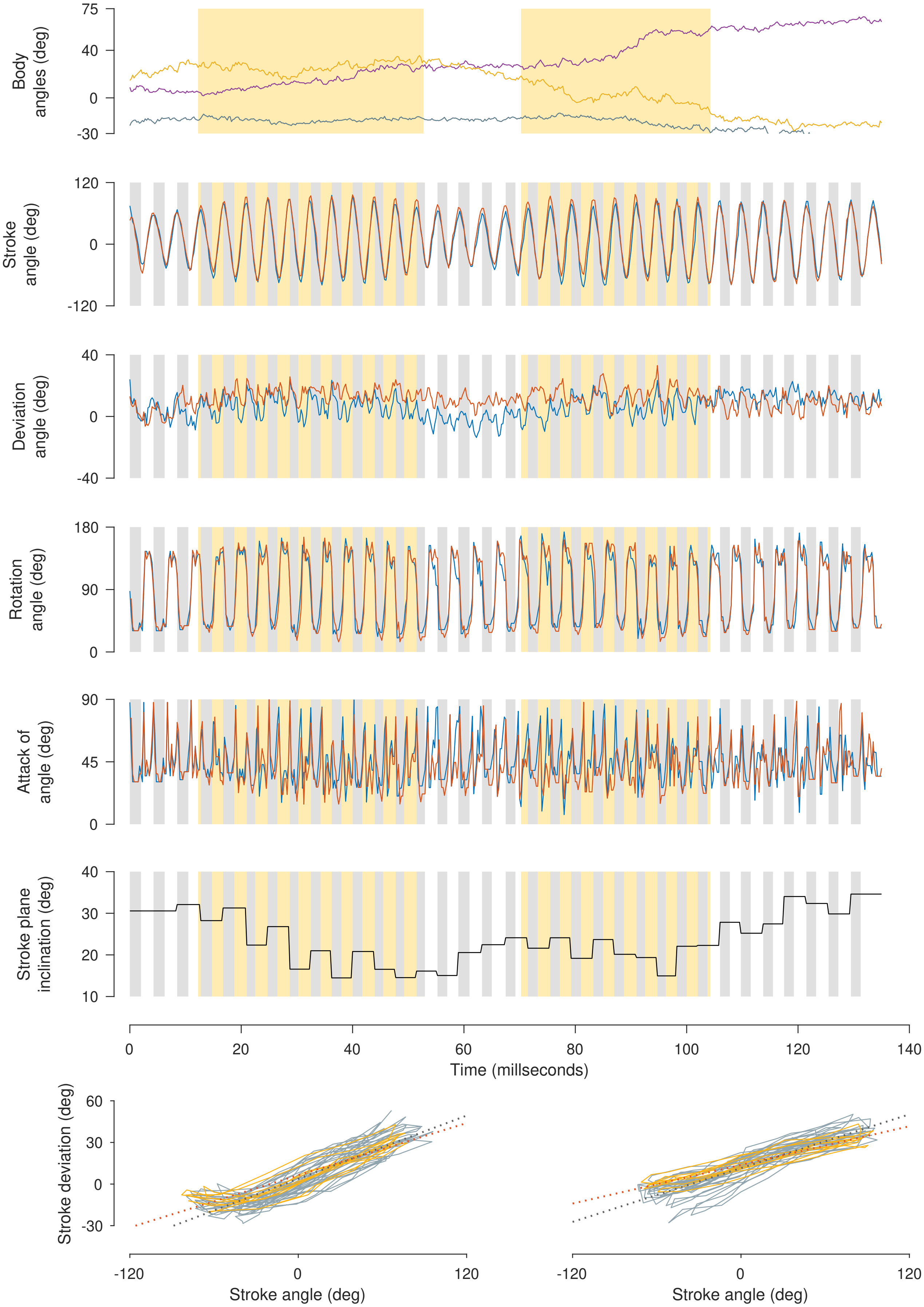

Raw plots (Fly-4)
Supplementary Information
Natesan, Wadhwa and Sane

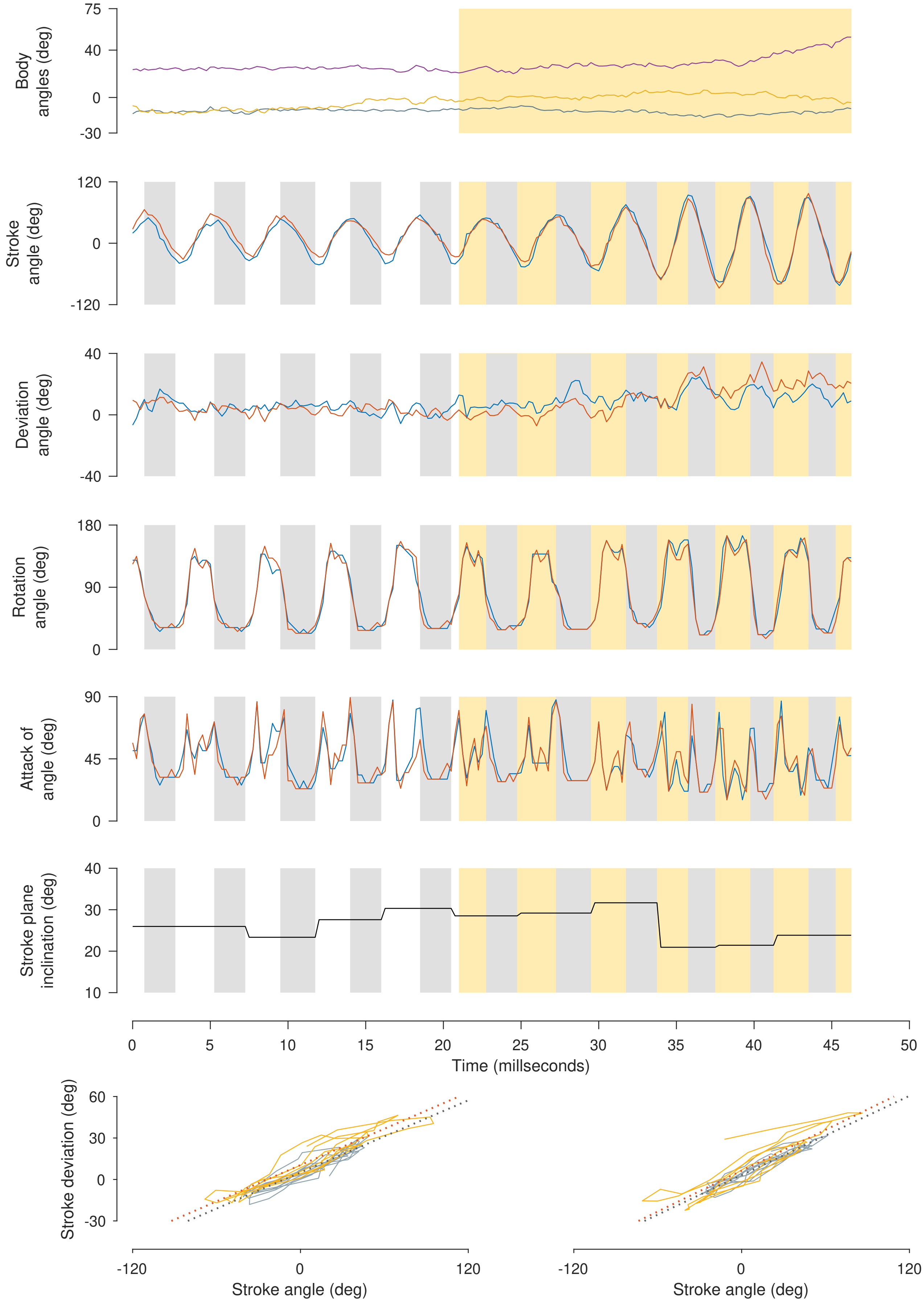

Raw plots (Fly-5)
Supplementary Information
Natesan, Wadhwa and Sane

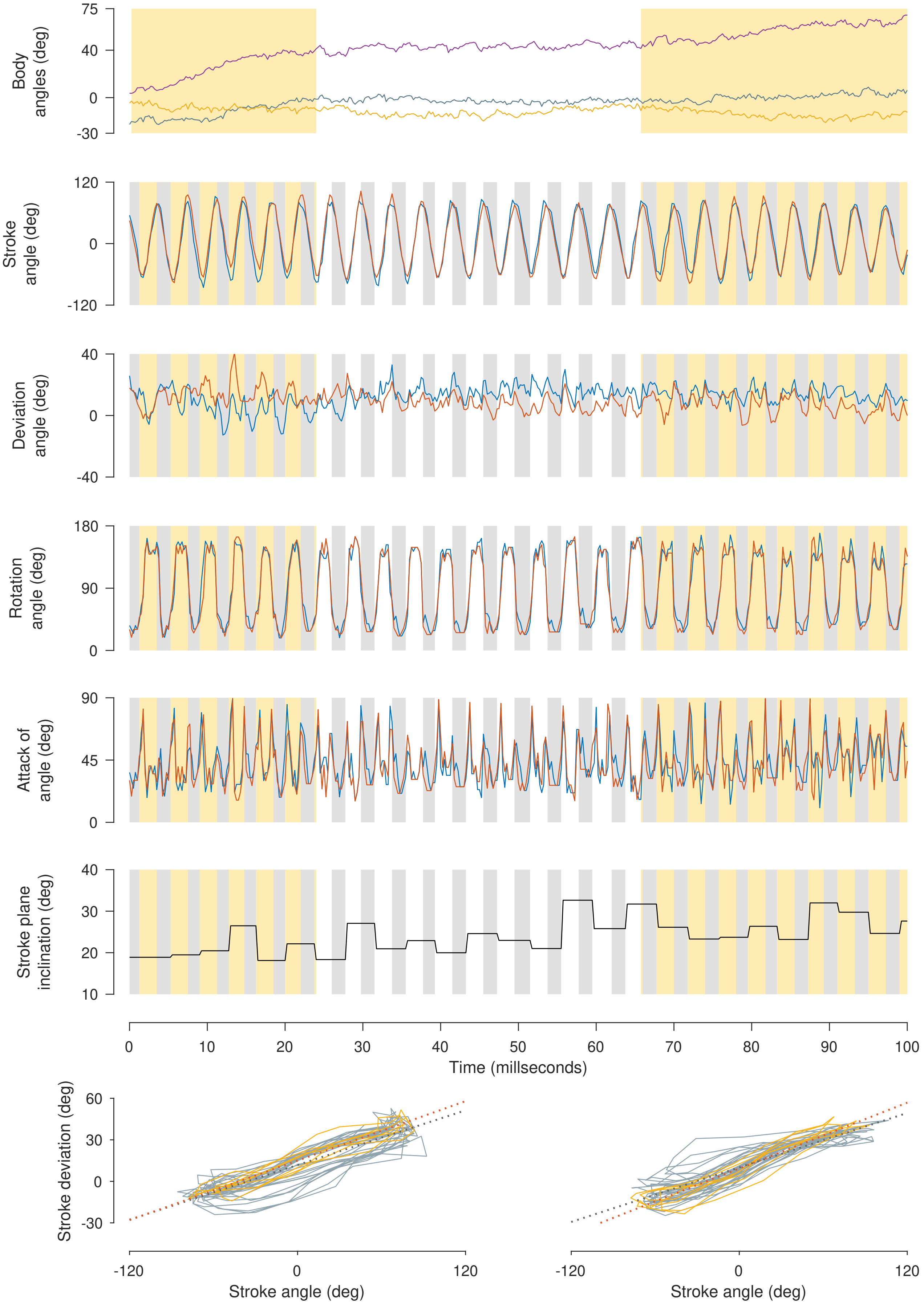

Wingbeat plots (Fly-2)
Supplementary Information
Natesan, Wadhwa and Sane

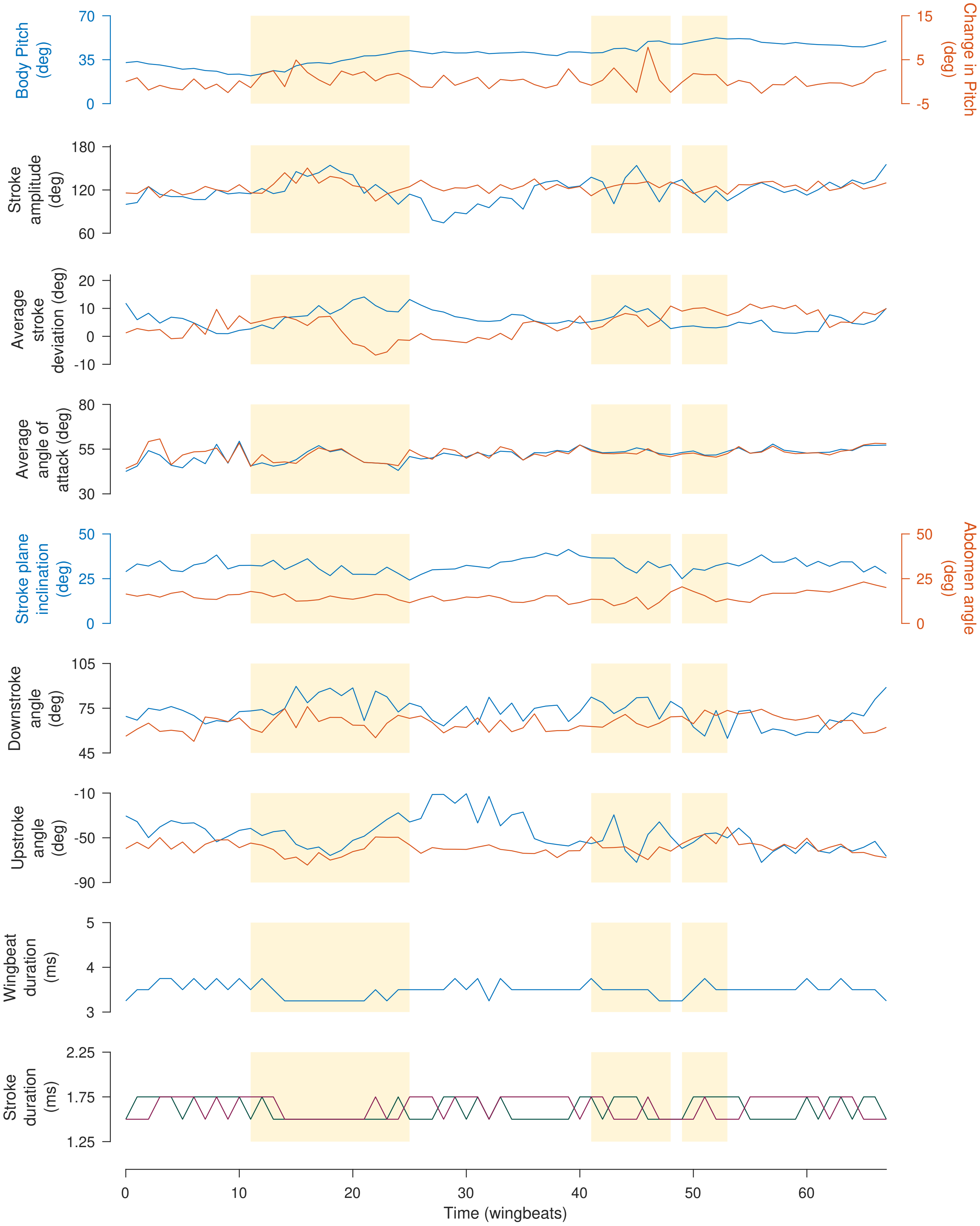

Wingbeat plots (Fly-3)
Supplementary Information
Natesan, Wadhwa and Sane

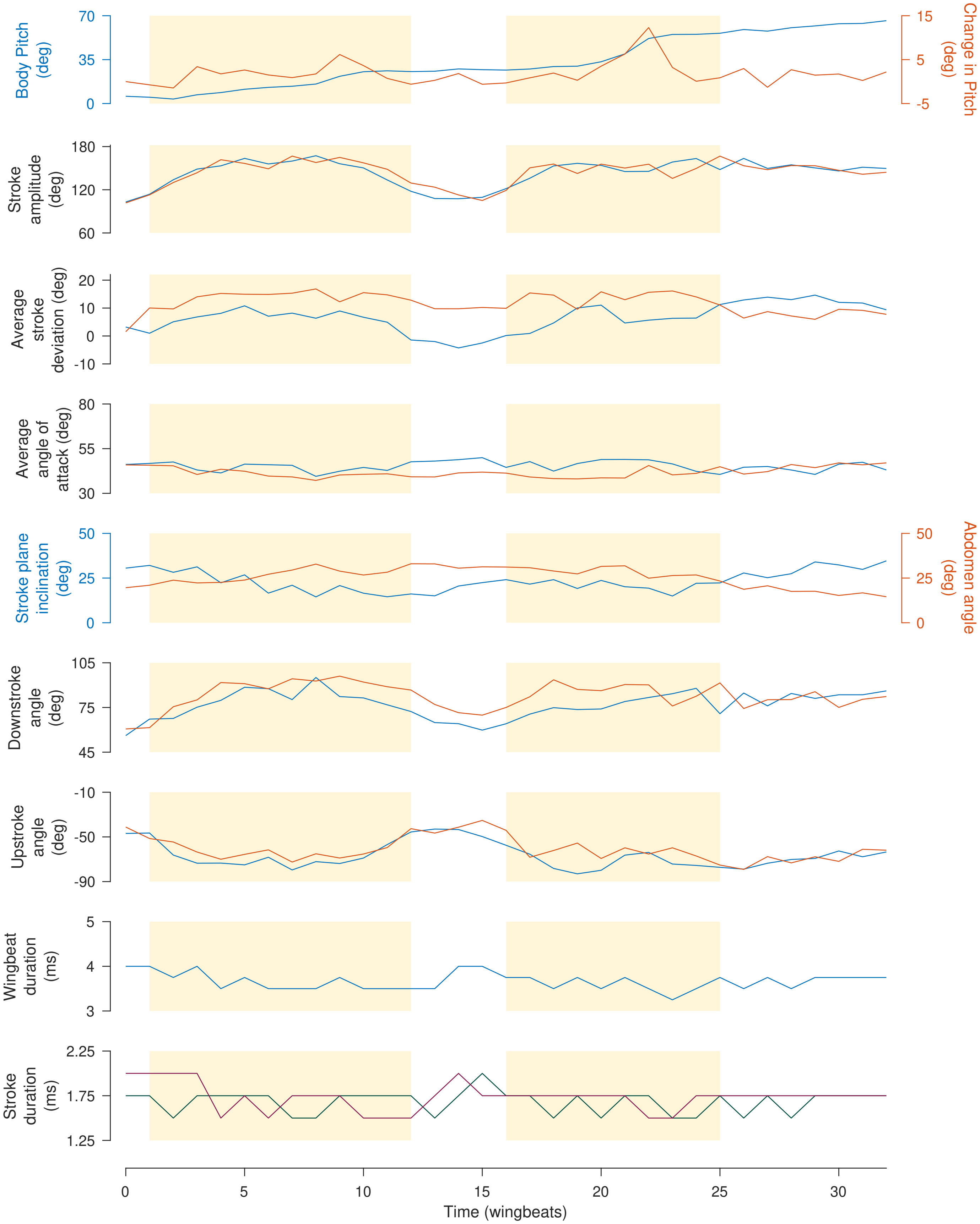

Wingbeat plots (Fly-4)
Supplementary Information
Natesan, Wadhwa and Sane

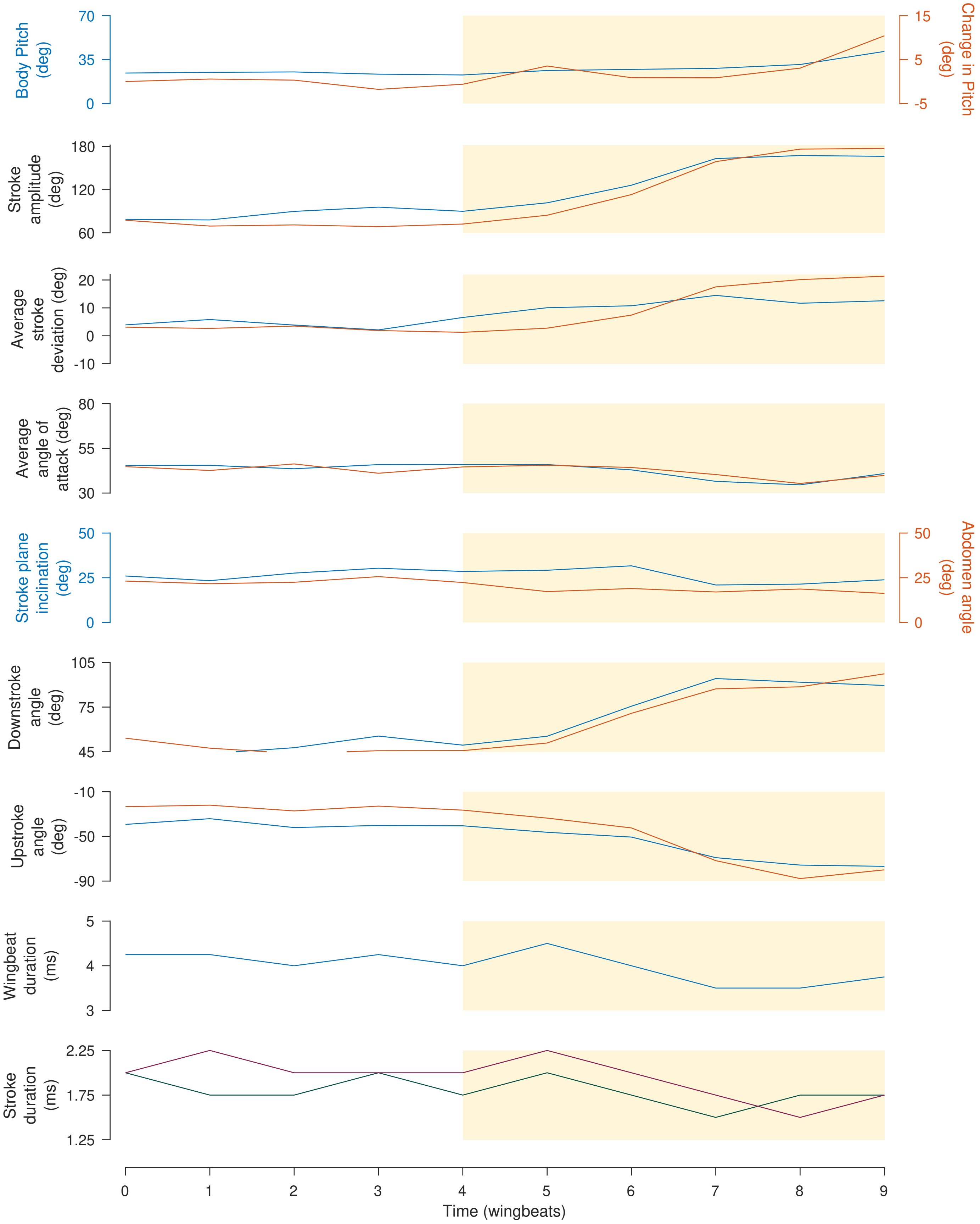

Wingbeat plots (Fly-5)
Supplementary Information
Natesan, Wadhwa and Sane